RECENTERING BEAM-COLUMN CONNECTIONS USING SHAPE MEMORY ALLOYS

A Thesis
Presented to
The Academic Faculty

by

Bradley W. Penar

In Partial Fulfillment
of the Requirements for the Degree
Master of Science in Civil Engineering

School of Civil and Environmental Engineering
Georgia Institute of Technology
August 2005

RECENTERING BEAM-COLUMN CONNECTIONS USING SHAPE MEMORY ALLOYS

Approved by:

Dr. Reginald DesRoches, Advisor
School of Civil and Environmental Engineering
Georgia Institute of Technology

Dr. Roberto Leon, Co-advisor
School of Civil and Environmental Engineering
Georgia Institute of Technology

Dr. Laurence Jacobs
School of Civil and Environmental Engineering
Georgia Institute of Technology

Date Approved: 11 July 2005

ACKNOWLEDGEMENTS

First and foremost, I would like to thank my wonderful wife, Rachel, for her support throughout the whole graduate school experience. I couldn't have done it without you. I still can't believe how you can make everything turn out so perfect... from our coordinated move to Atlanta, to our beautiful wedding, to the perfect timing of the arrival of our little girl. You make me feel like the luckiest person in the world.

I would like to thank my advisors, Dr. Reginald DesRoches and Dr. Roberto Leon, for their guidance and support. Many thanks to Dr. Jacobs for reviewing my thesis. I would also like to thank my officemates; Jason McCormick, Jamie Padgett, Monique Hite, and Laura Barbero-Buffa. We did have the best office in the whole building, well, besides the tight quarters and the 95 degree temperatures.

I would like to thank Mike the Machinist for helping me out. Thank you for putting me in touch with Winn-Tech to get the Nitinol bars machined. If it wasn't for you, I'd still be waiting for GTRI to call me back. I must also thank Buddy Evans from Steel Inc. in Scottdale, Georgia for donating much of the steel that was used for this project.

TABLE OF CONTENTS

ACKNOWLEDGEMENTS . . . . . **iii**

LIST OF TABLES . . . . . **vii**

LIST OF FIGURES . . . . . **viii**

LIST OF SYMBOLS AND ABBREVIATIONS . . . . . **xvi**

SUMMARY . . . . . **xix**

I INTRODUCTION **1**

1.1 Outline of thesis 2

II LITERATURE REVIEW **3**

2.1 Overview of Nitinol shape memory alloys 3

2.1.1 Microstructure 5

2.1.1.1 Shape memory effect 7

2.1.1.2 Superelastic effect 9

2.1.2 Stress-strain-temperature relationships 10

2.1.3 Physical properties 11

2.1.3.1 Cyclic properties 12

2.1.3.2 Strain rate effects 16

2.1.3.3 Temperature dependence 16

2.1.3.4 Corrosion resistance 18

2.1.4 Application of Nitinol in passive seismic devices 18

2.1.4.1 Damping and recentering applications 18

2.1.4.2 Partially restrained steel connections using Nitinol 20

2.2 Moment resisting frame connections 24

2.2.1 Performance of steel MRF during the Northridge earthquake 27

2.3 Partially restrained steel connections 29

2.4 Recentering connections 30

2.4.1 Post-tensioned precast concrete moment frame connections 30

2.4.2 Post-tensioned steel connections 32

III EXPERIMENTAL PROCEDURES 36
3.1 Loading scheme 36
3.2 Lateral bracing system 37
3.3 Actuator 41
3.4 Loading Procedure 41
3.5 Instrumentation and data acquisition 42
3.5.1 Beam instrumentation 46
3.5.2 Column instrumentation 49
3.5.3 Overall assemblage instrumentation 51
3.5.4 Tendon instrumentation 51
3.6 Preliminary analysis and design 54
3.6.1 Results of preliminary analysis 55
3.7 Component tests 57
3.7.1 A36 Steel rod tests 58
3.7.2 Superelastic Nitinol rod tests 63
3.8 Connection specifications 67
3.8.1 Test setup with A36 steel tendons 67
3.8.2 Test setup with superelastic Nitinol tendons 69
IV EXPERIMENTAL RESULTS AND DISCUSSION 72
4.1 A36 Steel tendon tests 72
4.1.1 Test I 72
4.1.2 Test II 79
4.1.3 Test III 85
4.2 Superelastic Nitinol tendon test 87
4.2.1 Higher cycle test 93
4.3 Comparison of results 96
V CONCLUSIONS 98
5.1 Recommendations for future research 100
APPENDIX A DATA REDUCTION 102
A.1 Moment 102
A.2 Stress in tendons 102

A.3 Rotations . . . 102
A.3.1 Total rotation . . . 102
A.3.2 Concentrated rotation . . . 103
A.3.3 Elastic rotation . . . 103
A.3.4 Plastic rotation . . . 103
A.3.5 Cumulative total rotation . . . 104
A.3.6 Cumulative plastic rotation . . . 104
A.4 Principal strain from strain gauge rosettes . . . 104
A.5 Principal strain angle from strain gauge rosettes . . . 104
APPENDIX B STEEL TENDON TEST DATA . . . 105
B.1 Test I on 04/25/05 . . . 105
B.2 Test II on 04/27/05 . . . 134
B.3 Test III on 04/29/05 . . . 163
APPENDIX C NITINOL TENDON TEST DATA . . . 187
C.1 Initial testing . . . 187
C.2 Higher drift cycle testing . . . 216
REFERENCES . . . 217

LIST OF TABLES

2-1 Properties of Nitinol compared to typical structural steel [19]. 5

3-1 SAC Loading Protocol 42

3-2 Instrumentation setup in data acquisition system (channels 0-31) 44

3-3 Instrumentation setup in data acquisition system (channels 32-55) 45

3-4 Results from preliminary DRAIN-2DX analysis 56

4-1 Elastic stiffness for steel tendon test I 73

4-2 Comparison of Nitinol tendon connection with A36 steel connections 97

LIST OF FIGURES

2-1 Simplified illustration of the phases of SMA. 6

2-2 Hysteresis associated with phase transformations in SMA [75]. 7

2-3 Nickel-Titanium phase diagram with change in M_s as a function of nickel content [56]. 8

2-4 Crystallographic changes during the shape memory effect cycle. 9

2-5 Crystallographic changes during the superelastic effect cycle. 10

2-6 Stress-strain-temperature relationships in Nitinol. 11

2-7 Effects of repeated cyclic deformation on residual strain at various temperatures [23]. 13

2-8 Effect of repeated load cycles on hysteresis of superelastic Nitinol [40]. 13

2-9 Stress-strain behavior for a) 1.8 mm diameter and b) 25.4 mm diameter Nitinol wire subjected to quasistatic cyclic loading [22]. 14

2-10 Comparison of Nitinol wire and bars subjected to quasistatic cyclic loading showing a) loading stress plateau, σ_L , b) unloading stress plateau, σ_{UL}, c) residual strain,ϵ_r and d) equivalent viscous damping ratio, ξ_{eq} [22]. 15

2-11 Comparison of damping properties with respect to specimen size [49]. 15

2-12 Effect of ambient temperature on the stress-displacement behavior of Nitinol with various compositions [69]. 17

2-13 Supplemental recentering device showing a) top view and b) lateral view [25]. . . . 19

2-14 Not recentering device utilizing prestrained superelastic wire acting as counteracting springs [25]. 20

2-15 Functioning scheme of a recentering device [25]. 21

2-16 Three cathedrals in Italy have been successfully retrofitted using Nitinol devices; a) the bell tower of the S. Giorgio Church in Trignano [39], b) the tympanum of S. Francesco Basilica in Assisi [7], and c) the facade of the S. Feliciano Cathedral in Foligno [7]. 22

2-17 a) University of Notre Dame connection b) Closeup of top angle connector with supplemental superelastic rods [1]. 23

2-18 Test setup of beam-column connection using martensitic Nitinol tendons as the primary source of moment resistance [54]. 24

2-19 Results from tests by Ocel [54] that show a) Moment/Total Rotation Comparison of first 3% drift cycle and b) Equivalent viscous damping per drift intensity for initial, retest, and dynamic tests 25

2-20 Development of plastic hinges contribute to significant energy dissipation [28]. . . 26

2-21 Typical welded MRF connection prior to 1994 [28]. 27

2-22 Post-Northridge earthquake moment connection details using a) reinforcing cover plates [27], b) haunch brackets [27], and c) Reduced beam section [8]. 30

2-23 Unbonded post-tensioned precast concrete beam-column subassemblage used by El-Sheikh et al. [26]. 31

2-24 Nonlinear elastic load-deflection behavior with inset showing opening of gaps at the beam-column joint during lateral loading [26]. 31

2-25 a) Post-tensioned (PT) moment connection developed by Ricles et al. with b) showing a moment resisting frame with PT connections [60]. 33

2-26 a) Post-tensioned (PT) moment connection with concrete filled steel tube columns developed by Ricles et al. [59] and b) Post-tensioned friction damped moment connection developed by Rojas et al. [63]. 33

2-27 a) Schematic of the post-tensioned energy dissipating connection [15]. b) Moment rotation curve of the PTED connection showing flag shaped hysteresis [14]. 35

3-1 Idealization of the loading scheme for the beam-column test setup. 37

3-2 Schematic of the subassemblage test setup. Lateral supports have been omitted for clarity. 38

3-3 Schematic of the subassemblage test setup showing lateral bracing system 39

3-4 SAC loading protocol 42

3-5 Picture of test setup with inset showing directional orientation 46

3-6 AutoCAD detail of beam instrumentation 47

3-7 AutoCAD detail of string potentiometer location 48

3-8 Picture showing connection of LVDT to beam and column 48

3-9 AutoCAD detail of column instrumentation 49

3-10 AutoCAD detail of column panel zone instrumentation 50

3-11 Picture showing strain gauge rosettes within the column panel zone 50

3-12 Picture showing full bridge strain gauge configuration attached to the pinned-pinned struts 52

3-13 Picture showing Epsilon Technology Corp. extensometers and high elongation strain gauges attached to the A36 steel tendons 52

3-14 Picture showing MTS extensometer attached to the superelastic Nitinol tendon . . . 53

3-15 Diagram of the connection model used in DRAIN-2DX 55

3-16 Picture showing a typical component test setup 57

3-17 Schematic of the specimen used for the A36 steel monotonic test 58

3-18 Stress versus gross strain (from crosshead displacement) for A36 steel rod specimens tested monotonically 59

3-19 Stress versus strain (from extensometer) for A36 steel rod specimens tested monotonically . . . 59
3-20 Schematic of the specimen used for the A36 steel cyclic test . . . 60
3-21 Displacement history for A36 steel rod specimen tested cyclically . . . 61
3-22 Stress versus gross strain (from crosshead displacement) for A36 steel rod specimen tested cyclically . . . 61
3-23 Equivalent viscous damping (ξ_{eq}) is a function of both the energy dissipated (E_D) and the maximum strain energy (E_{So}) for that particular cycle [11] . . . 62
3-24 Equivalent viscous damping versus maximum cyclic strain for A36 steel rod specimen tested cyclically . . . 63
3-25 Schematic of the specimen used for the superelastic Nitinol rod tests . . . 64
3-26 Loading protocol for the superelastic Nitinol rod tests . . . 64
3-27 Stress versus strain (from extensometer) for the superelastic Nitinol rod tests for a) specimen heat treated at 350 °C and b) specimen heat treated at 400 °C . . . 65
3-28 Comparison between superelastic Nitinol rod tests for specimens heat treated at 350 °C and 400 °C . . . 66
3-29 AutoCAD detail of the A36 steel tendon connection . . . 68
3-30 AutoCAD detail of the A36 steel tendon . . . 68
3-31 AutoCAD detail of the superelastic Nitinol tendon connection . . . 70
3-32 Picture of the superelastic Nitinol tendon connection highlighting modifications . . . 70
3-33 AutoCAD detail of the superelastic Nitinol tendon . . . 71
4-1 Picture of the steel tendon test I connection setup . . . 72
4-2 Graphs showing summary of results for steel tendon test I . . . 74
4-3 Gap opening versus actuator displacement for steel tendon test I . . . 75
4-4 Average gap opening versus actuator displacement for steel tendon test I . . . 76
4-5 Picture of the steel tendon test I at 4% interstory drift . . . 76
4-6 Stress versus strain plots for all tendons for steel tendon test I . . . 78
4-7 Graphs showing summary of results for steel tendon test II . . . 80
4-8 Gap opening versus actuator displacement for steel tendon test II . . . 81
4-9 Average gap opening versus actuator displacement for steel tendon test II . . . 82
4-10 Stress versus strain plots for all tendons for steel tendon test II . . . 82
4-11 Steel tendon test II connection at 0.04 radian drift cycle . . . 83
4-12 Yielding and local buckling of beam flanges after the first 0.04 drift cycle of steel tendon test II . . . 84

4-13 Actuator displacement time history for steel tendon test III 85
4-14 Graphs showing summary of results for steel tendon test III 86
4-15 Actuator displacement time history for the Nitinol tendon test 88
4-16 Nitinol tendon connection at 0.04 radian interstory drift 88
4-17 Graphs showing summary of results for Nitinol tendon test 89
4-18 Gap opening versus actuator displacement for the Nitinol tendon test 90
4-19 Average gap opening versus actuator displacement for the Nitinol tendon test . . . 91
4-20 Stress versus strain plots for all tendons for the Nitinol tendon test 92
4-21 Actuator force versus actuator displacement for the higher drift cycles of the Nitinol tendon test 93
4-22 Nitinol tendon connection at the 9% drift cycle 94
4-23 Failure of the Nitinol tendon connection was due to weld fractures at the 9% drift cycle 94
4-24 Actuator force versus actuator displacement plot for the first 5% drift cycle 95
B-1 Actuator displacement history for steel tendon test I on 04/25/05. 105
B-2 Actuator force versus actuator displacement for steel tendon test I on 04/25/05. . . 106
B-3 Moment versus total rotation for steel tendon test I on 04/25/05. 107
B-4 Moment versus plastic rotation for steel tendon test I on 04/25/05. 108
B-5 Moment versus concentrated rotation for steel tendon test I on 04/25/05. 109
B-6 Gap opening versus actuator displacement for steel tendon test I on 04/25/05. . . . 110
B-7 Average gap opening versus actuator displacement for steel tendon test I on 04/25/05. 111
B-8 Gap opening angle versus total rotation for steel tendon test I on 04/25/05. 112
B-9 Moment versus strain in Up West steel tendon for steel tendon test I on 04/25/05. . 113
B-10 Moment versus strain in Up East steel tendon for steel tendon test I on 04/25/05. . . 114
B-11 Moment versus strain in Down West steel tendon for steel tendon test I on 04/25/05. 115
B-12 Moment versus strain in Down East steel tendon for steel tendon test I on 04/25/05. 116
B-13 Stress versus strain in Up West steel tendon for steel tendon test I on 04/25/05. . . . 117
B-14 Stress versus strain in Up East steel tendon for steel tendon test I on 04/25/05. . . . 118
B-15 Stress versus strain in Down West steel tendon for steel tendon test I on 04/25/05. . 119
B-16 Stress versus strain in Down East steel tendon for steel tendon test I on 04/25/05. . 120
B-17 Moment versus flange strain in north beam for steel tendon test I on 04/25/05. . . . 121
B-18 Moment versus flange strain in south beam for steel tendon test I on 04/25/05. . . . 122

B-19 Moment versus flange strain in upper portion of column for steel tendon test I on 04/25/05. 123

B-20 Moment versus flange strain in lower portion of column for steel tendon test I on 04/25/05. 124

B-21 Moment versus vertical displacement in beam for steel tendon test I on 04/25/05. . 125

B-22 Moment versus strain in center panel zone rosette for steel tendon test I on 04/25/05. 126

B-23 Moment versus principle strains in center panel zone rosette for steel tendon test I on 04/25/05. 127

B-24 Moment versus strain in top north panel zone rosette for steel tendon test I on 04/25/05. 128

B-25 Moment versus principle strains in top north panel zone rosette for steel tendon test I on 04/25/05. 129

B-26 Moment versus strain in bottom south panel zone rosette for steel tendon test I on 04/25/05. 130

B-27 Moment versus principle strains in bottom south panel zone rosette for steel tendon test I on 04/25/05. 131

B-28 Principle strain angles versus maximum principal strains in panel zone rosettes for steel tendon test I on 04/25/05. 132

B-29 Principle strain angles versus minimum principal strains in panel zone rosettes for steel tendon test I on 04/25/05. 133

B-30 Actuator displacement history for steel tendon test II on 04/27/05. 134

B-31 Actuator force versus actuator displacement for steel tendon test II on 04/27/05. . . 135

B-32 Moment versus total rotation for steel tendon test II on 04/27/05. 136

B-33 Moment versus plastic rotation for steel tendon test II on 04/27/05. 137

B-34 Moment versus concentrated rotation for steel tendon test II on 04/27/05. 138

B-35 Gap opening versus actuator displacement for steel tendon test II on 04/27/05. . . . 139

B-36 Average gap opening versus actuator displacement for steel tendon test II on 04/27/05. 140

B-37 Gap opening angle versus total rotation for steel tendon test II on 04/27/05. 141

B-38 Moment versus strain in Up West steel tendon for steel tendon test II on 04/27/05. . 142

B-39 Moment versus strain in Up East steel tendon for steel tendon test II on 04/27/05. . 143

B-40 Moment versus strain in Down West steel tendon for steel tendon test II on 04/27/05. 144

B-41 Moment versus strain in Down East steel tendon for steel tendon test II on 04/27/05. 145

B-42 Stress versus strain in Up West steel tendon for steel tendon test II on 04/27/05. . . 146

B-43 Stress versus strain in Up East steel tendon for steel tendon test II on 04/27/05. . . 147

B-44 Stress versus strain in Down West steel tendon for steel tendon test II on 04/27/05. 148

B-45 Stress versus strain in Down East steel tendon for steel tendon test II on 04/27/05. . 149

B-46 Moment versus flange strain in north beam for steel tendon test II on 04/27/05. . . 150

B-47 Moment versus flange strain in south beam for steel tendon test II on 04/27/05. . . 151

B-48 Moment versus flange strain in upper portion of column for steel tendon test II on 04/27/05. 152

B-49 Moment versus flange strain in lower portion of column for steel tendon test II on 04/27/05. 153

B-50 Moment versus vertical displacement in beam for steel tendon test II on 04/27/05. . 154

B-51 Moment versus strain in center panel zone rosette for steel tendon test II on 04/27/05. 155

B-52 Moment versus principle strains in center panel zone rosette for steel tendon test II on 04/27/05. 156

B-53 Moment versus strain in top north panel zone rosette for steel tendon test II on 04/27/05. 157

B-54 Moment versus principle strains in top north panel zone rosette for steel tendon test II on 04/27/05. 158

B-55 Moment versus strain in bottom south panel zone rosette for steel tendon test II on 04/27/05. 159

B-56 Moment versus principle strains in bottom south panel zone rosette for steel tendon test II on 04/27/05. 160

B-57 Principle strain angles versus maximum principal strains in panel zone rosettes for steel tendon test II on 04/27/05. 161

B-58 Principle strain angles versus minimum principal strains in panel zone rosettes for steel tendon test II on 04/27/05. 162

B-59 Actuator displacement history for steel tendon test III on 04/29/05. 163

B-60 Actuator force versus actuator displacement for steel tendon test III on 04/29/05. . 164

B-61 Moment versus total rotation for steel tendon test III on 04/29/05. 165

B-62 Moment versus plastic rotation for steel tendon test III on 04/29/05. 166

B-63 Moment versus concentrated rotation for steel tendon test III on 04/29/05. 167

B-64 Gap opening versus actuator displacement for steel tendon test III on 04/29/05. . . 168

B-65 Average gap opening versus actuator displacement for steel tendon test III on 04/29/05. 169

B-66 Gap opening angle versus total rotation for steel tendon test III on 04/29/05. 170

B-67 Moment versus strain in Down West steel tendon for steel tendon test III on 04/29/05. 171

B-68 Moment versus strain in Down East steel tendon for steel tendon test III on 04/29/05. 172

B-69 Stress versus strain in Down West steel tendon for steel tendon test III on 04/29/05. 173

B-70 Stress versus strain in Down East steel tendon for steel tendon test III on 04/29/05. 174

B-71 Moment versus flange strain in north beam for steel tendon test III on 04/29/05. . . 175

B-72 Moment versus flange strain in south beam for steel tendon test III on 04/29/05. . . 176

B-73 Moment versus flange strain in upper portion of column for steel tendon test III on 04/29/05. 177

B-74 Moment versus flange strain in lower portion of column for steel tendon test III on 04/29/05. 178

B-75 Moment versus strain in center panel zone rosette for steel tendon test III on 04/29/05. 179

B-76 Moment versus principle strains in center panel zone rosette for steel tendon test III on 04/29/05. 180

B-77 Moment versus strain in top north panel zone rosette for steel tendon test III on 04/29/05. 181

B-78 Moment versus principle strains in top north panel zone rosette for steel tendon test III on 04/29/05. 182

B-79 Moment versus strain in bottom south panel zone rosette for steel tendon test III on 04/29/05. 183

B-80 Moment versus principle strains in bottom south panel zone rosette for steel tendon test III on 04/29/05. 184

B-81 Principle strain angles versus maximum principal strains in panel zone rosettes for steel tendon test III on 04/29/05. 185

B-82 Principle strain angles versus minimum principal strains in panel zone rosettes for steel tendon test III on 04/29/05. 186

C-1 Actuator displacement history for Nitinol tendon test. 187

C-2 Actuator force versus actuator displacement for Nitinol tendon test. 188

C-3 Moment versus total rotation for Nitinol tendon test. 189

C-4 Moment versus plastic rotation for Nitinol tendon test. 190

C-5 Moment versus concentrated rotation for Nitinol tendon test. 191

C-6 Gap opening versus actuator displacement for Nitinol tendon test. 192

C-7 Average gap opening versus actuator displacement for Nitinol tendon test. 193

C-8 Gap opening angle versus total rotation for Nitinol tendon test. 194

C-9 Moment versus strain in Up West Nitinol tendon for Nitinol tendon test. 195

C-10 Moment versus strain in Up East Nitinol tendon for Nitinol tendon test. 196

C-11 Moment versus strain in Down West Nitinol tendon for Nitinol tendon test. 197

C-12 Moment versus strain in Down East Nitinol tendon for Nitinol tendon test. 198

C-13 Stress versus strain in Up West Nitinol tendon for Nitinol tendon test. 199
C-14 Stress versus strain in Up East Nitinol tendon for Nitinol tendon test. 200
C-15 Stress versus strain in Down West Nitinol tendon for Nitinol tendon test. 201
C-16 Stress versus strain in Down East Nitinol tendon for Nitinol tendon test. 202
C-17 Moment versus flange strain in north beam for Nitinol tendon test. 203
C-18 Moment versus flange strain in south beam for Nitinol tendon test. 204
C-19 Moment versus flange strain in upper portion of column for Nitinol tendon test. . . 205
C-20 Moment versus flange strain in lower portion of column for Nitinol tendon test. . . 206
C-21 Moment versus vertical displacement in beam for Nitinol tendon test. 207
C-22 Moment versus strain in center panel zone rosette for Nitinol tendon test. 208
C-23 Moment versus principle strains in center panel zone rosette for Nitinol tendon test. 209
C-24 Moment versus strain in top north panel zone rosette for Nitinol tendon test. 210
C-25 Moment versus principle strains in top north panel zone rosette for Nitinol tendon test. 211
C-26 Moment versus strain in bottom south panel zone rosette for Nitinol tendon test. . . 212
C-27 Moment versus principle strains in bottom south panel zone rosette for Nitinol tendon test. 213
C-28 Principle strain angles versus maximum principal strains in panel zone rosettes for Nitinol tendon test. 214
C-29 Principle strain angles versus minimum principal strains in panel zone rosettes for Nitinol tendon test. 215
C-30 Actuator force versus actuator displacement for the higher drift cycles of the Nitinol tendon test. 216

LIST OF SYMBOLS AND ABBREVIATIONS

at%	Atom percent
A_f	Austenite finish temperature
A_s	Austenite start temperature
Al	Aluminum
A_{tendon}	Area of a single tendon
b_f	Flange width
cm	Centimeter
Cu	Copper
d_c	Column depth
d_b	Beam depth
d’	vertical distance between tendons
E_D	Energy dissipated by damping
E_{So}	Maximum strain energy
Fe	Iron
FCAW	Flux cored arc welding
FEMA	Federal Emergency Management Agency
FR	Fully restrained
F_y	Yield strength
g	Gram
GPa	Gigapascal

k_e	Elastic stiffness
LVDT	Linear variable differential transducer
M_d	Critical temperature above which stress induced martensite is unable to form
M_f	Martensite finish temperature
M_s	Martensite start temperature
Mp_{beam}	Plastic moment capacity of the beam
M_W	Moment magnitude
mm	Millimeter
Mn	Manganese
MPa	Megapascal
MRF	Moment resisting frame
Nb	Niobium
Ni	Nickel
NiO_2	Nickel Dioxide
PR	Partially restrained
PS	Partial strength
PT	Post-tensioned
PTED	Post-tensioned energy dissipating
R_C	Rockwell C hardness
SMA	Shape memory alloys
SMAW	Shielded metal arc welding
Ti	Titanium
W	Watt

Zn	Zinc
ϵ_r	Residual strain
$\mu\Omega$	Micro-Ohms
Ω	Ohms
σ_L	Loading stress plateau
σ_{UL}	Unloading stress plateau
σ_{tendon}	Stress in the tendon
$\theta_{conc.}$	Concentrated rotation
$\theta_{plastic}$	Plastic rotation
θ_{total}	Total rotation
ξ_{eq}	Equivalent viscous damping
°C	Degrees celsius

SUMMARY

Shape memory alloys are a class of alloys that display the unique ability to undergo large plastic deformations and return to their original shape either through the application of heat (shape memory effect) or by relieving the stress causing the deformation (superelastic effect). This research takes advantage of the unique characteristics of shape memory alloys in order to provide a moment resisting connection with recentering capabilities.

In this study, superelastic Nitinol, a nickel-titanium form of shape memory alloy that exhibits a flag-shaped stress versus strain curve, is used as the moment transfer elements within a partially restrained steel beam-column connection. Experimental testing consists of a one-half scale interior connection where the loading is applied at the column tip. A pseudo-static cyclic loading history is used which is intended to simulate earthquake loadings. The energy dissipation characteristics, moment-rotation characteristics, and deformation capacity of the connection are quantified. Results are then compared to tests where A36 steel tendons are used as the moment transfer elements. The superelastic Nitinol tendon connection showed superior performance to the A36 steel tendon connection, including the ability to recenter without residual deformation.

CHAPTER I

INTRODUCTION

The 1994 Northridge earthquake demonstrated that fully restrained (FR) welded connections in special moment resisting frames were much more susceptible to damage than was previously thought. Prior to the Northridge earthquake, structural engineers believed that modern buildings constructed with steel frames could resist very intense ground motions with only limited structural damage. However, brittle fractures were found in the connections of over 150 steel framed buildings in the Northridge area [46]. The poor performance was influenced by many factors, including the design assumptions and details of the connection, material properties, worksmanship, and inspection practices.

A research effort was initiated by the Federal Emergency Management Agency (FEMA), termed the SAC Steel Project, with the objective of identifying the deficiencies of the pre-Northridge connection design and to investigate alternative moment resisting connection designs. The SAC Steel Project re-evaluated the effectiveness of using partially restrained (PR) connections as opposed to fully restrained (FR) connections. It was determined that properly detailed bolted PR connections are able to provide equal or superior seismic performance to that of FR connections [44]. Bolted PR connections, such as T-stub and end plate bolted connections, are attractive for use in seismic regions for various reasons. First, field welding which was a contributing cause to many of the brittle fractures in the Northridge earthquake is not required. Also, a greater redundancy and toughness of the structural system is provided as more of these connections would be required due to lower initial stiffnesses and lower yielding strengths when compared to FR connections. Furthermore, bolted

PR connections have been shown to provide a large structural strength reserve capacity. Finally, excellent ductility and energy dissipation is able to be achieved.

The goal of this study was to assess the feasibility of incorporating superelastic Nitinol, a type of shape memory alloy (SMA), into a partially restrained, partial strength steel connection. Superelastic Nitinol has the the unique ability to withstand large strains (6-8%) that are crystallographically reversible, thereby leaving the material with no residual deformation upon unloading. Not only will the connection have all of the advantages of bolted PR connections that were discussed, but will have a recentering capability due to the lack of residual deformation.

A steel beam-column connection that utilizes superelastic Nitinol tendons as the moment transfer elements was tested as part of this work and compared to tests that incorporated A36 steel tendons. The study investigates the behavior of the connections when subjected to cyclic loading. The experimental work was augmented by analytical modeling of the connection using the nonlinear finite element analysis program DRAIN-2DX.

1.1 Outline of thesis

This thesis is organized into five chapters with the following contents. Chapter 2 is a literature review highlighting relevant previous research. Chapter 3 describes the experimental procedures, detailing the test setup, loading system, and instrumentation used throughout the testing. Also included in Chapter 3 are the connection details, describing in detail the preliminary analysis and design as well as reporting the results from tests on individual components. Chapter 4 outlines all of the testing events along with a discussion of the results. Finally, in Chapter 5, conclusions and future research needs are given.

CHAPTER II

LITERATURE REVIEW

Shape memory alloys (SMA) are a type of metallic alloy that offer several unique characteristics including shape memory effect, superelastic properties, modulus of elasticity/temperature relationships, high damping characteristics, and large recoverable strains. This research is intended to take advantage of the unique characteristics of shape memory alloys in order to provide a moment resisting connection with recentering capabilities. The following chapter gives an introduction to the material properties of shape memory alloys focusing on Nitinol, the material that will be used in this study. Also, prior use of shape memory alloys for seismic applications will be discussed, as well as the need for a new seismic resistant moment connection that provides good energy dissipation, high damping, and recentering capabilities. Finally, previous research on recentering connections will be reviewed.

2.1 Overview of Nitinol shape memory alloys

Shape memory alloys are a class of metals that, after being plastically deformed, revert back to their original shape either through the application of heat or by relieving the stress causing the deformation. The reason for this recoverable deformation is that plastic deformation in shape memory alloys is due to reversible transformations of their crystalline structure as opposed to the motion of dislocations, or slip, typically found in most metals [6]. The temperature-induced transformation between martensite and austenite phases leads to a shape memory effect, in which deformations are recovered by heating the material. The stress-induced transformation leads to a superelastic (or pseudo-elastic) effect, in which plastic deformations are recovered automatically upon removal of the stress causing

the deformation. Many alloy systems have been identified that exhibit shape memory properties but the system based on a nearly equiatomic composition of nickel and titanium provides the best combination of material properties and is the most readily available. Nickel-titanium (NiTi) shape memory alloys were discovered in the 1960's at the U.S. Naval Ordinance Laboratory (NOL) and are more commonly referred to by the acronym, Nitinol.

An ambitious, multi-year study was undertaken by the European Union in the 1990's to investigate the use of shape memory alloys in seismic applications [48]. The first phase of the MANSIDE project included a detailed study of various alloy systems that exhibited shape memory properties, including NiTi, CuZnAl, CuAlNi, FeMn, MnCu, and NiTiNb. It was concluded that NiTi, or Nitinol, exhibited the most optimal properties for seismic structural applications such as superelasticity, large recoverable strains and excellent corrosion resistance. Therefore, this study will focus solely on Nitinol SMA, unless otherwise noted. Table 2-1 compares some properties of Nitinol to those of structural steel.

Table 2-1: Properties of Nitinol compared to typical structural steel [19].

	Nitinol		Structural
	Austenite Phase	**Martensite Phase**	**Steel**
Physical Properties			
Melting point	1240–1310°C		1500°C
Density	6.45 g/cm^3		7.849 g/cm^3
Thermal conductivity	0.28 W/cm °C	0.14 W/cm °C	0.65 W/cm °C
Coeff. of thermal expansion	11.3 x 10^{-6} /°C	6.6 x 10^{-6} /°C	11.7 x 10^{-6} /°C
Mechanical Properties			
Recoverable elongation	up to 8%		0.2%
Modulus of elasticity	30–83 GPa	21–41 GPa	200 GPa
Yield strength	195–690 MPa	70–140 MPa	248–517 MPa
Ultimate tensile strength	895–1900 MPa		448–827 MPa
Elongation at failure	5–50% (typically ~ 25%)		~ 20%
Poisson ratio	0.33		0.27–0.30
Hot workability	Quite Good		Good
Cold workability	Difficult due to rapid work hardening		Good
Machinability	Difficult, abrasive techniques preferred		Good
Hardness	30–60 R_C		Varies
Weldability	Quite good		Very good
Electrical Properties			
Resistivity	100 $\mu\Omega\cdot$ cm	80 $\mu\Omega\cdot$ cm	13–125 $\mu\Omega\cdot$ cm
Chemical Properties			
Corrosion performance	Excellent (similar to stainless steel)		Fair

2.1.1 Microstructure

The ability of shape memory alloys to undergo large deformations with little residual strain through either the shape memory effect or the superelastic effect can be most easily understood by looking at the microstructure of the material. Shape memory alloys exist in either one of two phases: austenite or martensite. Furthermore, the martensite phase can be crystallographically reoriented by a completely reversible process known as twinning. When many twin variants are arranged into a single favored variant, the structure is said to be de-twinned. Figure 2-1 is a simplified, two-dimensional illustration of the microstructure of the different phases of SMA.

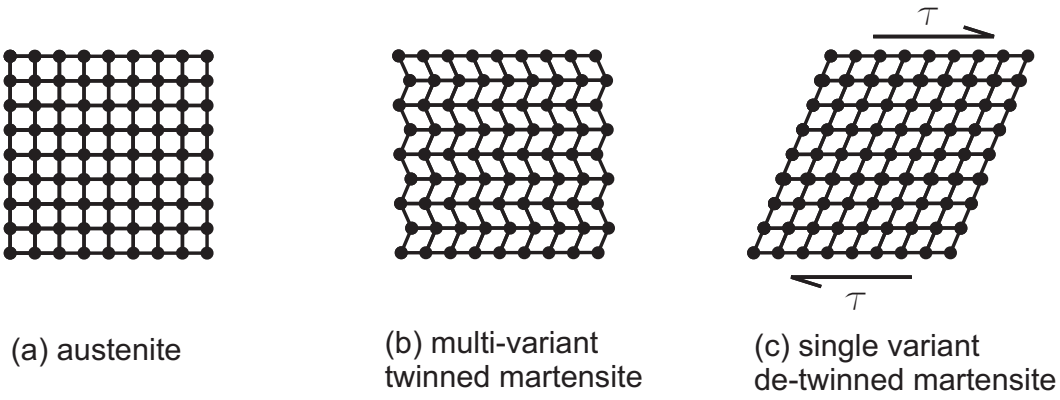

Figure 2-1: Simplified illustration of the phases of SMA.

The temperatures at which the phase changes occur in SMA are clearly defined for a given composition. Austenite begins to form at a specific temperature known as the austenite start temperature, or A_s. The phase transformation is completed at a slightly higher temperature known as the austenite finish temperature, or A_f. During the reverse phase transformation, the transformation to martensite begins at the temperature known as the martensite start temperature, or M_s. This transformation is completed at a slightly lower temperature known as the martensite finish temperature, or M_f. There is a hysteresis associated with phase transformations of SMA in that the reverse transformation to martensite occurs at approximately 20°C lower than the transformation to austenite (see Figure 2-2).

The atoms in both austenite and martensite phases have an ordered structure and, during phase transformations, the martensite takes on the same ordering of the austenite, and vice-versa. This so-called inherent ordering makes possible the unique shape memory properties of Nitinol [75]. Austenite is more stable at higher temperatures, while martensite is more stable at lower temperatures. Therefore, raising the temperature of martensite, whether in a twinned or de-twinned orientation, above A_f results in austenite. Similarly, lowering the temperature of austenite below M_f will result in martensite. The transformation from austenite to martensite will generally form martensite of the twinned form because the microstructure of austenite is more similar to that of twinned martensite rather than de-twinned martensite.

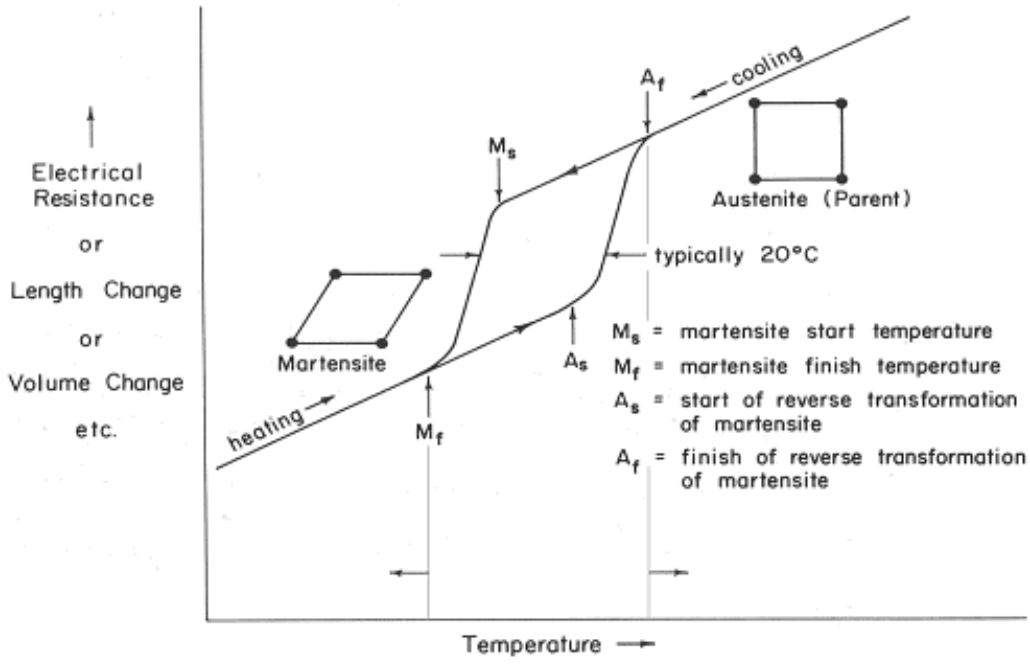

Figure 2-2: Hysteresis associated with phase transformations in SMA [75].

Figure 2-3 shows the nickel-titanium phase diagram and also the difference in M_s temperature as a function of nickel content. Recall that Nitinol is a nearly 50 at% Ni composition. In the phase diagram, NiTi II is the austenite phase (CsC1-type B2 structure) while NiTi III is the martensite phase (B19' monoclinic geometry) [56].

2.1.1.1 Shape memory effect

At temperatures below M_f, the material is in the martensite form and exhibits the shape memory effect. The crystallographic change during a shape memory effect cycle is illustrated in Figure 2-4. During deformation, the heavily twinned martensite begins to accommodate the change in shape by twin boundary movement in a process known as de-twinning. Once the crystal has been de-twinned, a residual deformation will remain once the load is removed. The shape recovery begins upon heating the SMA above the A_f temperature whereby a phase transformation from martensite to austenite occurs and the residual deformation is recovered. Upon cooling, the material again

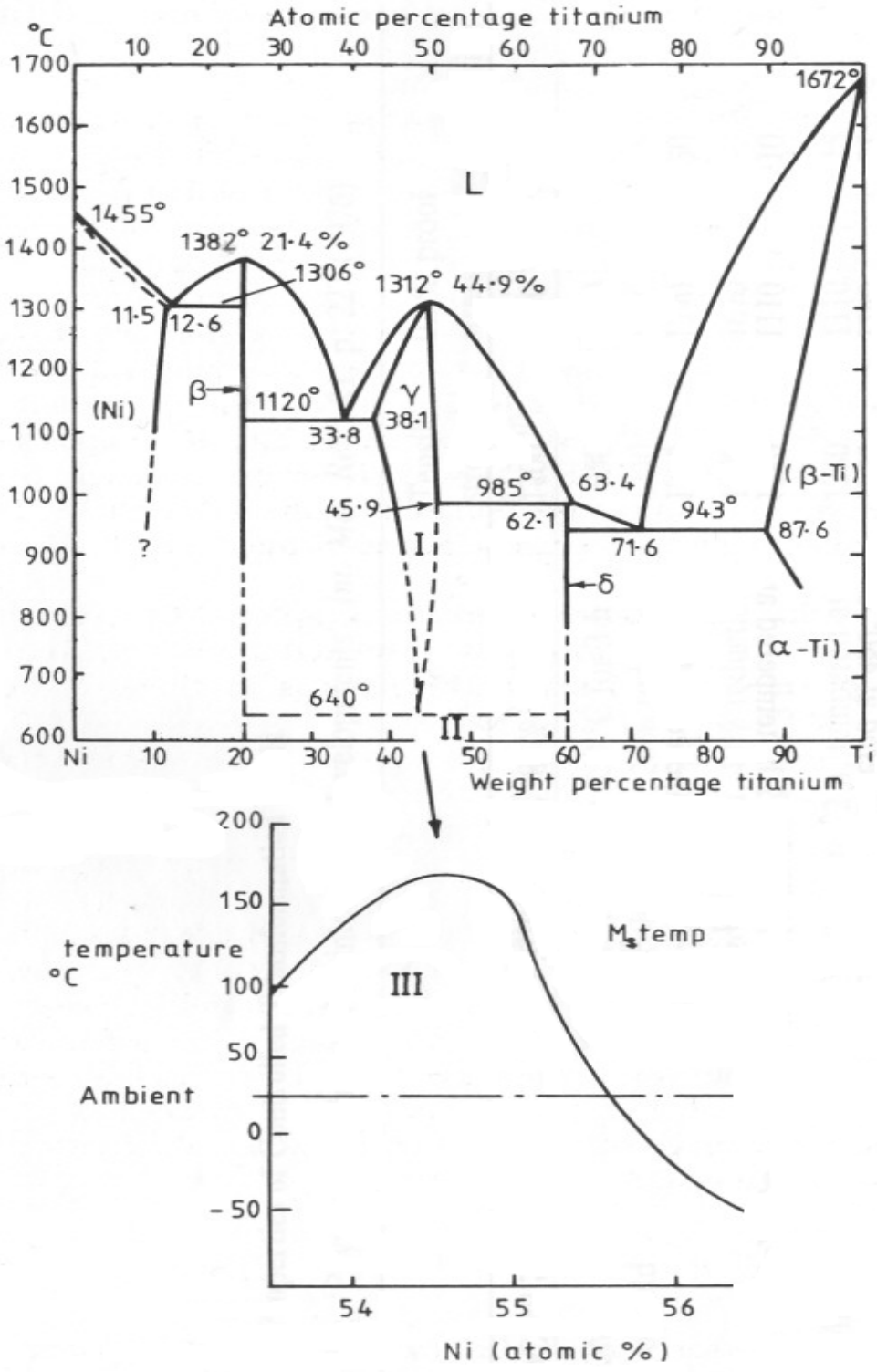

Figure 2-3: Nickel-Titanium phase diagram with change in M_s as a function of nickel content [56].

returns to the twinned martensite form, thus completing the shape memory effect cycle.

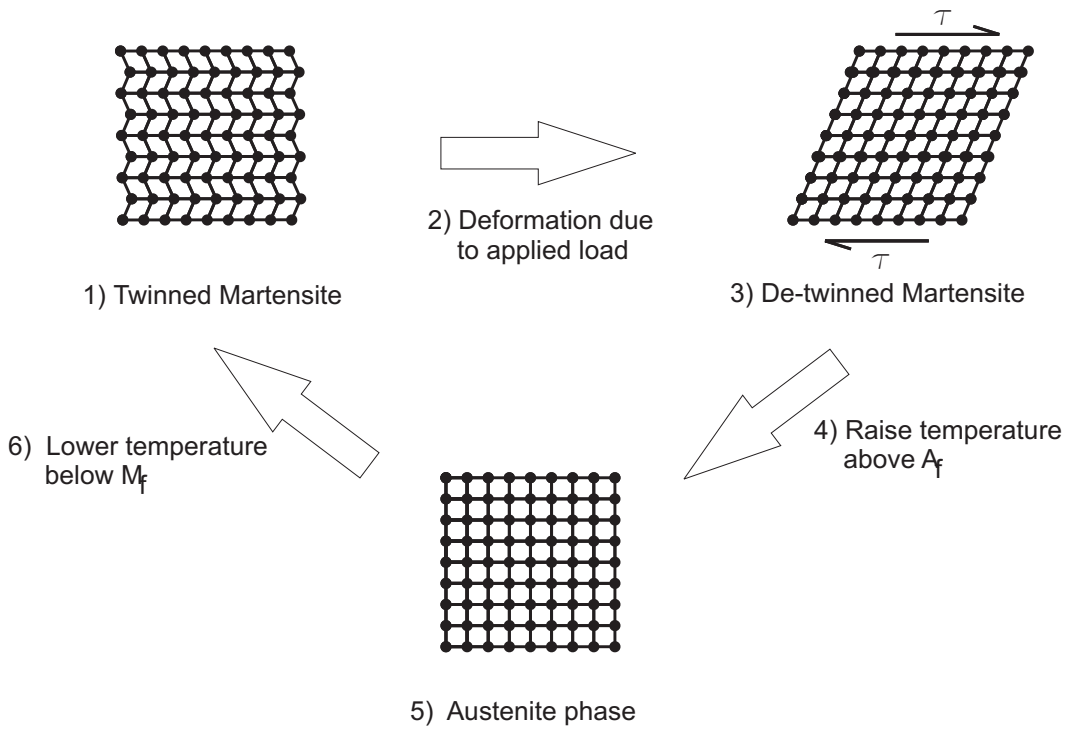

Figure 2-4: Crystallographic changes during the shape memory effect cycle.

2.1.1.2 Superelastic effect

The formation of martensite is a thermoelastic process, meaning there is an equivalence between temperature and stress. A decrease in temperature is equivalent to an increase in stress, both of which stabilize martensite due to the fact that martensite crystal growth upon cooling increases internal stresses. Under no stress, martensite forms at M_s. However, in the same material, if a stress is applied, martensite is able to form above the M_s temperature. Martensite formed above the M_s in this manner is termed stress-induced martensite and this transformation leads to the superelastic effect in Nitinol.

The crystallographic changes during a superelastic effect cycle are shown in Figure 2-5. Initially, the temperature needs to be above A_f so that the specimen is in the austenite phase. If a large enough stress is applied, the specimen will undergo a phase transformation to stress-induced martensite.

Upon unloading, a reverse transformation back to austenite will occur, thereby allowing recovery of any deformation. Throughout this process, the temperature remains constant. It should be noted that this process must not only occur above the A_f, but must also be below a critical temperature, M_d. An increase in difficulty to form stress-induced martensite continues to increase with temperature until M_d, above which permanent slip occurs as opposed to the formation of stress-induced martensite [75].

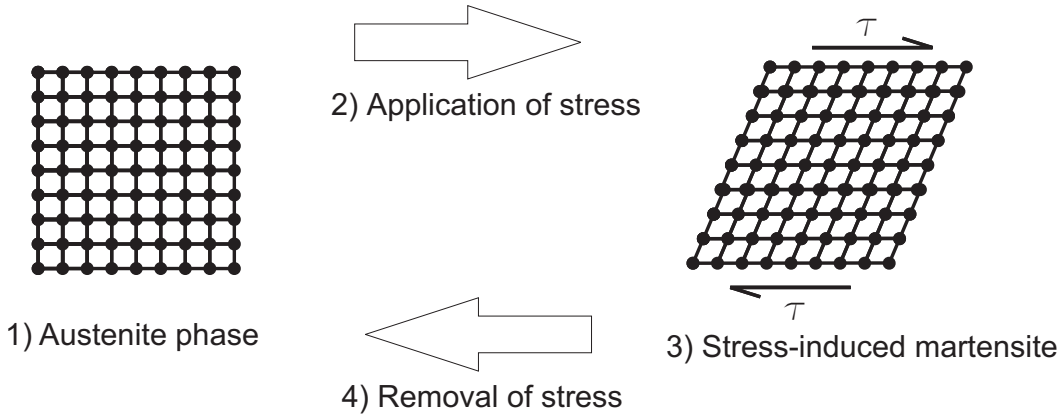

Figure 2-5: Crystallographic changes during the superelastic effect cycle.

2.1.2 Stress-strain-temperature relationships

Figure 2-6 shows an idealized plot of the stress-strain-temperature relationships in Nitinol. For a temperature below the martensite finish temperature (M_f), Nitinol exhibits the shape memory effect. Superelastic behavior, sometimes referred to as flag-shaped superelasticity, will occur if the temperature is above the austenite finish temperature (A_f), yet below a critical temperature (M_d) where stress-induced martensite is able to form. When the material is above M_d, the material undergoes typical plastic deformation.

The transformation temperatures of Nitinol are highly dependent on composition [55]. Small differences in the nickel content (see Figure 2-3) can determine whether a specimen will exhibit the superelastic effect or the shape memory effect at ambient temperatures. Furthermore, various

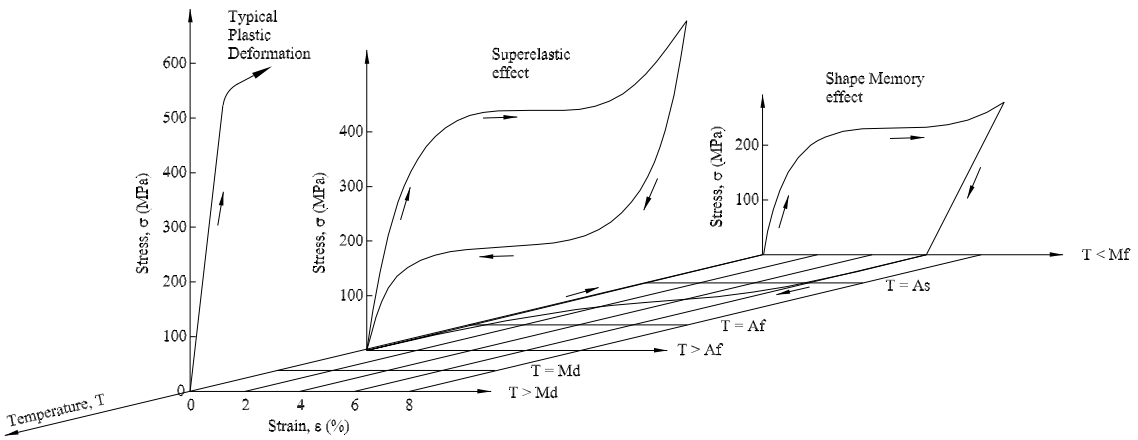

Figure 2-6: Stress-strain-temperature relationships in Nitinol.

thermo-mechanical processes, such as annealing treatments, have an impact on the transformation temperatures which, in turn, affect the stress-strain behavior of the specimen. Several studies have been undertaken to determine the effect of various annealing treatments on the transformation temperatures in Nitinol [37, 45, 50].

2.1.3 Physical properties

Nitnol possesses certain characteristics making it ideal for use in seismic design and retrofits. Some of these characteristics include stable hysteretic behavior, large amount of energy dissipation, good damping, and good corrosion resistance. Low residual strains associated with superelastic Nitinol can be exploited to give a device with recentering capabilities. Some potential drawbacks of Nitinol include the changing of mechanical behavior based on strain rate and ambient temperature. Another disadvantage may be the deterioration of properties with cycling. Most civil engineering applications would require larger specimen diameters while the experimental data suggests a deterioration of properties with increasing specimen size. The following section summarizes the physical properties of Nitinol applicable to seismic design and retrofit including a discussion of the possible shortcomings of the material.

2.1.3.1 Cyclic properties

In order to evaluate the possibility of using Nitinol in seismic devices, the cyclic behavior must be examined due to the fact that members under an earthquake load will experience repeated load cycles. There have been numerous studies investigating the cyclic behavior of Nitinol with different loading schemes (i.e. torsion, bending, tension-only, tension/compression), material types (i.e. superelastic, shape-memory), specimen sizes, alloy composition, thermo-mechanical treatments, strain rates, and strain amplitudes. However, these studies often give conflicting results. The results from tension-only cycling experiments on superelastic Nitinol will be presented here as they are most relevant to this particular study.

Dolce and Cardone [23] performed experimental tests on superelastic austenitic wire samples (1-2 mm in diameter) cycled in tension. The study concluded that the superelastic wire specimens were ideal for seismic applications, based on their energy dissipating and recentering (small residual strain) features. However, these tests did reveal that repeated cyclic deformation leads to gradual increases in residual strain (see Figure 2-7). Tests by Strnadel et al. [70] showed the same trends on plate tensile specimens. The accumulation of permanent dislocations that occur during the stress-induced martensitic transformation results in the increasing residual strains with cycling. Furthermore, the accumulation of dislocations also inhibits the formation of stress-induced martensite, leading to a decrease in the forward transformation stress. The reverse transformation stress is also reduced but not as much as the forward transformation stress causing a decrease in the area of the hysteresis and, therefore, a decrease in the energy dissipation capabilities of the specimen with repeated load cycles [19, 31, 51, 66, 70, 74]. According to DesRoches and Smith [20], the number of cycles that would be considered for seismic applications is in the range of 5-10 . Looking at Figure 2-8, this would result in an approximately 40% decrease in the stress plateau in later cycles compared to the first cycle.

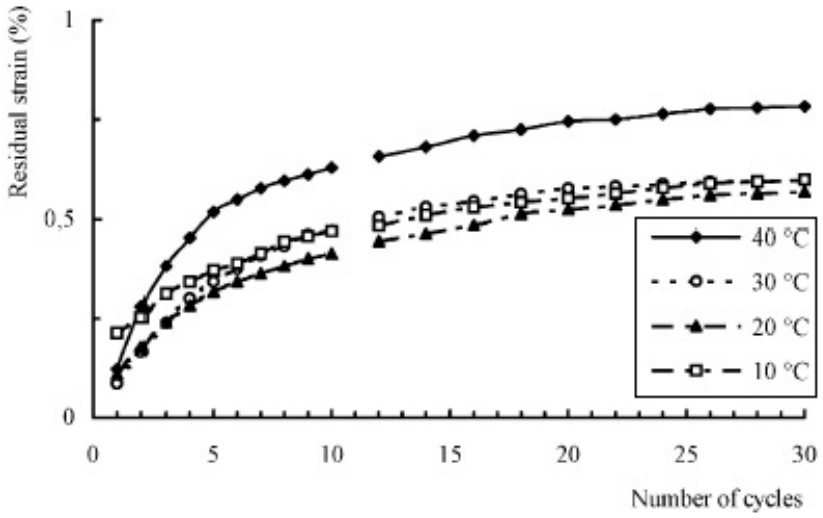

Figure 2-7: Effects of repeated cyclic deformation on residual strain at various temperatures [23].

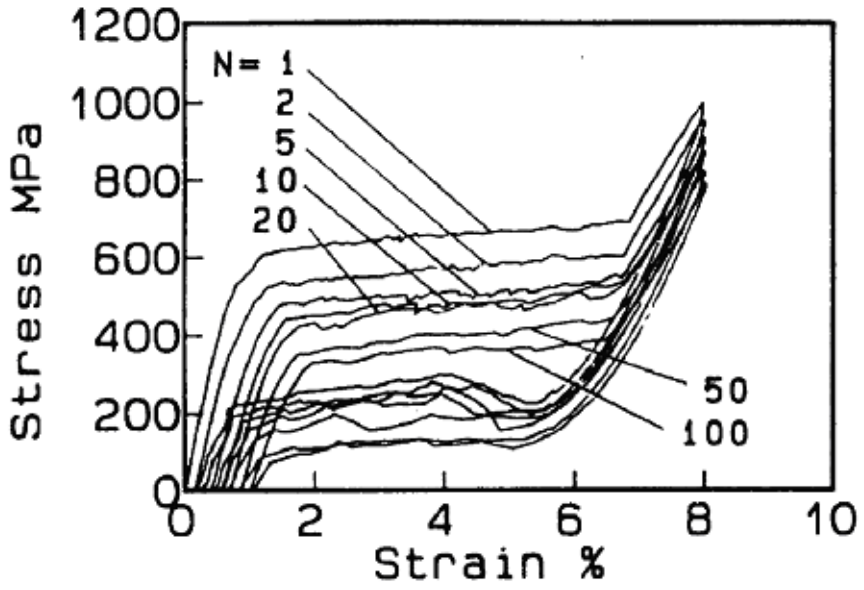

Figure 2-8: Effect of repeated load cycles on hysteresis of superelastic Nitinol [40].

DesRoches et al. [22] tested superelastic Nitinol cyclically in both wire and bar form (1.8-25.4 mm diameter). Both wire and bar forms showed nearly ideal superelastic properties (see Figure 2-9). However, the wire form showed higher strength and damping properties when compared to the bars. The recentering capabilities, based on residual strains, were not affected by section size. Cyclical strain amplitudes greater than 6% led to a degradation in the damping and recentering properties. Figure 2-10 shows the effect of differing specimen size on multiple parameters.

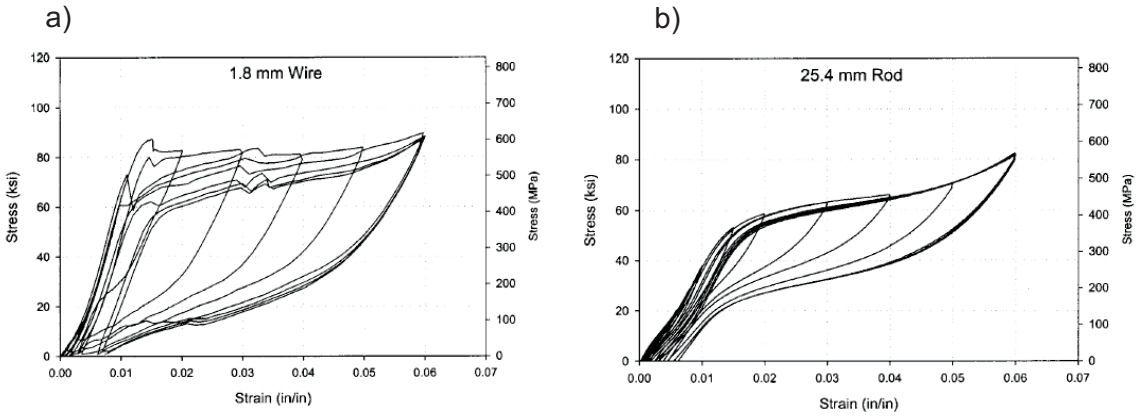

Figure 2-9: Stress-strain behavior for a) 1.8 mm diameter and b) 25.4 mm diameter Nitinol wire subjected to quasistatic cyclic loading [22].

Damping is an important parameter to discuss as it can significantly reduce the response of structures during seismic events. From experiments by McCormick and DesRoches [49] , the damping potential of both superelastic wires and superelastic bars were typically less than 7% equivalent viscous damping (ξ_{eq}) . These values are generally regarded as being too low for superelastic Nitinol to be used in a purely damping application. Figure 2-11 summarizes the results and also shows the energy dissipated per unit volume as a function of strain level.

The degradation of the cyclical properties of superelastic Nitinol, known as fatigue, can be improved with more cold-working, annealing at lower temperatures, cycling under lower stresses, and cycling at faster rates [31]. An investigation by Scherngell and Kneissl [64] showed that fatigue can also be improved by thermo-mechanical training in which the specimens were loaded with a

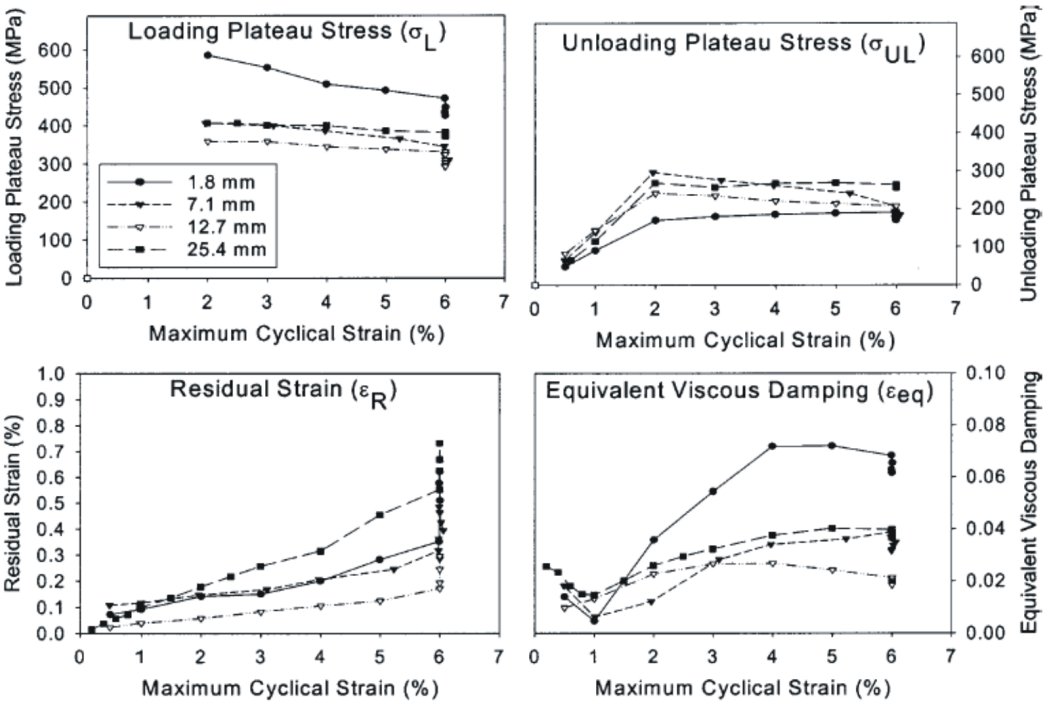

Figure 2-10: Comparison of Nitinol wire and bars subjected to quasistatic cyclic loading showing a) loading stress plateau, σ_L , b) unloading stress plateau, σ_{UL}, c) residual strain,ϵ_r and d) equivalent viscous damping ratio, ξ_{eq} [22].

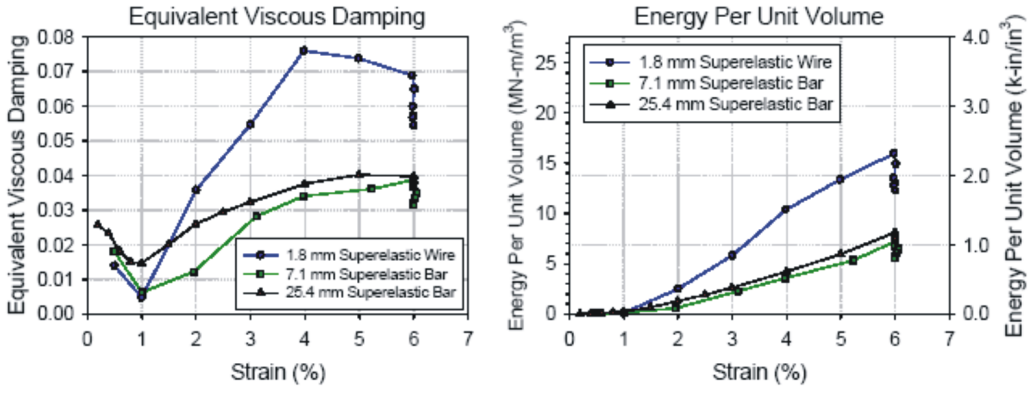

Figure 2-11: Comparison of damping properties with respect to specimen size [49].

constant training stress and repeatedly thermally cycled between the martensite finish temperature (M_f) and the critical temperature (M_d) where stress-induced martensite is able to form. Other studies have focused on purely mechanical training of specimens to stabilize the cyclical properties [4, 23, 70, 73, 76].

2.1.3.2 Strain rate effects

The properties of superelastic Nitinol that are affected by strain rate are the loading plateau stress, unloading plateau stress, equivalent viscous damping, and residual strain. Studies on strain rate effects have led to conflicting results and is open to much debate. Tobushi et al. [73] reported an increase in the hysteresis and, therefore, damping capacity with increasing strain rate . Other researchers have found that increased loading rates have led to reductions in the hysteresis and energy dissipation [21, 23, 43]. However, DesRoches et al. [22] found that strain rate had negligible effects on the recentering properties of the samples tested (1.8 mm - 25.4 mm in diameter).

It is generally believed that strain rate effects are due to the heat generated while going through the phase transformations. The forward stress-induced martensitic transformation is exothermic while the reverse transformation is endothermic. Therefore, high strain rates during transformation result in temperature changes, which in turn have significant influence on the stress-strain response [43]. Differences in specimen sizes, testing conditions, and the range of variation of the strain rates of the various studies can have a large impact on the results.

2.1.3.3 Temperature dependence

Ambient temperature may likely be the single most important factor when predicting the mechanical behavior of superelastic Nitinol. Recall that the formation of martensite is a thermoelastic process, meaning there is an equivalence between temperature and stress. A consequence of this fact is that a single specimen may exhibit the superelastic effect at higher temperatures and the shape

memory effect at lower temperatures. Figure 2-12 shows the effect of ambient temperatures on the stress-displacement plots of Nitinol with various compositions. The dependence of the mechanical properties of Nitinol on ambient temperature poses a threat to many potential seismic applications and may limit their use in regions were large temperature ranges are expected.

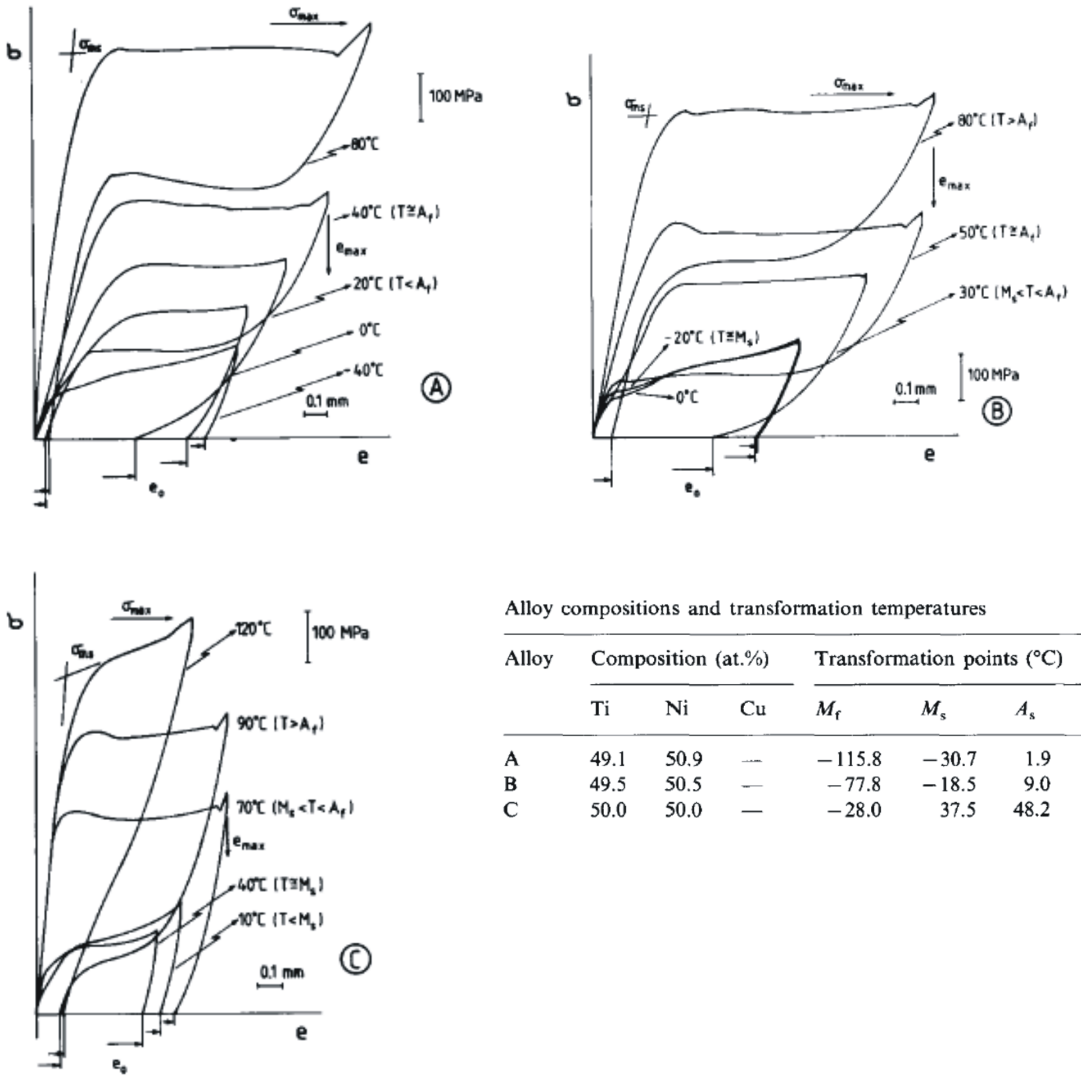

Alloy compositions and transformation temperatures

Alloy	Composition (at.%)			Transformation points (°C)			
	Ti	Ni	Cu	M_f	M_s	A_s	A_f
A	49.1	50.9	—	−115.8	−30.7	1.9	44.6
B	49.5	50.5	—	−77.8	−18.5	9.0	53.0
C	50.0	50.0	—	−28.0	37.5	48.2	77.8

Figure 2-12: Effect of ambient temperature on the stress-displacement behavior of Nitinol with various compositions [69].

2.1.3.4 Corrosion resistance

Nitinol has excellent corrosion resistance that is comparable to stainless steel. The excellent corrosion resistance is provided by a thin and stable oxide (NiO_2) coating that occurs naturally on Nitinol and is known as a passive film [50]. The passive film is a result of the heat treatment that is typically performed on Nitinol during processing. Studies have also shown that Nitinol is highly resistant to corrosion from sea water [48].

2.1.4 Application of Nitinol in passive seismic devices

Recently, the focus in seismic design and retrofit has become more performance based which has led to the use of passive energy dissipation devices in structures in order to reduce interstory drift and structural response. Metallic yield dampers, friction dampers, viscoelastic dampers, viscous fluid dampers, and tuned mass dampers have all been developed and installed in structures for performance enhancement under earthquake loads [67]. Many applications of these devices are discussed in detail in works by Constantinou et al. [18] and Hanson and Soong [35]. Many shortcomings associated with these devices could be overcome with the use of Nitinol shape memory alloys. Recentering capabilities, high energy dissipation per unit mass, excellent fatigue properties, strain hardening at large strains, stress plateaus to limit force transmission, and excellent corrosion resistance are all properties of Nitinol that could be exploited to give a passive seismic device with superior performance to those of traditional dampers. The following section outlines the possibilities for the use of Nitinol in seismic mitigation.

2.1.4.1 Damping and recentering applications

The widest use of Nitinol for seismic applications is for passive damping and recentering applications. Thomson et al. [72] tested a simple application using superelastic Nitinol wire to constrain a

cantilever beam. The analytical and experimental results showed an increase in the equivalent viscous damping ratio by a factor of six in the first fundamental mode . As part of the aforementioned MANSIDE (Memory Alloys for New Seismic Isolation and energy dissipation Devices) project, Dolce et al. [25] proposed and tested three types of Nitinol devices; supplemental recentering devices (SRCD), not recentering devices (NRD), and recentering devices (RCD) . The supplemental recentering device (SRCD) utilized superelastic Nitinol wire which provided only 4-5% equivalent viscous damping but had the ability to recenter (see Figure 2-13).

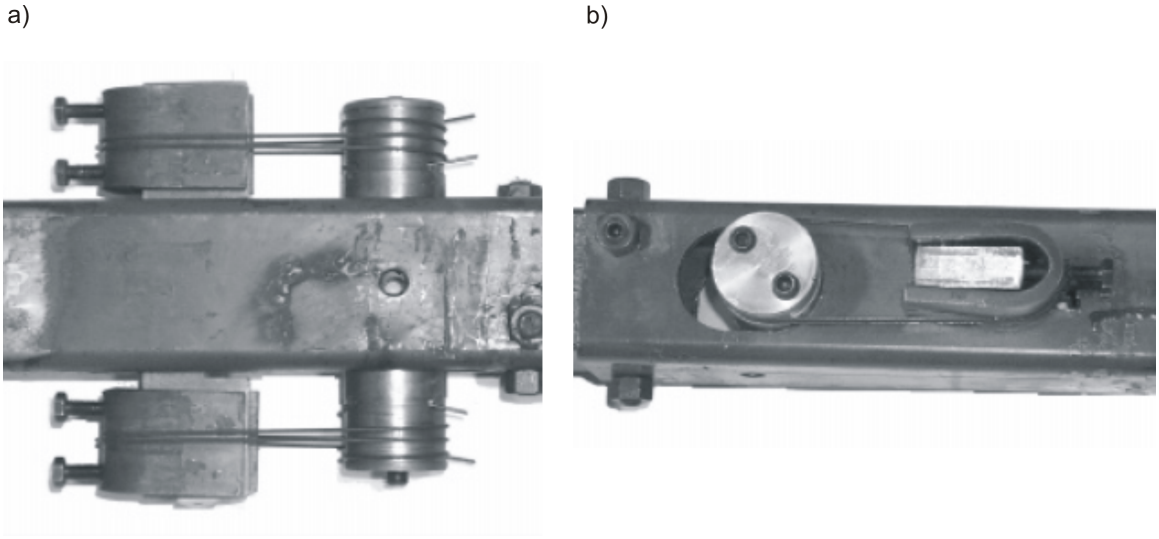

Figure 2-13: Supplemental recentering device showing a) top view and b) lateral view [25].

The not recentering device (NRD) shown in Figure 2-14 utilized prestrained superelastic wire acting as counteracting springs. The NRD was able to provide up to 40% equivalent viscous damping but ended with large residual strains. The RCD is simply a combination of the two other devices and had the advantage of high service load stiffness, recentering capabilities, and good damping (up to 16% equivalent viscous damping). Figure 2-15 provides the functioning scheme of the recentering device (RCD). Similar devices to the RCD were created by both Krumme et al. [42] and Sweeney et al. [71]. In order to study seismic retrofit techniques on existing buildings, the recentering device (RCD) was incorporated into a brace for an existing 2 story reinforced concrete frame

structure that was designed for gravity loads only [24]. Quasi-static cyclic pushover tests were performed and displacements up to twice the design displacements were reached with the structure showing a strong recentering capability.

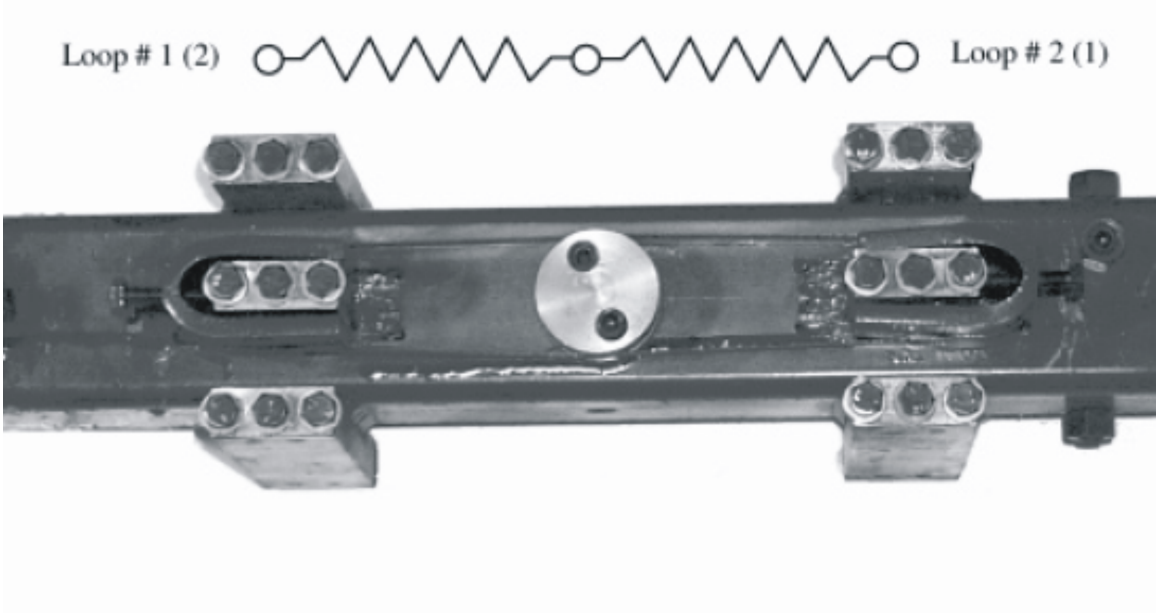

Figure 2-14: Not recentering device utilizing prestrained superelastic wire acting as counteracting springs [25].

Three cathedrals in Italy have been successfully retrofitted using Nitinol devices (see figure 2-16) in order to protect the structures from future seismic damage [7, 39]. In all cases, the devices offered two distinct advantages; first, superelastic alloys offered high elongations at a constant force to control displacements and, second, the devices could be implemented using non-intrusive techniques. There have been numerous other conceptual studies that have investigated the use of Nitinol as damping devices through either analytical or experimental testing [2, 3, 5, 16, 32, 34, 36, 38].

2.1.4.2 Partially restrained steel connections using Nitinol

Very little research has been done that incorporates Nitinol into steel connections. The performance of partially restrained steel connections could be improved by introducing Nitinol, a ductile damping connecting element. Tests were done at the University of Notre Dame on a connection that was

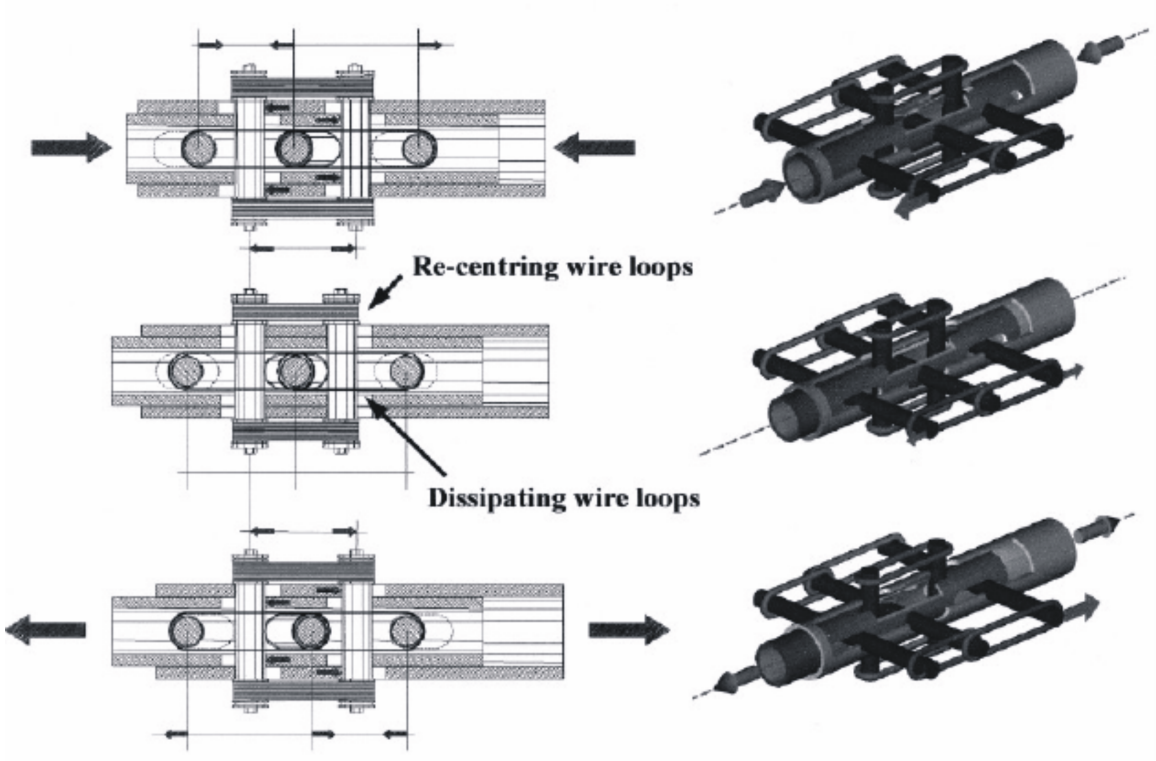

Figure 2-15: Functioning scheme of a recentering device [25].

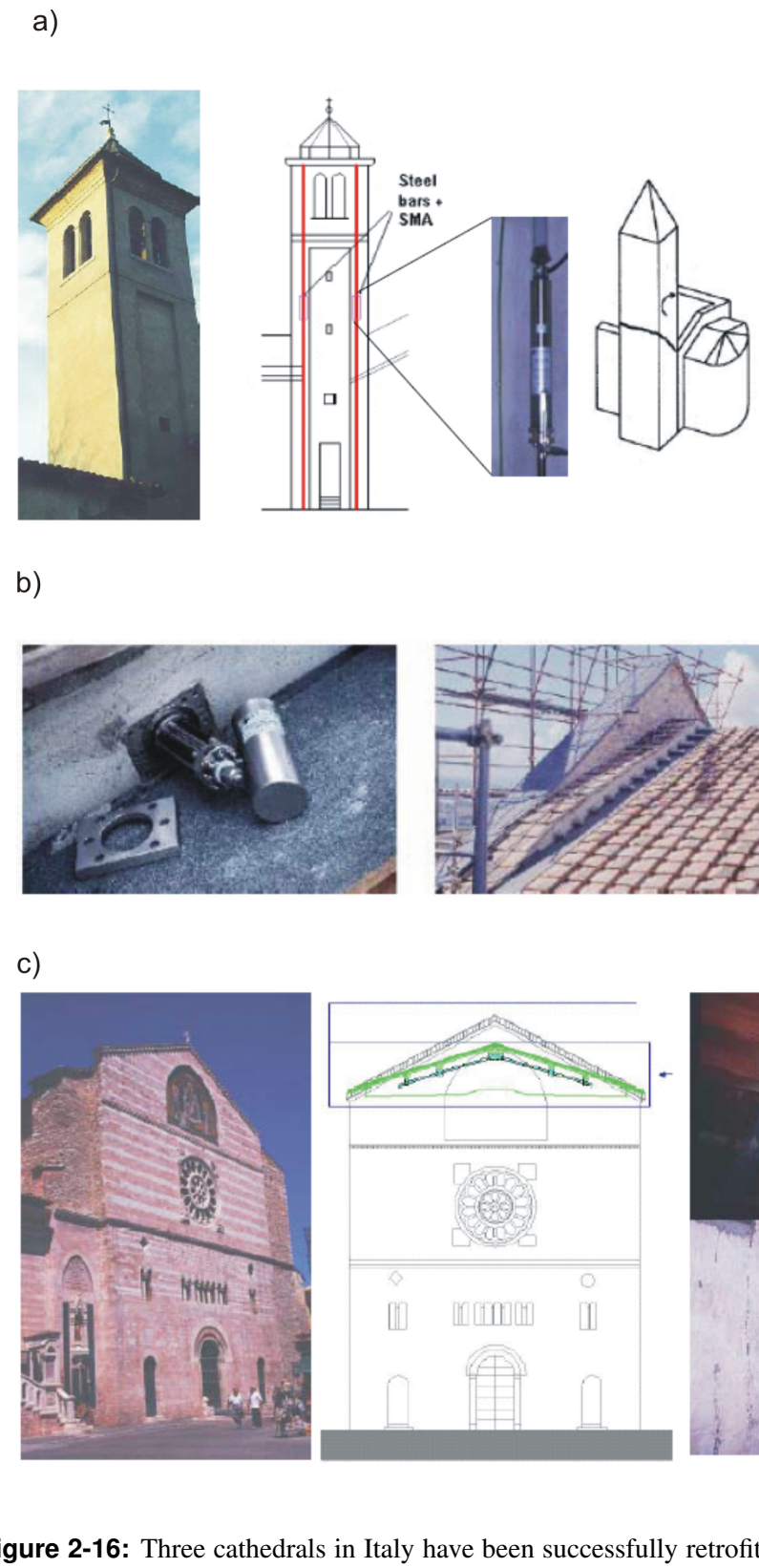

Figure 2-16: Three cathedrals in Italy have been successfully retrofitted using Nitinol devices; a) the bell tower of the S. Giorgio Church in Trignano [39], b) the tympanum of S. Francesco Basilica in Assisi [7], and c) the facade of the S. Feliciano Cathedral in Foligno [7].

composed of top and seat angles connected by bolts and a number of superelastic Nitinol bars that crossed the column (see Figure 2-17). Analytical studies showed that the connection showed promising response reduction and recentering capabilities [1]. However, little was published on this connection, and no experimental results could be found in the open literature after the work was abandoned because the Nitinol specimens failed to exhibit superelastic behavior [30].

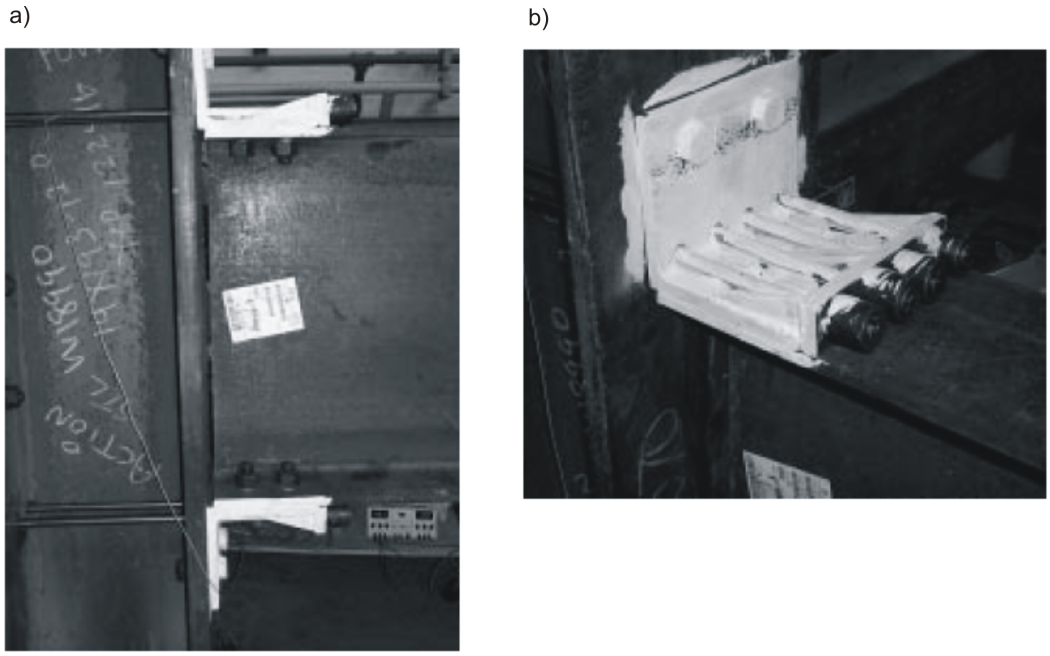

Figure 2-17: a) University of Notre Dame connection b) Closeup of top angle connector with supplemental superelastic rods [1].

Another test, performed by Ocel et al. [53], investigates beam-column connections using martensitic, or shape memory, Nitinol tendons. The connection was designed such that the Nitinol tendons were the primary source of moment resistance in the connection (see Figure 2-18). The connection was found to exhibit a stable hysteresis for cyclical loads up to 4% interstory drift, which corresponds to a strain of 5% in the Nitinol bars. After the test, the Nitinol rods were heated for approximately 8 minutes at 300°Cin order to initiate the shape memory effect. The rods recovered approximately 76% of their undeformed shape, and after being retested they showed a

nearly-identical behavior to the original connection [54]. The connection was also tested dynamically corresponding to a 3.95% strain per second in the Nitinol tendons. The connection under dynamic loads performed similar to the initial tests also showing a stable and repeatable hysteretic behavior. However, the dynamic tests transferred approximately 15% less moment and dissipated approximately 65% less energy (see Figure 2-19) [54].

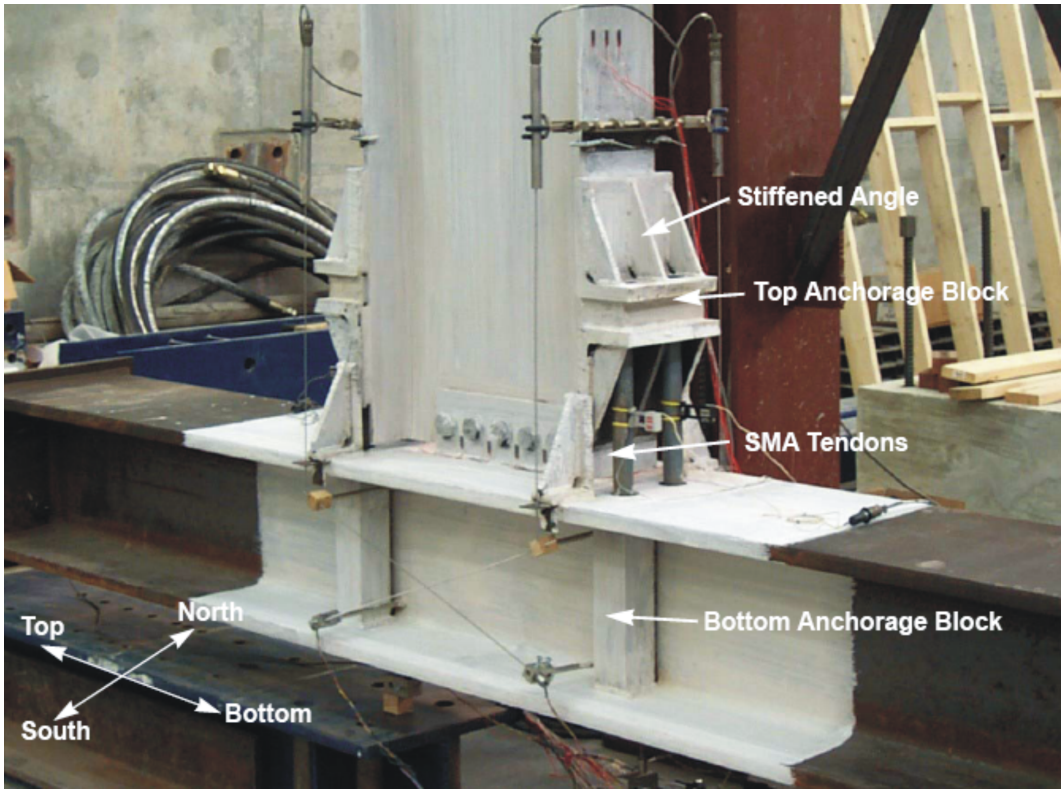

Figure 2-18: Test setup of beam-column connection using martensitic Nitinol tendons as the primary source of moment resistance [54].

2.2 Moment resisting frame connections

The basic structural support for all steel framed buildings consists of a series of horizontal steel beams framed into vertical steel columns. This frame must be able to resist the vertical loads such as the self weight of the building and the horizontal lateral loads due to wind and earthquakes. Some steel framed buildings are able to resist lateral loads by using diagonal braces, others resist

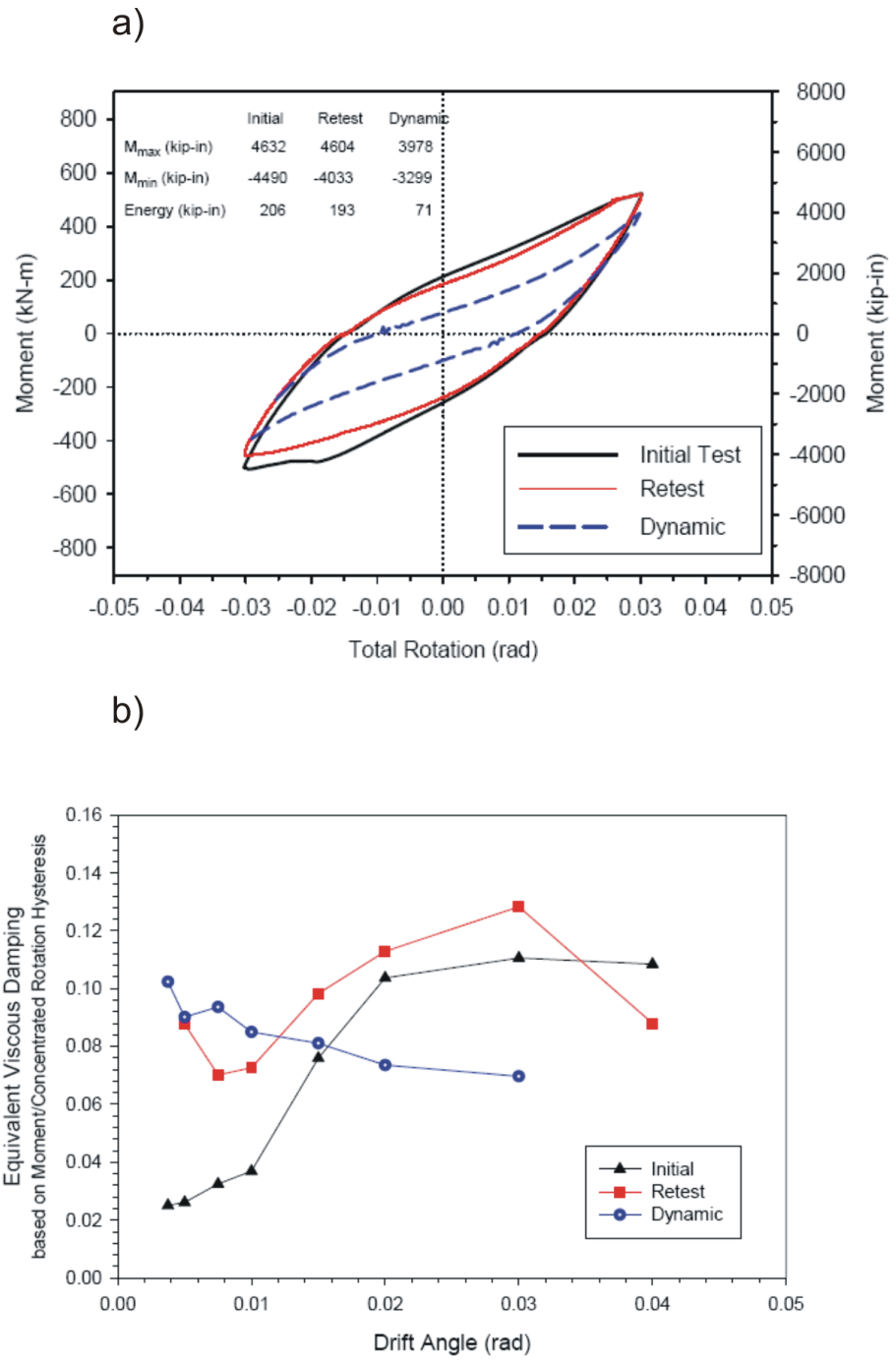

Figure 2-19: Results from tests by Ocel [54] that show a) Moment/Total Rotation Comparison of first 3% drift cycle and b) Equivalent viscous damping per drift intensity for initial, retest, and dynamic tests .

lateral loads through the use of masonry or concrete walls. In steel moment resisting frame (MRF) buildings, the beams are rigidly connected to the columns and are, therefore, able to resist lateral loads without the use of additional braces or walls.

Steel MRF buildings have been heavily used in seismic zones because of their perceived ductility. A building that is capable of ductile behavior is able to undergo large inelastic deformations without significant degradation of strength, and without the development of instabilities which contribute to building collapse. Design forces specified by building codes are related to the amount of ductility of the structural system. The higher the ductility of the building system, the lower the design forces because ductile systems are capable of resisting loads that are far greater than their elastic limit strength. The intended deformations consist of the development of plastic hinges within the beam or plastic shear deformation in the column panel zones or a combination of the two (see Figure 2-20). This "strong column, weak beam" relationship allows for significant energy dissipation. The damage is expected to consist of moderate yielding and localized buckling, as opposed to brittle fractures.

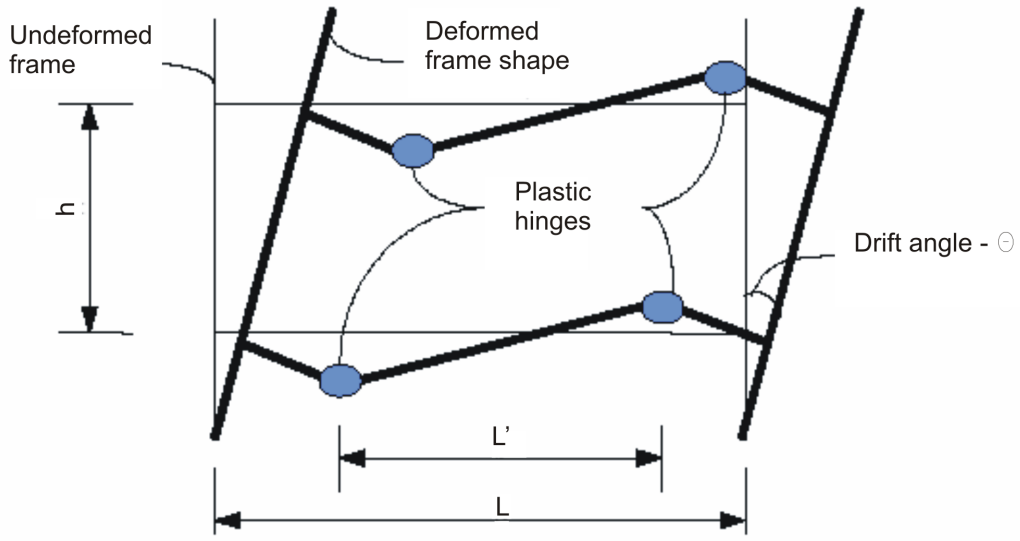

Figure 2-20: Development of plastic hinges contribute to significant energy dissipation [28].

2.2.1 Performance of steel MRF during the Northridge earthquake

In the past, engineers believed that MRF buildings with welded joints were among the most ductile building designs contained in building codes. The typical connection used (see Figure 2-21) was believed to be capable of developing large plastic rotations without significant strength degradation. After the Northridge earthquake of January 17, 1994 it became apparent that this connection design had some serious shortcomings. Following that earthquake, it was found that many steel MRF buildings had experienced brittle fractures of the beam-to-column connections. The plastic hinges did not form in the beams and the connections were damaged. The observed brittle fractures that occurred were contrary to the fundamental assumption of ductile behavior.

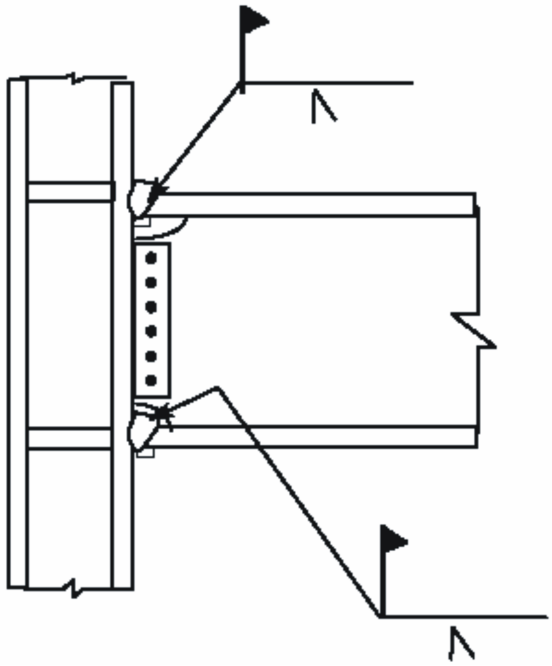

Figure 2-21: Typical welded MRF connection prior to 1994 [28].

The brittle fractures that occurred as a result of the 1994 Northridge earthquake surprised the structural engineering community. The earthquake was considered to be moderate, with a moment magnitude (M_W) of only 6.7. In many cases, the brittle fractures occurred at very low levels of

plastic demand [28]. While inadequate workmanship and quality control issues may have played a role in some of the damage, it is believed that most of the damaged buildings were constructed consistent with modern codes and standards of practice [46]. Brittle fractures occurred in new and old buildings, tall and short buildings, and in conventional and important structures. [47]. The SAC Steel Project was created to address immediate (Phase 1) and long-term (Phase 2) needs related to solving the performance problems with welded steel moment resisting frame connections.

Results of the SAC Steel Project indicate that there were a number of contributing causes of the Northridge damage. The basic connection geometry was inherently flawed in that it concentrated stresses at some of the weakest points in the assembly. The geometry also made it difficult to weld without large defects that could lead to fractures. Due to increasing labor costs, designers favored the use of a lower number of connections with larger member sizes to faster erect buildings, resulting in larger loads to be carried by the connections. Also, in the mid 1960's, the construction industry favored the use of the flux-cored arc welding (FCAW) process over the conventional shielded metal arc welding (SMAW). Results of the SAC steel project showed that FCAW tended to produce welds with very low toughness. The low toughness was further exacerbated by excessive deposition rates which were commonly employed by welders in order to make the connections more quickly.

Other material properties also played a role in the Northridge damage. As steel mills adopted more modern production processes, steels produced now tend to have higher yield strengths than before. Because ASTM specifications prescribe minimum yield strength, but not maximum; A36 steel often has yield strengths that exceed A572 Gr50 steel. In order to employ a "strong column, weak beam" connection strategy, A572 Gr50 steel is commonly used in columns while A36 steel is commonly specified for the beams. Although the A36 steel became stronger, the increase in base metal yield strength could cause the weld metal in the joints to become under-matched, contributing to its vulnerability [28].

Design practice in the 1980's and early 1990's encouraged the design of moment resisting connections with relatively weak column panel zones. Panel zone shear deformation results in a local kinking of the column flanges near the welded joints and further increases the stress and strain demands of the welds. Other contributing causes include poor detailing practices, poor welding practices and poor inspection practices [29].

2.3 Partially restrained steel connections

One of the SAC research initiatives was to evaluate the effectiveness of various types of bolted, partially restrained (PR) connections as an alternative to fully restrained (FR) welded connections. On the global scale, PR connections have smaller initial stiffnesses and yielding strength when compared with fully welded counterparts. As a result, more connections are required in lateral bracing systems to control drift resulting in a tougher and more redundant structural system. On the local scale, PR connections can provide more yielding mechanisms and alternate load paths than welded connections, resulting in better local ductility when the connection is properly detailed. For more information, the reader is referred to a comprehensive literature review on partially restrained bolted connections performed by Leon [44].

2.4 Recentering connections

Several alternative moment connection details have been proposed since the Northridge earthquake, including the use of reinforcing cover plates [27], bolted or welded haunch brackets [41], or the reduction of the beam flange width to control the plastic hinge rotation [8] (see Figure 2-22). All of these details are intended to force inelastic deformation to develop in the beams away from the connection. Consequently, following a design level earthquake, beams with these types of connections will have permanent damage after the formation of the plastic hinges, resulting in residual drift of the frame. A connection that provides energy dissipation as well as recentering capability is ideal. The following section presents previous analytical and experimental research into connections of both concrete and steel that provide recentering and/or energy dissipation capabilities.

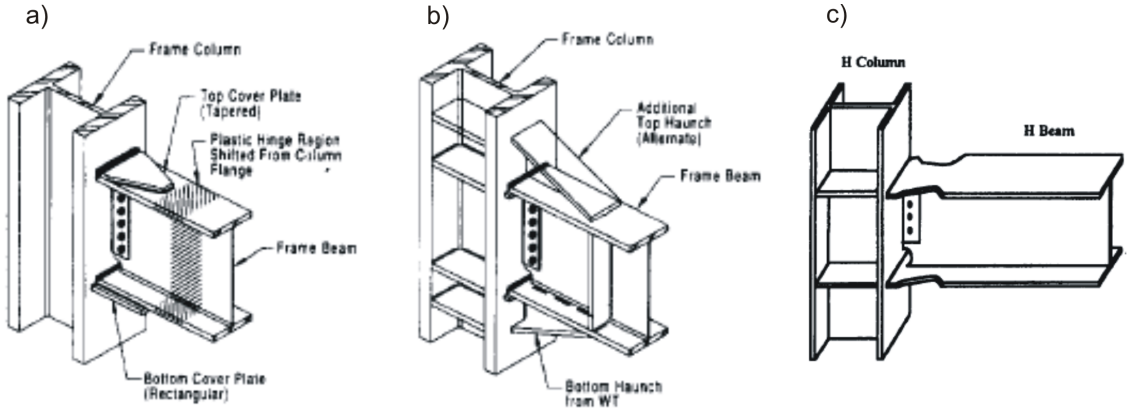

Figure 2-22: Post-Northridge earthquake moment connection details using a) reinforcing cover plates [27], b) haunch brackets [27], and c) Reduced beam section [8].

2.4.1 Post-tensioned precast concrete moment frame connections

In parallel with post-Northridge steel research, moment resisting connections using post-tensioning (PT) concepts were developed for precast concrete construction. Several studies have been undertaken to investigate unbonded PT precast interior beam-column joint subassemblages where the behavior under lateral loads is governed by the opening of gaps at the joints between the beam and

column members (see Figures 2-23 and 2-24) [10, 26, 58]. This type of connection offers desirable seismic performance characteristics such as a self-centering capability and the ability to undergo large nonlinear lateral displacements without significant structural damage . However, the lateral displacements during a severe earthquake may be large due to inadequate energy dissipation capabilities [52].

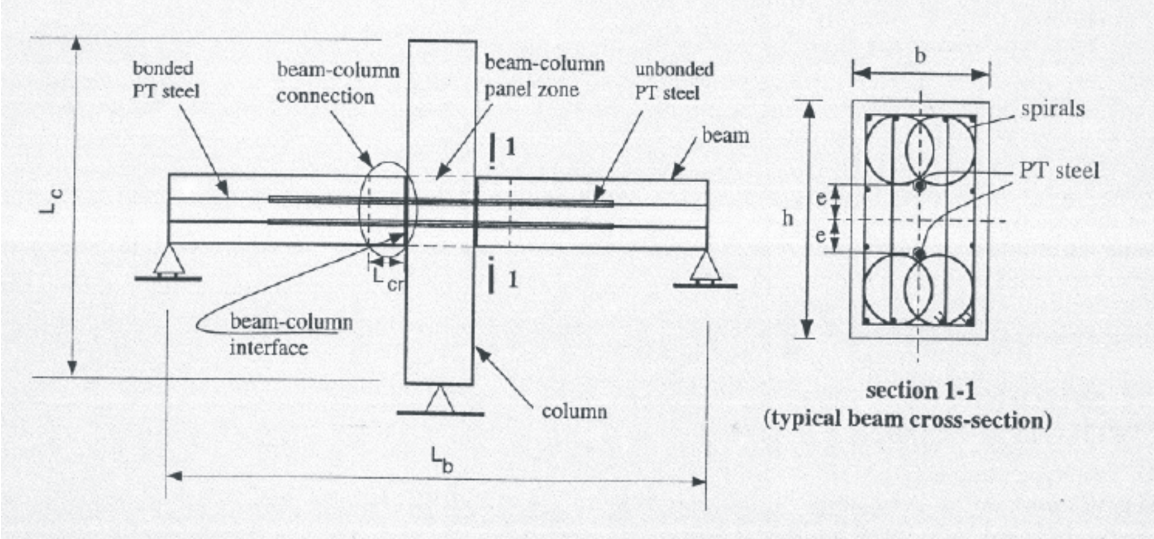

Figure 2-23: Unbonded post-tensioned precast concrete beam-column subassemblage used by El-Sheikh et al. [26].

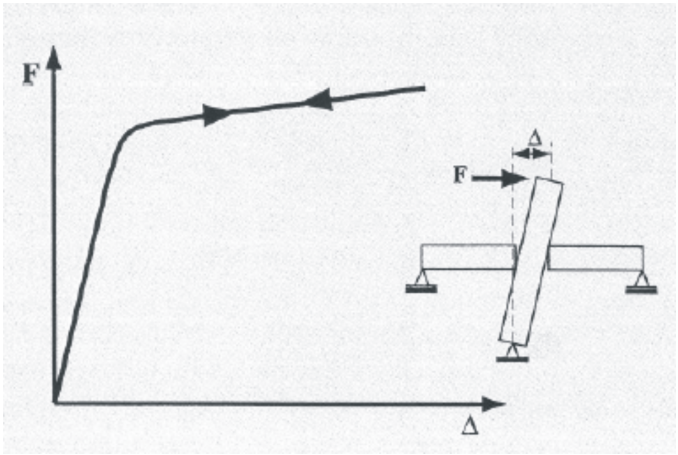

Figure 2-24: Nonlinear elastic load-deflection behavior with inset showing opening of gaps at the beam-column joint during lateral loading [26].

In order to reduce lateral displacement demands during a seismic event, supplemental passive energy dissipation techniques have been adopted. The use of mild, unprestressed steel reinforcement through the precast concrete beam-column connections in addition to the PT steel has been investigated [9, 65, 68]. These partially post-tensioned systems are referred to as "hybrid" precast concrete frame systems due to the mixed use of mild steel and PT steel reinforcement across the beam-column joints. Morgen et al. [52] investigated the use of a friction damper used externally at selected beam-column joints as an alternative to the use of hybrid systems for increased energy dissipation.

2.4.2 Post-tensioned steel connections

The post-tensioning technology that was first used in precast concrete frame connections has been extended to steel moment resisting frames. Ricles et al. [60] first developed a post-tensioned (PT) steel moment connection with bolted top and seat angles and high strength steel strands running through the column anchored away from the connection. (see Figure 2-25). Energy dissipation occurs in the angles while other structural members remain elastic. Analytical and experimental results showed that the connection has initial stiffness similar to a typical welded connection, structural response of a MRF with this connection was enhanced when compared to a typical welded connection, and that the connection was self-centering without residual deformation [33, 60, 61, 62].

The post-tensioned steel moment connection has also been extended to use with concrete filled steel tube columns [59] and friction dampers [63] with similar results. Figure 2-26 shows schematics of these other post-tensioned steel connections.

A post-tensioned energy dissipating (PTED) connection has been studied analytically and experimentally by Christopoulos et al. [12, 13, 14, 15]. Figure 2-27a shows a schematic of the this connection. The PTED connection is based on the concept of the hybrid precast concrete connection that was presented earlier. The system incorporates high strength post-tensioned steel bars

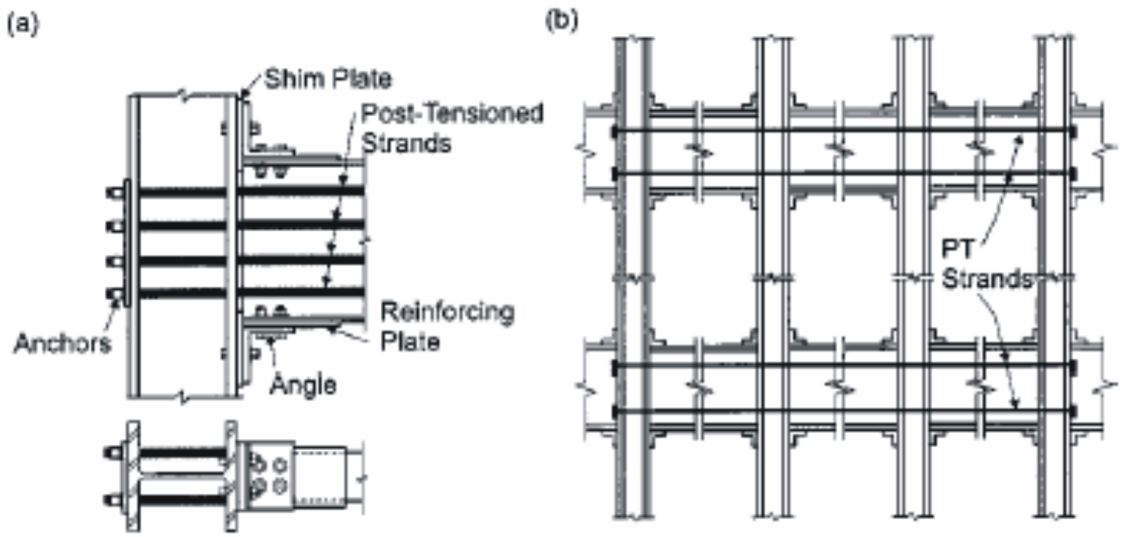

Figure 2-25: a) Post-tensioned (PT) moment connection developed by Ricles et al. with b) showing a moment resisting frame with PT connections [60].

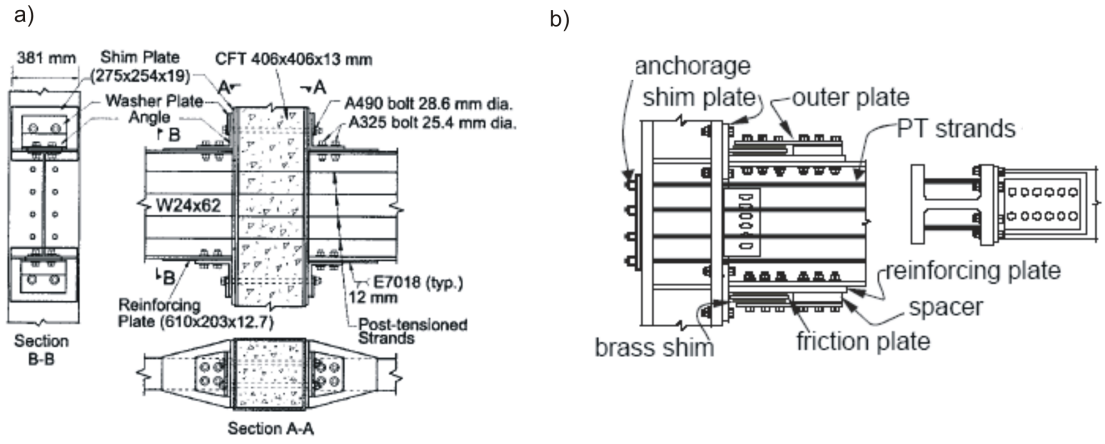

Figure 2-26: a) Post-tensioned (PT) moment connection with concrete filled steel tube columns developed by Ricles et al. [59] and b) Post-tensioned friction damped moment connection developed by Rojas et al. [63].

(Dywidag bars) along with energy dissipating bars attached to the underside of the beam flange. The energy dissipating bars (also Dywidag bars) were inserted into steel cylinders to limit buckling in order to develop stable inelastic axial deformations. Experiments were conducted on both full scale subassemblage specimens and a 1/2 scale frame assembly incorporating two exterior and one interior PTED connection. The connection is able to undergo large deformations with energy dissipation while keeping the beam and column undamaged and without residual drift. Experimental moment-rotation curves of the PTED connection showed a flag shaped hysteresis (see Figure 2-27b).

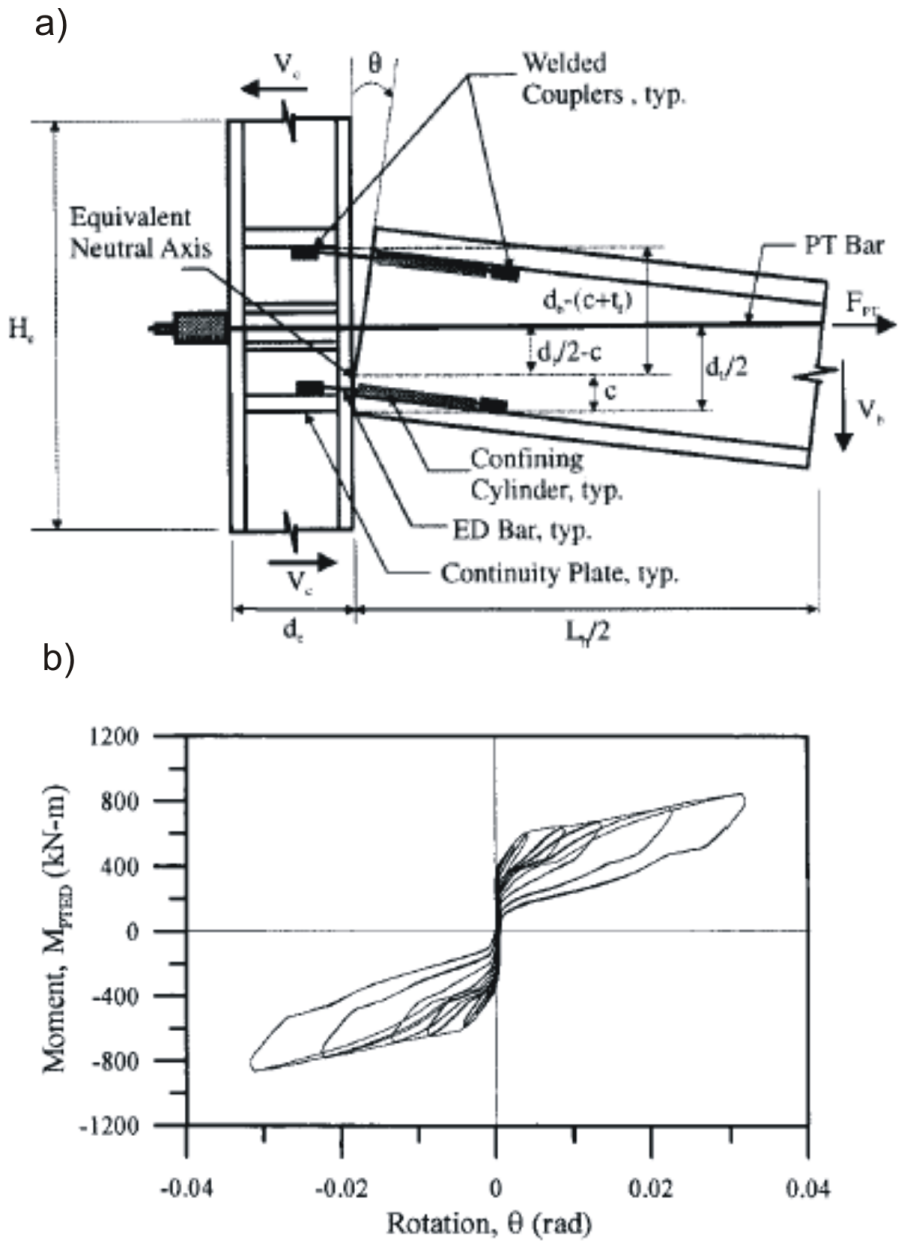

Figure 2-27: a) Schematic of the post-tensioned energy dissipating connection [15]. b) Moment rotation curve of the PTED connection showing flag shaped hysteresis [14].

CHAPTER III

EXPERIMENTAL PROCEDURES

The 1/2 scale steel connection subassemblages were tested at the Georgia Institute of Technology Structures Lab. The Structures Lab contains a large concrete reaction wall and a 4′ thick concrete strong floor suitable for conducting such tests. The tests were run in accordance with SAC testing protocols [17] to the extent that this was possible. The following chapter describes the loading scheme, lateral bracing system, data acquisition system, and instrumentation that were used for the subassemblage tests. The analysis techniques that were used in order to determine the connection forces for design are detailed. Also, this chapter describes preliminary component tests that were performed on the superelastic Nitinol and A36 steel tendons. Finally, detailed specifications of the connections that were tested are presented.

3.1 Loading scheme

Figure 3-1 shows an idealization of the loading scheme for the beam-column test setup. The displacement is applied to the top of the column while the beam ends are idealized as roller supports. In order to obtain the roller-type support at the beam ends, a pinned-pinned strut was attached to both the beam and the strong floor that allows for horizontal motion while restraining vertical motion. Figure 3-2 shows a schematic of the test setup. The struts (HSS 6.000x0.375) were attached to T-beam stubs through the use of ball joint bearings which offered a wide range of unrestrained motion.

A rotating pin assembly at the column base allowed for in-plane rotation while restraining all other motion. The pin support was bolted to a W14x120 section that was post-tensioned to the floor

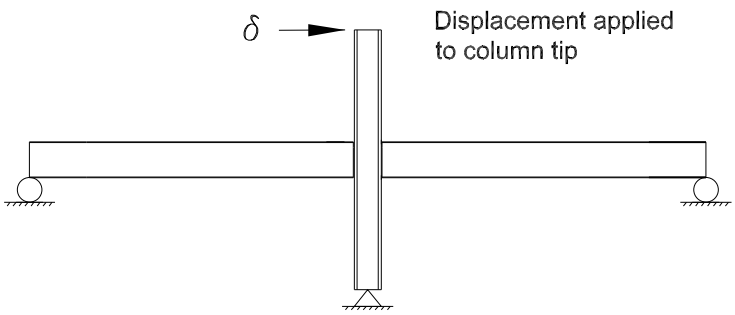

Figure 3-1: Idealization of the loading scheme for the beam-column test setup.

using Dywidag bars.

The displacement was applied to the top of the column assembly through the use of a hydraulic, servo-valved actuator that will be described in detail in a later section. The actuator was attached to two sections (W14x120 and W24x104) that brought the actuator away from the strong wall so the actuator piston would be near mid-stroke once attached to the column assembly. The actuator was not connected directly to the column but to a short, stiffened W14x257 section with a welded base plate which was, in turn, bolted to the welded end plate of the actual column.

3.2 Lateral bracing system

A frame that was originally constructed for previous connection tests was used to accomodate lateral support of the test assembly (see Figure 3-3). Two W14x120 sections with 1.25″ thick, 18″ square base plates were post tensioned to the strong floor. These columns were spaced 4′8″ center-to-center and were stabilized by two sets of diagonal braces between the columns. The diagonal braces consisted of L4x4x3/8 sections bolted to tabs which were, in turn, welded onto the column flanges. The L5x5x3/8 angle which was bolted to the cantilevered HSS6x4x1/4 was used to prevent out-of-plane motion of the upper portion of the test column. In order to reduce friction between the test column and the angle, 1/4″ thick Teflon sheets were epoxied to the angle at the contact surface. The pin assembly at the base of the column also acted as a lateral support.

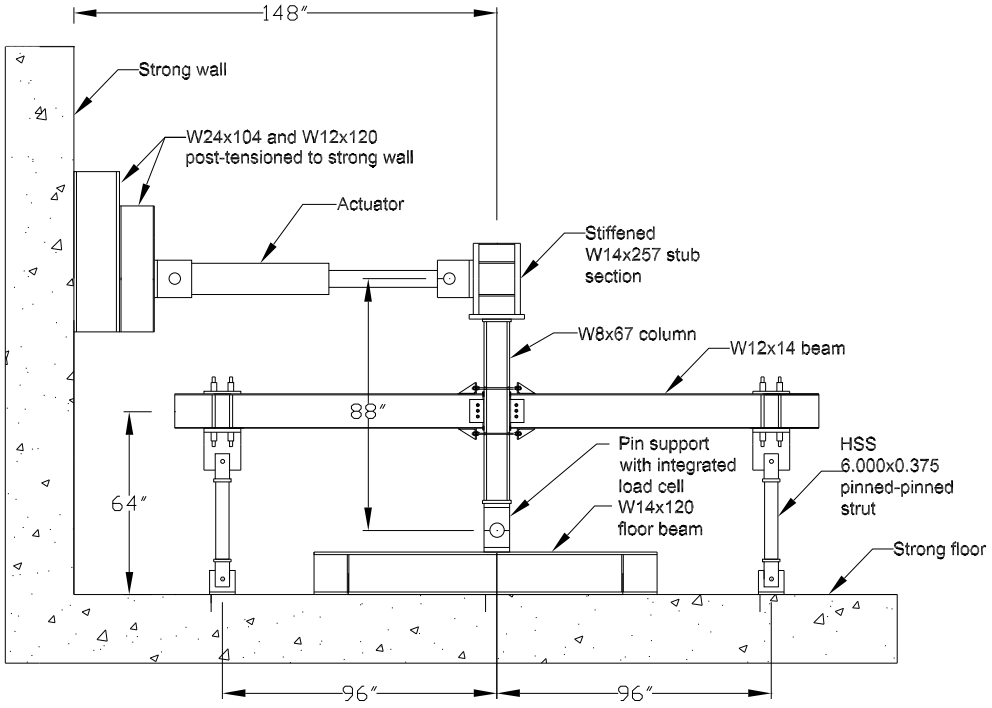

Figure 3-2: Schematic of the subassemblage test setup. Lateral supports have been omitted for clarity.

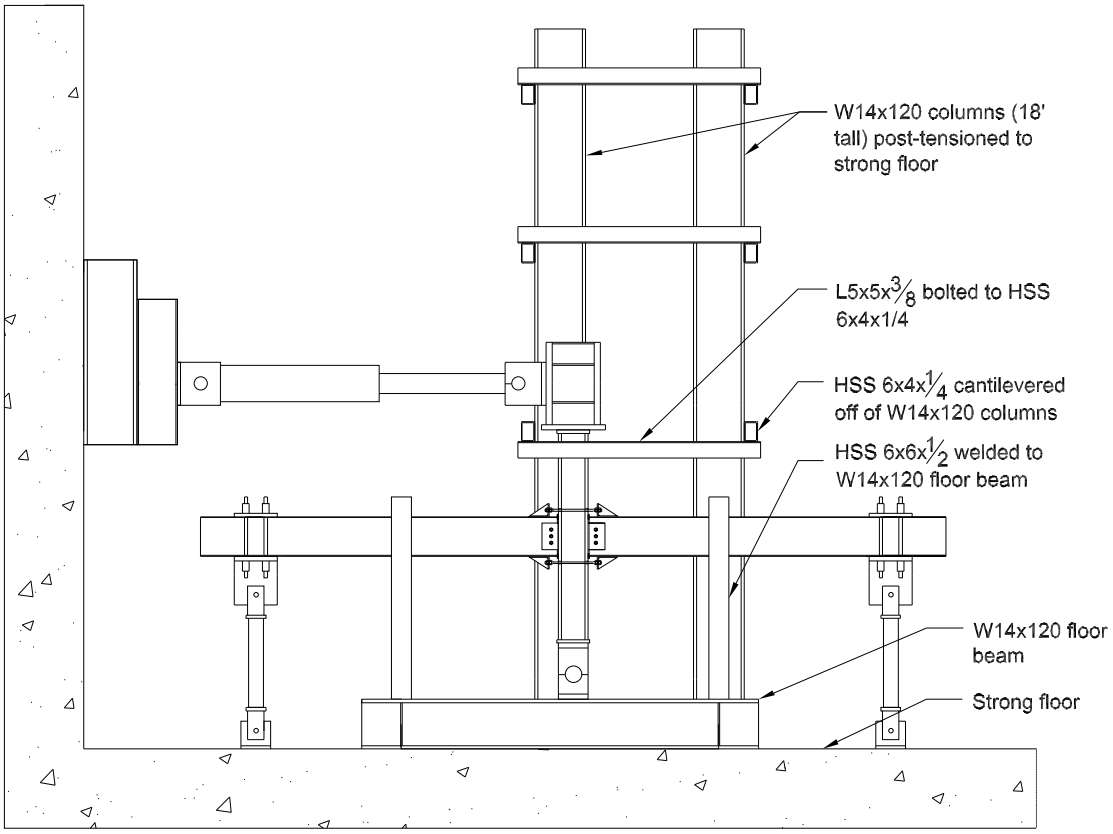

Figure 3-3: Schematic of the subassemblage test setup showing lateral bracing system

Lateral support at midspan of either beam was accomplished by HSS 6x6x1/2 sections that were welded to the W14x120 floor beam. Again, 1/4″ thick Teflon sheets were epoxied to the tube sections at the contact surface in order to reduce friction.

3.3 Actuator

A hydraulic, servo-valved actuator was connected to the top of the test column assembly. The MTS Model 243.45 actuator has a maximum capacity of 146 kips in compression and 100 kips in tension with a stroke length of 30“. Each end of the actuator has a pin connection in order to maintain axial load on the piston while reducing the possibility of excessive side loads. Integrated into the actuator is a Temposonics Transducer that measures the actuator displacement and a load cell to measure the force. The actuator was controlled using an MTS Test Star II Controller and TestWare-SX Control software. The TestWare software allows the user to specify the loading rate, the desired displacement limits, and the number of cycles during testing.

3.4 Loading Procedure

The basic loading history for the testing program consisted of stepwise increasing deformation cycles in accordance with the SAC protocol [17]. The parameter used to control the loading history is the interstory drift angle defined as interstory displacement divided by the story height. For the loading scheme used in this study, interstory drift angle is calculated as the column deflection divided by the column height. Displacement control was used with the displacements applied at the top of the column assembly using the MTS hydraulic actuator. The loading is intended to be quasi-static with a loading rate of 2 inches column deflection per minute. Table 3-1 and Figure 3-4 show the stepwise loading used in this study.

Table 3-1: SAC Loading Protocol

Load Step	Number of cycles	Drift (rad)	Actuator Displacement (in.)
1	6	0.00375	0.33
2	6	0.00500	0.44
3	6	0.00750	0.66
4	4	0.01000	0.88
5	2	0.01500	1.32
6	2	0.02000	1.76
7	2	0.03000	2.64
8	2	0.04000	3.52

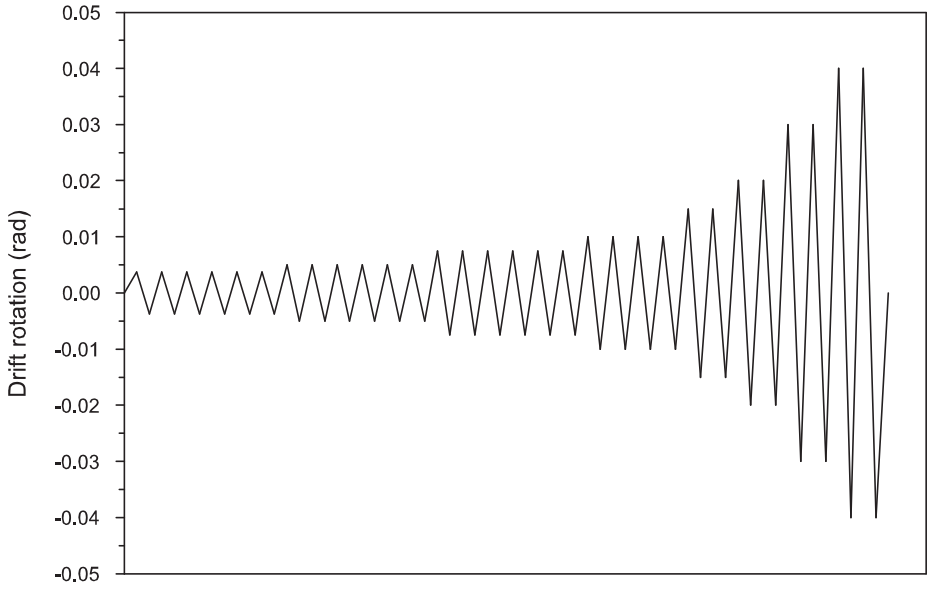

Figure 3-4: SAC loading protocol

3.5 Instrumentation and data acquisition

The test subassemblies were instrumented with a variety of sensors including axial strain gauges, high elongation axial strain gauges, strain gauge rosettes, load cells, linear variable differential transducers (LVDT's), extensometers, and string potentiometers. Detailed information of the sensor types and locations is presented later in this section. The data from all of the sesors was collected

using an OPTIM Electronics MEGADAC model 3415AC data acquisition system. The MEGADAC is able to provide both constant current and voltage excitation for all of the instruments used here when required. Tables 3-2 and 3-3 describe the data input channels, names, and sensor types. Figure 3-5 shows the basis for the naming scheme used for the instrumentation (i.e. north vs. south, top vs. bottom). The 48 channels of data were scanned at a rate of 2 Hz throughout the testing. The MEGADAC system was controlled through OPTIM Electronic's Test Control Software (TCS) on a remote computer.

Table 3-2: Instrumentation setup in data acquisition system (channels 0-31)

Channel	Input Module	Terminal Block	Card Gain	Sensor Name	Sensor Type	Comments
0			100	North Beam top middle	FLA-5-11-5L	w/ dummy gauge
1			100	North Beam top side	FLA-5-11-5L	w/ dummy gauge
2			100	North Beam bottom middle	FLA-5-11-5L	w/ dummy gauge
3	AD-1 808QB/350	STB 808QB	100	North Beam bottom side	FLA-5-11-5L	w/ dummy gauge
4			100	South Beam top middle	FLA-5-11-5L	w/ dummy gauge
5			100	South Beam top side	FLA-5-11-5L	w/ dummy gauge
6			100	South Beam bottom middle	FLA-5-11-5L	w/ dummy gauge
7			100	South Beam bottom side	FLA-5-11-5L	w/ dummy gauge
8			100	Column Up north middle	FLA-5-11-5L	w/ dummy gauge
9			100	Column Up north side	FLA-5-11-5L	w/ dummy gauge
10			100	Column Up south middle	FLA-5-11-5L	w/ dummy gauge
11	AD-1 808QB/350	STB 808QB	100	Column Up south middle	FLA-5-11-5L	w/ dummy gauge
12			100	Column Down north middle	FLA-5-11-5L	w/ dummy gauge
13			100	Column Down north side	FLA-5-11-5L	w/ dummy gauge
14			100	Column Down south middle	FLA-5-11-5L	w/ dummy gauge
15			100	Column Down south middle	FLA-5-11-5L	w/ dummy gauge
16			1	SMA Up West	YEFLA-5-11-5LT	high elongation strain gauge
17			1	SMA Up East	YEFLA-5-11-5LT	high elongation strain gauge
18			1	SMA Down West	YEFLA-5-11-5LT	high elongation strain gauge
19	AD-1 808FB-1	STB 808FB 120 Ω	1	SMA Down East	YEFLA-5-11-5LT	high elongation strain gauge
20			100	North Strut Load Cell	FLA-5-11-5L	Full Bridge Configuration
21			100	South Strut Load Cell	FLA-5-11-5L	Full Bridge Configuration
22			100	Pin Load Cell	Strainsert Model SPA-160	Integrated pin/load cell
23			100	PZ Center Up/Down	FRA-5-11-5L	Rosette 1
24			100	PZ Center North/South	FRA-5-11-5L	Rosette 1
25			100	PZ Center 45	FRA-5-11-5L	Rosette 1
26			100	PZ Top North Up/Down	FRA-5-11-5L	Rosette 2
27	AD-1 808FB-1	STB 808FB 120 Ω	100	PZ Top North North/South	FRA-5-11-5L	Rosette 2
28			100	PZ Top North 45	FRA-5-11-5L	Rosette 2
29			100	PZ Bottom South Up/Down	FRA-5-11-5L	Rosette 3
30			100	PZ Bottom South North/South	FRA-5-11-5L	Rosette 3
31			100	PZ Bottom South 45	FRA-5-11-5L	Rosette 3

Table 3-3: Instrumentation setup in data acquisition system (channels 32-55)

Channel	Input Module	Terminal Block	Card Gain	Sensor Name	Sensor Type	Comments
32			1	LVDT Top North West	DCTH500 LVDT	0.5” LVDT
33			1	LVDT Top South West	DCTH500 LVDT	0.5” LVDT
34			1	LVDT Bottom North West	DCTH500 LVDT	0.5” LVDT
35	AD-1 808FB-1	PC 1216A	1	LVDT Bottom South West	DCTH500 LVDT	0.5” LVDT
36			1	empty		
37			1	empty		
38			1	empty		
39			1	empty		
40			1	LVDT from actuator	Temposonics transducer	0-10 V output from controller
41			1	Load cell from actuator	146 k comp/100 k tens	0-10 V output from controller
42			1	empty		
43	AD-1 808FB-1	STB 808FB 350 Ω	1	empty		
44			1	North Beam Mid Deflection	P-2A	0-2” String Potentiometer
45			1	South Beam Mid Deflection	P-2A	0-2” String Potentiometer
46			1	Column Mid Deflection	P-5A	0-5” String Potentiometer
47			1			
48			100	SMA Up West	2” gauge length extensometer	Model 3542-0200-020-ST
49			100	SMA Up East	2” gauge length extensometer	Model 3542-0200-020-ST
50			100	SMA Down West	2” gauge length extensometer	Model 3542-0200-020-ST
51	AD-1 808FB-1	STB 808FB 350 Ω	100	SMA Down East	1” gauge length extensometer	Model 632.31E-24
52			1	empty		
53			1	empty		
54			1	empty		
55			1	empty		

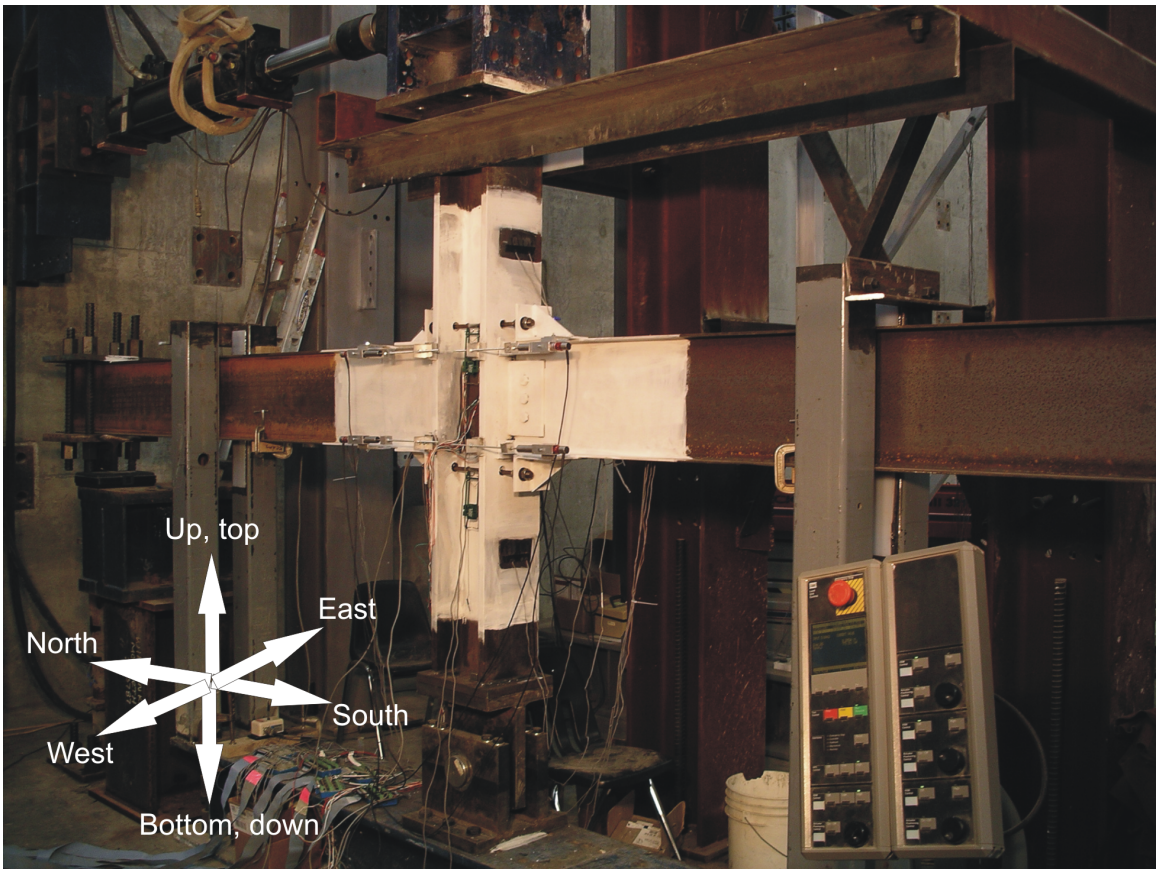

Figure 3-5: Picture of test setup with inset showing directional orientation

3.5.1 Beam instrumentation

Axial strain gauges were placed a distance equal to the depth of the beam (d_b) away from the connection, specifically 12“ from the edge of the angle anchor. These strain gauges were monitored to ensure that the moment within the beam remained elastic throughout the testing. The strain gauges used were Texas Instruments FLA-5-11L 120 ohm strain gauges. A half bridge completion dummy gauge configuration was used for the strain gauges placed on the beams. The reason for the dummy gauges is that the data acquition input cards were configured for 350 ohm strain gauges and the dummy gauges were used to circumvent this problem. Two strain gauges were placed at each location (middle of beam flange and halfway between middle and flange edge) at both the top and

bottom of the beam. (see Figure 3-6)

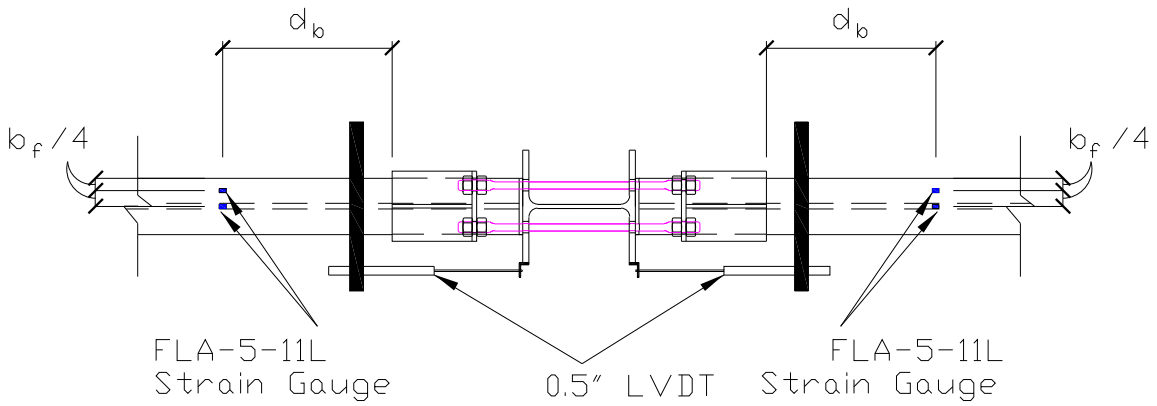

Figure 3-6: AutoCAD detail of beam instrumentation

String potentiometers with a maximum displacement of 2 inches were placed near the midlength of the beam in order to determine the beam deflections (see Figure 3-7).

LVDT's (linear variable differential transducers) were placed at the interface between the beam and columns in order to measure the relative rotation between the two (see Figure 3-6). Horizontally, the LVDT's were placed at the level of the beam flanges and were afixed to the beam and columns by a series of aluminum bars and angles (see Figure 3-8). This measurement is important in quantifying the gap opening that will occur as a result of loading the connection. Four RDP Electronics Ltd. DCTH500 series LVDT's with a maximum displacment of 0.5 inches were used and placed on one side only of the connection. It was determined that it wasn't necessary to place another set of LVDT's on the other side of the connection as out of plane motion is adequately restrained and torsional effects in the beam are insignificant.

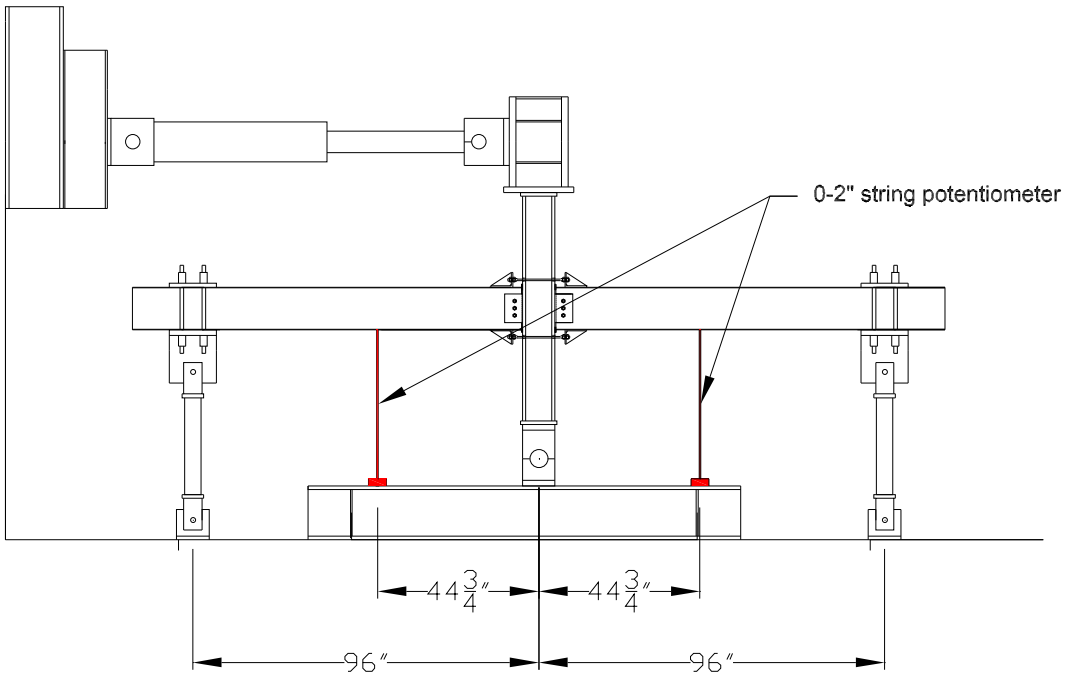

Figure 3-7: AutoCAD detail of string potentiometer location

Figure 3-8: Picture showing connection of LVDT to beam and column

3.5.2 Column instrumentation

The column was also instrumented with strain gauges (Texas Instruments model FLA-5-11L 120 ohm) placed at a column depth (d_c) distance away from the connection to ensure the strains are evenly linearly distributed throughout the cross section (see Figure 3-9). A dummy gauge configuration was also used for these sensors.

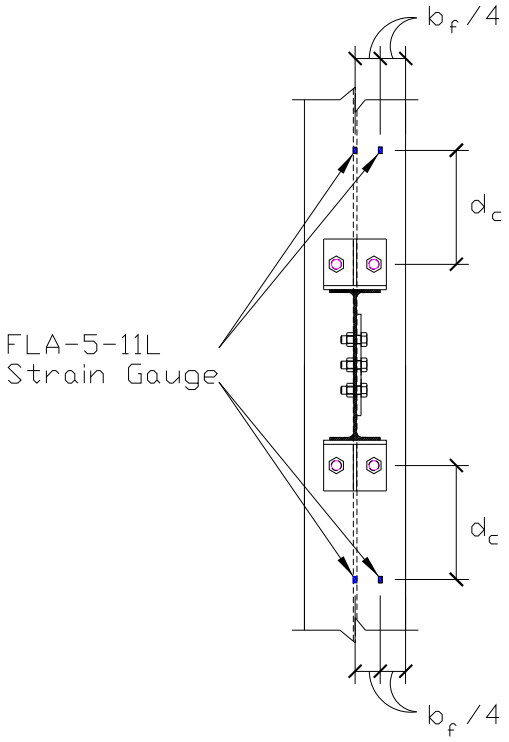

Figure 3-9: AutoCAD detail of column instrumentation

Strain gauge rosettes attached to the column measured the panel zone deformation (see Figures 3-10 and 3-11). Although five separate strain gauge rosettes were placed inside the column, only three were monitored (center, top-north, and bottom-south) in order to limit the number of data acquistion channels. Because the panel zone deformations were expected to remain elastic, it was determined that monitoring only three strain gauge rosettes would be adequate.

A string potentiometer with a maximum displacement of 5 inches measured the deflection of

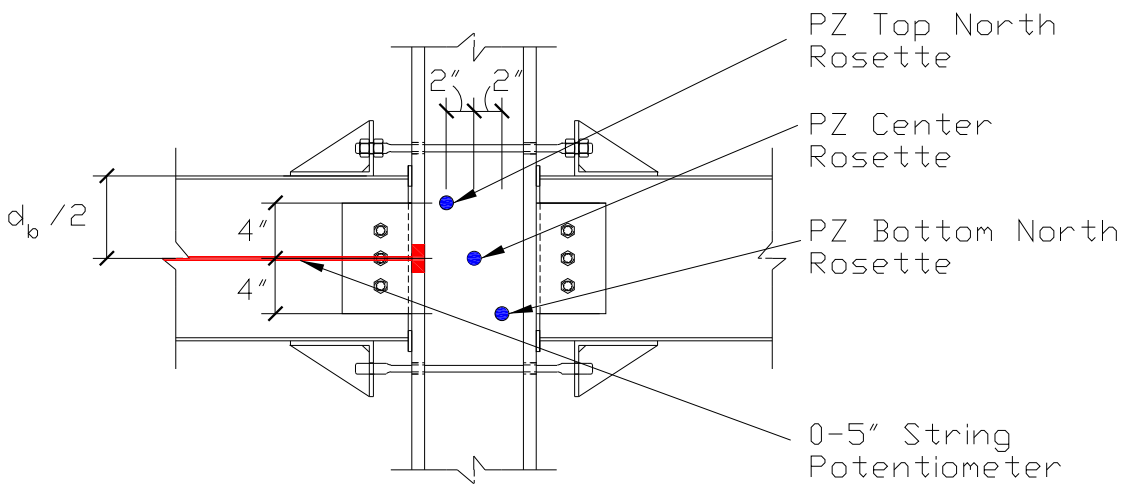

Figure 3-10: AutoCAD detail of column panel zone instrumentation

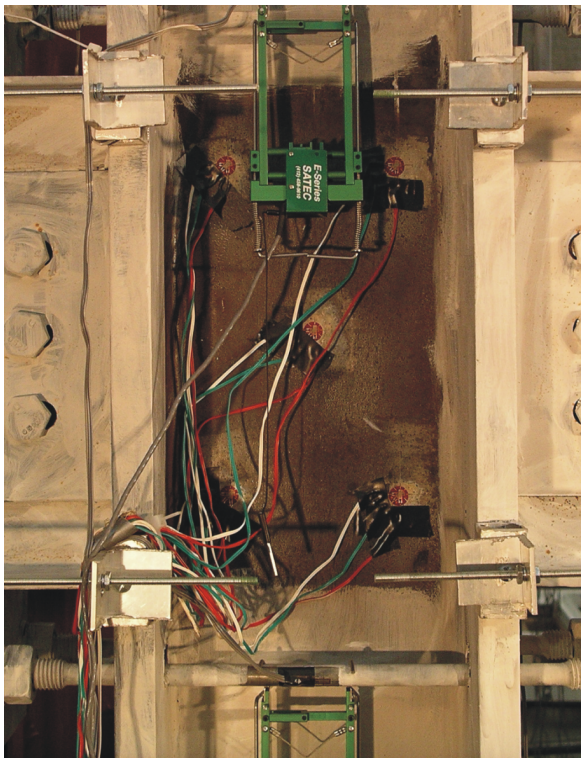

Figure 3-11: Picture showing strain gauge rosettes within the column panel zone

the column at the level of the connection (see Figure 3-10).

3.5.3 Overall assemblage instrumentation

The moment transferred by the connection was measured by a series of sensors. A temposonics transducer attached to the actuator measured the displacement at the column tip. Also attached to the actuator was a load cell that measured the force applied at the column tip. The pin connection at the bottom of the column also acted as a load cell. This integrated pin-load cell was configured to measure the force in the horizontal direction or the reaction from the actuator force. Full bridge strain gauges attached to the pinned-pinned struts acted as load cells which were used to verify the moment transferred by the connection (see Figure 3-12). A configuration in which two strain gauges (Texas Instruments FLA-5-11L 120 ohm gauges) were placed axially and two similar strain gauges were placed transversely allowed for a reading sensitive enough to accurately measure the load within the struts. Each pinned-pinned strut (north and south) was calibrated prior to testing to ensure correct load readings.

3.5.4 Tendon instrumentation

The tendons were instrumented with extensometers in order to measure their axial deformation. For the steel tendon tests, three of the four tendons were instrumented with Epsilon Technology Corp. Model 3542-0200-020-ST extensometers (see Figure 3-13). These extensometers have a gauge length of 2.0 inches with a travel of +/- 0.4 inches, equating to measurable strains of +/- 20%. For the Nitinol tendon tests, the fourth tendon (SMA Down East) was instrumented with an MTS Model 632.31E-24 extensometer with a gauge length of 1.0 in (see Figure 3-14).

Also used to measure axial deformation of the moment transferring tendons were high elongation strain gauges (Texas Instruments YEFLA-5-11-5LT). These strain gauges are theoretically able to measure strains up to 20%. These strain gauge were attached to the tendons for the A36 steel

Figure 3-12: Picture showing full bridge strain gauge configuration attached to the pinned-pinned struts

Figure 3-13: Picture showing Epsilon Technology Corp. extensometers and high elongation strain gauges attached to the A36 steel tendons

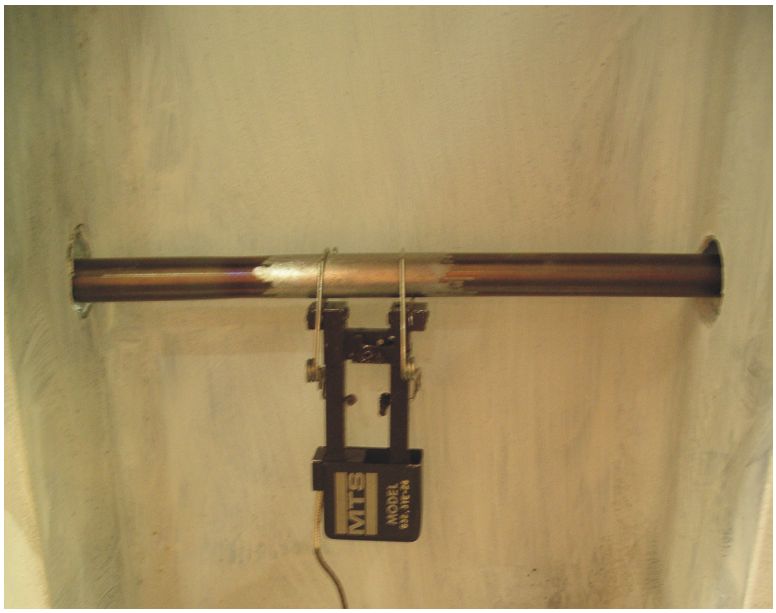

Figure 3-14: Picture showing MTS extensometer attached to the superelastic Nitinol tendon

tendon tests and can be seen in Figure 3-13. However, it was found that these strain gauges did not work well when measuring strains cyclically and were not used during the Nitinol tendon tests.

3.6 Preliminary analysis and design

It was determined initially that the subassemblage to be tested would be a half-scale interior connection with a loading scheme where the displacement would be applied to the column tip (see Figure 3-1). A W12x14 beam section was to be used and a W8x67 section was readily available and to be used as the column. This configuration allowed for a weak-beam, strong column relationship.

The design of the connection was predicated by simplifying the analysis of the internal forces. The superelastic Nitinol bars acted as the moment transfer elements and ran through the column while the shear tab was to transfer shear only. In order to ensure that the shear tab bolts did not transfer moment, long slotted holes were used to allow for that rotation. Like other recentering steel connections that have been tested [15, 60], the behavior of the connection is dictated by the gap opening at the interface between the beam and column.

A nonlinear static analysis was performed using a nonlinear finite element analysis program, DRAIN-2DX [57]. This analysis was used to obtain maximum forces and to size the A36 steel and Nitinol tendons. It was important to model the expected behavior and to ensure that the geometry of the model reflected the geometry of the actual connection; therfore, careful attention was given to the interface of the beam and column where the gap opening and closing would occur. Furthermore, the nonlinear response of the moment-tranferring tendons needed to be incorporated into the model.

A diagram of the connection modeled is shown in Figure 3-15. The beams and columns were modeled with plastic hinge elements. Although the beams and columns were expected to remain elastic, the model would be able to capture their behavior if they did not. As explained earlier, long slotted holes were used so that only shear was transferred by the shear tab. Therefore, the shear tab component was modeled as two nodes connected by a zero length element. The element transfers shear only and has a very low stiffness in the x-direction and low rotational stiffness. A rigid element was used to connect the ends of the moment transfering tendons to the beam. This element was made

rigid by giving it a very large moment of inertia making it extremely stiff. The moment transferring tendons were modeled using an inelastic truss element that had an initial stiffness and a secondary stiffness after yielding was reached. The strain hardening portion of the stress-strain curve was not modeled. DRAIN-2DX has a compression/tension link element that was used to model the gap behavior. This element had zero stiffness in tension and high stiffness in compression. A certain gap length could be specified before the high stiffness in compression was reached. The connection was then subjected to an interstory drift of 4% which was the intended capacity of the connection. Second order effects were ignored in the analysis.

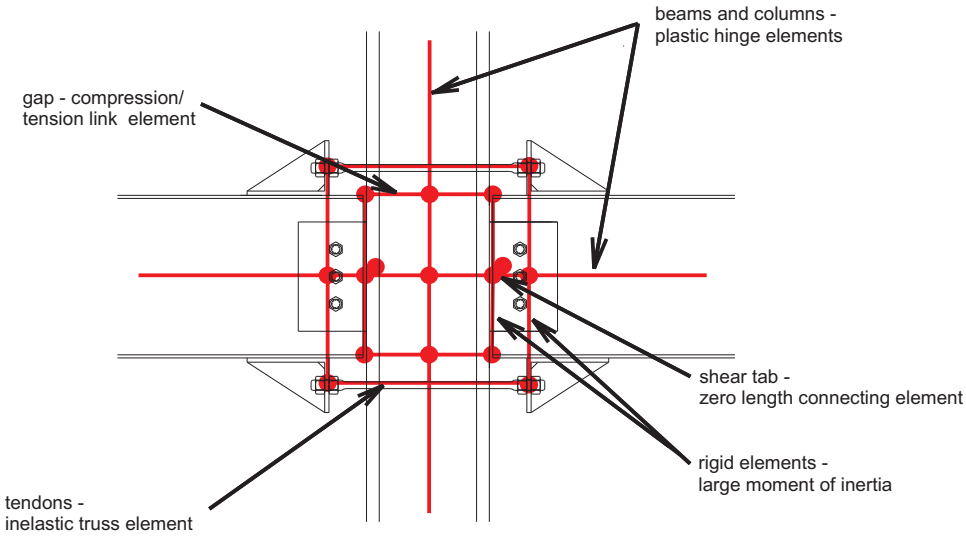

Figure 3-15: Diagram of the connection model used in DRAIN-2DX

3.6.1 Results of preliminary analysis

An important parameter that was evaluated was the M/Mp ratio, the ratio between the transferred moment to the plastic moment of the beam. The connection was intended to be partial strength where the beam was to remain elastic. Therefore, any inelastic deformation would be confined to the easily replaceable tendons. The model was able to predict how this ratio changed at 4% interstory drift based on the tendon bar area, bar gauge length, and distance between tendons. Also

given by the model was the maximum forces within the elements that could be expected and how the initial gap affected the moment transfer. When a small gap of even 1/8″ was included in the model, the connection was found to transfer a significantly smaller moment at 4% drift and also led to much smaller strains within the tendons which affects the amount of energy that can be dissipated by the connection. Therefore, it was determined that shims would need to be installed in order to ensure that the initial gap remains essentially zero. The results from the preliminary analyses are given in Table 3-4.

Table 3-4: Results from preliminary DRAIN-2DX analysis

		Superelastic Nitinol connection	**Superelastic Nitinol connection w/ $\frac{1}{8}$" gap**	**A36 Steel tendon connection**
Diameter of tendon	in	0.5	0.5	0.5
Area of two tendons	in^2	0.393	0.393	0.393
Gauge length, L_{tendon}	in	12	12	12
Distance between tendons, d'	in	15.9	15.9	15.9
Size of gap between beam/flange	in	0.0	0.125	0.0
Interstory drift	rad	0.04	0.04	0.04
Displacement at actuator	in	3.52	3.52	3.52
Actuator load	k	7.23	6.22	6.72
Force in each tendon	k	12.8	11.0	11.9
Stress in each tendon	ksi	65.0	56.0	60.5
Total extension in each tendon	in	0.448	0.205	0.451
Strain in each tendon		0.037	0.017	0.038
$M_{connection}$	k-in	636	547	591
Mp_{beam}	k-in	870	870	870
$M_{connection}/Mp_{beam}$		0.73	0.63	0.68
Force in struts	k	3.3	2.9	3.1

3.7 Component tests

In order to gain a better understanding of the material properties of the tendons, several tests were conducted on both A36 steel bars and superelastic Nitinol bars. The specimens were tested using a 250 kN (55 kip) MTS hydraulic testing testing frame fitted with MTS 647 hydraulic wedge grips. The desired loading protocal was input using an MTS TestStar controller. An MTS 632.31E-24 series extensometer were used to measure strains. The same OPTIM Electronics data collection system that was used for the connection tests was used to collect the load, displacement, and extensometer data for the component tests. A picture of a typical component test specimen inside the grips of the testing machine can be seen in Figure 3-16.

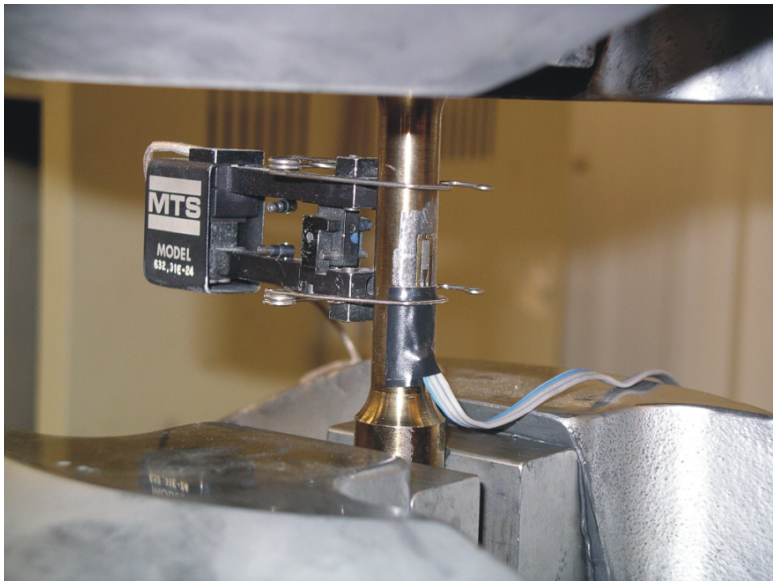

Figure 3-16: Picture showing a typical component test setup

3.7.1 A36 Steel rod tests

First, an A36 steel rod was tested pseudo-statically to failure to determine the overall stress-strain behavior. The specimen was machined to the specification shown in Figure 3-17 and was based on the ASTM E8 standard for tensile testing of metallic materials. For this test, strain values were obtained from an extensometer up to 2%, after which the extensometer was removed and gross strain was obtained by dividing the original gauge length from the crosshead displacement. Results from the monotonic tests on the A36 steel rod specimens are given in Figures 3-18 and 3-19. The ASTM A36 steel rod was found to have a yield stress of 52.5 ksi, an elastic modulus of 31,060 ksi, an ultimate strength of 82.0 ksi, and an ultimate strain of 35.3%.

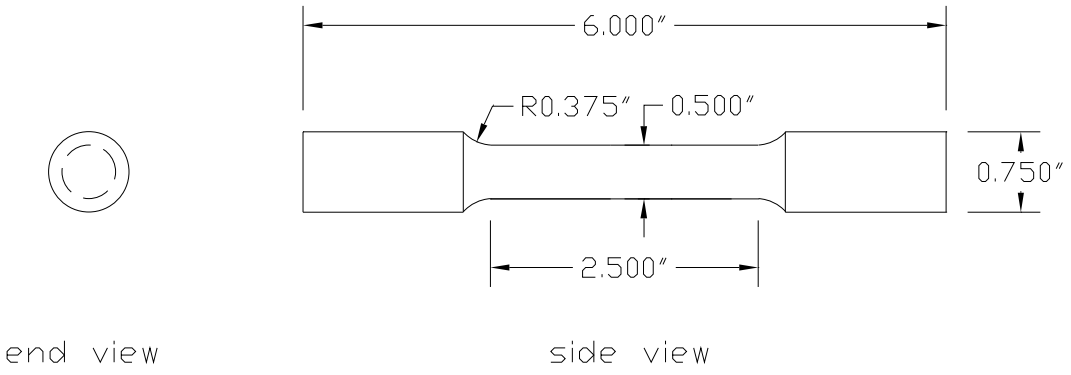

Figure 3-17: Schematic of the specimen used for the A36 steel monotonic test

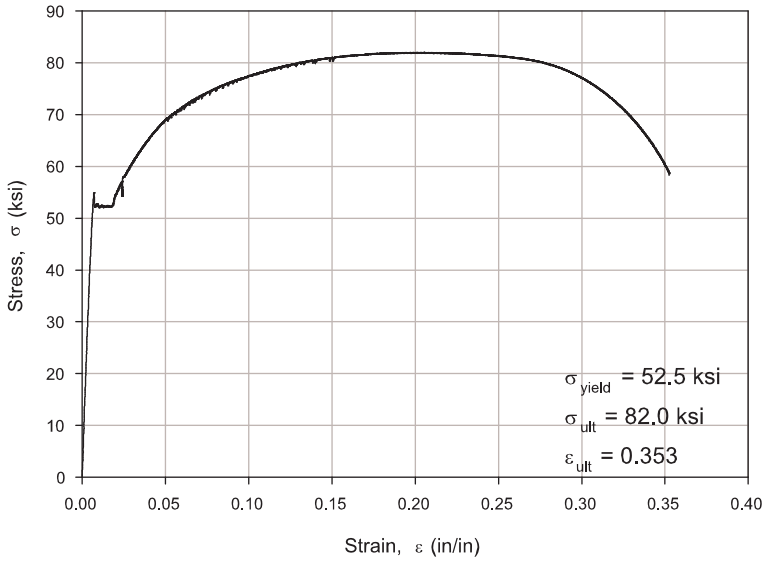

Figure 3-18: Stress versus gross strain (from crosshead displacement) for A36 steel rod specimens tested monotonically

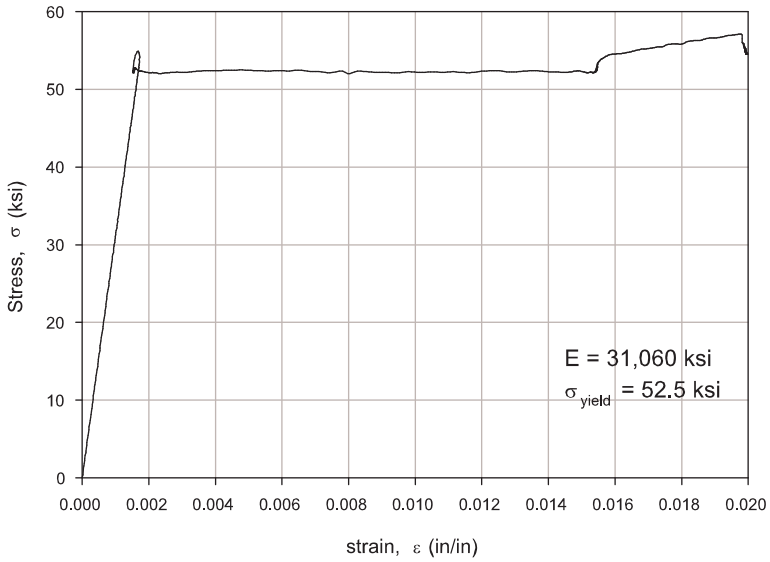

Figure 3-19: Stress versus strain (from extensometer) for A36 steel rod specimens tested monotonically

Next, a cyclic test was performed on an A36 steel rod which was intended to mimic the expected displacement history to be experienced by the A36 steel tendon during the connection subassemblage testing. A schematic of the specimen used for the A36 steel cyclic test is shown in Figure 3-20. It was determined from the preliminary analysis using DRAIN-2DX that the value of the interstory drift (in radians) that would be imposed on the connection during subassemblage testing would be nearly equal to the strain in the tendon (see Table 3-4). Therefore, the test was performed in displacement control with a strain history corresponding to the interstory drift from the SAC loading protocol (see Figure 3-21). The rate at which the rod was cycled was 0.025 Hz which is considered pseudo-static testing. The extensometer was not used during the A36 steel cyclic test due to concerns over buckling of the specimen which could potentially damage the extensometer. A plot of the stress versus gross strain for the A36 steel cyclic test is given in Figure 3-22. It can be seen from the figure that there is large residual strains at the points of zero stress because of the elastic unloading of the material.

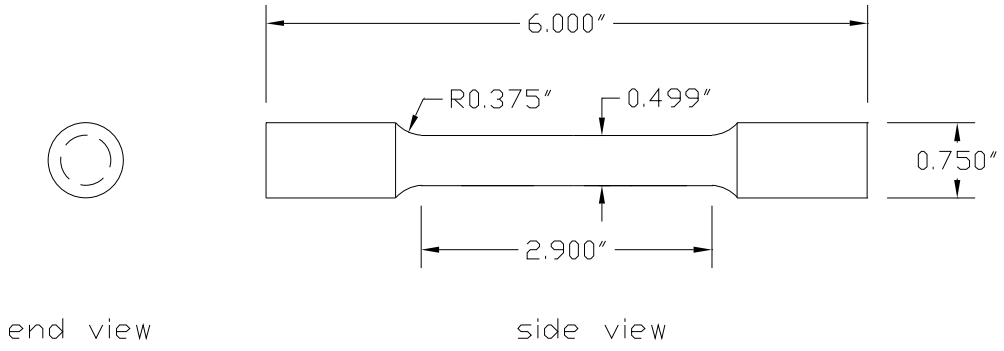

Figure 3-20: Schematic of the specimen used for the A36 steel cyclic test

Energy dissipation is an important parameter to focus on when considering earthquake applications. The energy dissipation can be calculated by integrating the area under the load/displacement

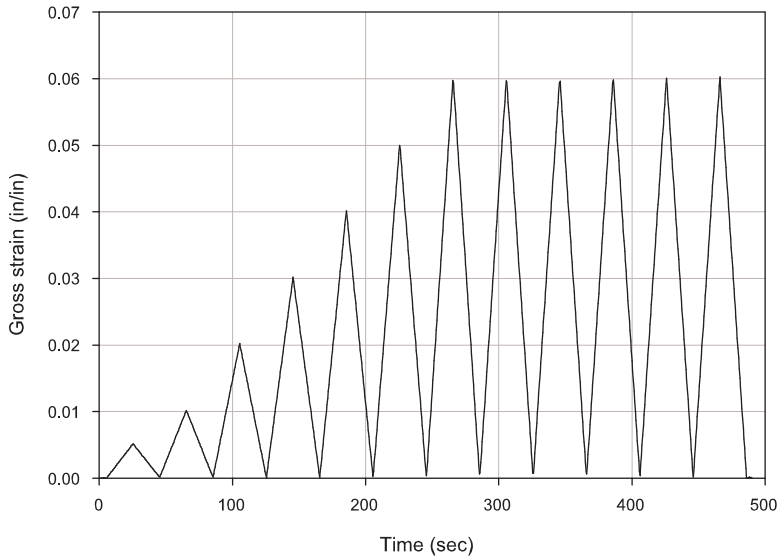

Figure 3-21: Displacement history for A36 steel rod specimen tested cyclically

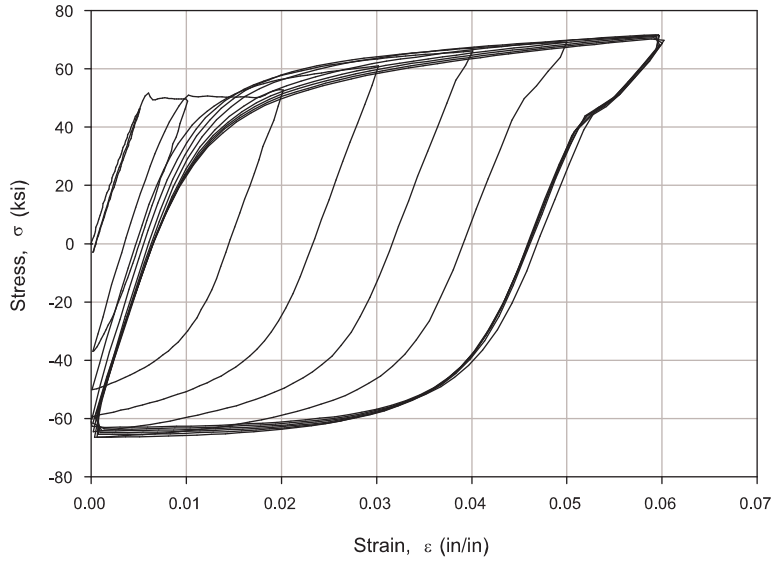

Figure 3-22: Stress versus gross strain (from crosshead displacement) for A36 steel rod specimen tested cyclically

curve using the trapezoidal rule. Furthermore, energy dissipation can be non-dimensionalized by calculating the equivalent viscous damping. Equivalent viscous damping is a function of both the dissipated energy (E_D) and the maximum strain energy (E_{So}) of a particular cycle (see Figure 3-23) and can be calculated using the following equation:

$$\xi_{eq} = \frac{1}{4\pi}\frac{E_D}{E_{So}} \tag{3.1}$$

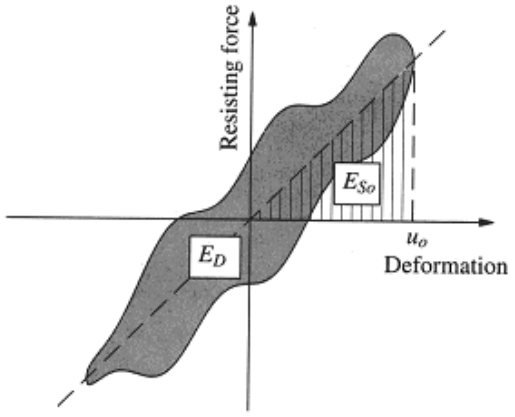

Figure 3-23: Equivalent viscous damping (ξ_{eq}) is a function of both the energy dissipated (E_D) and the maximum strain energy (E_{So}) for that particular cycle [11]

The equivalent viscous damping also normalizes the energy dissipation to the volume of the bar which is important when comparing bars with different lengths and diameters. The equivalent viscous damping versus the maximum strain in a cycle for the A36 steel rod specimen is shown in Figure 3-24. At the smaller strain cycles, the equivalent viscous damping is small because there is little yielding of the rod and, therefore, little energy is dissipated. However, at the 6% strain cycles the A36 steel rod that was tested exhibited an equivalent viscous damping value of nearly 19%.

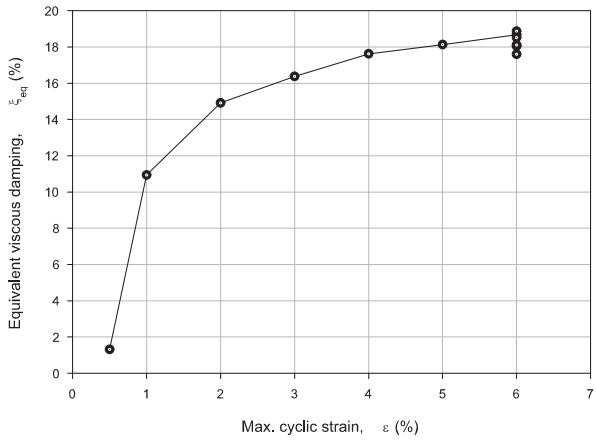

Figure 3-24: Equivalent viscous damping versus maximum cyclic strain for A36 steel rod specimen tested cyclically

3.7.2 Superelastic Nitinol rod tests

Superelastic Nitinol rods (0.5″ diameter) were tested in order to gain further insight into their material properties. The two specimens, as received from Special Metals, Inc., were hot-rolled, straightened, centerless ground, and heat treated to be superelastic (350 °C for 30 minutes and air cooled). Each specimen had a composition of 55.95 wt% nickel with the balance of titanium. The specimens were then machined from the original 0.75″ diameter rod to the specifications shown in Figure 3-25 which are based on the standard ASTM E8.

Because of the potential of losing superelastic properties after machining, the specimens were heat treated again after machining. One rod was heat treated at 350 °C for 30 minutes and immediately water quenched while the other was heat treated at 400 °C for 30 minutes and water quenched. The specimens were tested in extensometer strain control according to the loading protocol shown in Figure 3-26. As was the case for the A36 steel rods that were tested, the superelastic Nitinol rods were tested at a rate of 0.025 Hz (pseudo-static testing).

The stress-strain plots from the tests on the superelastic rods are presented in Figure 3-27. Both

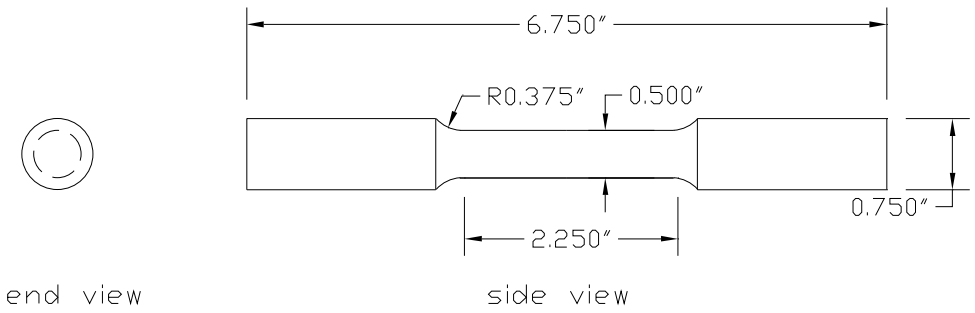

Figure 3-25: Schematic of the specimen used for the superelastic Nitinol rod tests

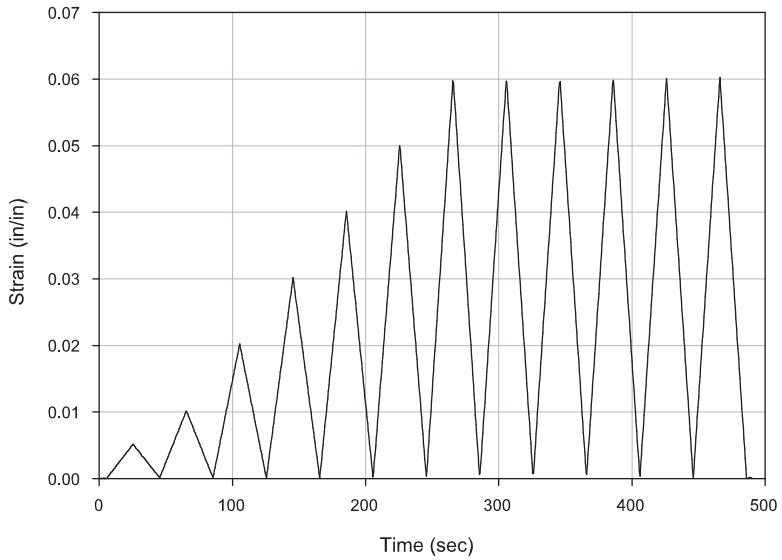

Figure 3-26: Loading protocol for the superelastic Nitinol rod tests

specimens showed good superelastic behavior with the formation of a clear loading plateau and the typical flag shaped hysteresis. The specimen that was heat treated at 350 °C only underwent two 6% strain cycles due to equipment issues.

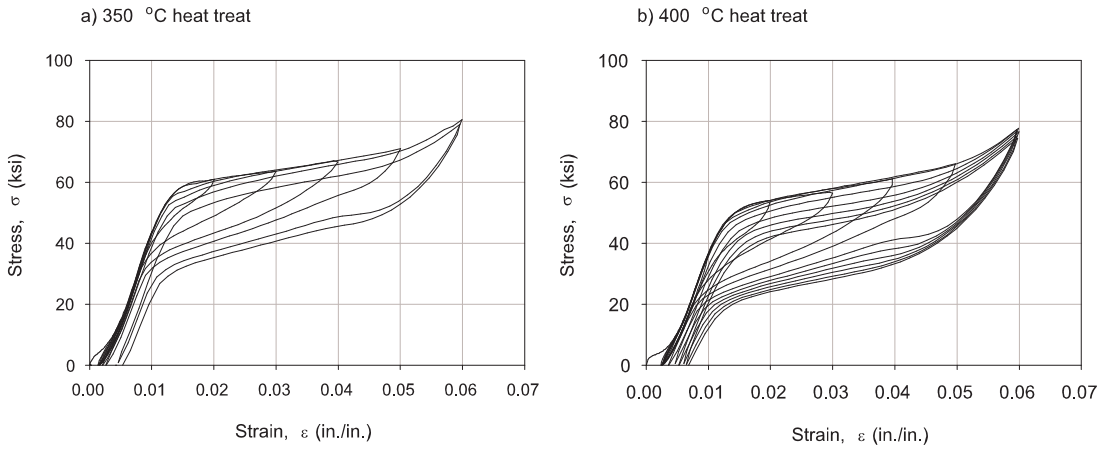

Figure 3-27: Stress versus strain (from extensometer) for the superelastic Nitinol rod tests for a) specimen heat treated at 350 °C and b) specimen heat treated at 400 °C

A comparison between the different specimens in terms of the residual strain, equivalent viscous damping, elastic modulus, and forward transformation stress is graphically shown in Figure 3-28. The 400 °C heat treated specimen showed a smaller elastic modulus and a smaller forward transformation stress yet did show a larger equivalent viscous damping due to a larger area contained within the hysteresis loops. A smaller forward transformation stress could be important in limiting forces transferred to the structure. A larger residual strain was shown by the 400 °C heat treated specimen. However, the residual strains for both specimens remained under 1% which is suitable for applications that take advantage of the recentering capabilities of superelastic Nitinol. The optimal annealing temperature chosen for this study was 400 °C as it provided a relatively better damping

capacity and a smaller forward transformation stress to limit the forces to be transferred while still maintaining reasonable residual strains.

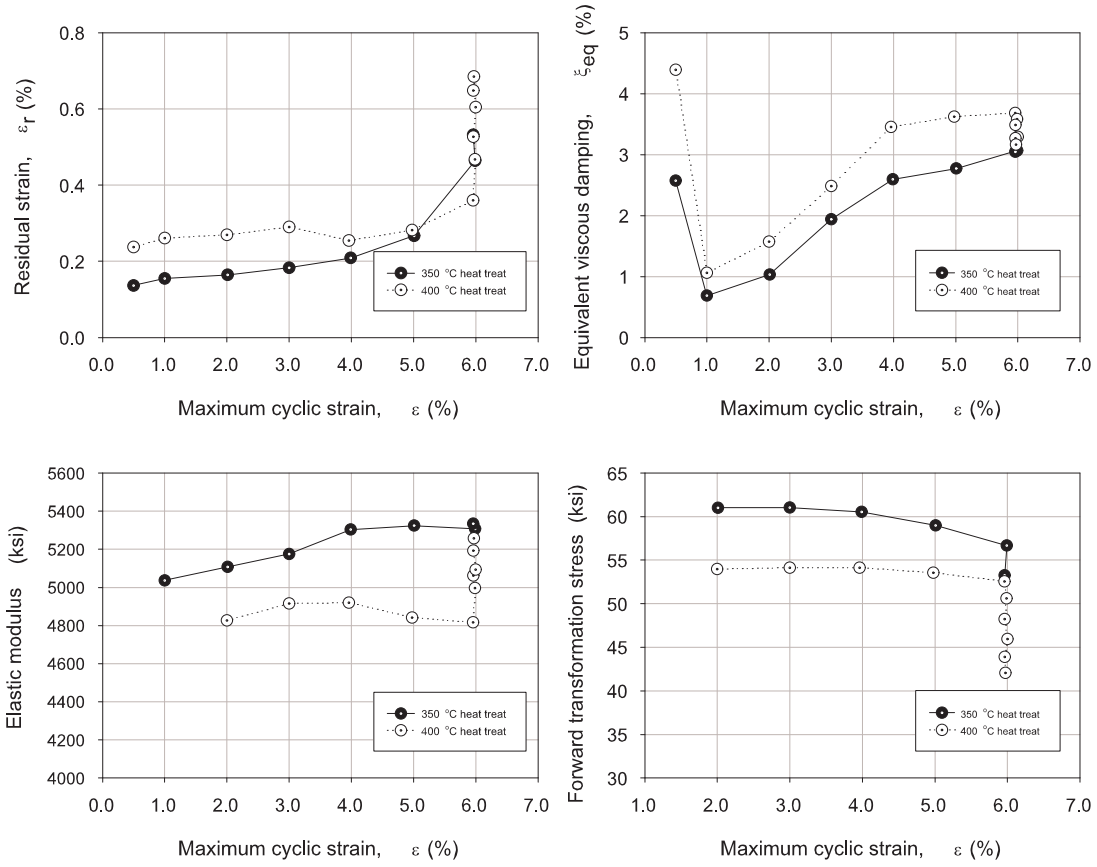

Figure 3-28: Comparison between superelastic Nitinol rod tests for specimens heat treated at 350 °C and 400 °C

3.8 Connection specifications

A series of tests on the connections subassemblages were conducted with either A36 steel tendons or superelastic Nitinol tendons. The following section describes the specifications for each of the connection types tested.

3.8.1 Test setup with A36 steel tendons

This connection was used to join a W8x67 column section to W12x14 beam sections. Figure 3-29 shows an AutoCAD detail of the connection that was tested. The shear tab used was a 5″x8″x3/8″ steel plate that was welded to the column flange. The shear tab had long slotted holes and A490 5/8″ diameter bolts were used to connect the shear tab to the beam web. Long slotted holes were used because the shear tab was assumed to only transfer shear and allowance was needed to allow for the gap to open at the interface between the column flange and the beam flange.

The A36 steel tendons run through 13/16″ holes drilled through the column and are attached to stiffened angle anchors by nuts that are screwed onto the threaded ends of the tendons. A detail of the A36 steel tendon is shown in Figure 3-30. The stiffened angle anchors (L6x4x5/16 section with 1/4″ angle stiffener) were welded to the beam flanges. At the interface between the column flange and the beam flange, steel shims were added to engage the tendons at low rotation levels.

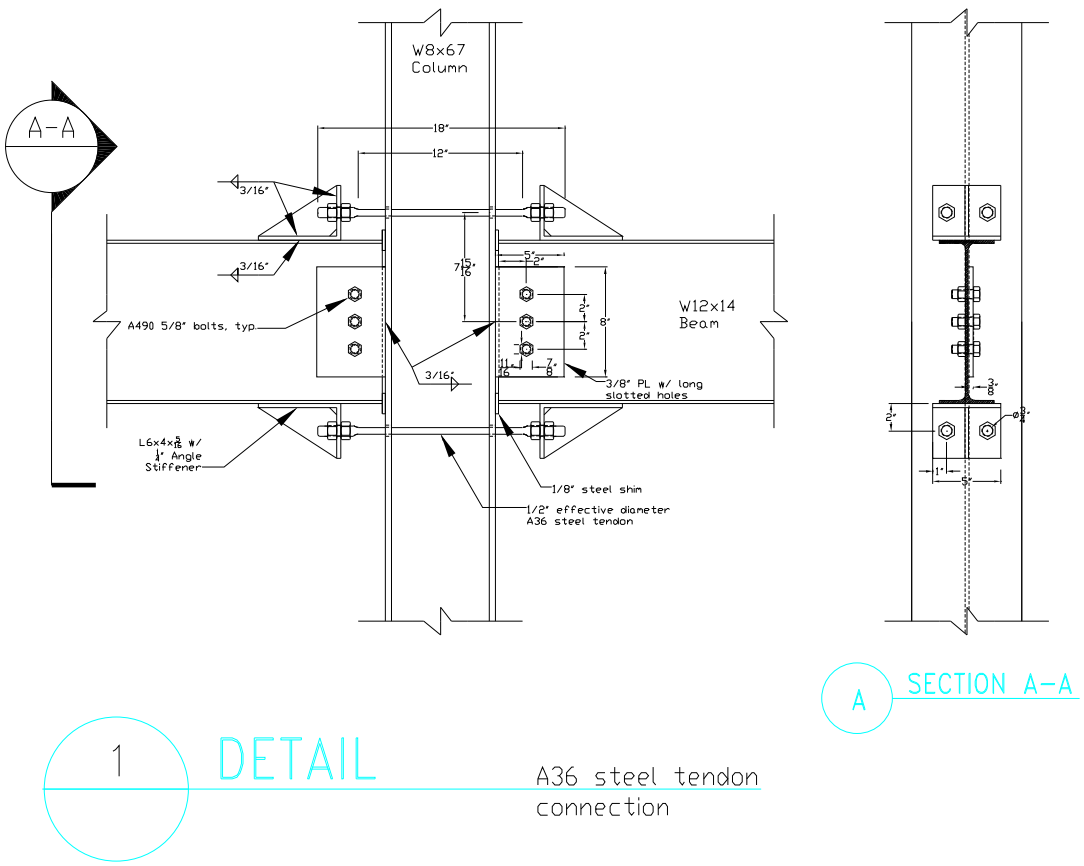

Figure 3-29: AutoCAD detail of the A36 steel tendon connection

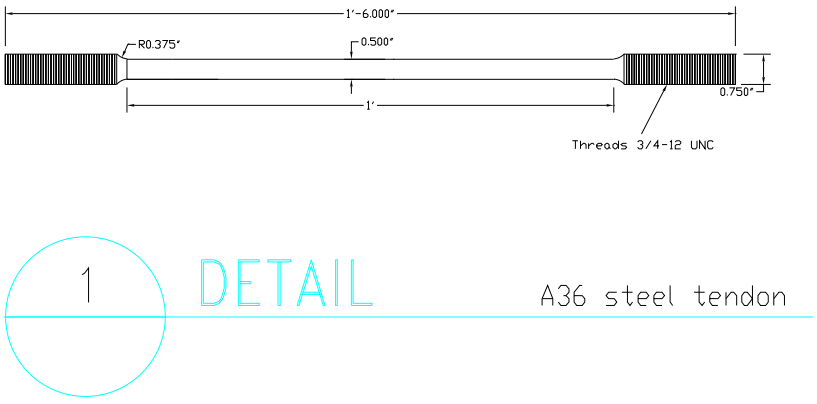

Figure 3-30: AutoCAD detail of the A36 steel tendon

3.8.2 Test setup with superelastic Nitinol tendons

The connection that utilized superelastic Nitinol tendons used the same column, beams, shear tab and angle anchors as the previous tests using A36 steel tendons. However, a few changes were made to the superelastic Nitinol tendon connection (see Figure 3-31). Because problems arose with the initial gap opening at the column flange/beam flange interface being too large, a larger 1/4″ shim was used. Also, mild steel bars (6″x1″x1/2″) were used to strengthen and to stiffen the column flange at the column flange/beam flange interface. Figure 3-32 shows a picture of the superelastic Nitinol tendon connection highlighting the modifications that were made. The superelastic Nitinol tendon was machined to the specifications shown in Figure 3-33 and was heat treated at 400 °C for one hour and then water quenched. The threads used for the Nitinol tendon were fine threads as opposed to the coarse threads that were used for the A36 steel tendon. Fine threads were used for the Nitinol tendon because of their superior strength and because they tend to minimize the stress risers at the thread location.

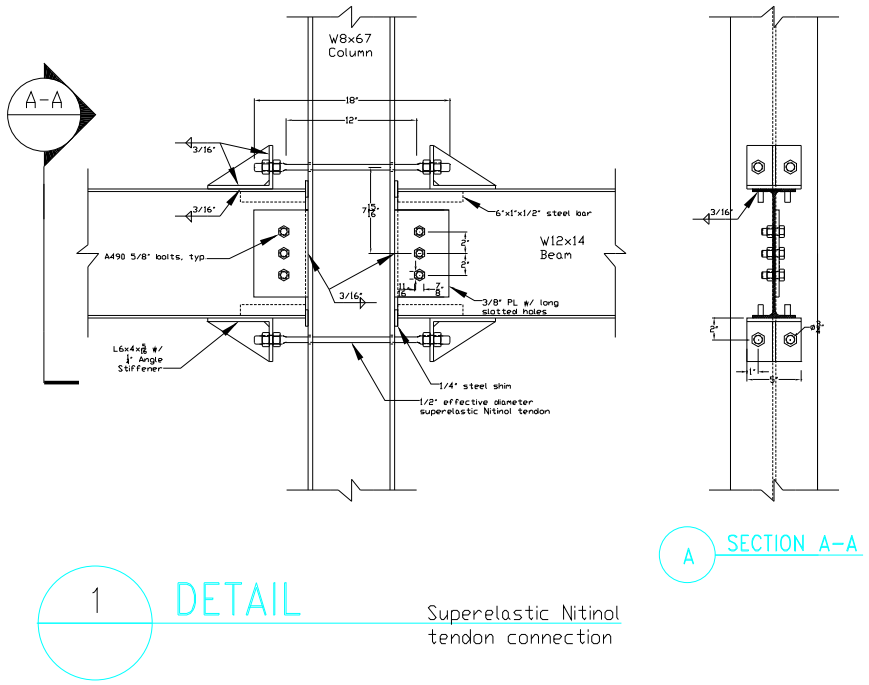

Figure 3-31: AutoCAD detail of the superelastic Nitinol tendon connection

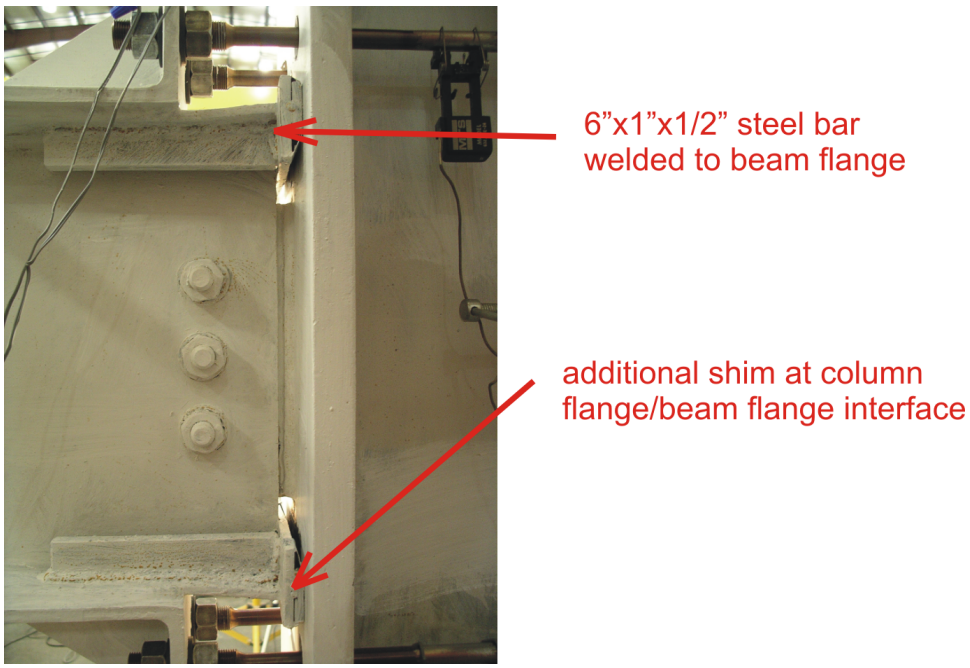

Figure 3-32: Picture of the superelastic Nitinol tendon connection highlighting modifications

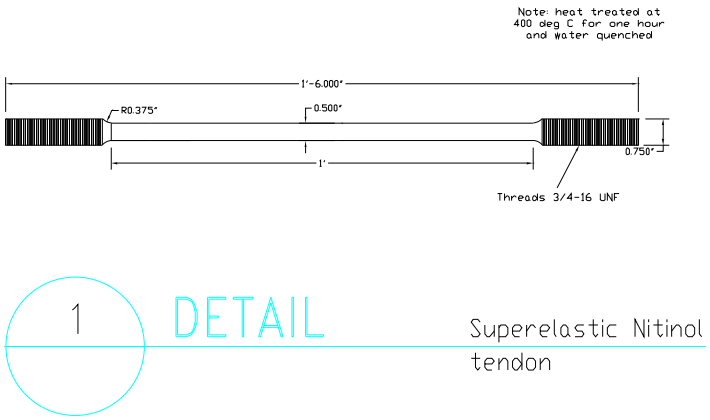

Figure 3-33: AutoCAD detail of the superelastic Nitinol tendon

CHAPTER IV

EXPERIMENTAL RESULTS AND DISCUSSION

This chapter provides a summary of all the connection subassemblage testing including three separate tests that were performed on a connection utilizing A36 steel tendons and the two tests performed on a connection utilizing superelastic Nitinol tendons. Following a description of the testing events is a discussion of the results where comparisons are made between the different tests.

4.1 A36 Steel tendon tests

4.1.1 Test I

The connection for the first test utilized A36 steel tendons and underwent a full SAC loading history as described in the previous chapter. A picture of the connection setup can be seen in Figure 4-1. The test was run under quasistatic loading at a rate of 2 in./min.

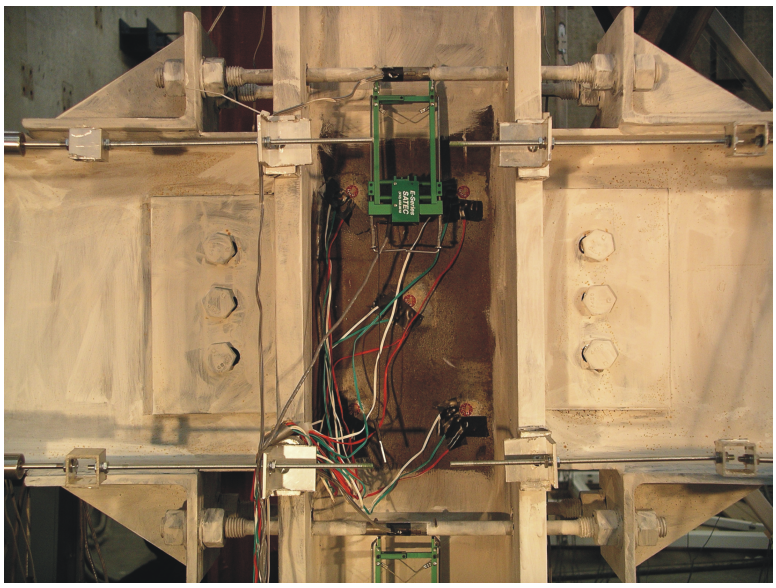

Figure 4-1: Picture of the steel tendon test I connection setup

Plots which summarize the results are shown in Figure 4-2. The equations used for determining the moment, total rotation, concentrated rotation, and the plastic rotation can be found in Appendix A. It can be seen from these plots that there was some asymmetry in the connection as shown by the increased moment/actuator force transferred in the negative direction. The elastic stiffness (k_e) of the connection is calculated by determining the moment that is transferred at the peak of the first cycle (0.00375 drift cycle) divided by the drift.

$$k_e = \frac{M}{\theta_{total}} \tag{4.1}$$

When the actuator was moving in the positive direction (to the south), the elastic stiffness was low (see Table 4-1) because the tendons were not engaging. The tendons did not engage in the positive direction until a drift of 0.015 radians (actuator displacement of 1.32 in.) was reached. Because the elastic stiffness was low, the elastic rotation for a given moment tended to be large leading to extremely small and even negative values for plastic rotation in the positive direction (see the plot of moment versus plastic rotation in Figure 4-2).

Table 4-1: Elastic stiffness for steel tendon test I

	Positive direction	Negative direction
Elastic stiffness	5166 k-in	8997 k-in

Figure 4-3 shows the difference in each of the four gap openings as measured by the LVDT's placed at the beam flanges. The gap closure is evidenced in this graph by the horizontal asymptote that occurs when the gap opening reads negative. Ideally, this plot should be symmetric and the horizontal asymptote should occur at low levels of drift as the tendons do not engage until the beam has a fulcrum on which to pivot. The effect of an initial gap was seen in the preliminary analysis using DRAIN-2DX which was discussed in the previous chapter. It was determined from the analysis as it was being carried out that it was important that the initial gap be as small as

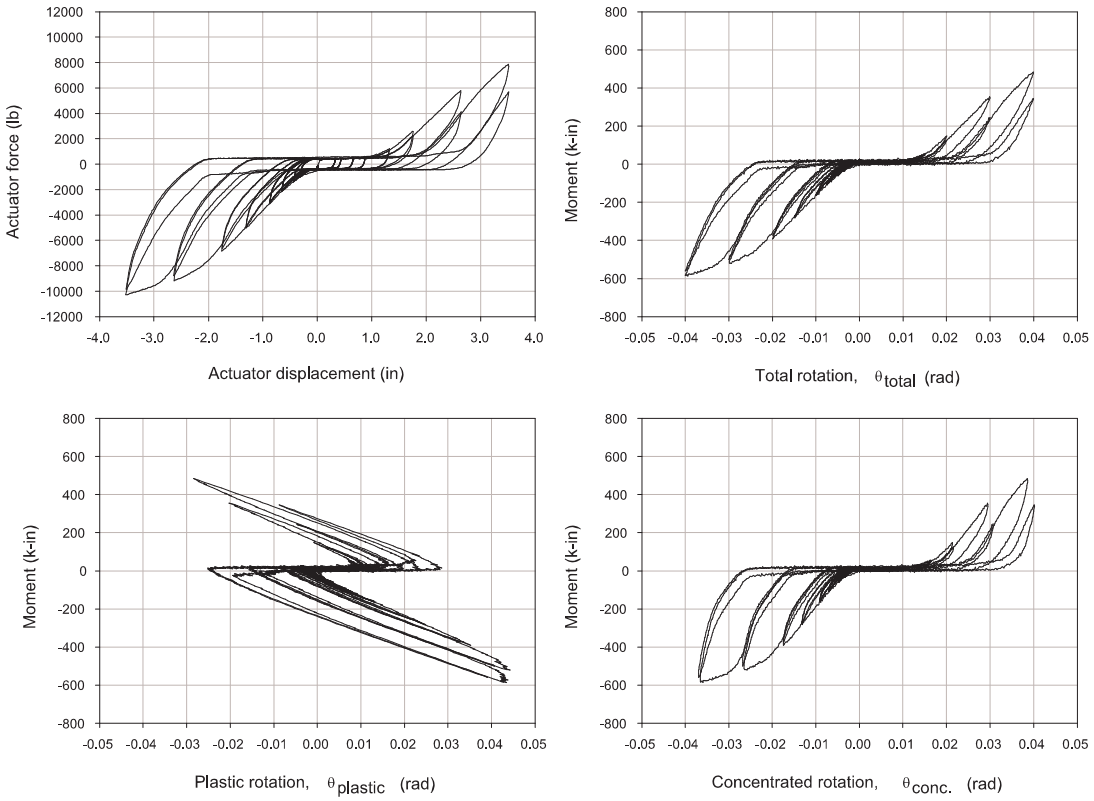

Figure 4-2: Graphs showing summary of results for steel tendon test I

possible in order to force the maximum deformation to occur in the tendons.

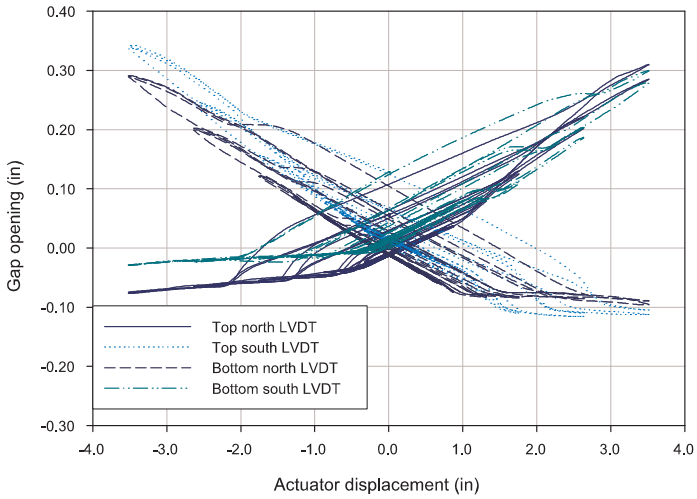

Figure 4-3: Gap opening versus actuator displacement for steel tendon test I

The average gap opening is calculated by averaging the readings from the LVDT's on either column face. A plot of the average gap opening versus the actuator displacement is shown in Figure 4-4. It was expected that the average gap opening would return to zero when the actuator displacement returned to its initial zero position. However, Figure 4-4 shows that the average gap opening continually increased throughout the testing. It is believed that after the A36 steel tendons would unload after a yielding response, the bars would go into compression and would then, in turn, push out against the angle anchors. A slipping would occur where the beams would push out from the column, thereby, increasing the average gap opening. Following a slipping event, an even larger imposed displacement was needed to engage the tendons leading to a stiffness degradation in the response. A picture of steel tendon test I at 4% interstory drift showing the gap opening angle is shown in Figure 4-5.

A plot of the tendon stress versus strain is presented in Figure 4-6. An issue arose when determining the behavior of the tendons which was how to calculate the stress in the tendons. A

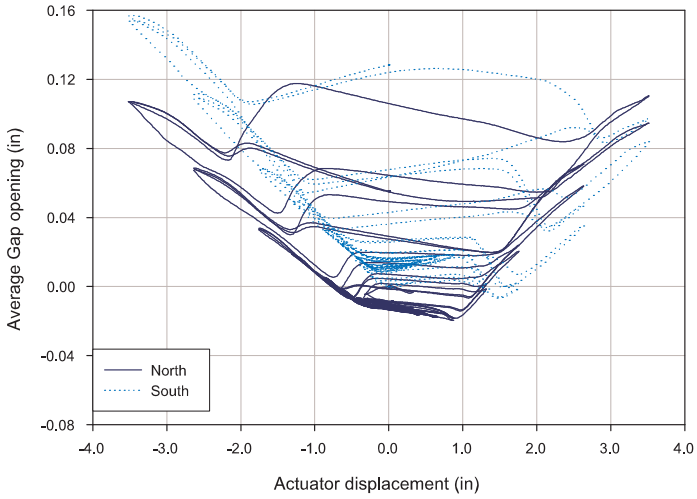

Figure 4-4: Average gap opening versus actuator displacement for steel tendon test I

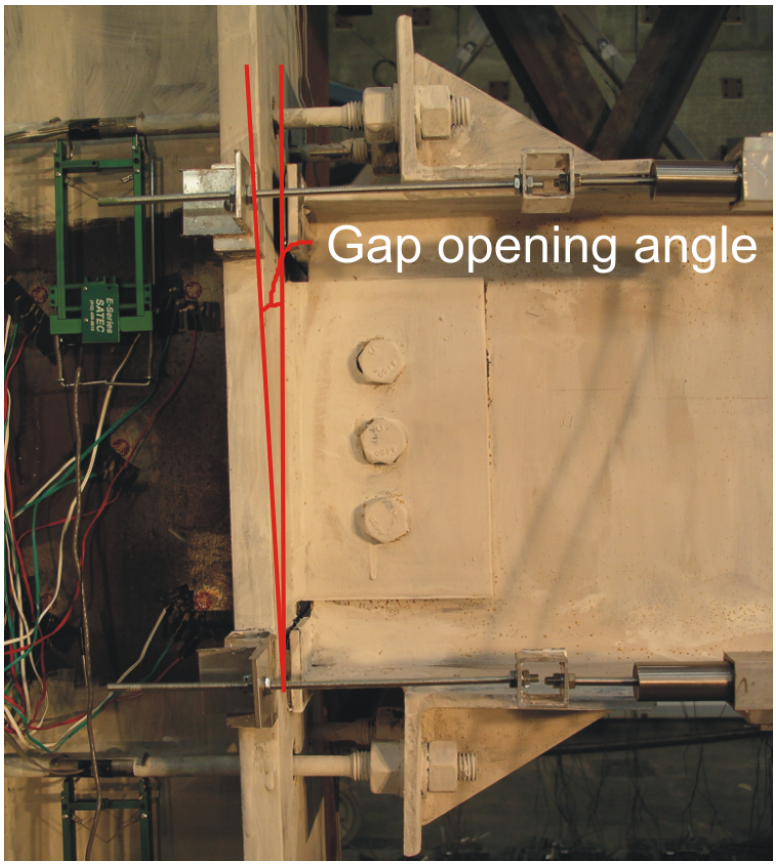

Figure 4-5: Picture of the steel tendon test I at 4% interstory drift

relationship was inferred by simple statics where the force in the bars was related to the moment transferred by the connection. However, this relationship is unable to tell if the bar is actually in tension or compression and assumes that all of the moment is transferred by the tendons, which may not necessarily be true. Another assumption made is that all the force is equally shared between the four tendons. The stress calculation for the tendons is given by the following equation:

$$\sigma = \left| \frac{M}{4 \cdot d' \cdot A_{tendon}} \right| \tag{4.2}$$

where M is the moment transferred by the connection, d' is the vertical distance between tendons, and A_{tendon} is the area of a single tendon. As can be seen in Figure 4-6, there were very few yielding events that occured in the tendons, most likely due to a combination of the presence of an initial gap and the slipping of the beams which both lead to larger imposed displacements needed to force yield level strains in the tendons. Also, the difference in the strain readings between the extensometer and the high elongation strain gauges should be noted. It was determined that the extensometer readings were more accurate because of debonding of the glue used to affix the strain gauge to the specimen which has been known to occur while using high elongation strain gauges.

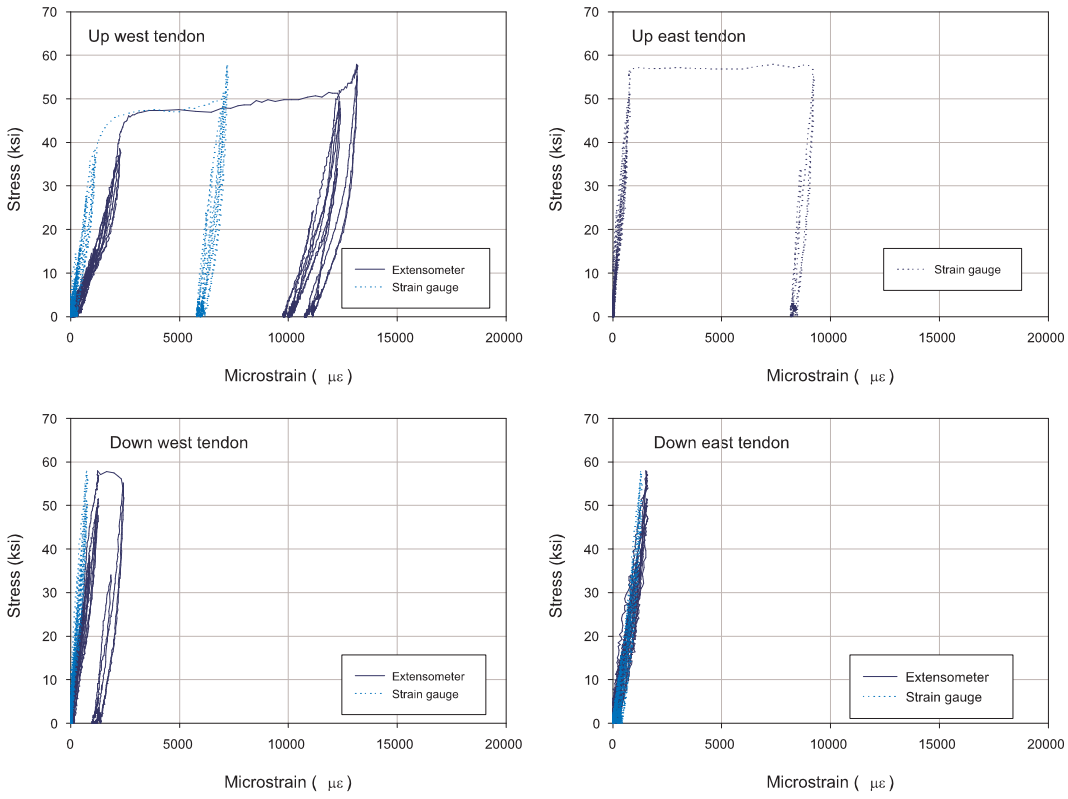

Figure 4-6: Stress versus strain plots for all tendons for steel tendon test I

4.1.2 Test II

Modifications were made to the connection setup for the steel tendon test II. First, both beams were moved closer toward the column in order to reduce the initial gap at the beam flange/column flange interface and to reduce any asymmetry within the connection. This was accomplished by loosening the bolts at the shear tab and using a rubber mallet to push the beams closer to the immovable column. Next, the shear tab bolts were fully tensioned. A slip critical interface at the shear tab was created in order to develop an initial elastic stiffness, as this was a problem for steel tendon test I. The friction that would have to be overcome as the the connection rotated would increase the moment transferred at the lower drift cycles. The same steel tendons that were used for steel tendon test I were also used for all subsequent steel tendon tests (Test II and Test III).

Figure 4-7 shows the actuator force versus actuator displacement plot as well as various moment/rotation plots for steel tendon test II. It can be seen that there was a larger initial elastic stiffness due to the friction in the shear tab. Also, the asymmetry in the connection was reduced by both beams being pushed up against the column. This is also illustrated by looking at a plot of the gap opening versus actuator displacement (see Figure 4-8). All of the plots look similar in terms of the amount the gap has to close before the horizontal asymptote is reached. However, by trying to create a connection that had a larger elastic stiffness by fully tensioning the bolts in the shear tab, the problem arose that the tendons were not engaging until after the friction was overcome and sliding occured. The friction force was not allowing the gap to close to create the pivot point at the interface between the beam and column. The LVDT's were reading nearly -1/8″ before the tendons were engaging as indicated by the horizontal asymptote in Figure 4-8. Again, the tendons were not engaging until after the closure of the gap.

Also, there was still problems with slipping of the beam after compression was developed in the tendons. A plot of the average gap opening versus actuator displacement (Figure 4-9) shows

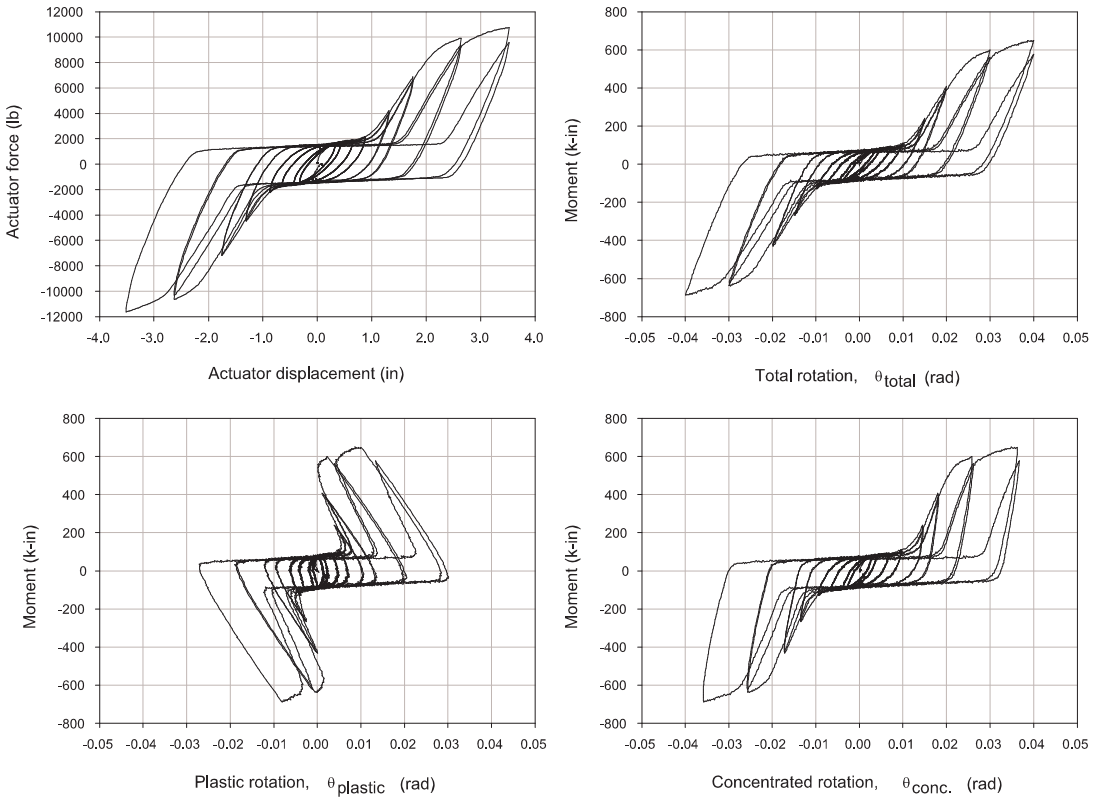

Figure 4-7: Graphs showing summary of results for steel tendon test II

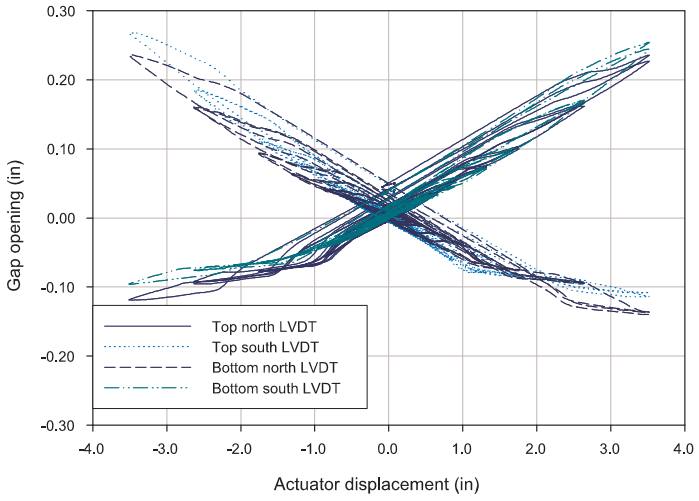

Figure 4-8: Gap opening versus actuator displacement for steel tendon test II

the average gap opening increasing as the test continues. The average gap opening increased less than it had during the steel tendon test I due to the presence of the friction force at the shear tab but did, in fact, increase. Again, slipping of the beams led to serious stiffness degradation in the connection. Evidence of the slip can also be seen in the tendon stress versus strain plots (Figure 4-10). Remember that the stress calculated for these plots is incorrect in that compression in the tendons is not accounted for. Nonetheless, when unloading after yielding events, discontinuities are seen in the strain readings when slipping of the beams occur.

Steel tendon test II was stopped during the final 0.04 radian drift cycle due to yielding of the beam flanges which led to local buckling (see Figures 4-11 and 4-12). The larger moment that was transferred by the connection due to the shear tab friction forces caused a large concentrated force at the beam flanges. At that point in the connection assembly, the reaction forces from all tendons get transferred. Upon noticing the yield lines in the white wash, the test was immediately stopped as the beam was to be re-used for subsequent tests. Because the strain gauges on the beams were placed a distance away from the connection, the force had distributed throughout the beams and the

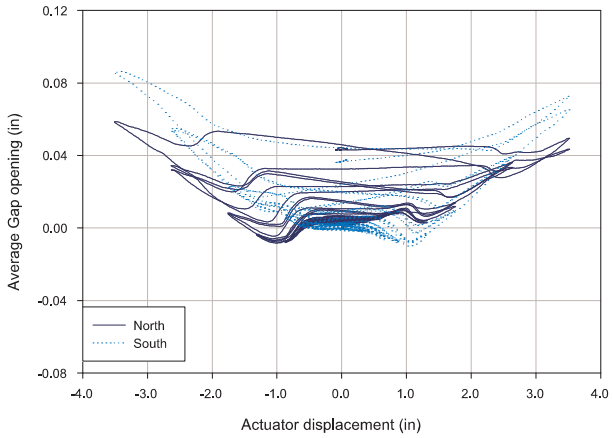

Figure 4-9: Average gap opening versus actuator displacement for steel tendon test II

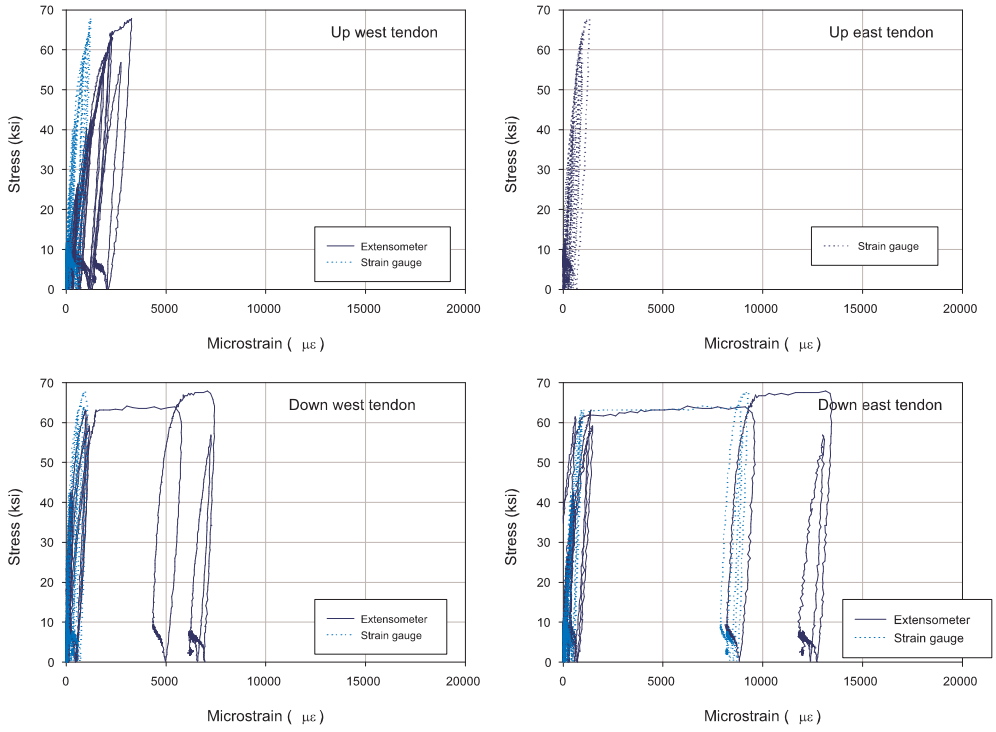

Figure 4-10: Stress versus strain plots for all tendons for steel tendon test II

strain gauges indicated that each beam was still in the linear range.

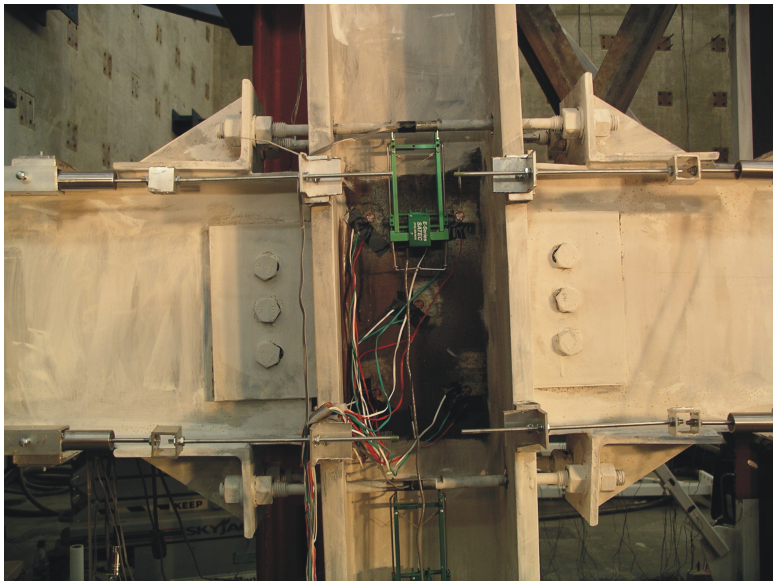

Figure 4-11: Steel tendon test II connection at 0.04 radian drift cycle

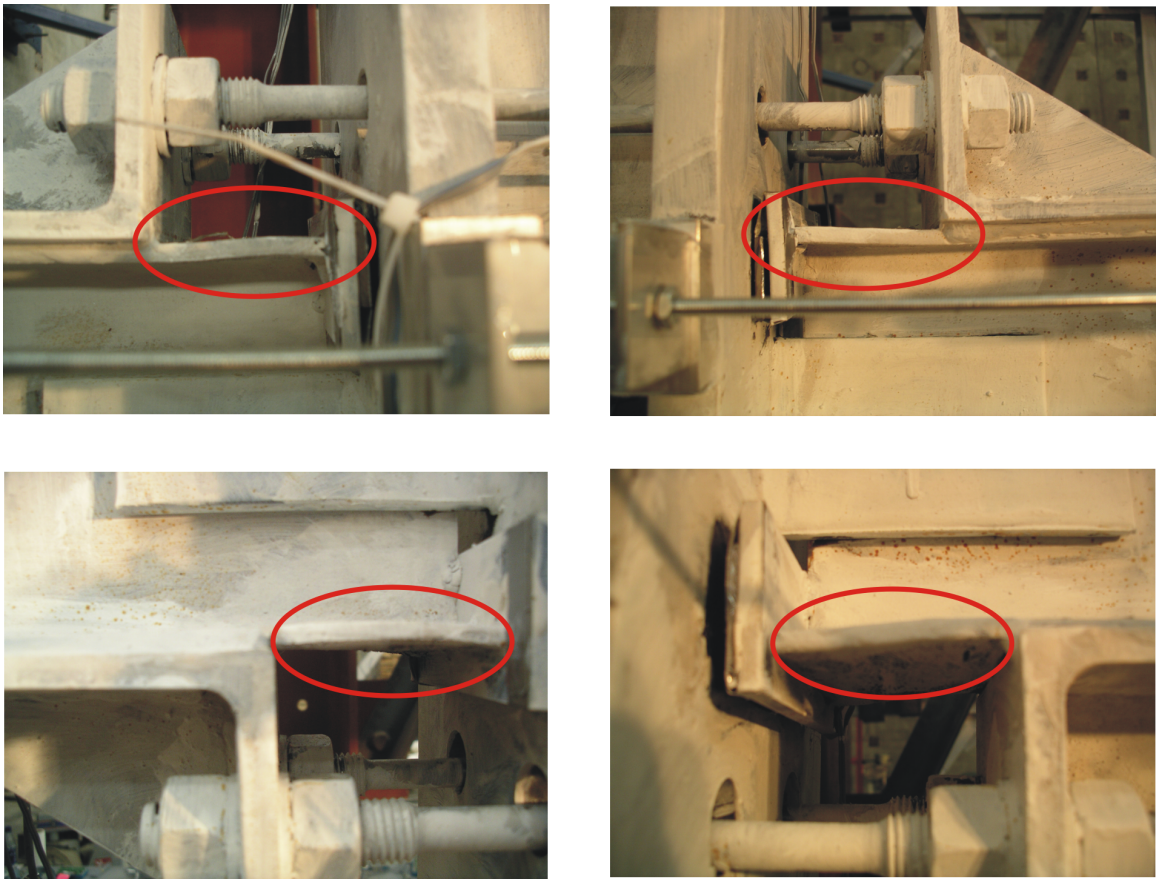

Figure 4-12: Yielding and local buckling of beam flanges after the first 0.04 drift cycle of steel tendon test II

4.1.3 Test III

It was inevitable that slippage of the beams were going to occur at higher interstory drift levels when using mild steel tendons in the connection configuration used in this study since the tendons would eventually go into compression after a yielding event. Steel tendon test II indicated that even tensioning the bolts in the shear tab would not provide enough force to counteract this phenomena. Steel tendon test III was performed with the goal of providing a connection using the A36 steel tendons that had good elastic stiffness at low drift levels without fully tensioning the bolts in the shear tab. To accomplish this, the outer nuts of the A36 steel tendons were first tightened against the angle anchors in order to try and reduce the initial gap, which, in turn, would effectively pretension the tendon in order to keep the beam held tightly to the column. The connection was tested at the three lowest drift cycles only. The actuator displacement history for steel tendon test III is given in Figure 4-13.

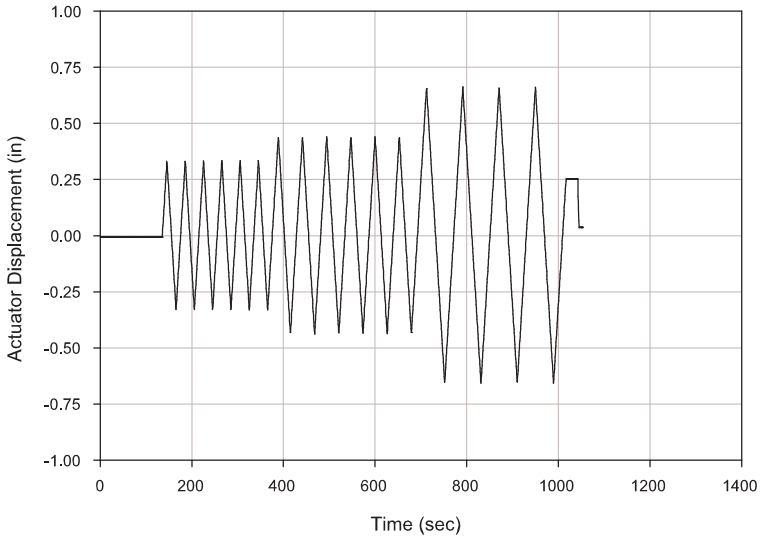

Figure 4-13: Actuator displacement time history for steel tendon test III

A number of plots from the A36 steel tendon test III are presented in Figure 4-14. As anticipated,

a larger elastic stiffness (29,785 k-in.) was experienced at the lower drift cycles when compared to the elastic stiffness from steel tendon test II (21,638 k-in.). The response of the connection was more or less linear due to the fact that the connection was tested at the lower drift cycles only, keeping the tendons within their elastic range.

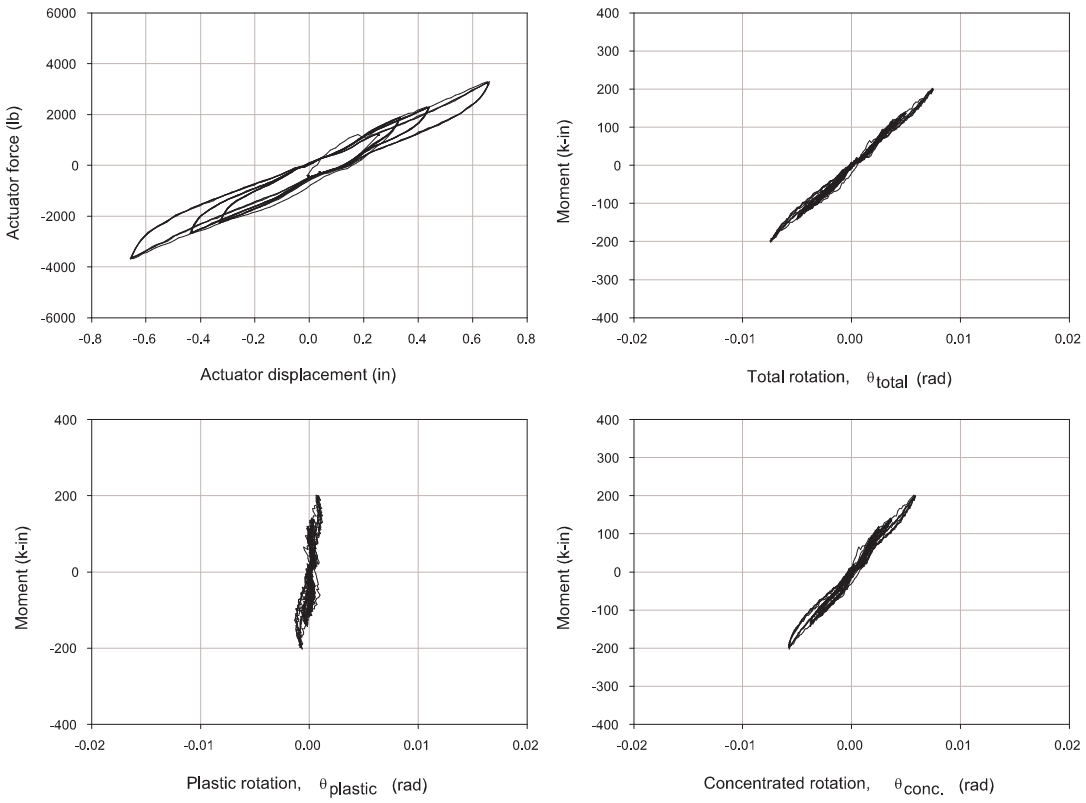

Figure 4-14: Graphs showing summary of results for steel tendon test III

4.2 Superelastic Nitinol tendon test

Many lessons were learned from the connection tests with the A36 steel tendons and it was anticipated that the use of superelastic Nitinol tendons would provide a connection with superior performance and overcome some of the shortcomings of the steel tendon connection. The fact that the Nitinol tendons would have small residual strains as compared to the steel tendons meant that slipping of the beam would be less of an issue due to the Nitinol tendons not developing as large of a compression stress and, therefore, the tendons would not push the beam away from the column. It was shown from the steel tendon test III that pretensioning the tendons in order to reduce the initial gap at the beam flange/column flange interface would lead to a connection with good initial elastic stiffness. Furthermore, a connection with superelastic Nitinol tendons would be recentering.

Before the testing was to begin, some modifications were made to the connection setup. Larger steel shims were added at the interface between the beams and column to try and reduce the amount of travel that has to take place before gap closure. Also, 6″x1″x1/2″ mild steel bars were welded to each side of the beam flanges. It was shown in steel tendon test II that the beam flanges were weak points within the connection. The steel bars were added to ensure adequate strength at that point by effectively increasing the flange area at the location of the application of a large concentrated force.

After the modifications were made, the superelastic Nitinol tendon test was performed. The test encompassed a full SAC loading history as shown in Figure 4-15. A picture of the Nitinol tendon connection at 0.04 radian drift is given in Figure 4-16. Figure 4-17 shows the actuator force versus actuator displacement plot and the various moment/rotation plots. Little asymmetry was seen in the connection as evidenced by these plots and the connection showed consistent behavior throughout the loading.

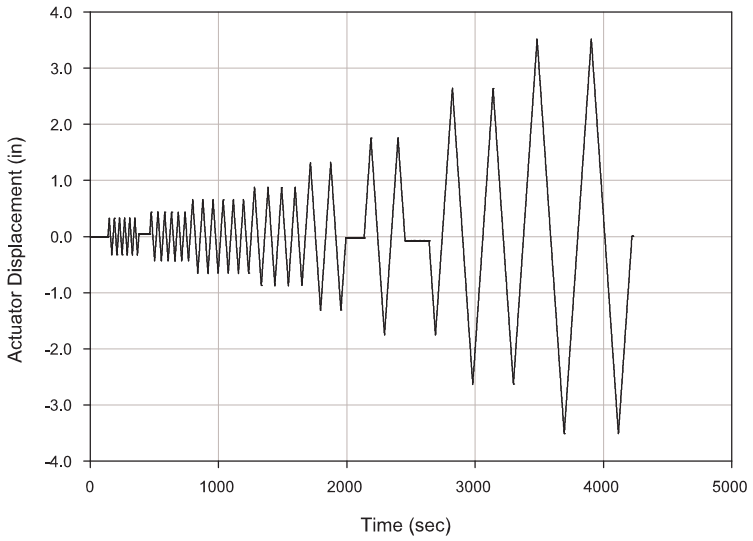

Figure 4-15: Actuator displacement time history for the Nitinol tendon test

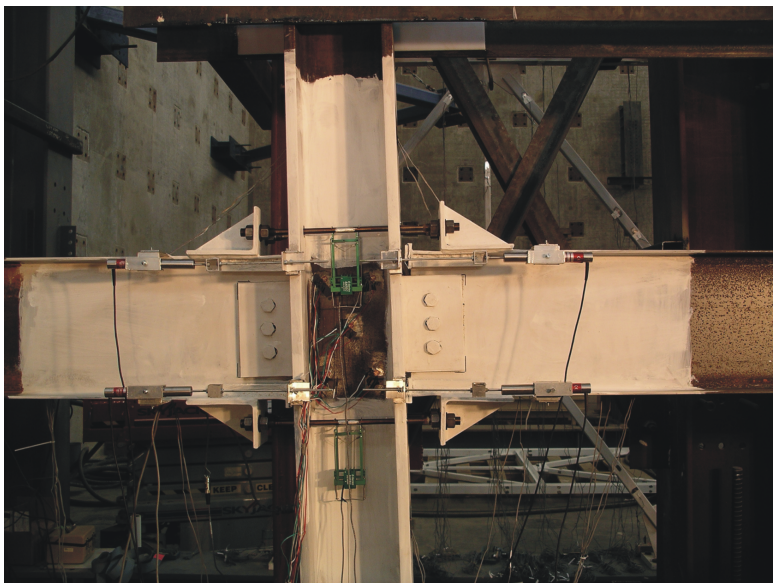

Figure 4-16: Nitinol tendon connection at 0.04 radian interstory drift

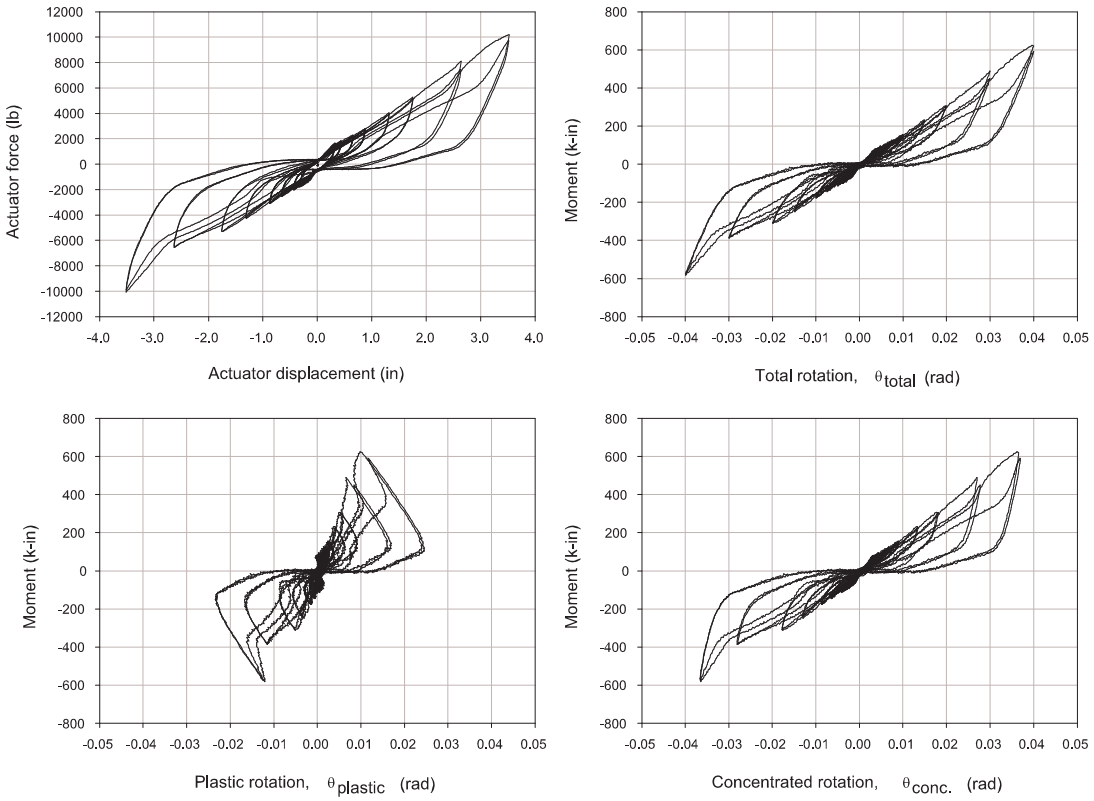

Figure 4-17: Graphs showing summary of results for Nitinol tendon test

The tendons engaged upon initial loading as evidenced by a initial elastic stiffness value of 20,914 k-in. This elastic stiffness was lower than that for steel tendon test III but can be accounted for by the fact that Nitinol has an elastic modulus much less than steel. Figure 4-18 shows that the initial gap remained very close to zero and Figure 4-19 shows that there was little slipping of the beam as the average gap opening only slightly increased as the testing progressed.

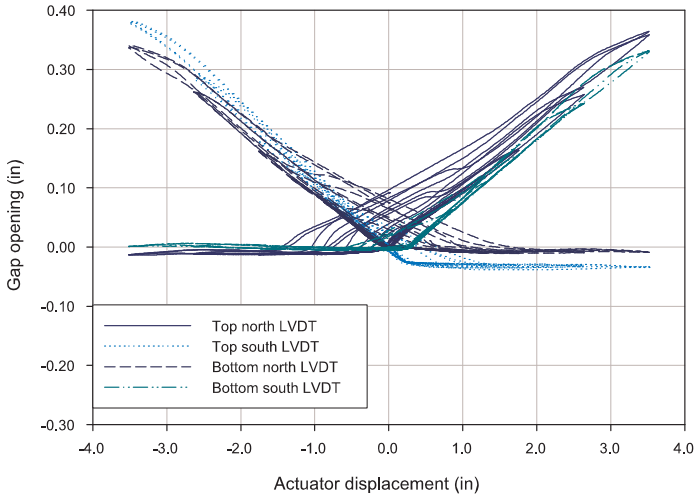

Figure 4-18: Gap opening versus actuator displacement for the Nitinol tendon test

The stress versus strain behavior in the tendons is presented in Figure 4-20. The Up west Nitinol tendon gave the highest strain readings of nearly 25,000 microstrain. It was expected that the tendons would have experienced strain values closer to 40,000 microstrain meaning that the connection had much capacity left after the 0.04 radian drift cycle. The forward transformation of the Nitinol tendons was only starting to occur at the drift levels that the connection was subjected to during this test. It should be noted that there is an increase in stiffness near the 15,000 microstrain level for all of the tendons. This seems to be some sort of strain hardening that is occurring before the forward transformation stress is reached.

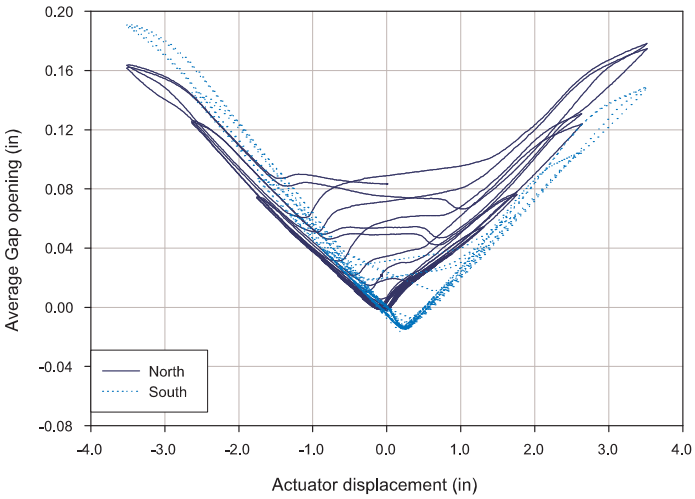

Figure 4-19: Average gap opening versus actuator displacement for the Nitinol tendon test

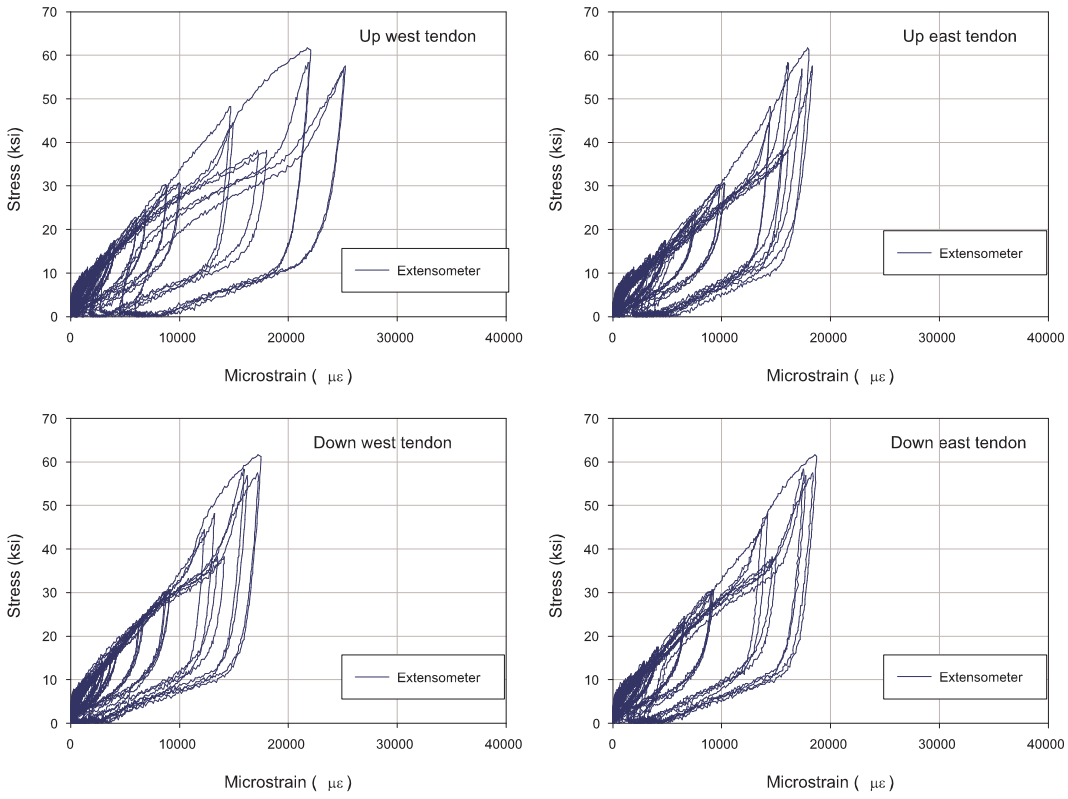

Figure 4-20: Stress versus strain plots for all tendons for the Nitinol tendon test

4.2.1 Higher cycle test

Because of the good performance from the Nitinol tendon test, the connection was then subjected to higher values of interstory drift (Two cycles each at 5%, 6%, 7%, 8% and 9% interstory drift). Due to a combination of computer and human error, most of the data from this test was irrecoverably lost. The actuator force versus actuator displacement plot is shown in Figure 4-21 with much of the data from this plot reconstructed from what can be recalled of the testing. The plot does show that there was stiffness degradation but no strength degradation at the higher cycles. The connection failed at the 9% drift cycle due to fractures of the welds which attached the 6″x1″x1/2″ bar to the beam flanges (see Figures 4-22 and 4-23).

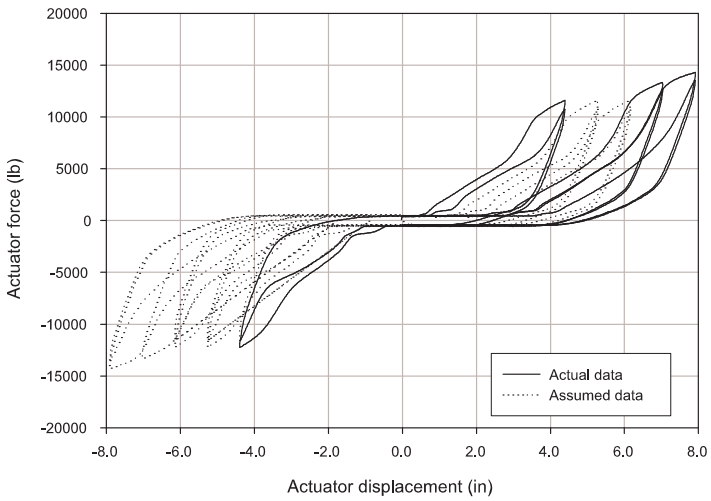

Figure 4-21: Actuator force versus actuator displacement for the higher drift cycles of the Nitinol tendon test

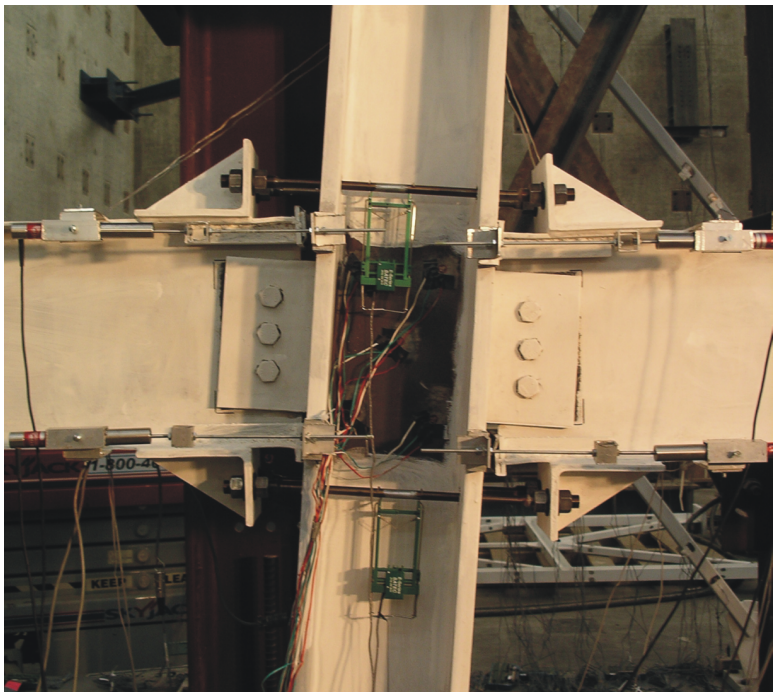

Figure 4-22: Nitinol tendon connection at the 9% drift cycle

Figure 4-23: Failure of the Nitinol tendon connection was due to weld fractures at the 9% drift cycle

Figure 4-24 gives only the first 5% drift cycle with points on the graph labeled where changes in stiffness occur. Between points *a* and *b*, there was almost zero stiffness in the connection due to the opening of the gap that occurred from the previous drift cycles. After the gap opening was overcome, the Nitinol tendons were able to undergo deformation and, therefore, transfer force as evidenced by the increase in stiffness between points *b* and *c*. The change in stiffness that occurs at point *c* is curious but is consistent with the change in stiffness that was seen in the tendons near the 15,000 microstrain level of the Nitinol tendon test (see Figure 4-20). Between point *d* and *e*, the forward transformation stress in the Nitinol tendons is just being reached where the plateau in the loading curve of superelastic Nitinol occurs. At point *e*, the connection begins to unload and the stiffness seen between points *e* and *f* is due to the initial elastic unloading of the superelastic Nitinol. Between points *f* and *g*, the unloading plateau is reached where the reverse transformation of the superelastic Nitinol occurs. Finally, between points *g* and *h*, there is almost zero stiffness and the connection undergoes rigid body motion until the gap opening is overcome and the tendons engage once again as the connection is cycled in the other direction.

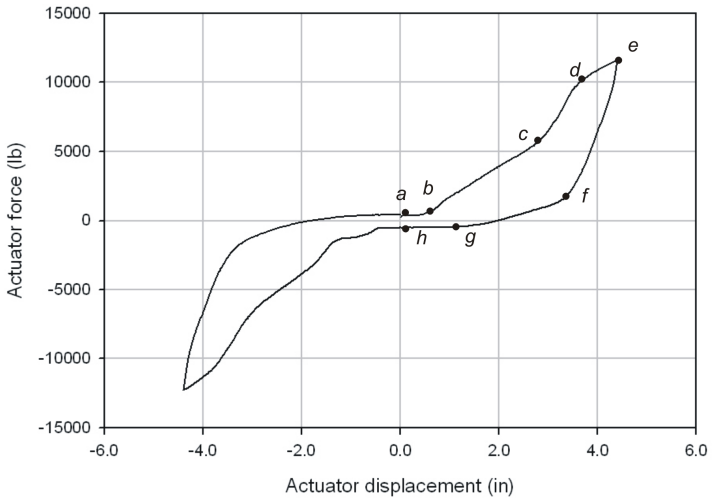

Figure 4-24: Actuator force versus actuator displacement plot for the first 5% drift cycle

4.3 Comparison of results

Table 4-2 gives a comparison of the Nitinol tendon connection to the A36 steel connections. Steel tendon test II had the maximum actuator load and therefore, maximum moment transferred due to the additional moment resistance in the connection from the friction force at the shear tab. All of the connections were considered partial strength connections because the M_{max}/Mp_{beam} ratio was less than unity for all tests. The calculation for Mp_{beam} was based on a yield strength of the beam of 50 ksi. The elastic stiffness for steel test I had the lowest value due to a large initial gap opening at the beam flange/column flange interface. The elastic stiffness calculated for the Nitinol tendon test was lower than the other two steel tendon tests which can be attributed to the material properties of superelastic Nitinol as compared to A36 steel. The elastic modulus for superelastic Nitinol, as obtained from the results of the component tests reported in Chapter 3, was on the order of 5,000 ksi as opposed to 30,000 ksi for mild steel.

The amount of energy dissipated by the connections as presented in Table 4-2 are recorded as the integration of the moment versus total rotation curve using approximate trapezoidal rule integration techniques. Steel tendon test III, by far had the least amount of energy dissipated because the connection did not undergo as many drift cycles and the stress in the tendons was kept below yielding. The Nitinol tendon test dissipated about half the amount of energy as steel tendon test II. Recall that the steel test II had additional energy dissipated as a result of the friction forces developed at the shear tab. However, the Nitinol tendon connection was never expected to dissipate as much energy as the steel connection due to the flag-shaped nature of the material's stress/strain curve. Had the steel tendons been able to develop large compression stress, the amount of energy dissipation would have been much greater. It is only important to note that the amount of energy dissipated by the Nitinol connection is of the same order as the steel tendon connection and energy dissipation leads to a reduction of the structural response during earthquake events.

Finally, the main advantage of the Nitinol connection over all the other connections tested is that the Nitinol connection showed recentering capabilities (the connection rotation returns to zero when the moment is zero). A building built with superelastic Nitinol connections would have very little residual drift of the frame even after a severe earthquake event provided that the building is detailed in such a way that residual deformation does not occur at the base of the columns.

Table 4-2: Comparison of Nitinol tendon connection with A36 steel connections

		Steel test I	Steel test II	Steel test III	Nitinol test
Actuator load, max.	k	10.3	11.6	3.7	10.2
Actuator displacement, max.	in	3.52	3.52	0.66	3.52
Total rotation, max.	radian	0.0400	0.0400	0.0075	0.0400
Cumulative total rotation	radian	1.398	1.322	0.340	1.393
Moment, max.	k-in	586.9	687.9	202.0	624.8
M_{max}/Mp_{beam} [a]		0.68	0.79	0.23	0.72
Elastic stiffness [b]	k-in	7080	21640	29790	20910
Plastic rotation, max.	radian	0.044	0.030	0.001	0.025
Cumulative plastic rotation	radian	4.618	1.583	0.234	1.399
Concentrated rotation, max.	radian	0.040	0.037	0.006	0.037
Energy dissipated [c]	k-in	22.8	83.2	1.2	45.9
Recentering connection?		No	No	No	Yes

[a] based on F_y=50 ksi
[b] based on the average of elastic stiffnesses in positive and negative direction
[c] recorded as the integration of the moment versus total rotation hysteresis

CHAPTER V

CONCLUSIONS

In this study, the use of superelastic Nitinol tendons as the primary moment transfer elements within a steel interior beam-column connection was investigated. Analytical and experimental testing showed that incorporating superelastic Nitinol into a steel connection can be a viable means of providing a partially restrained (PR), partial strength (PS) connection.

Analytical modeling of the connection was undertaken using the nonlinear finite element analysis program DRAIN-2DX. The analysis was used as a design aid in order to obtain the maximum forces that would be experienced by the members during the experimental testing phase of the project. Two connection types were modeled and eventually tested experimentally; one in which superelastic Nitinol tendons were used as the primary moment transfer elements and one in which A36 steel tendons were used in an identical configuration.

In order to gain a better understanding of the material properties of the tendons to be used, several component tests were conducted on both A36 steel bars and superelastic Nitinol bars. The damping capacity of each material was characterized as well as the optimal annealing temperature for the superelastic Nitinol tendons to be used during the experimental testing phase.

Experimental testing of a 1/2 scale interior connection subassemblage included three tests performed on a connection utilizing A36 steel tendons and two tests performed on a connection utilizing superelastic Nitinol tendons. The A36 steel tendon connections that were tested experienced slippage of the beams as the A36 steel tendons went into compression and pushed out against the angle anchors. The slippage increased the gap opening at the beam flange/column flange interface

and led to a stiffness degradation in the response as larger imposed displacements were needed to engage the tendons. The Nitinol tendons did not develop as large of a compression force because of their inherent material properties (small residual strains upon unloading) and, therefore, slippage of the beams was less of an issue. The superelastic Nitinol connection eventually failed at the 9% drift cycle due to fracture of the welds at the beam flange stiffening elements. The superelastic Nitinol connection that was tested as part of this study offered significant energy dissipation capabilities and showed recentering capabilities. In addition, the innovative connection design offers several advantages over conventional steel moment connections, as listed below.

- The problematic practice of field welding would not be necessary when using a connection of this type. Field welding is considered to be a contributing cause to the brittle failures of steel moment connections during the Northridge earthquake.
- A greater toughness and redundancy would be provided to a structural system as the low initial stiffnesses and low yielding strengths would precipitate the need for more of these connections while little extra labor would be required for their construction.
- The connections have a large structural strength reserve capacity. Superelastic Nitinol has a high capacity for deformation with a substantial stiffness after yield. Plus, when the tendons undergo large strains on the order of 6-8%, strain hardening of the material occurs, leading to even larger strength capacity.
- The connection could undergo repeated earthquake type loadings with little damage due to the good low and high cycle fatigue behavior of the Nitinol material.
- Any damage to the connection would be confined to the easily replaceable Nitinol tendon components, if properly detailed. During experimental testing, the steel beams and columns remained below their plastic moment capacity even at interstory drift levels of 9%.

- Energy dissipation and associated damping capability leads to a reduction in the structural response during earthquake loadings.
- A connection of this type is self centering without residual deformation.

5.1 Recommendations for future research

This proof of concept study showed the feasibility of incorporating superelastic Nitinol into an interior steel beam-column connection. However, more research must take place before general acceptance of a connection of this type. Most of all, there needs to be better characterization of the material properties of superelastic Nitinol. This study tested a 1/2 scale connection with a relatively small tendon diameter. Little is known of the properties of larger diameter superelastic Nitinol rods which would be needed for most practical applications of a connection of this type.

An analytical model needs to be developed which can predict the hysteretic behavior of the connection, including moment/rotation behavior and local effects. After implementation of this model, parametric analytical studies could be undertaken to optimize the connection design.

Some consideration should be given to ways of improving the connection that was tested as part of this study. First, some of the deformation capacity of the tendons was lost due to slippage of the beams away from the columns. Had a composite floor system been used, the slippage most likely would not have occurred, causing there to be more deformation and, therefore, energy dissipation in the tendons. Experimental and analytical testing that incorporates composite floor systems should be looked at. Perhaps testing that only simulates the effect of composite floor systems could be achieved in which the beam is restrained from slipping away from the column. Another way of improving the connection by increasing the deformation in the tendons could be to either shorten the length of the tendons or even increasing the distance between the top and bottom tendons. Again, a model which better predicts the hysteretic behavior of the connection could help in optimizing the

experimental design.

Nitinol is expensive, but recent advances in the manufacturing and processing of the material have lowered the cost. The costs can no longer be considered prohibitive, especially when considering potential savings in repairs of these connections. A cost/benefit analysis would be informative in showing if savings from repair costs could offset initial additive costs of implementation.

Also, different connection designs that possibly take better advantage of the properties of superelastic Nitinol need to be developed. Other types of connections may include designs with prestressed Nitinol, or possibly hybrid schemes with both shape memory Nitinol and superelastic Nitinol. A connection design where the tendons are allowed to go into compression (perhaps buckling restrained) may be found to be most advantageous. Also, more field applicable designs need to be explored. The connection that was tested as part of this study might interfere with slab systems because the tendons were located on the outside of the beam flanges.

APPENDIX A

DATA REDUCTION

The equations presented here were used when reducing the instrumentation data from the subassemblage tests.

A.1 Moment

The moment transferred by the connection (M) was calculated by:

$$M = (P_{NS} - P_{SS}) \cdot L_b \tag{A.1}$$

where P_{NS} is the load in the north strut, P_{SS} is the load in the south strut and L_b is the beam length measured from column centerline to strut centerline.

A.2 Stress in tendons

The stress calculation for the tendons is given by the following equation:

$$\sigma = \left| \frac{M}{4 \cdot d' \cdot A_{tendon}} \right| \tag{A.2}$$

where M is the moment transferred by the connection, d' is the distance between tendons, and A_{tendon} is the area of a single tendon.

A.3 Rotations

A.3.1 Total rotation

The total rotation of the connection was calculated by:

$$\theta_{total} = \frac{\delta_c}{H_c} \tag{A.3}$$

where δ_c is the column tip displacement measured by the actuator LVDT and H_c is the height of the column measured from the centerline of the bottom pin/load cell assembly to the actuator centerline.

A.3.2 Concentrated rotation

The concentrated rotation of the connection was calculated by:

$$\theta_{conc.} = \frac{1}{2}\left(\frac{\delta_{TN} - \delta_{TS}}{d_{LVDT}} - \frac{\delta_{BN} - \delta_{BS}}{d_{LVDT}}\right) \tag{A.4}$$

where δ_{XY} are the displacements measured by the beam to column LVDT's (TN for top north, BS for bottom south, etc.) and d_{LVDT} is the distance between top and bottom LVDT's.

A.3.3 Elastic rotation

The elastic rotation of the connection was calculated by:

$$\theta_{elastic} = \frac{M}{k_e} \tag{A.5}$$

where M is the moment from equation A.1 and k_e is the elastic stiffness.

A.3.4 Plastic rotation

The plastic rotation of the connection was calculated by:

$$\theta_{plastic} = (\theta_{total} - \theta_{elastic}) \tag{A.6}$$

A.3.5 Cumulative total rotation

The cumulative total rotation of the connection was calculated by:

$$\theta_{total_{cum}} = \sum_{i=1}^{n} \left| \theta_{total_i} - \theta_{total_{i-1}} \right| \tag{A.7}$$

where θ_{total_i} is the total rotation at data point i and n is the number of data points.

A.3.6 Cumulative plastic rotation

The cumulative plastic rotation of the connection was calculated by:

$$\theta_{plastic_{cum}} = \sum_{i=1}^{n} \left| \theta_{plastic_i} - \theta_{plastic_{i-1}} \right| \tag{A.8}$$

where $\theta_{plastic_i}$ is the total rotation at data point i and n is the number of data points.

A.4 Principal strain from strain gauge rosettes

The principle strains ϵ_1 and ϵ_2 are obtained from the following equations:

$$\epsilon_1 = \frac{1}{2}(\epsilon_A + \epsilon_C) + \frac{1}{2}\sqrt{(\epsilon_A - \epsilon_C)^2 + (2\epsilon_B - \epsilon_A - \epsilon_C)^2} \tag{A.9}$$

$$\epsilon_2 = \frac{1}{2}(\epsilon_A + \epsilon_C) - \frac{1}{2}\sqrt{(\epsilon_A - \epsilon_C)^2 + (2\epsilon_B - \epsilon_A - \epsilon_C)^2} \tag{A.10}$$

where ϵ_A is the strain gauge oriented horizontally, ϵ_C is the strain gauge oriented vertically and ϵ_B is the strain gauge oriented at a 45 degree angle.

A.5 Principal strain angle from strain gauge rosettes

The principle strain angle ϕ_1 is obtained from the following equation:

$$\phi_1 = \frac{1}{2} tan^{-1} \frac{2\epsilon_B - \epsilon_A - \epsilon_C}{\epsilon_A - \epsilon_C} \tag{A.11}$$

APPENDIX B

STEEL TENDON TEST DATA

B.1 Test I on 04/25/05

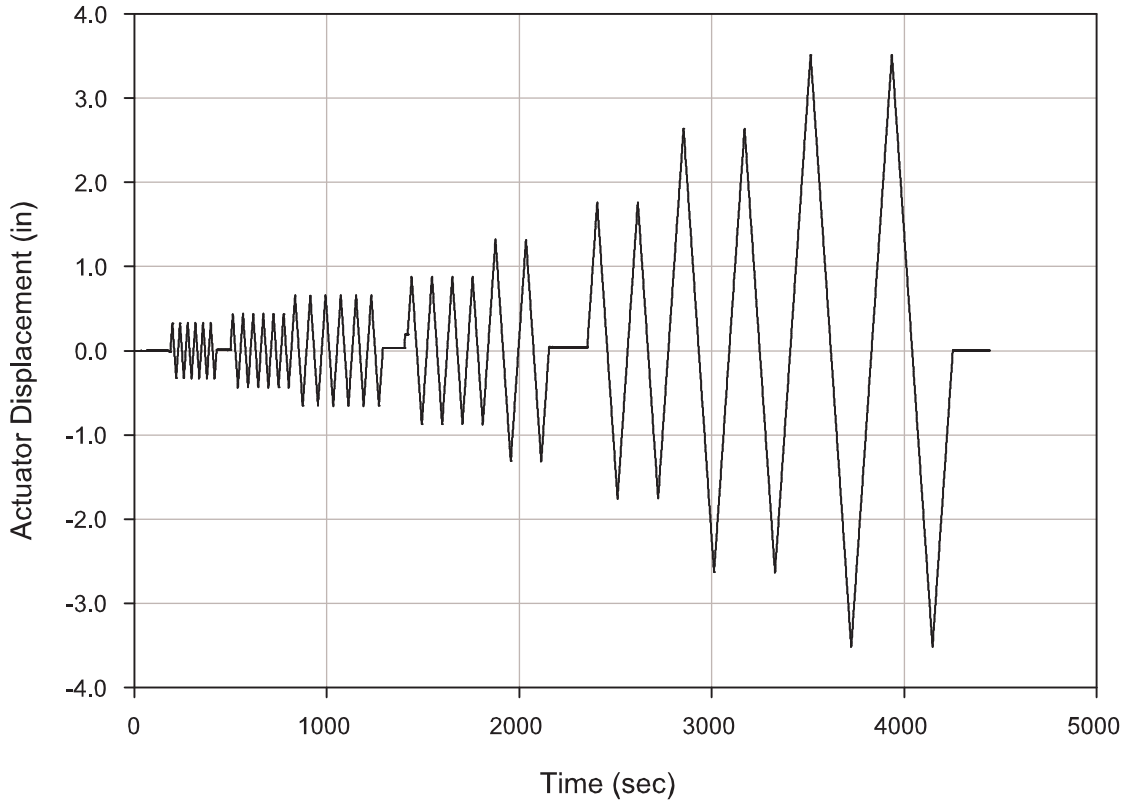

Figure B-1: Actuator displacement history for steel tendon test I on 04/25/05.

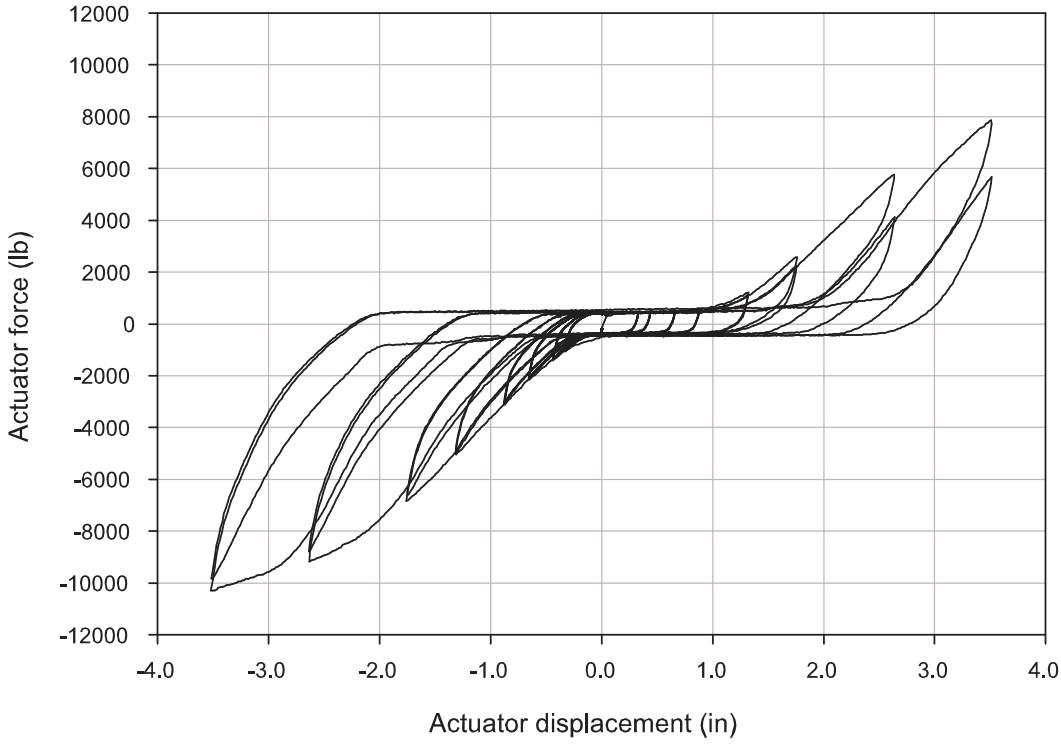

Figure B-2: Actuator force versus actuator displacement for steel tendon test I on 04/25/05.

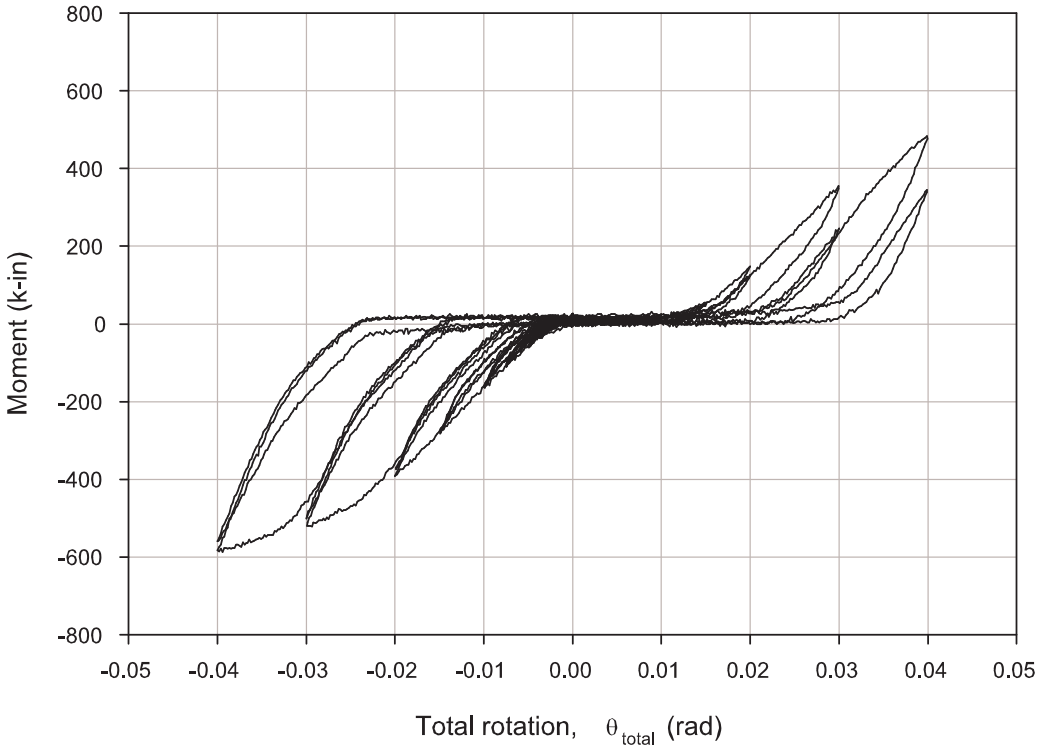

Figure B-3: Moment versus total rotation for steel tendon test I on 04/25/05.

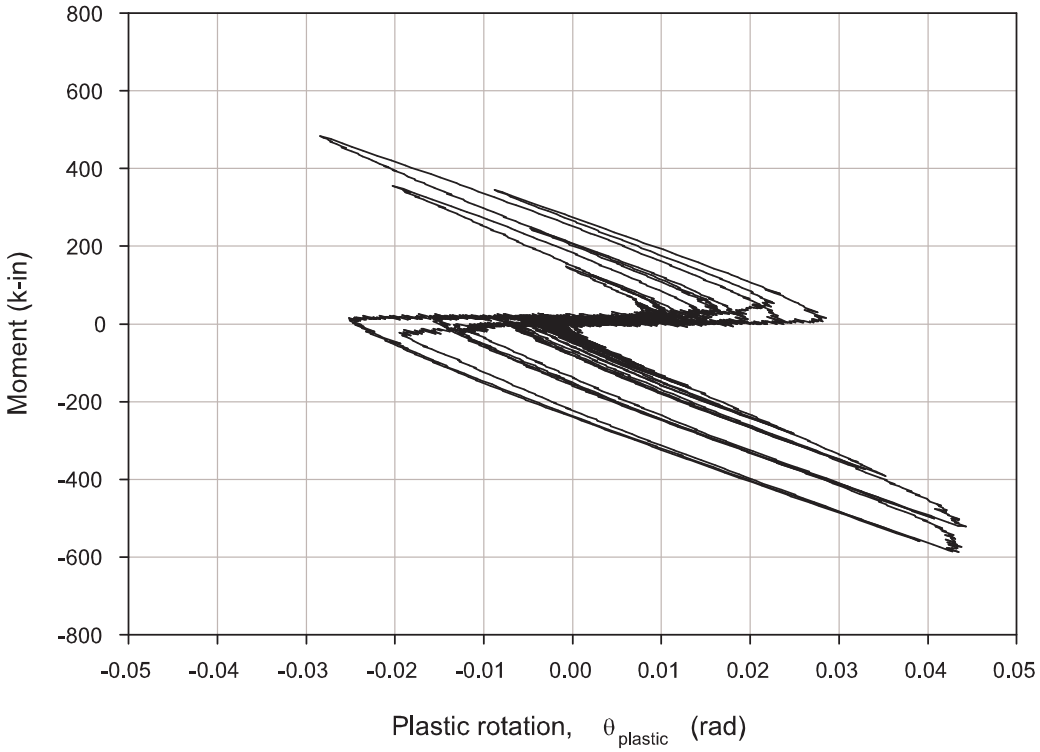

Figure B-4: Moment versus plastic rotation for steel tendon test I on 04/25/05.

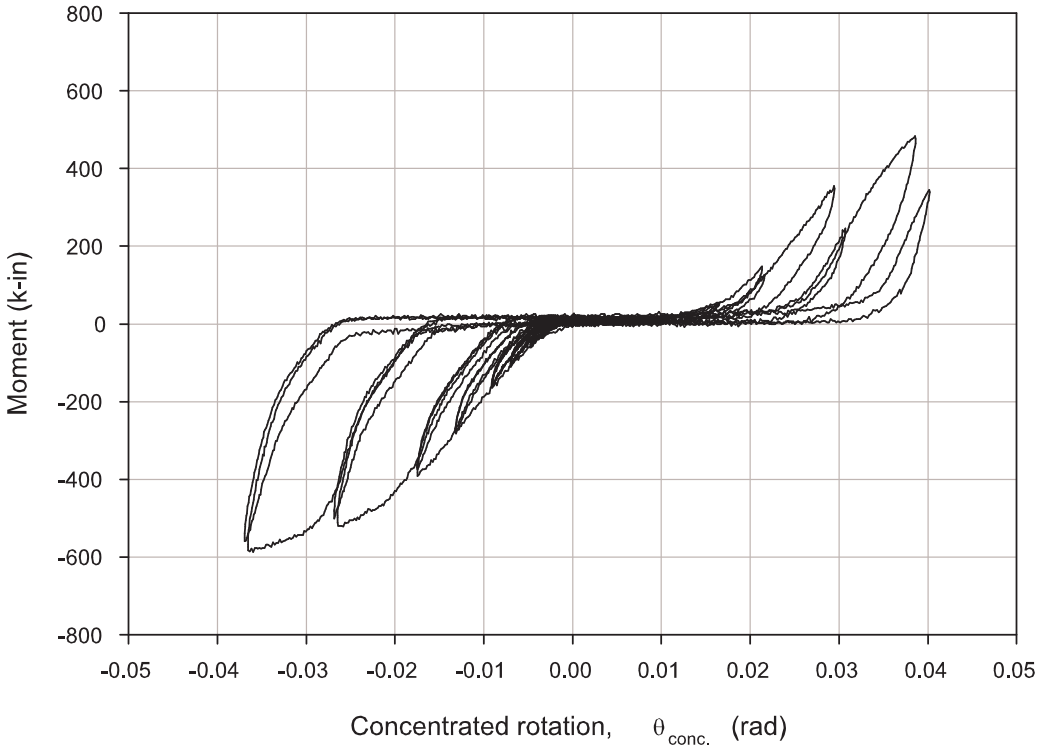

Figure B-5: Moment versus concentrated rotation for steel tendon test I on 04/25/05.

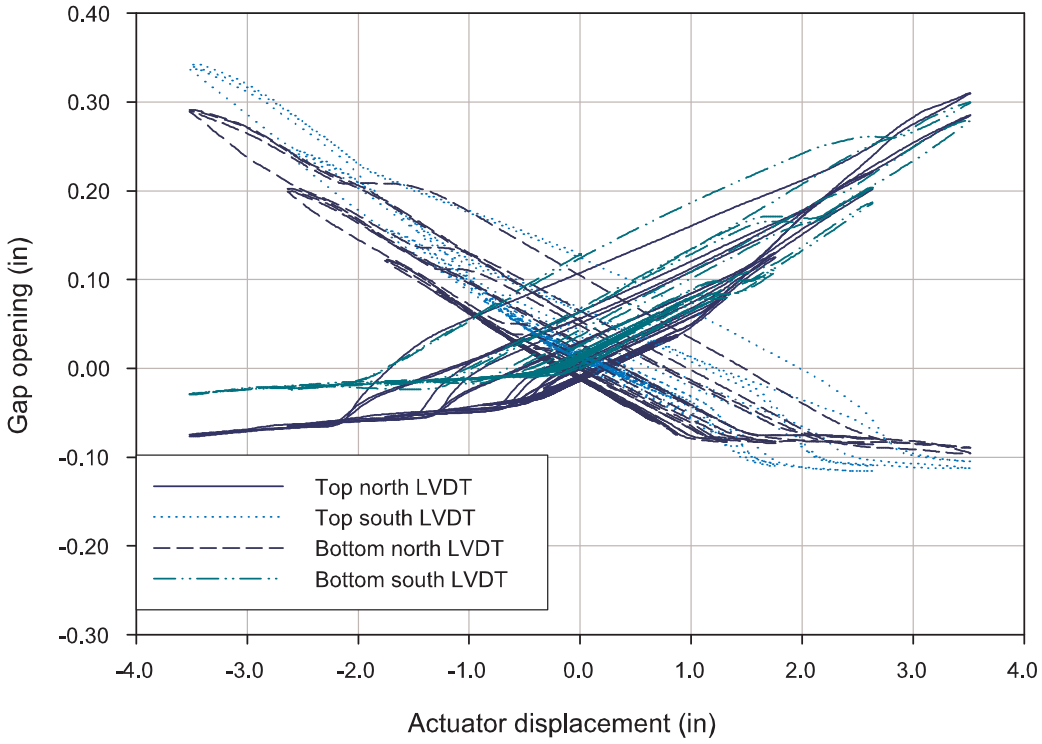

Figure B-6: Gap opening versus actuator displacement for steel tendon test I on 04/25/05.

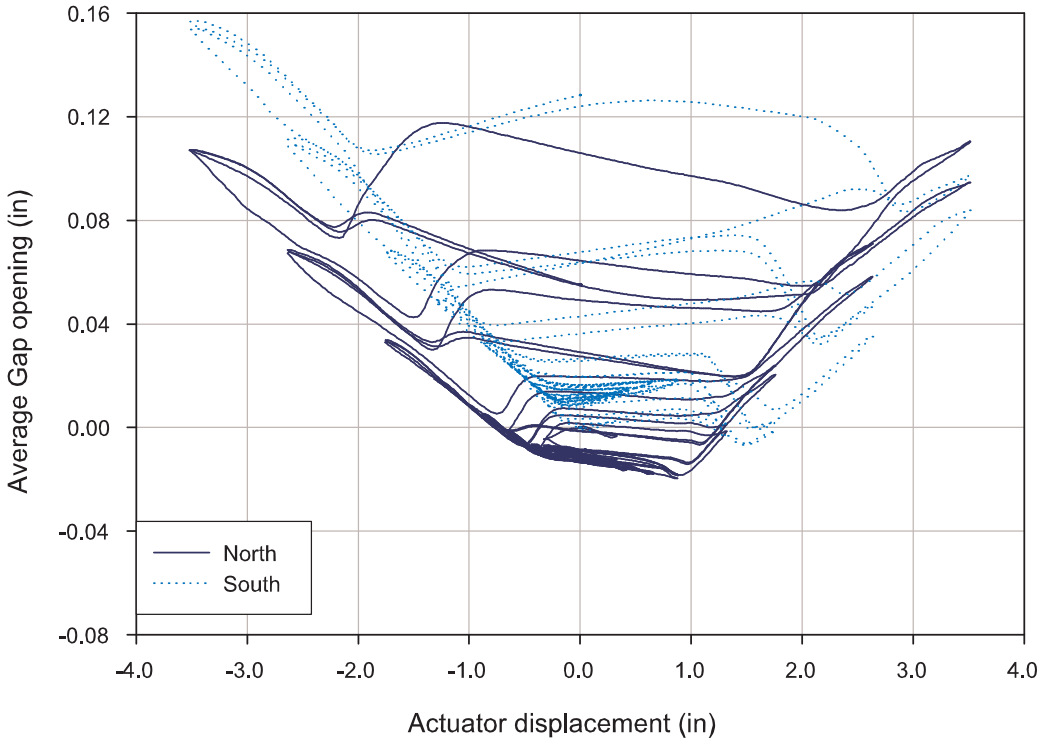

Figure B-7: Average gap opening versus actuator displacement for steel tendon test I on 04/25/05.

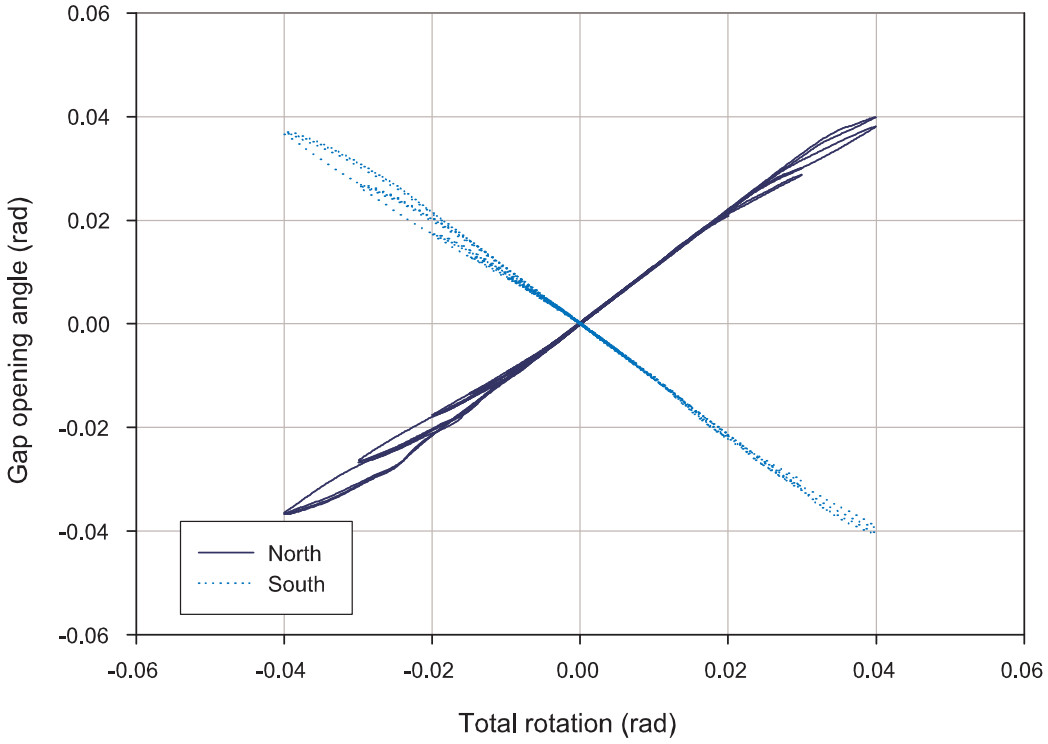

Figure B-8: Gap opening angle versus total rotation for steel tendon test I on 04/25/05.

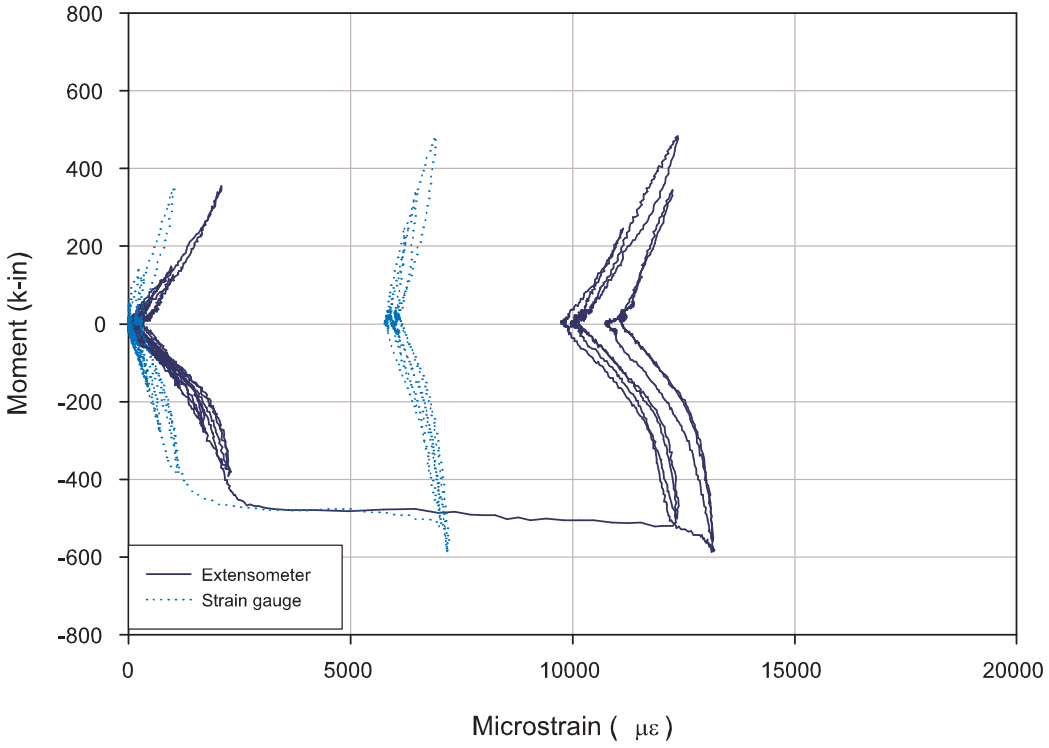

Figure B-9: Moment versus strain in Up West steel tendon for steel tendon test I on 04/25/05.

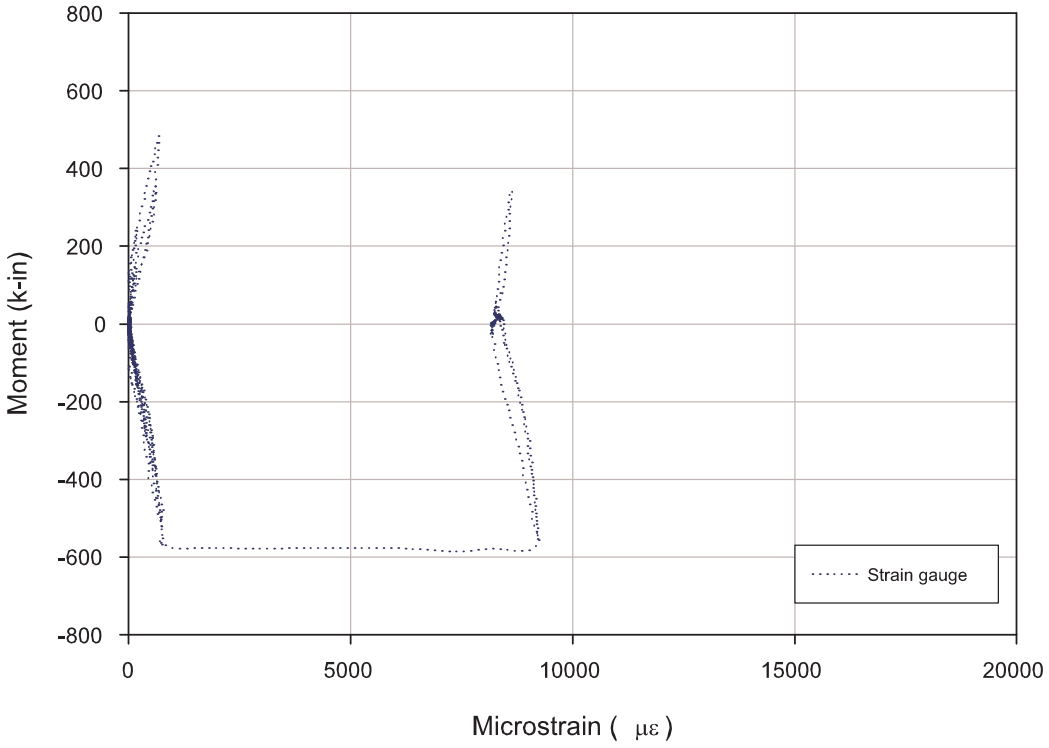

Figure B-10: Moment versus strain in Up East steel tendon for steel tendon test I on 04/25/05.

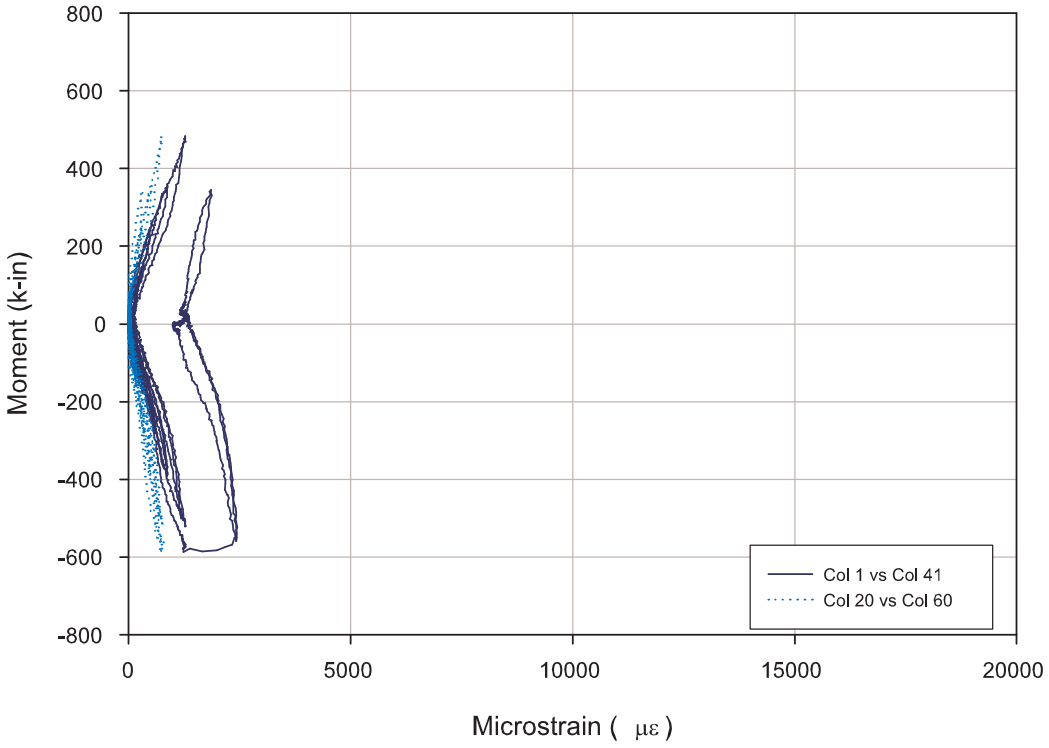

Figure B-11: Moment versus strain in Down West steel tendon for steel tendon test I on 04/25/05.

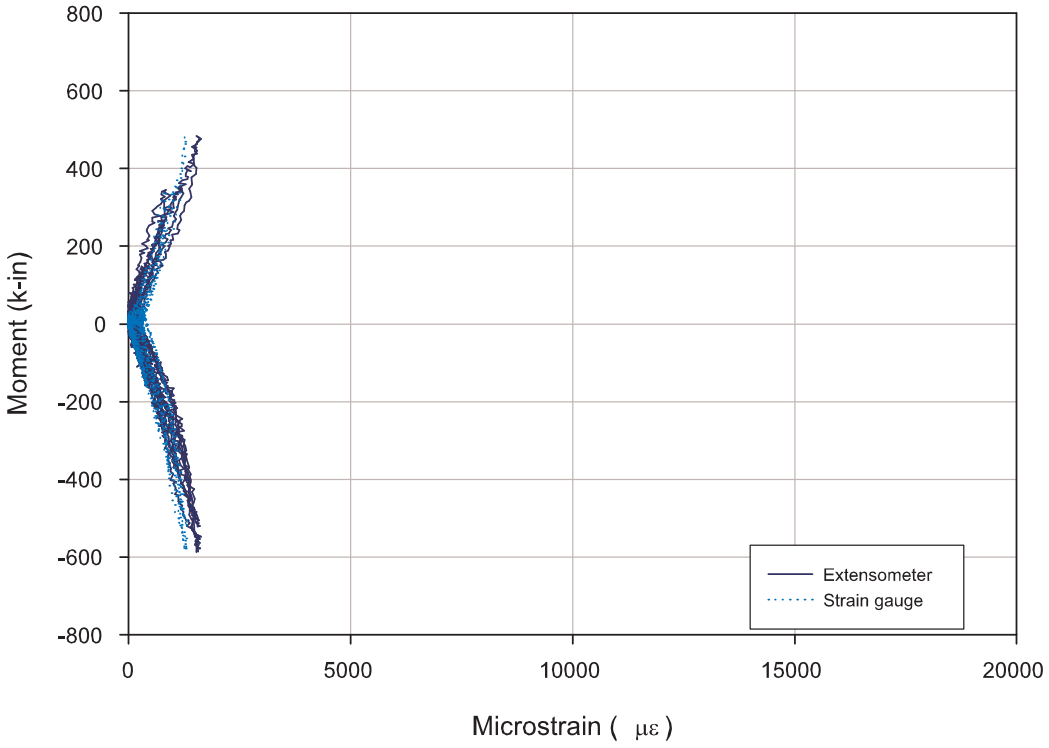

Figure B-12: Moment versus strain in Down East steel tendon for steel tendon test I on 04/25/05.

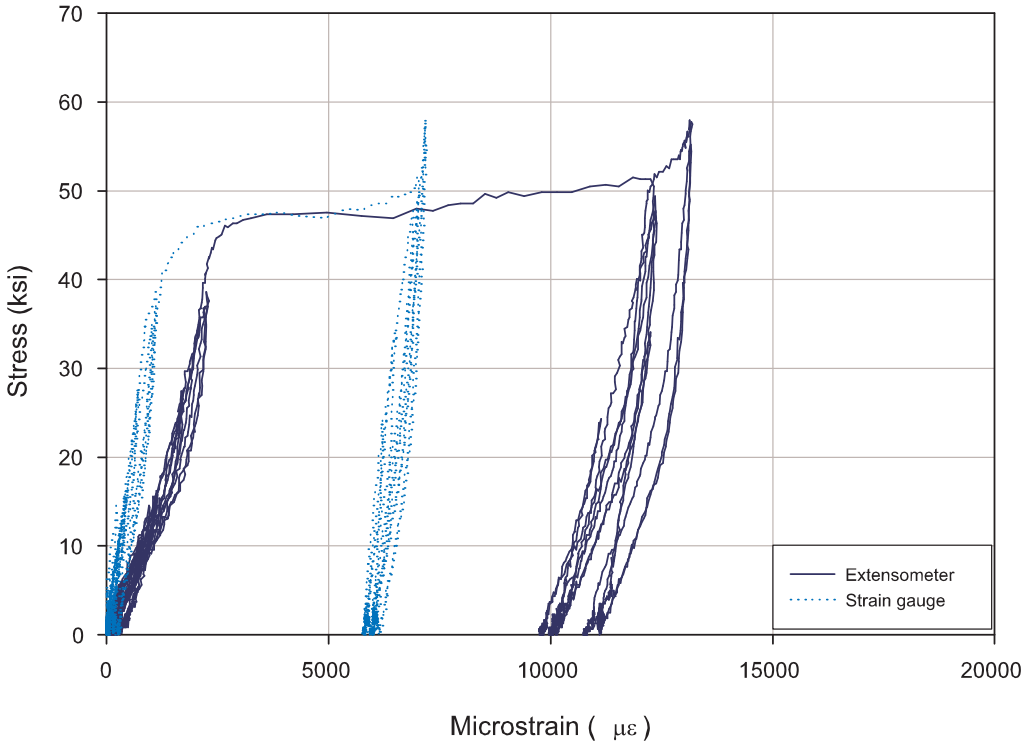

Figure B-13: Stress versus strain in Up West steel tendon for steel tendon test I on 04/25/05.

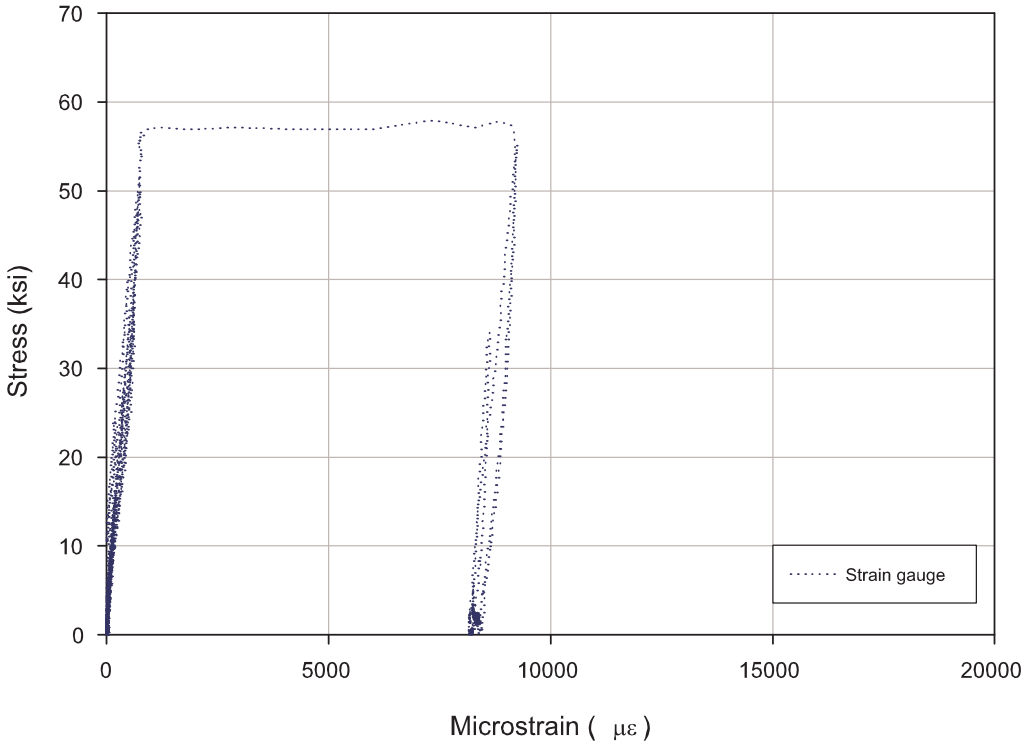

Figure B-14: Stress versus strain in Up East steel tendon for steel tendon test I on 04/25/05.

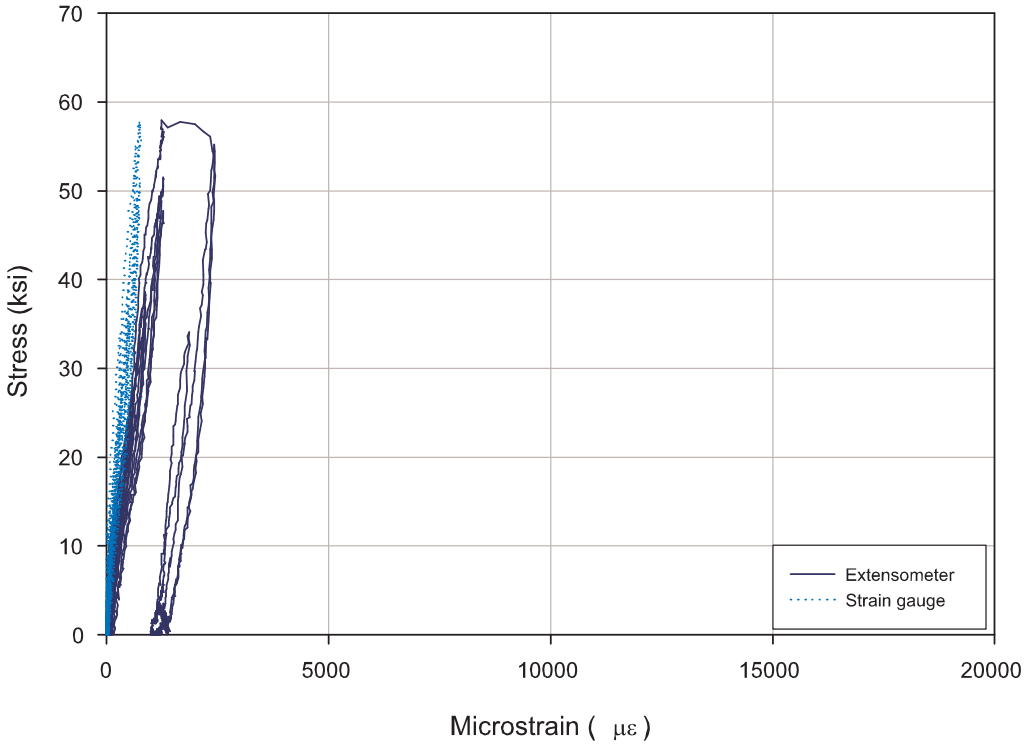

Figure B-15: Stress versus strain in Down West steel tendon for steel tendon test I on 04/25/05.

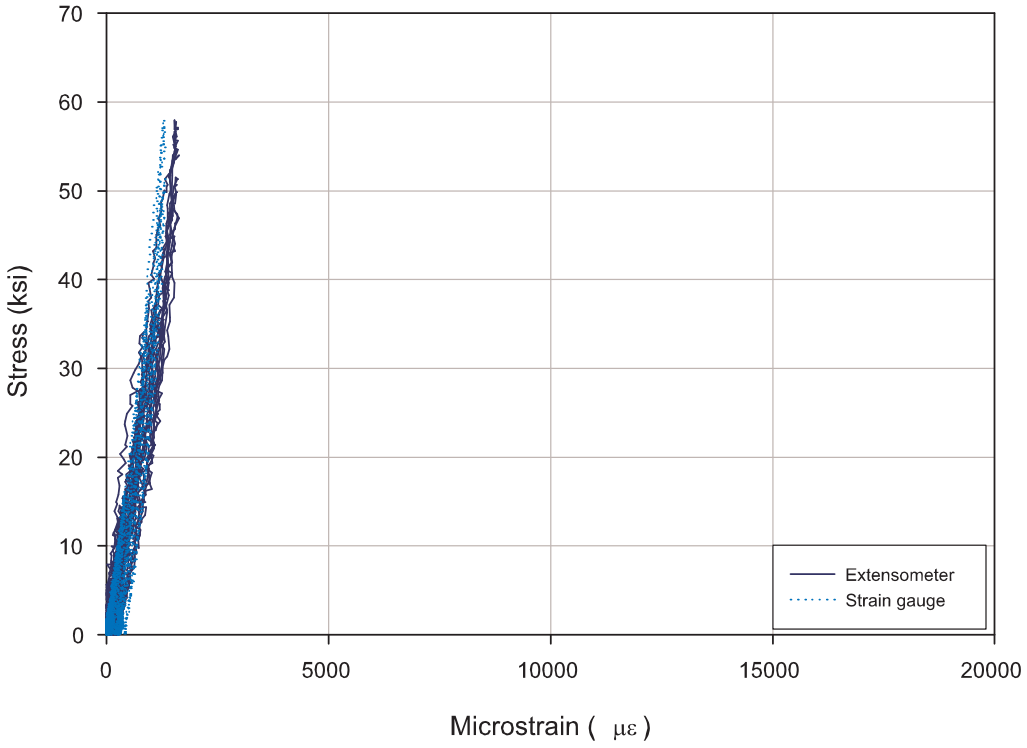

Figure B-16: Stress versus strain in Down East steel tendon for steel tendon test I on 04/25/05.

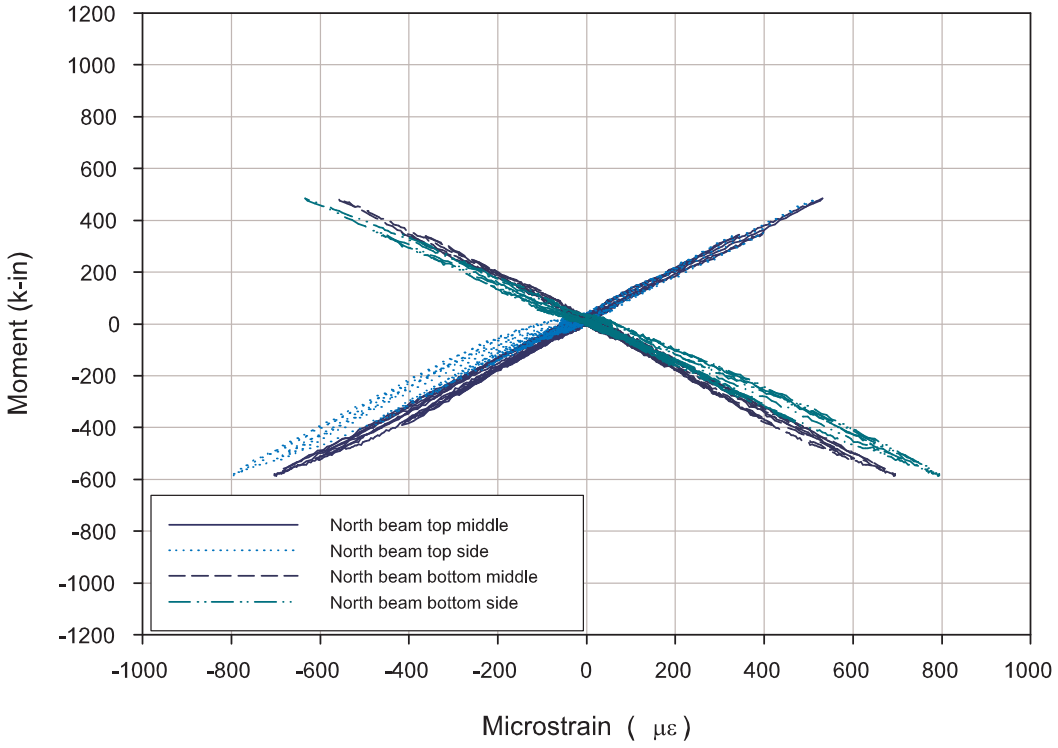

Figure B-17: Moment versus flange strain in north beam for steel tendon test I on 04/25/05.

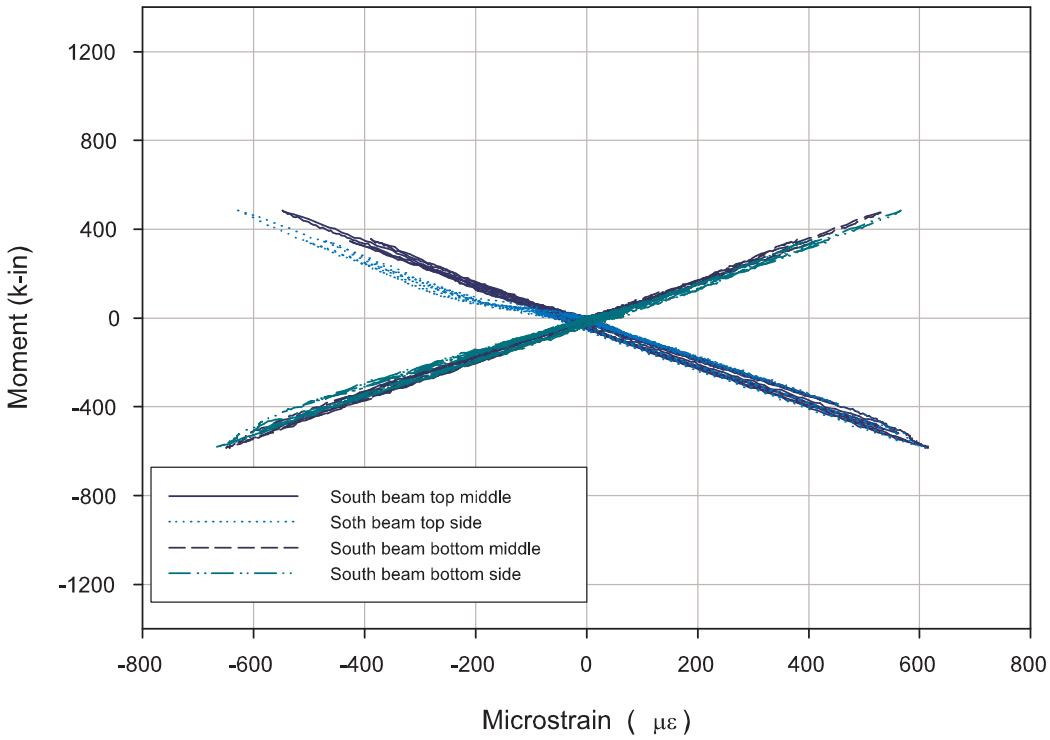

Figure B-18: Moment versus flange strain in south beam for steel tendon test I on 04/25/05.

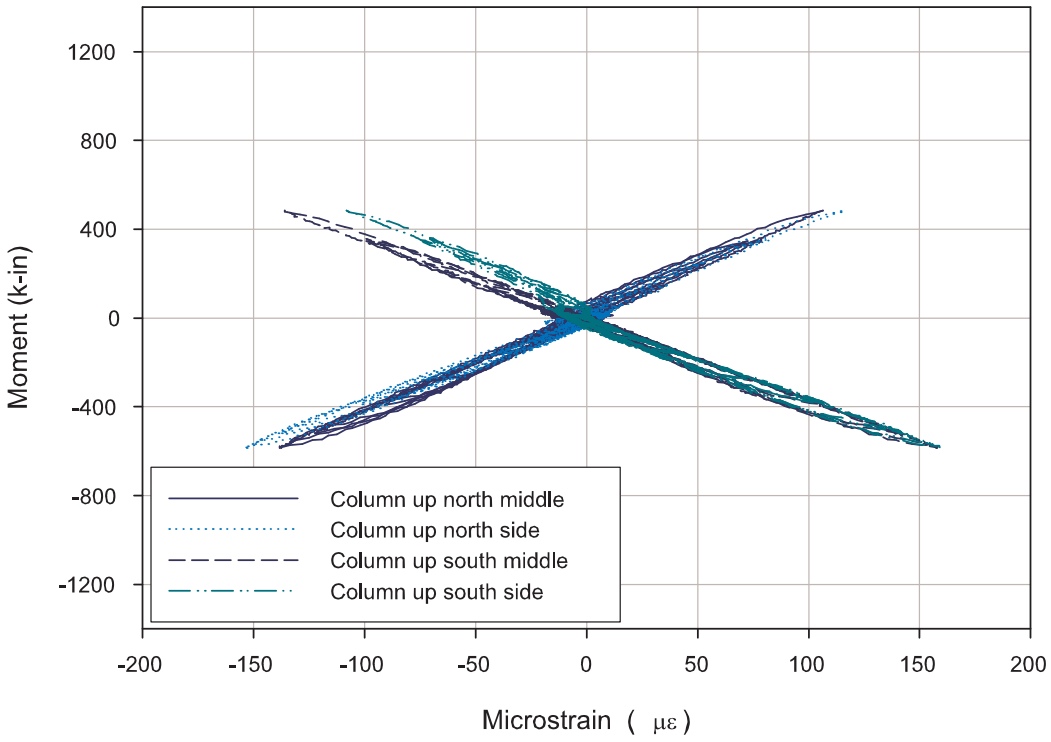

Figure B-19: Moment versus flange strain in upper portion of column for steel tendon test I on 04/25/05.

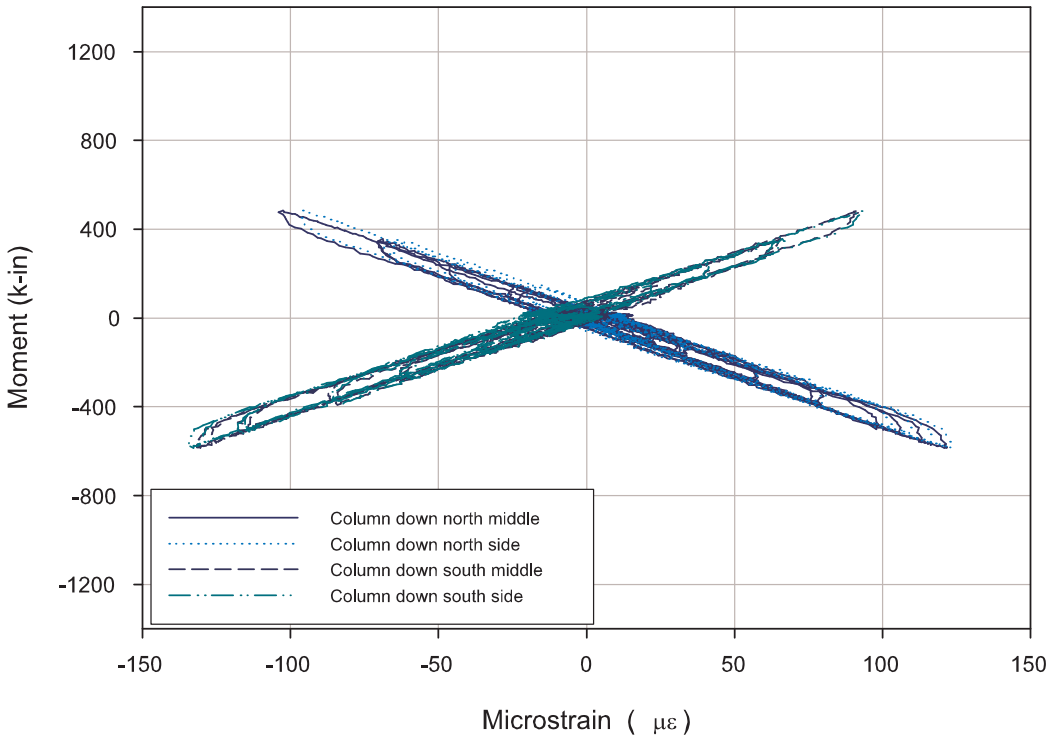

Figure B-20: Moment versus flange strain in lower portion of column for steel tendon test I on 04/25/05.

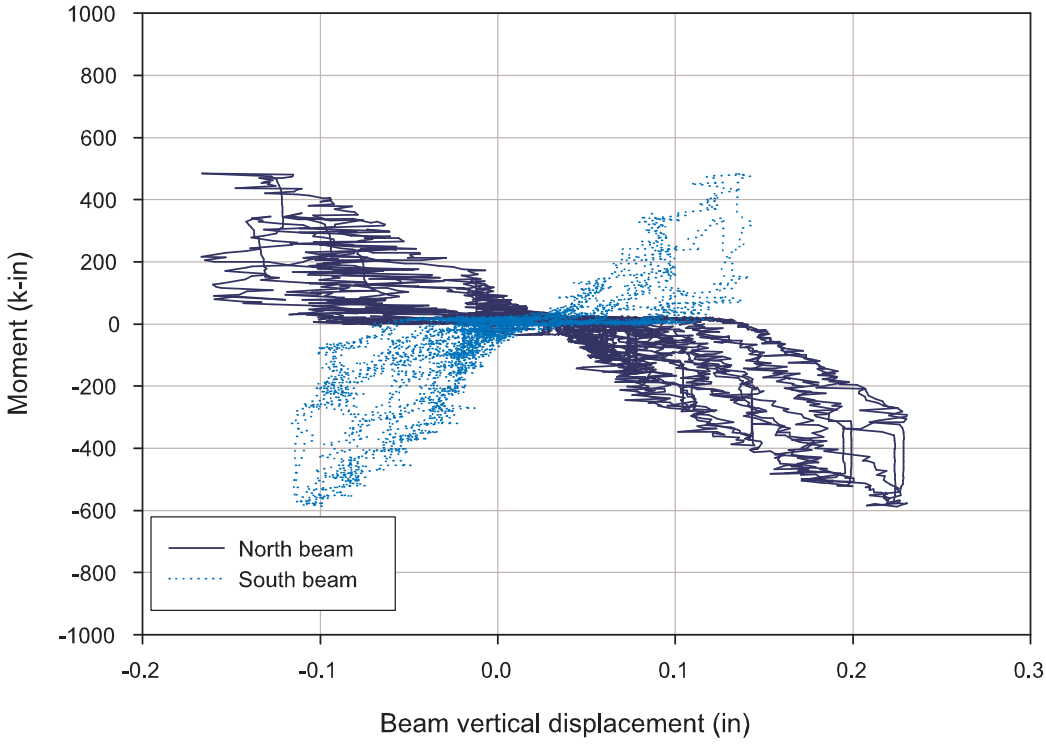

Figure B-21: Moment versus vertical displacement in beam for steel tendon test I on 04/25/05.

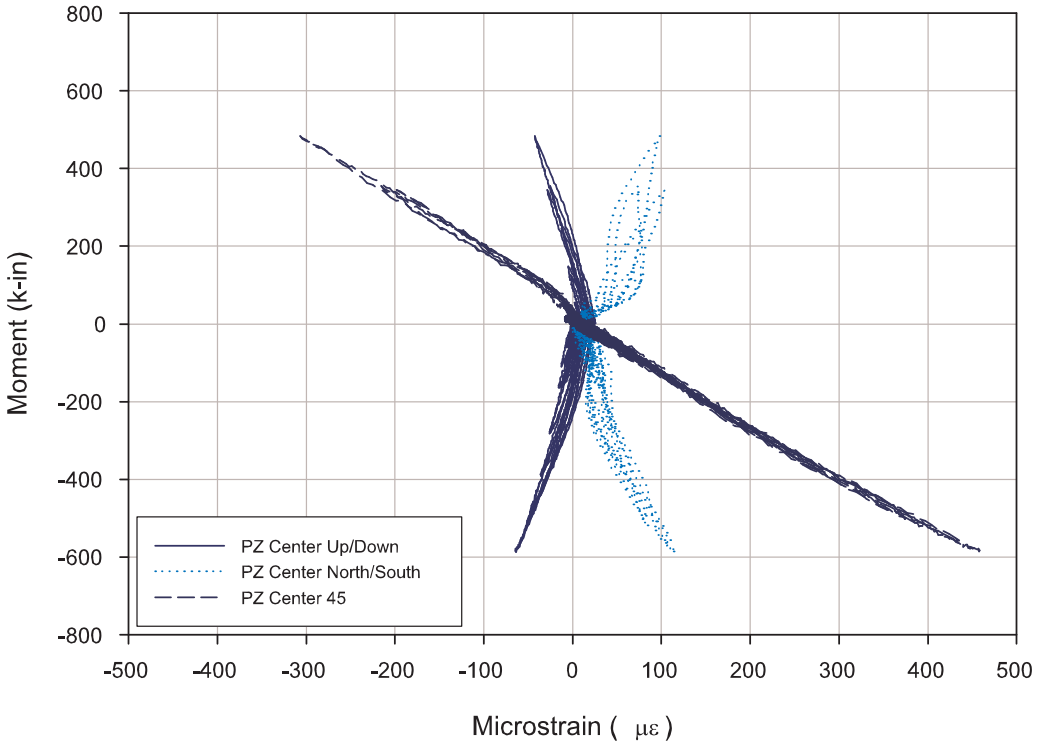

Figure B-22: Moment versus strain in center panel zone rosette for steel tendon test I on 04/25/05.

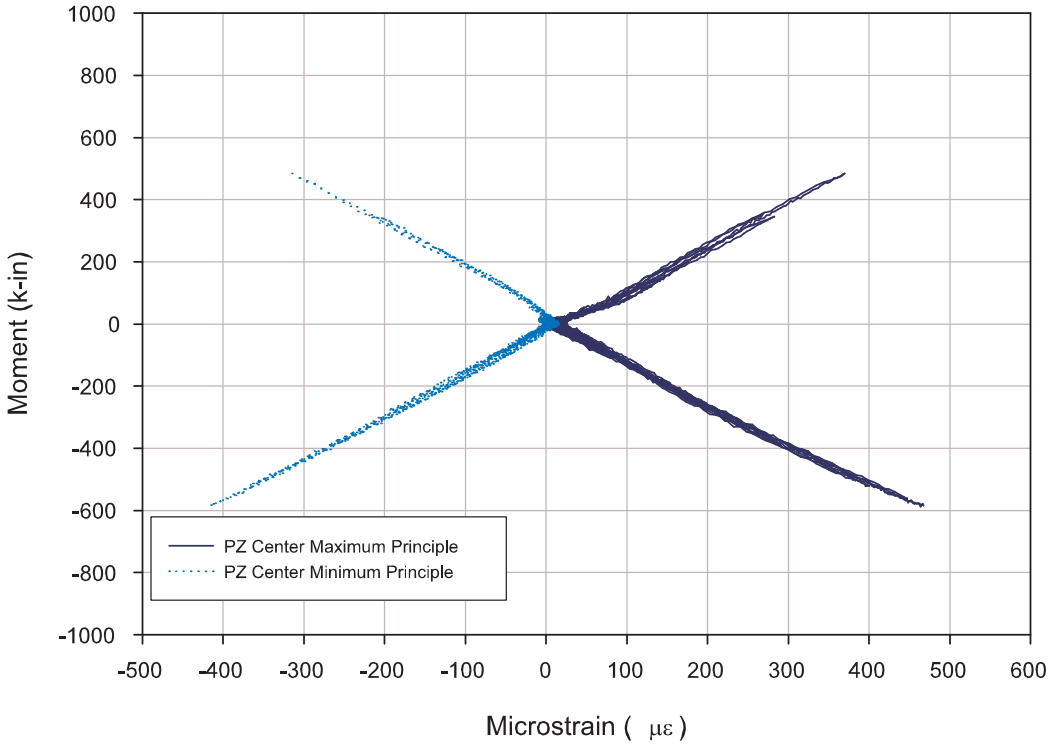

Figure B-23: Moment versus principle strains in center panel zone rosette for steel tendon test I on 04/25/05.

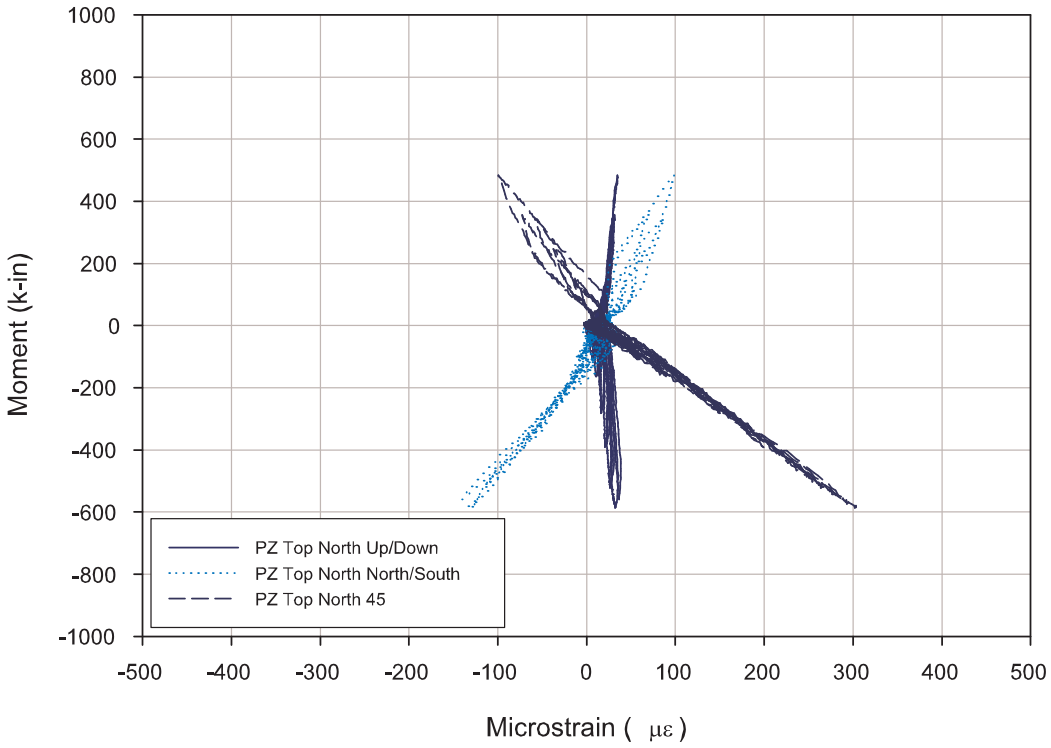

Figure B-24: Moment versus strain in top north panel zone rosette for steel tendon test I on 04/25/05.

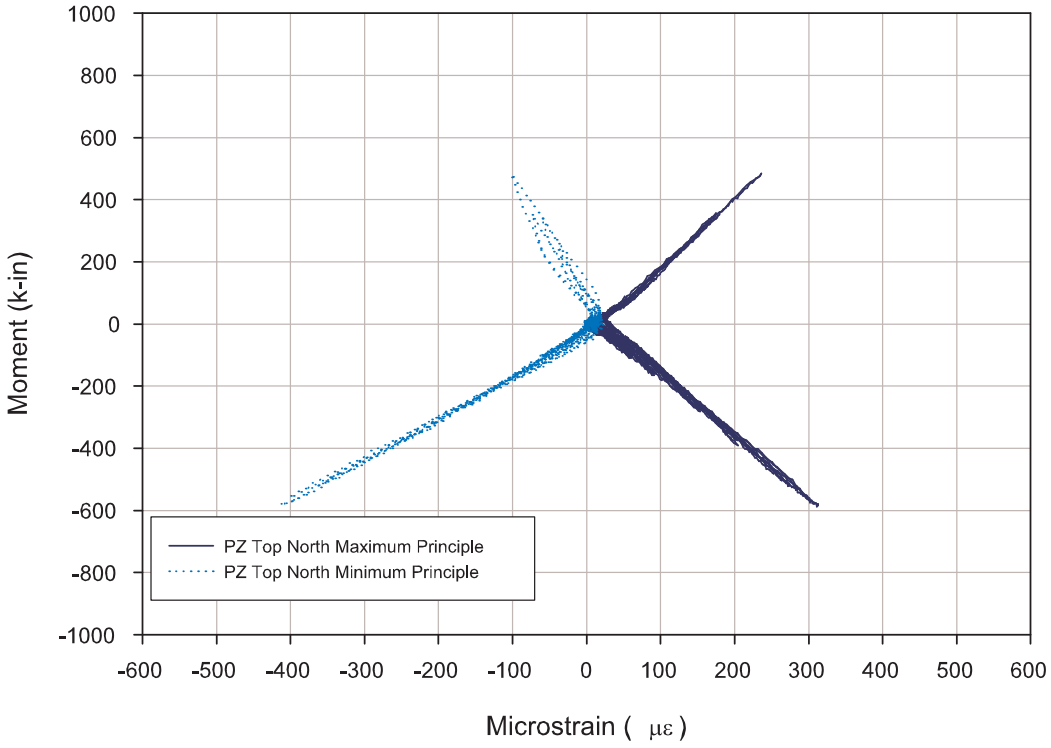

Figure B-25: Moment versus principle strains in top north panel zone rosette for steel tendon test I on 04/25/05.

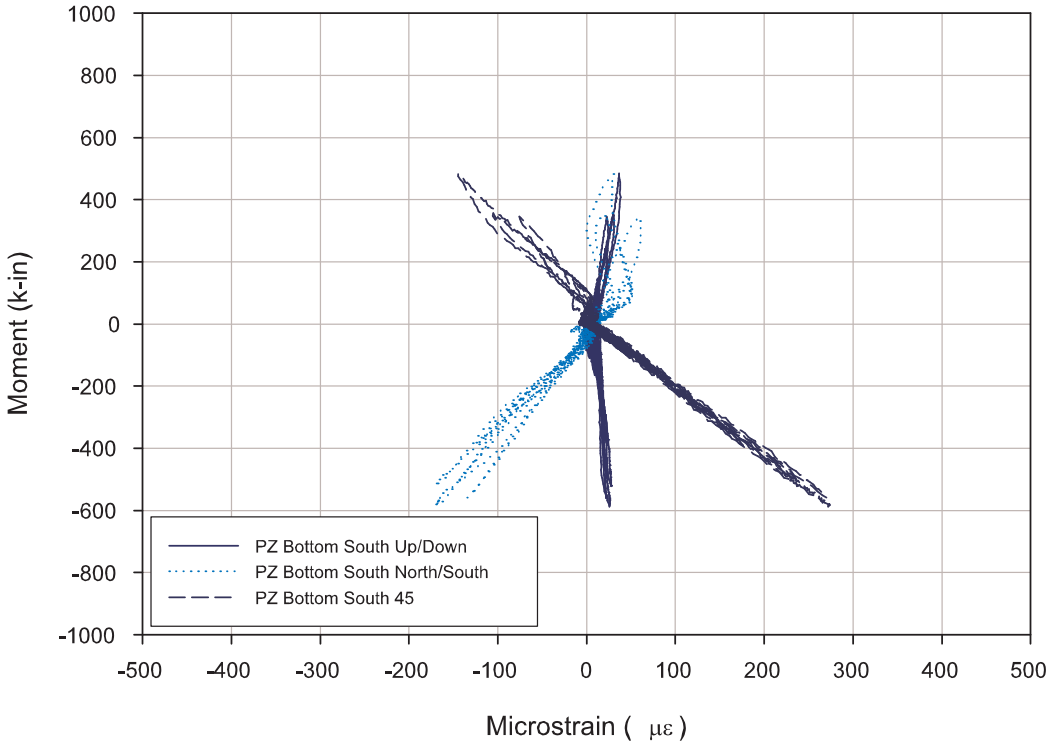

Figure B-26: Moment versus strain in bottom south panel zone rosette for steel tendon test I on 04/25/05.

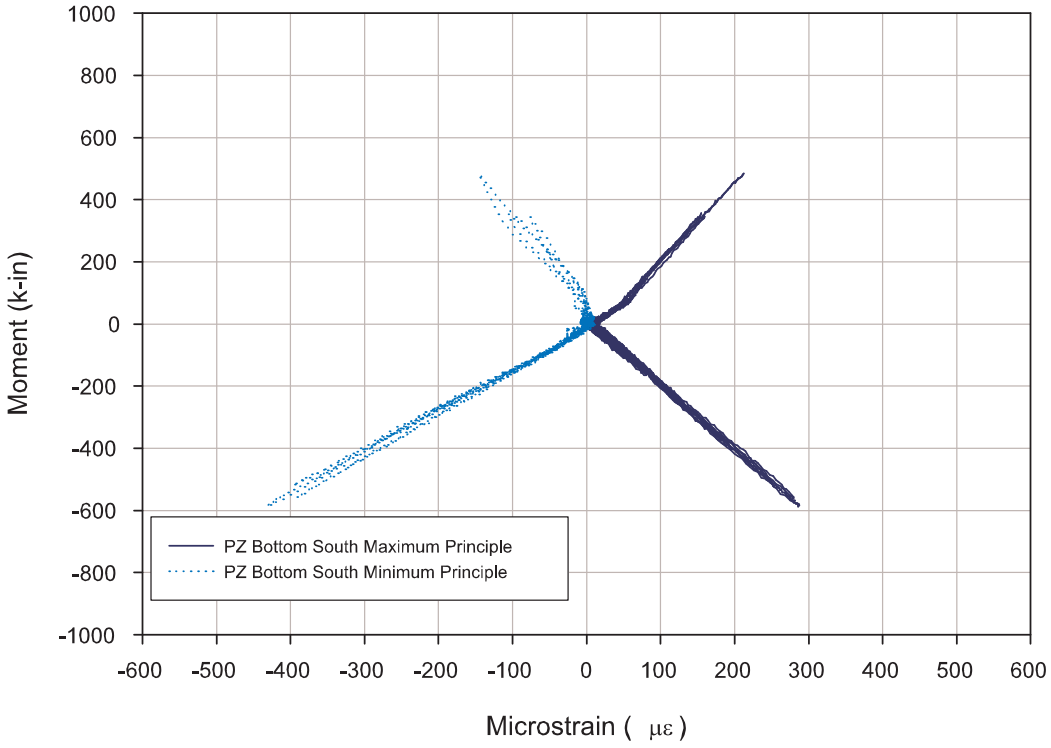

Figure B-27: Moment versus principle strains in bottom south panel zone rosette for steel tendon test I on 04/25/05.

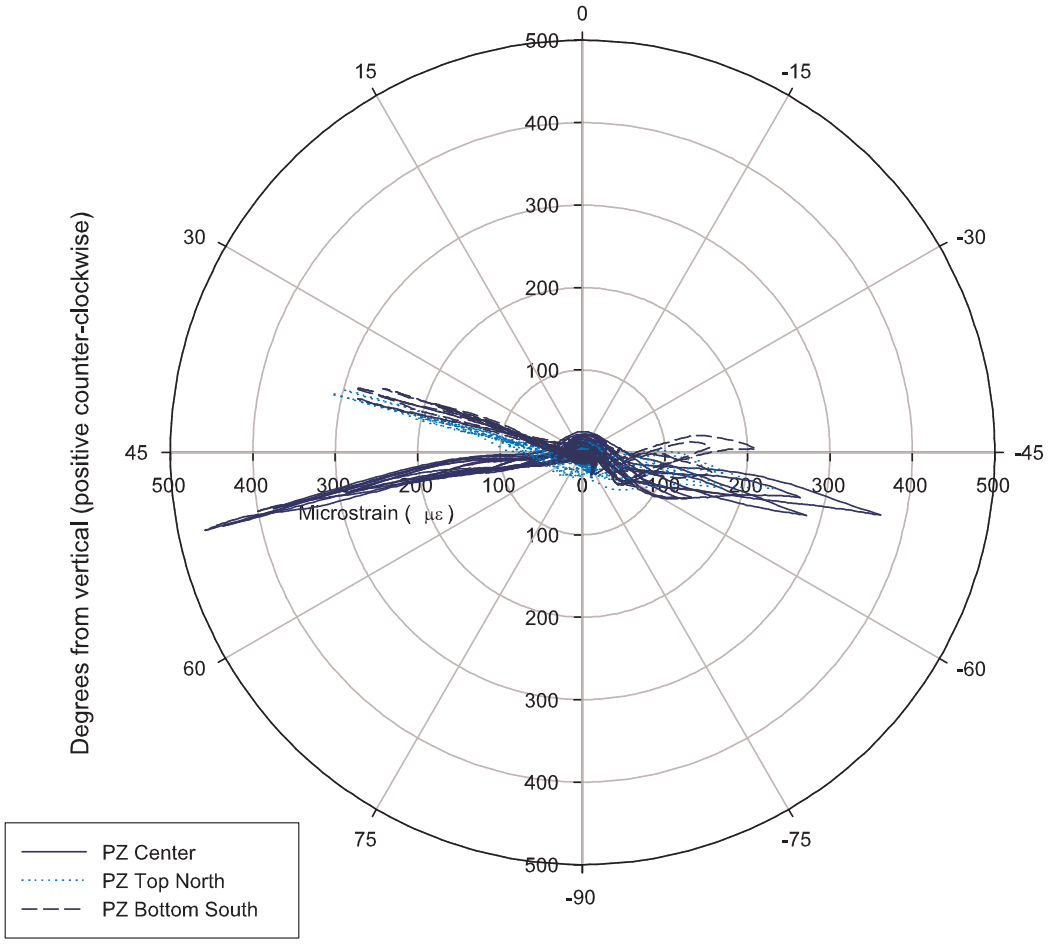

Figure B-28: Principle strain angles versus maximum principal strains in panel zone rosettes for steel tendon test I on 04/25/05.

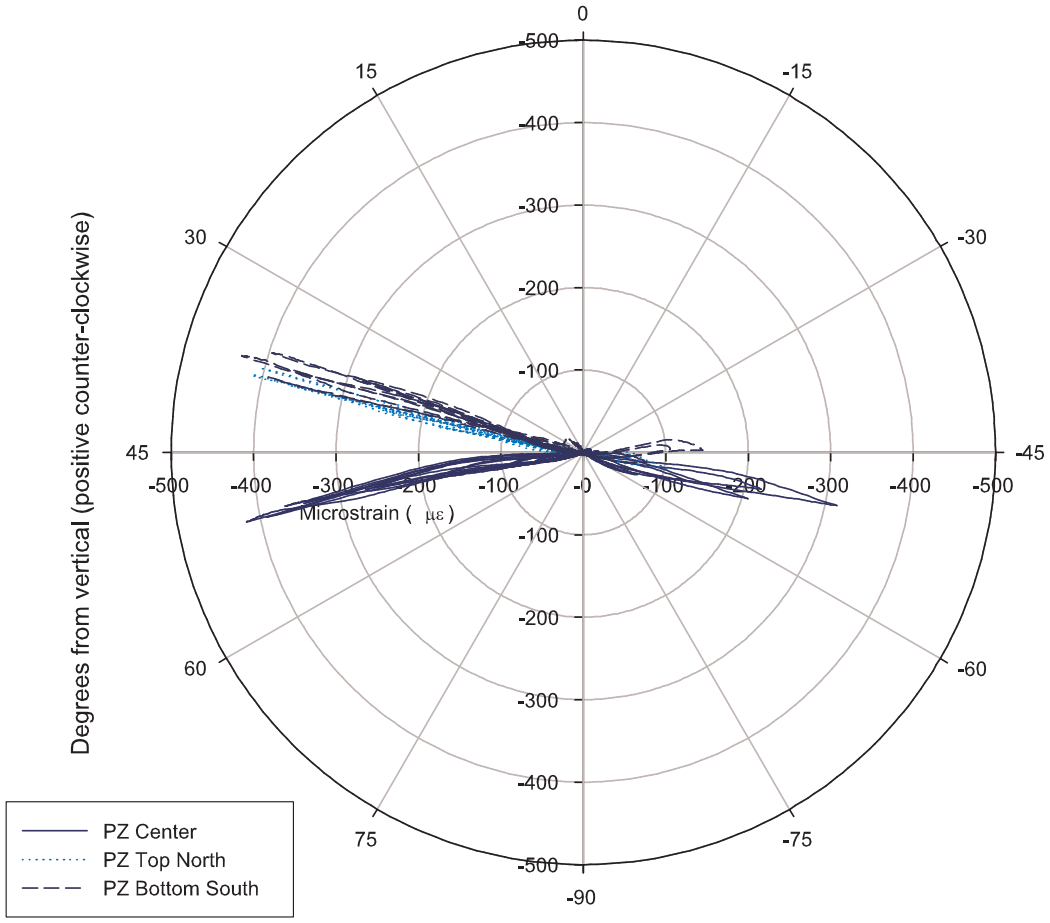

Figure B-29: Principle strain angles versus minimum principal strains in panel zone rosettes for steel tendon test I on 04/25/05.

B.2 Test II on 04/27/05

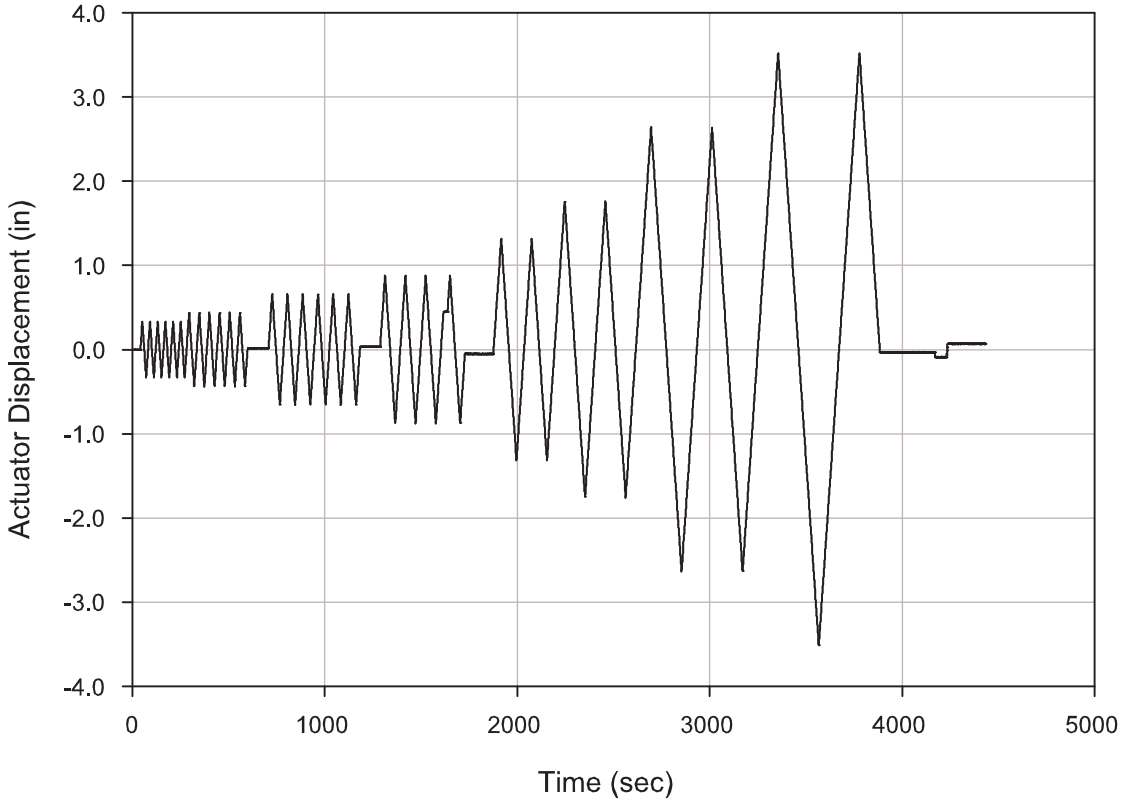

Figure B-30: Actuator displacement history for steel tendon test II on 04/27/05.

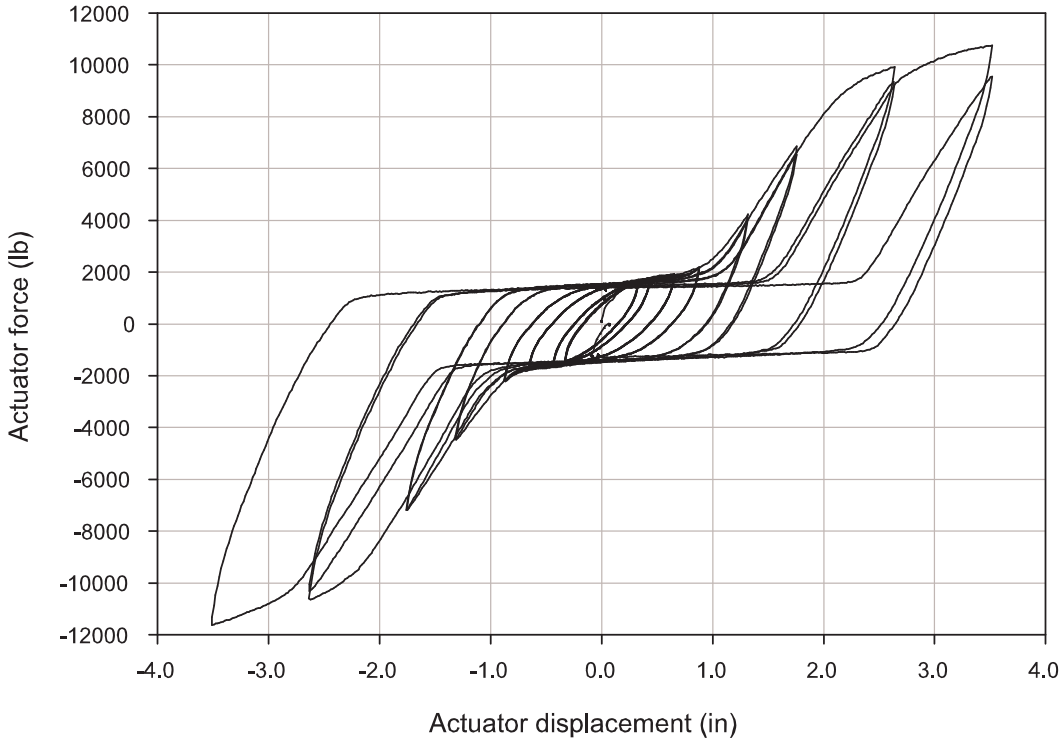

Figure B-31: Actuator force versus actuator displacement for steel tendon test II on 04/27/05.

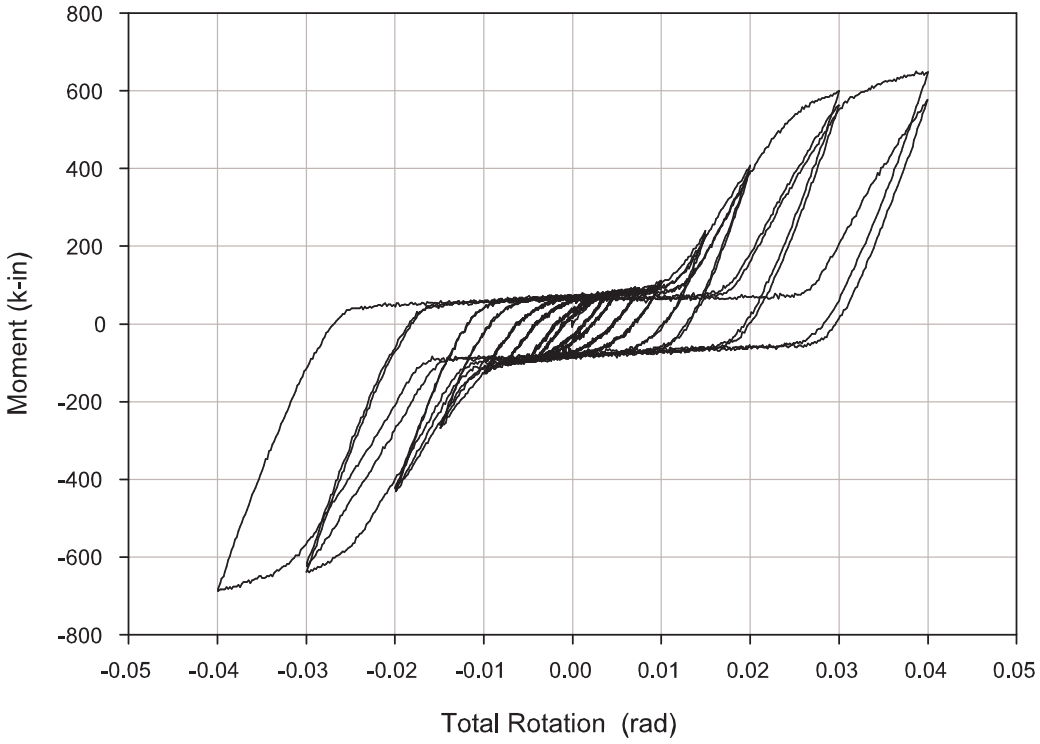

Figure B-32: Moment versus total rotation for steel tendon test II on 04/27/05.

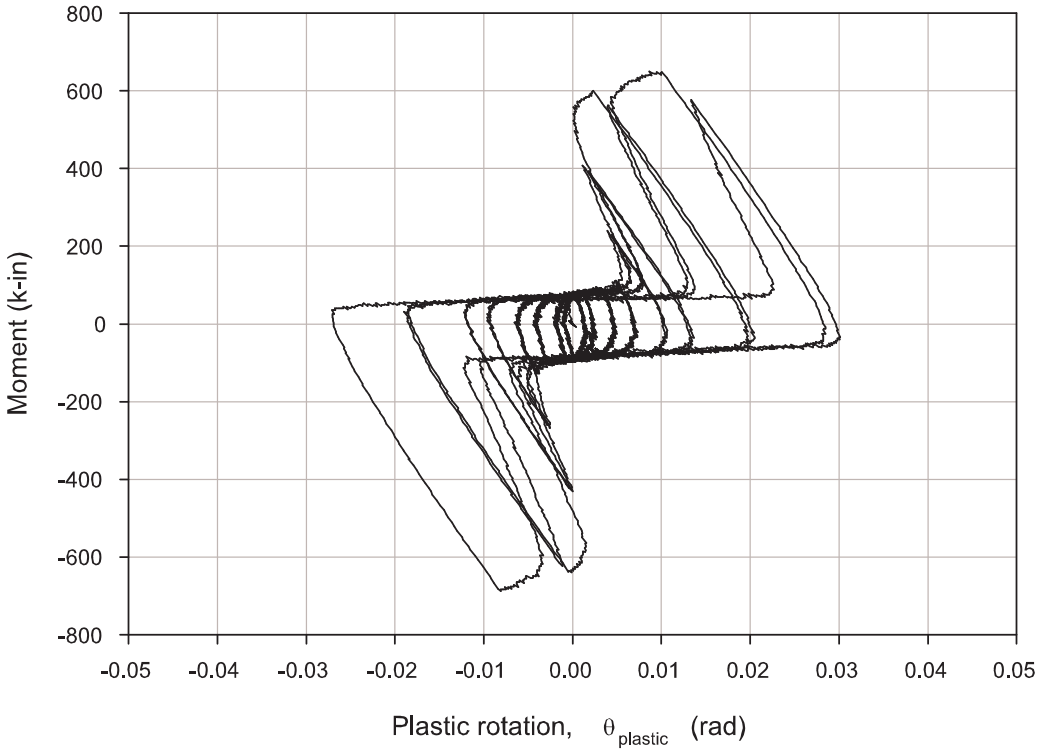

Figure B-33: Moment versus plastic rotation for steel tendon test II on 04/27/05.

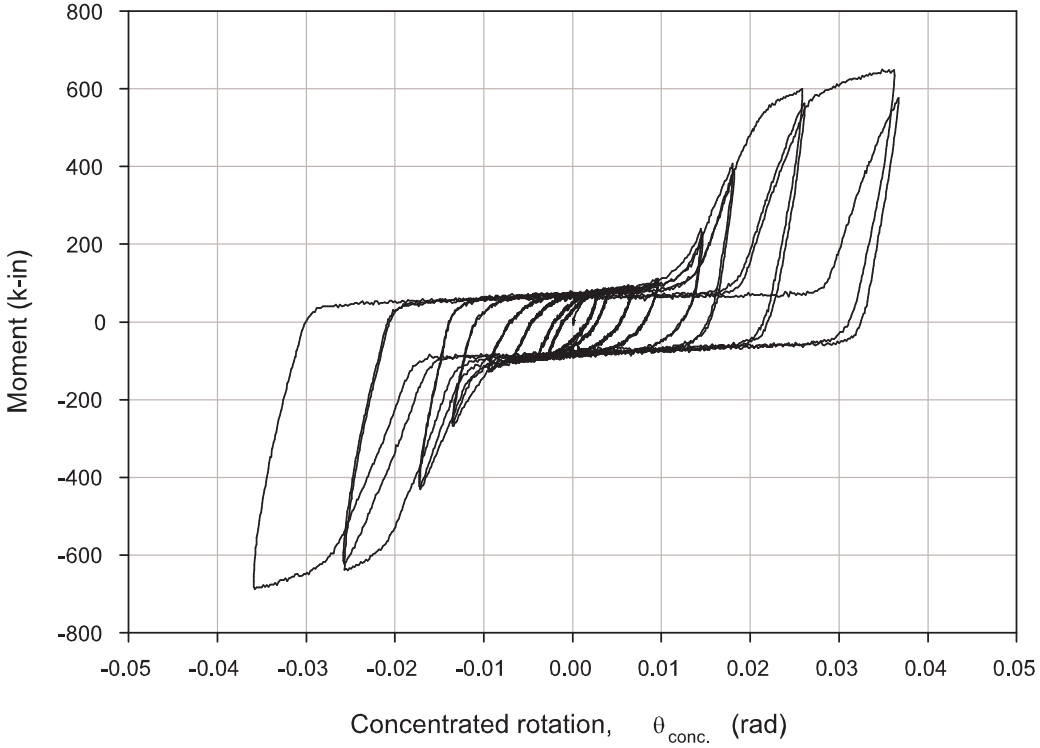

Figure B-34: Moment versus concentrated rotation for steel tendon test II on 04/27/05.

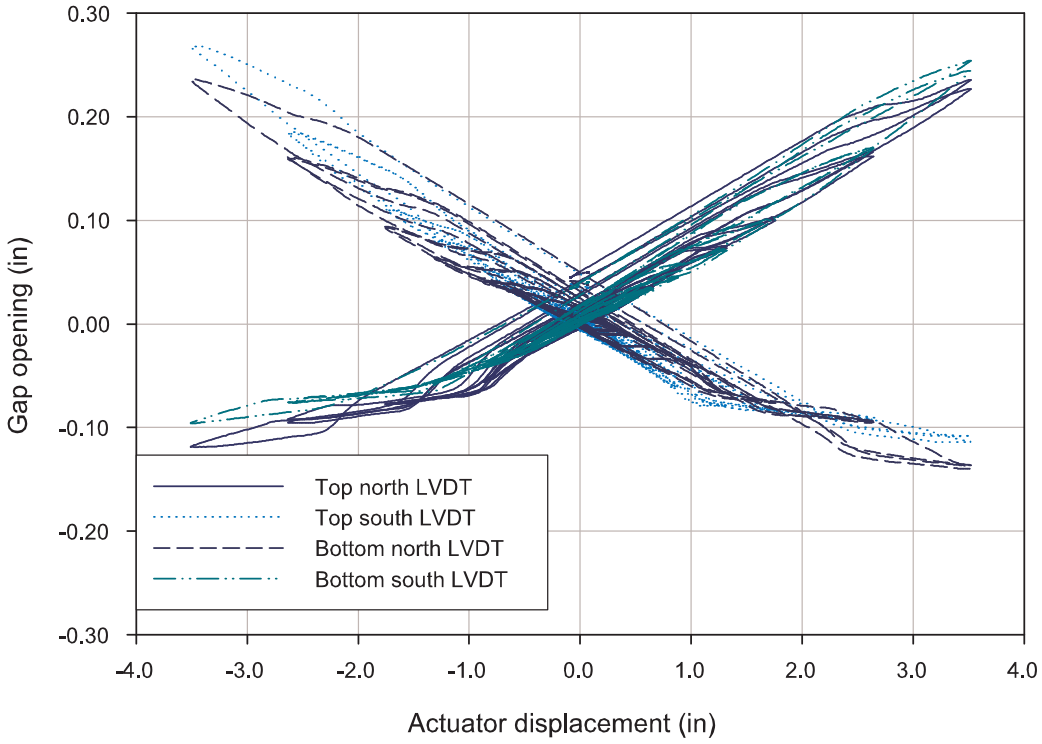

Figure B-35: Gap opening versus actuator displacement for steel tendon test II on 04/27/05.

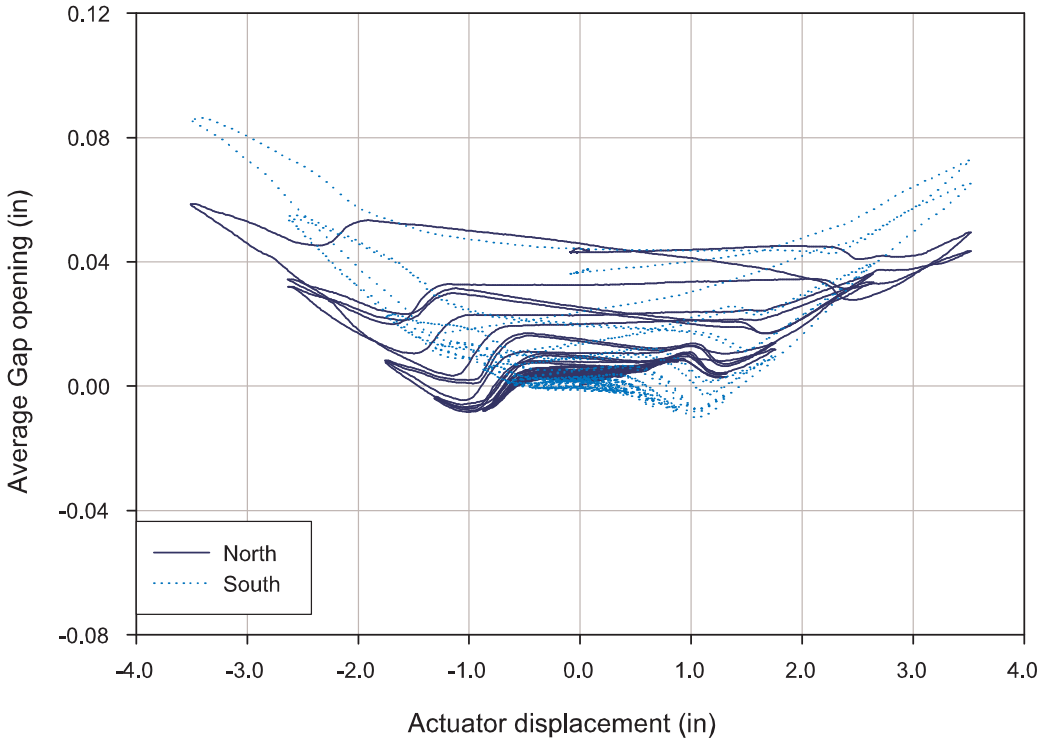

Figure B-36: Average gap opening versus actuator displacement for steel tendon test II on 04/27/05.

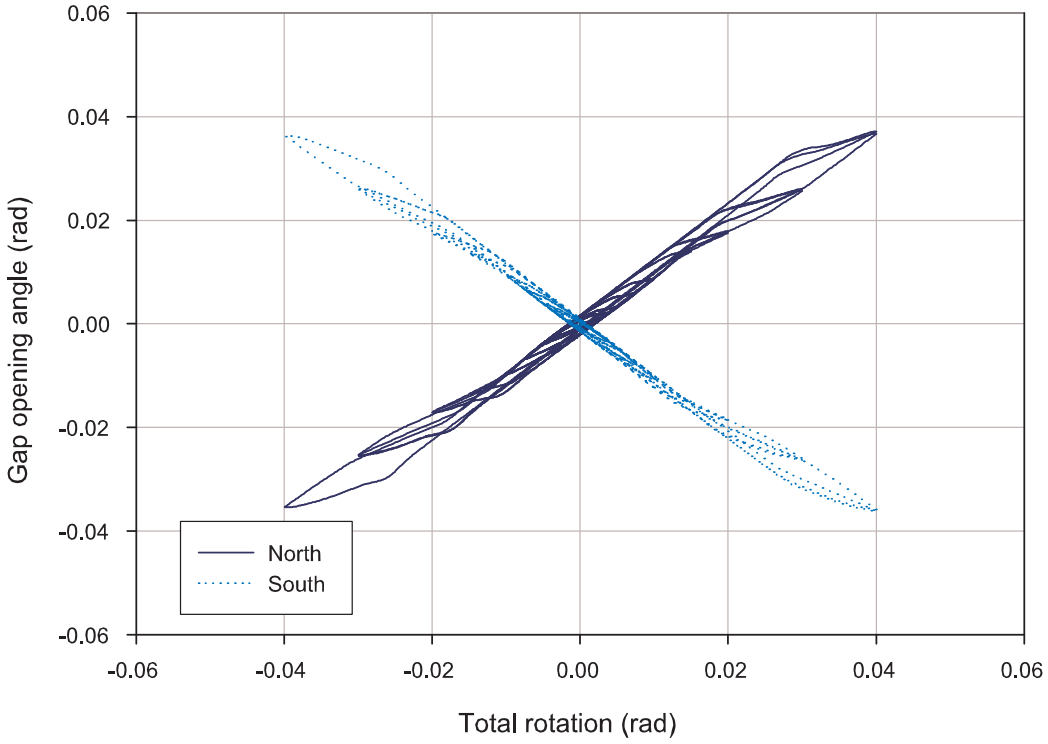

Figure B-37: Gap opening angle versus total rotation for steel tendon test II on 04/27/05.

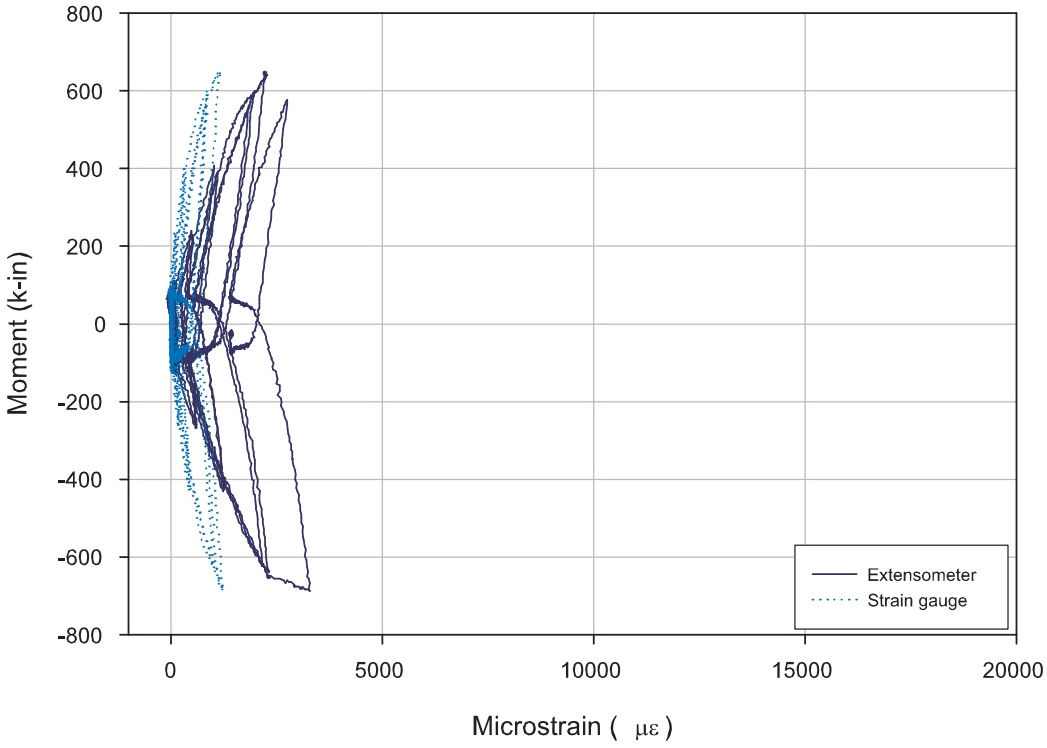

Figure B-38: Moment versus strain in Up West steel tendon for steel tendon test II on 04/27/05.

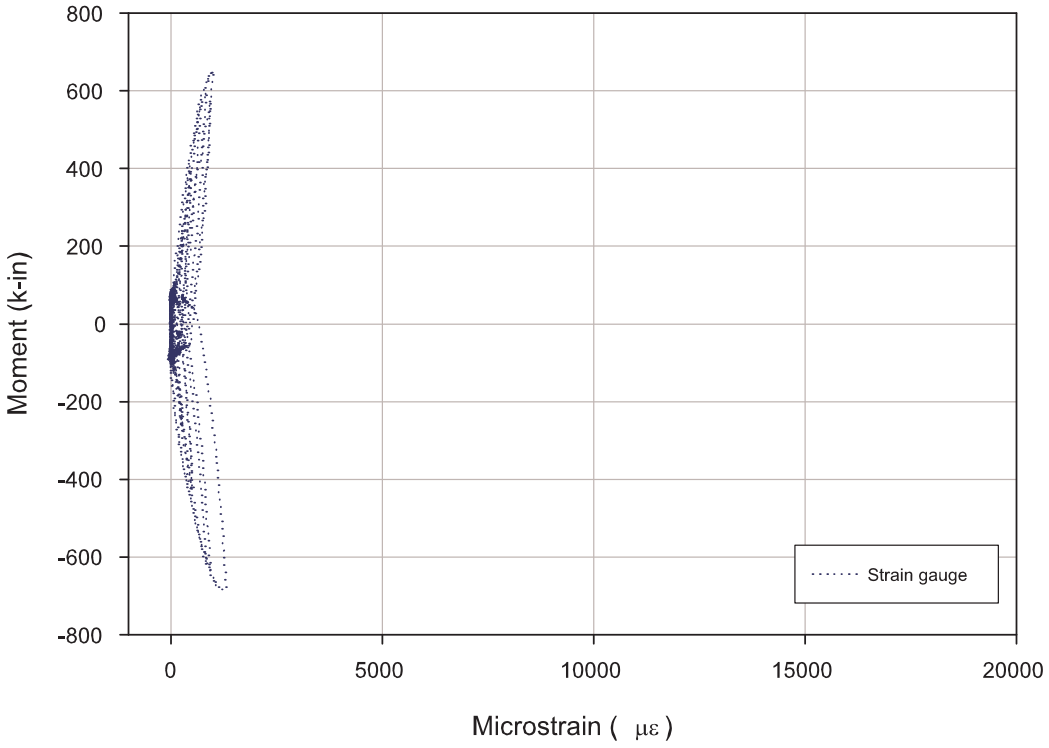

Figure B-39: Moment versus strain in Up East steel tendon for steel tendon test II on 04/27/05.

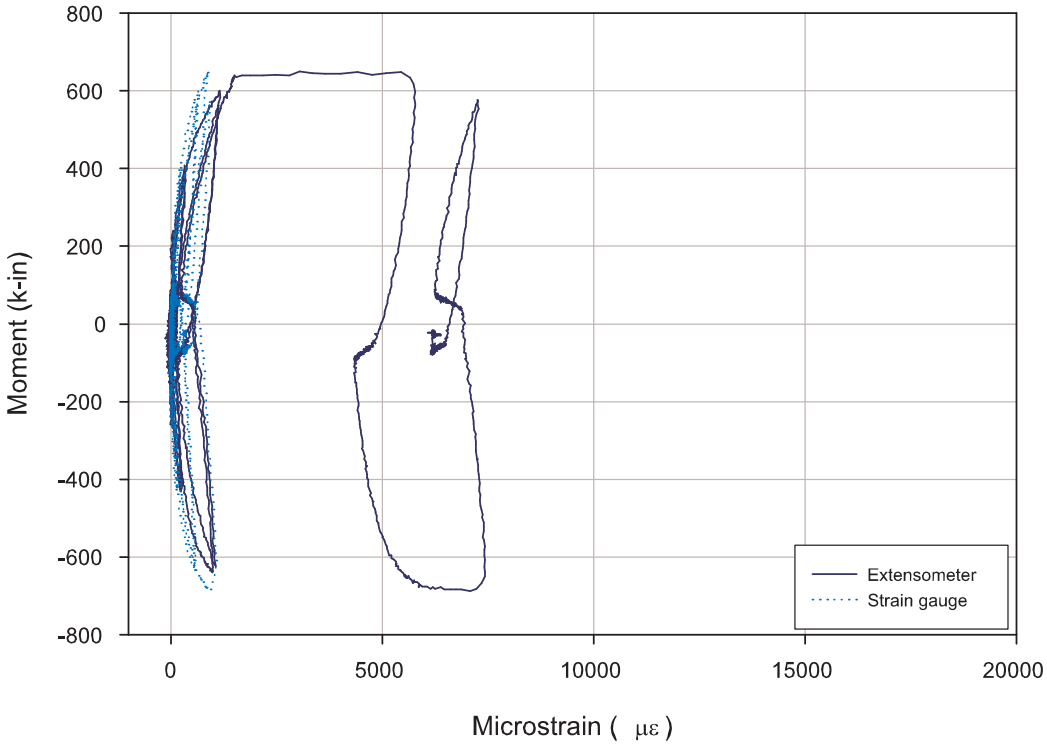

Figure B-40: Moment versus strain in Down West steel tendon for steel tendon test II on 04/27/05.

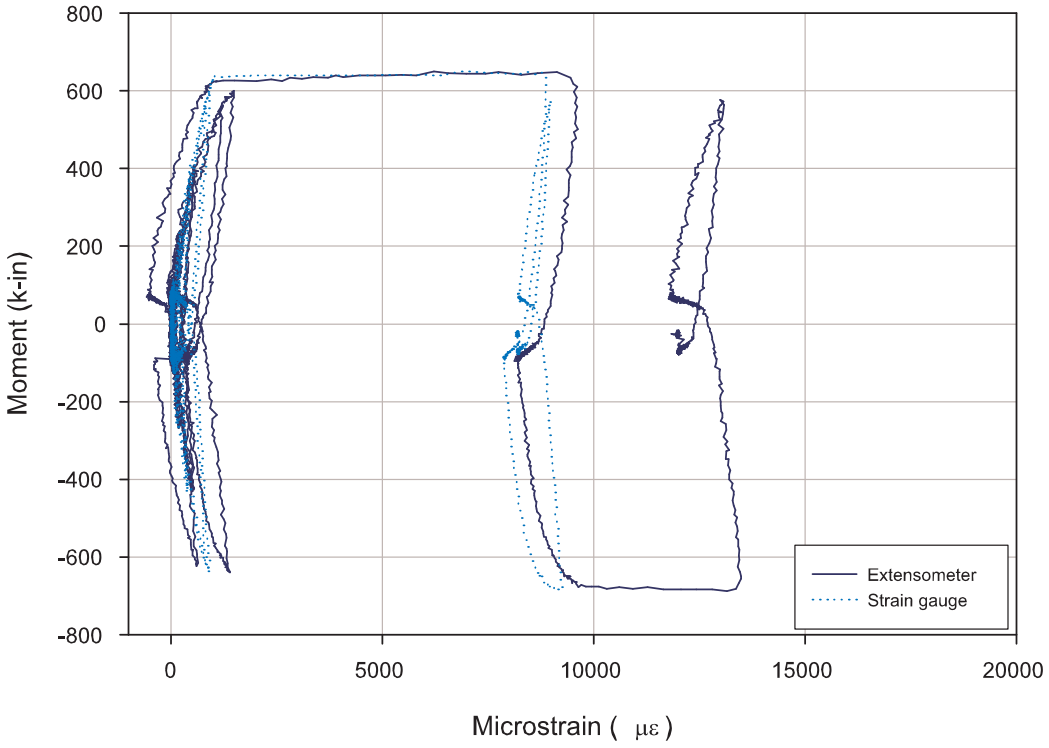

Figure B-41: Moment versus strain in Down East steel tendon for steel tendon test II on 04/27/05.

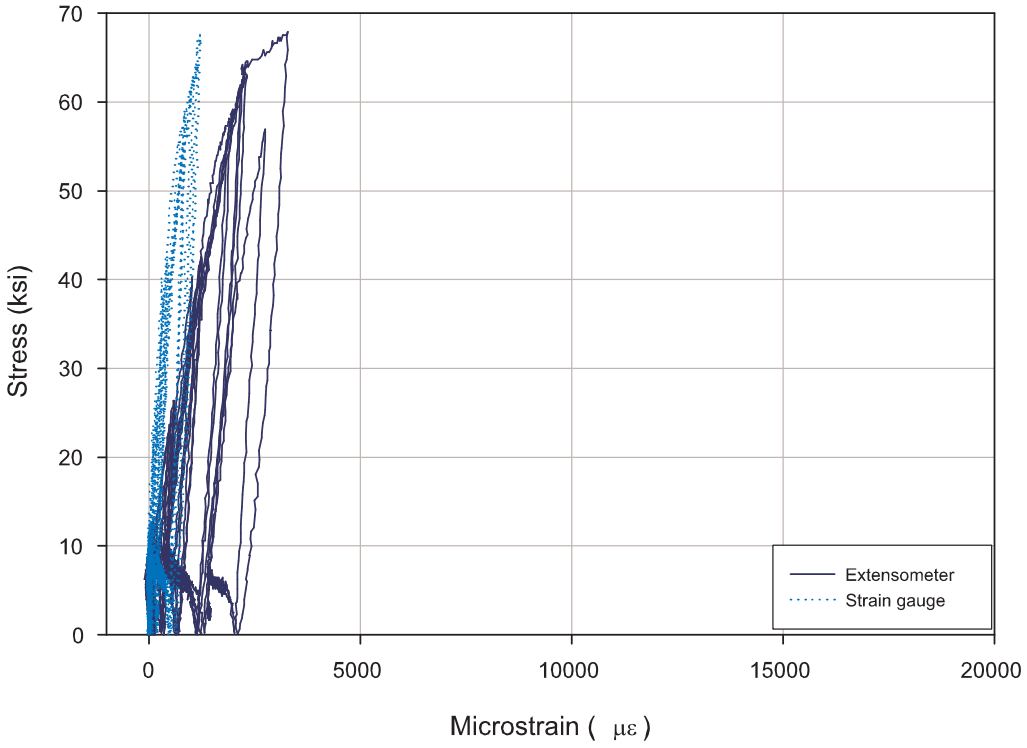

Figure B-42: Stress versus strain in Up West steel tendon for steel tendon test II on 04/27/05.

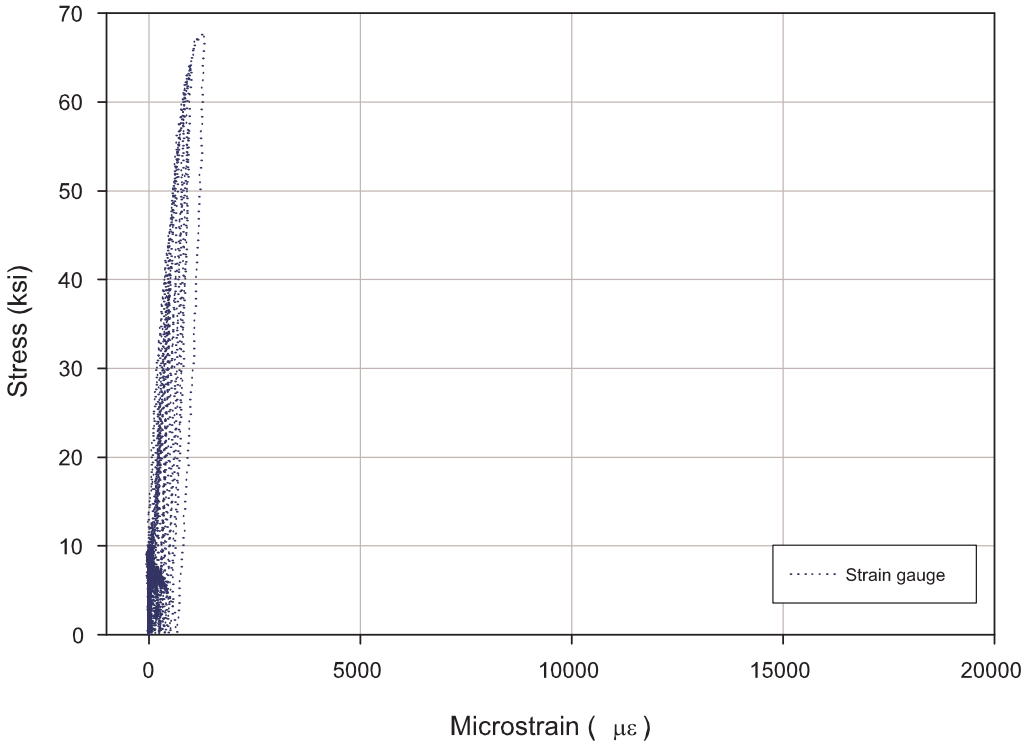

Figure B-43: Stress versus strain in Up East steel tendon for steel tendon test II on 04/27/05.

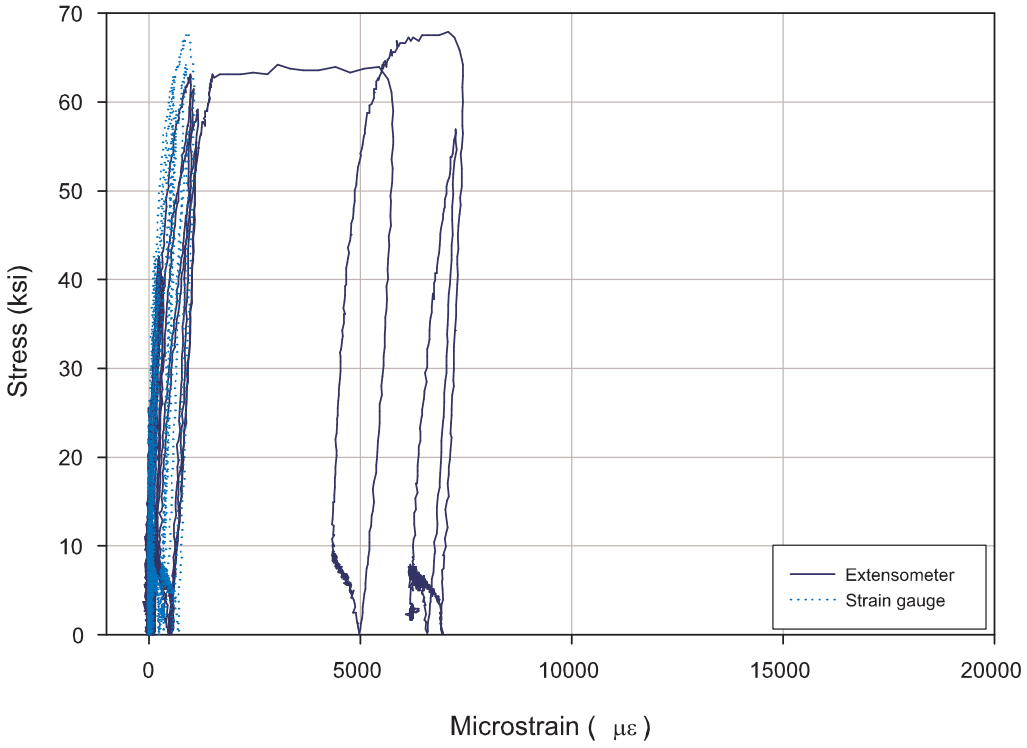

Figure B-44: Stress versus strain in Down West steel tendon for steel tendon test II on 04/27/05.

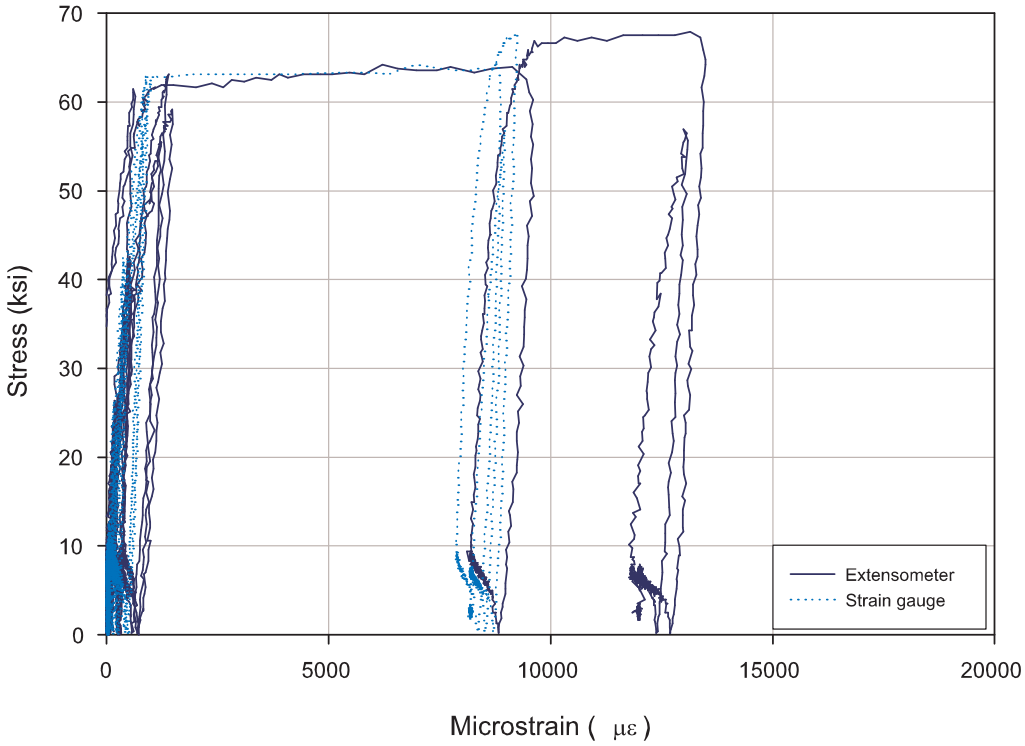

Figure B-45: Stress versus strain in Down East steel tendon for steel tendon test II on 04/27/05.

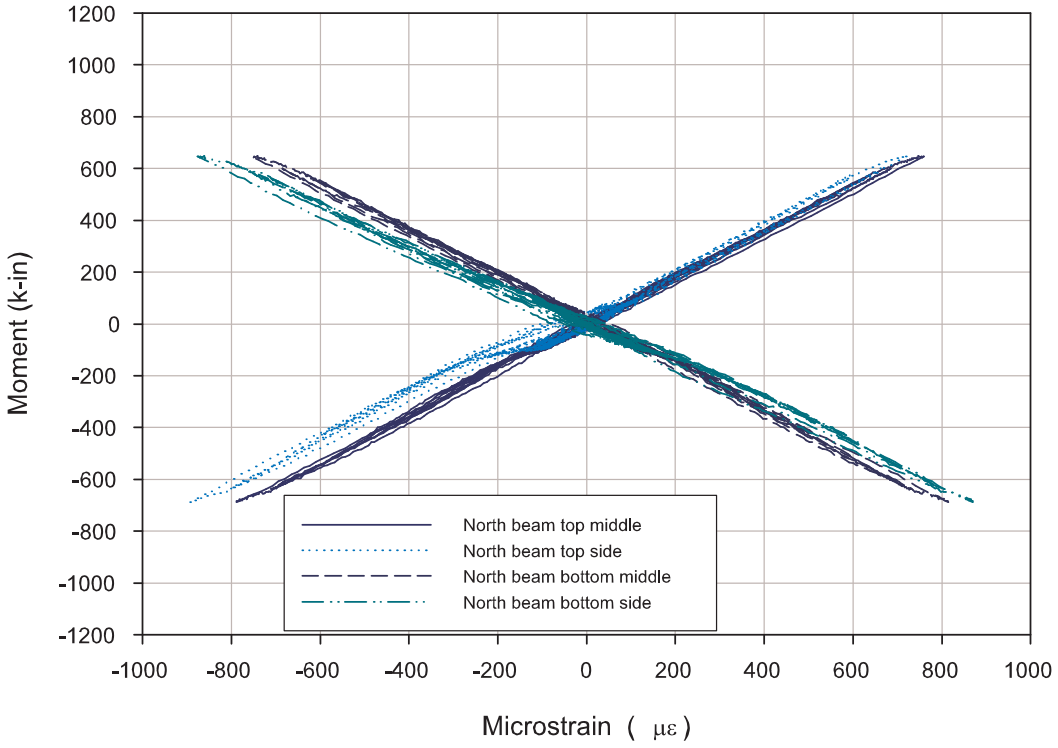

Figure B-46: Moment versus flange strain in north beam for steel tendon test II on 04/27/05.

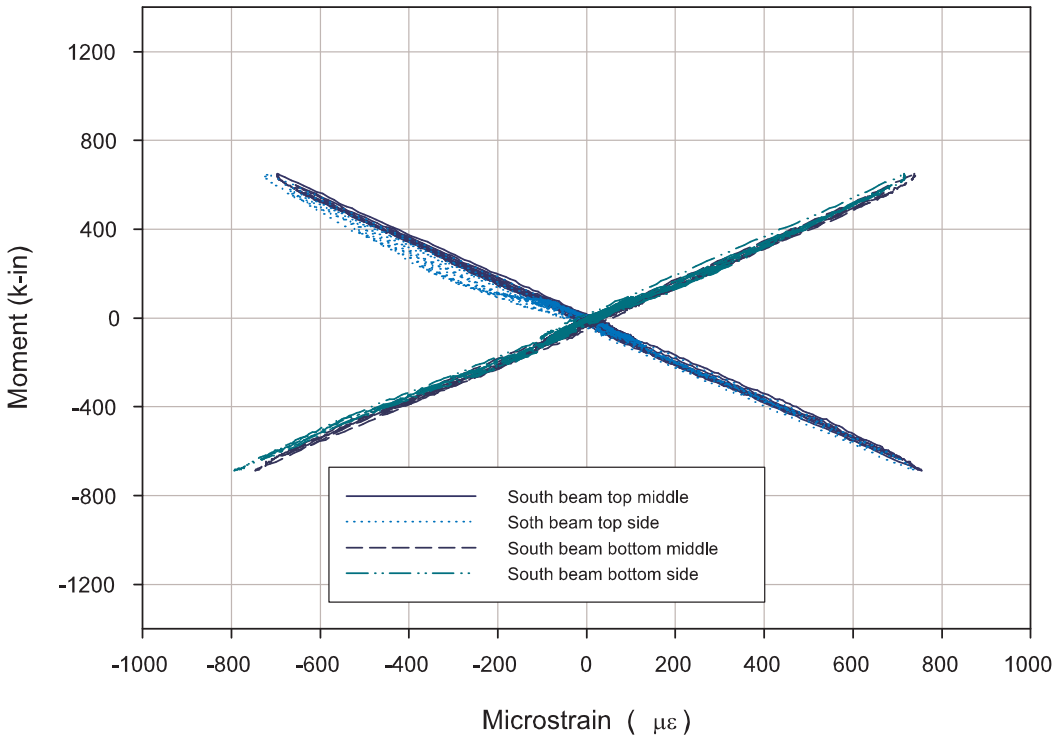

Figure B-47: Moment versus flange strain in south beam for steel tendon test II on 04/27/05.

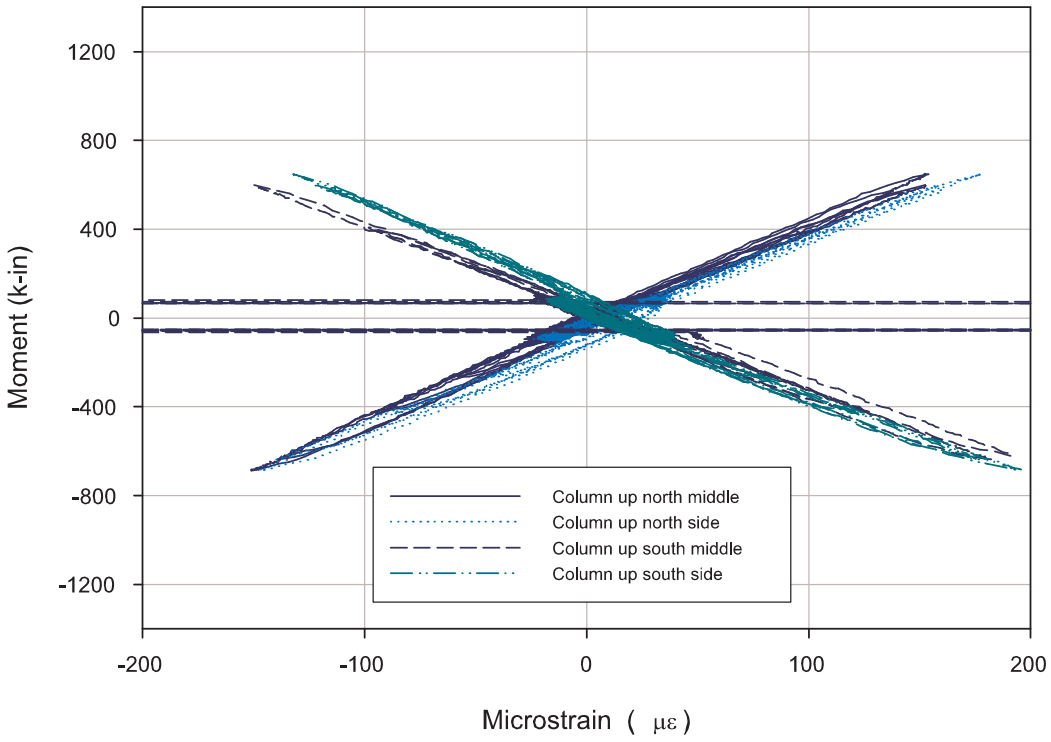

Figure B-48: Moment versus flange strain in upper portion of column for steel tendon test II on 04/27/05.

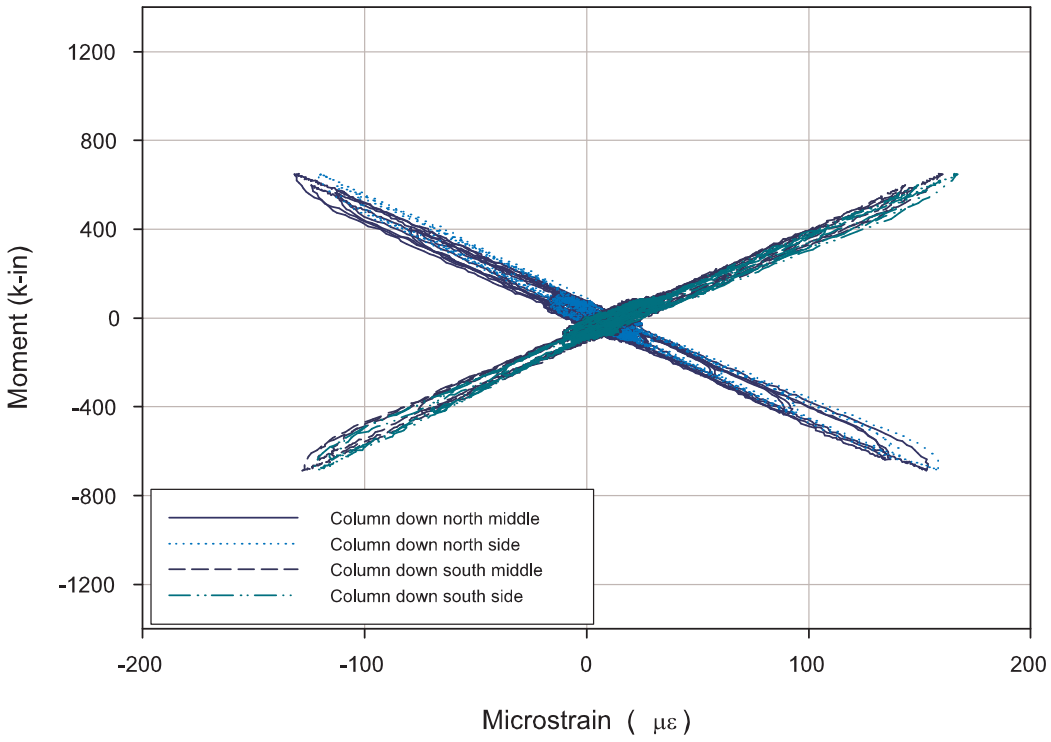

Figure B-49: Moment versus flange strain in lower portion of column for steel tendon test II on 04/27/05.

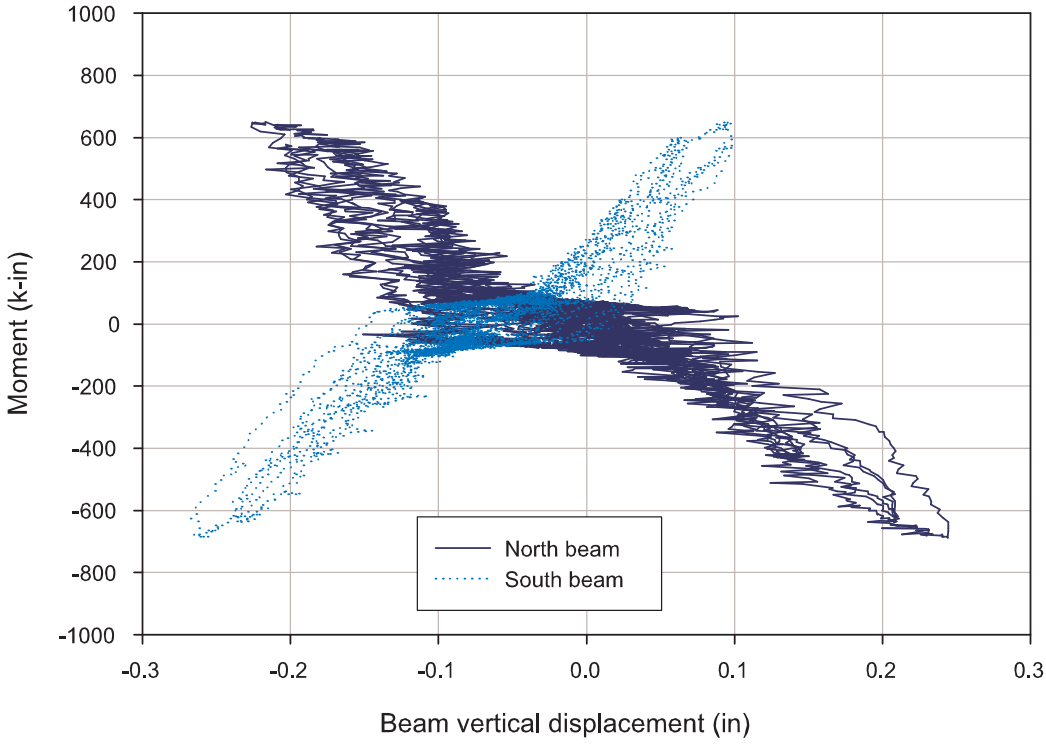

Figure B-50: Moment versus vertical displacement in beam for steel tendon test II on 04/27/05.

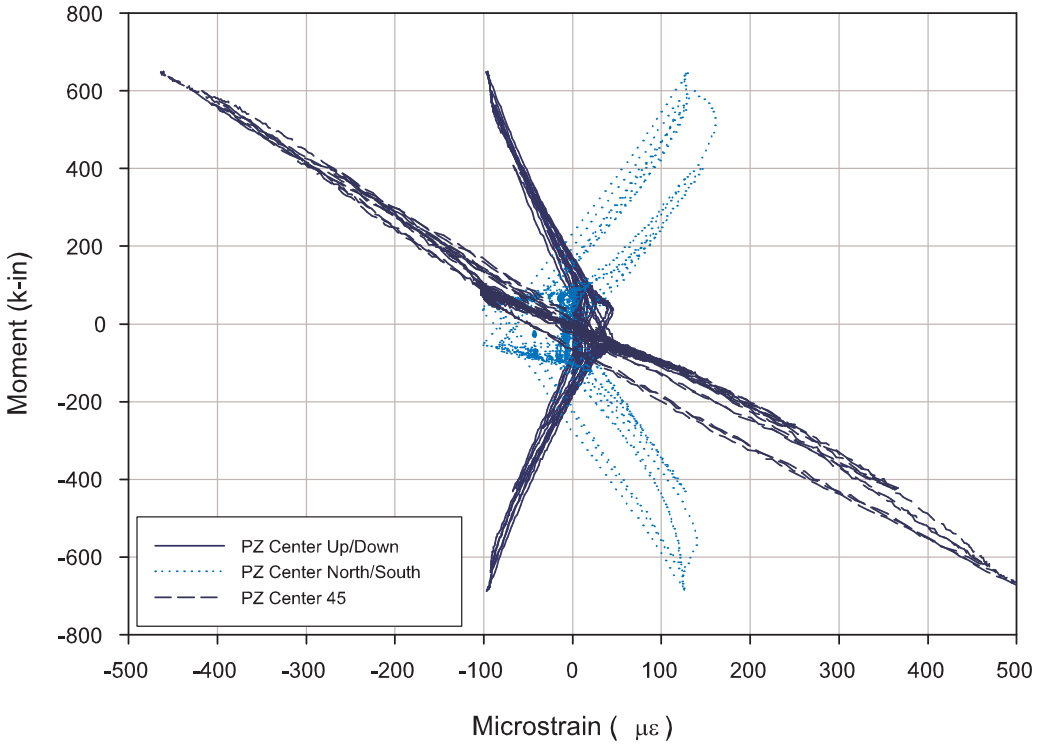

Figure B-51: Moment versus strain in center panel zone rosette for steel tendon test II on 04/27/05.

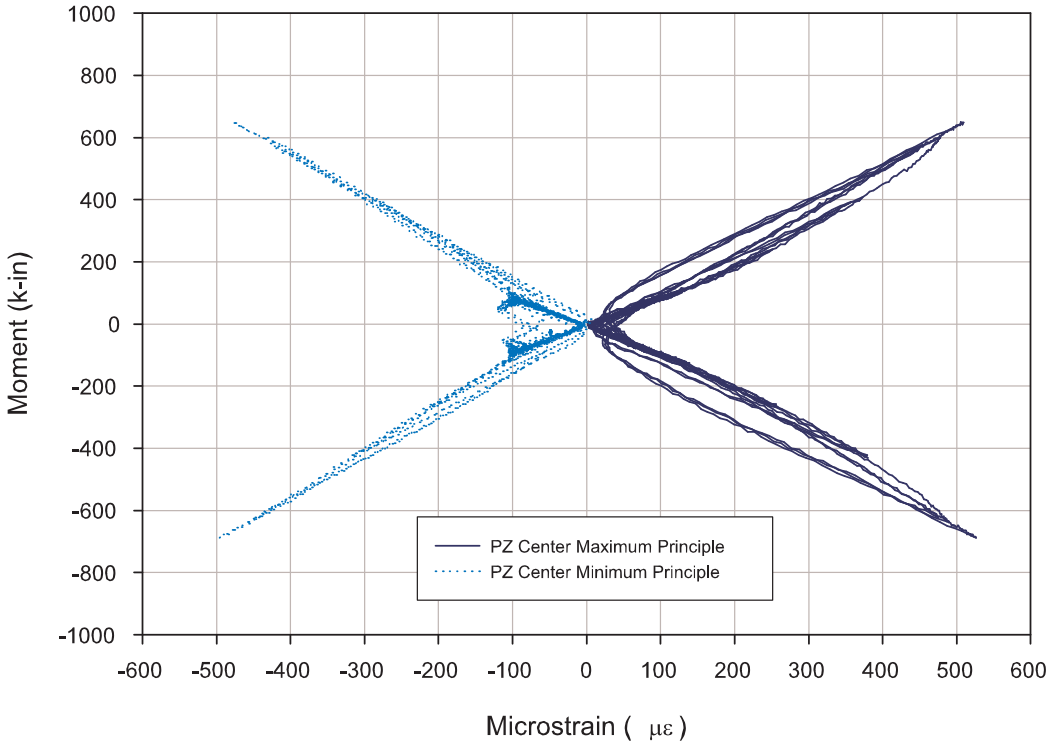

Figure B-52: Moment versus principle strains in center panel zone rosette for steel tendon test II on 04/27/05.

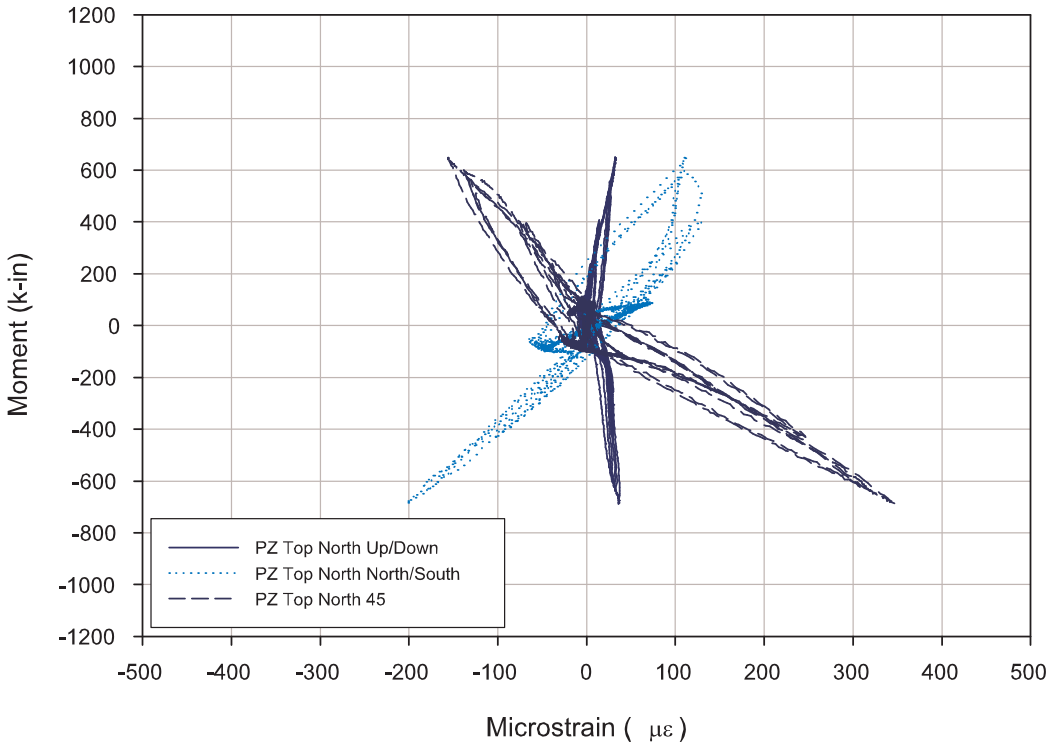

Figure B-53: Moment versus strain in top north panel zone rosette for steel tendon test II on 04/27/05.

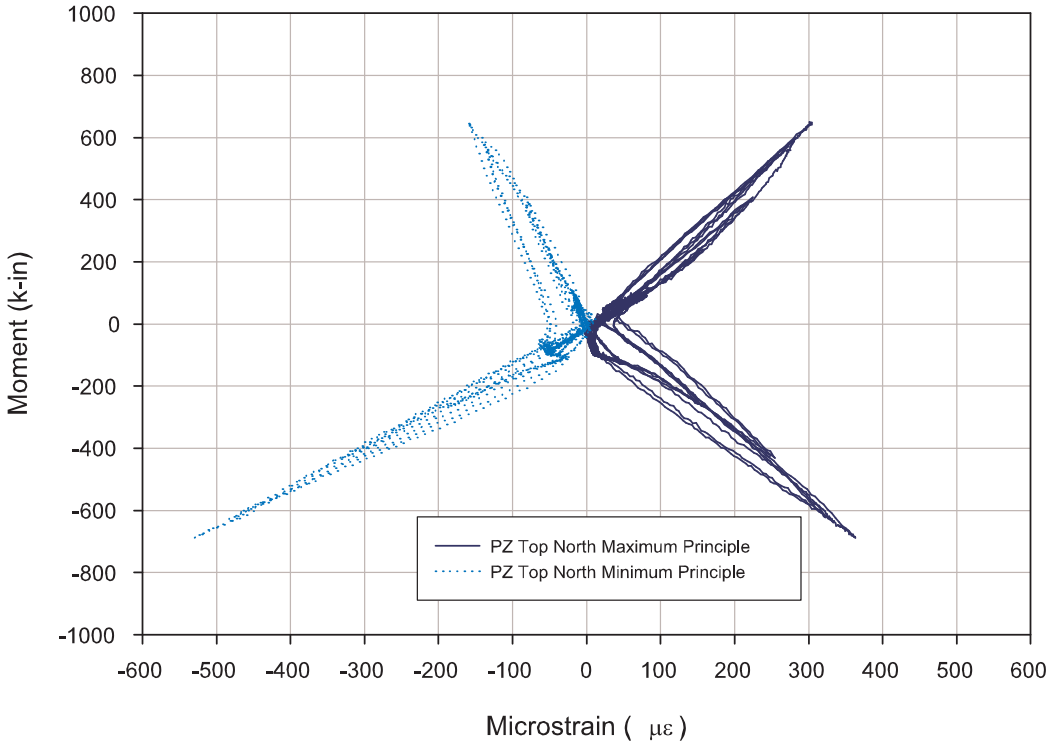

Figure B-54: Moment versus principle strains in top north panel zone rosette for steel tendon test II on 04/27/05.

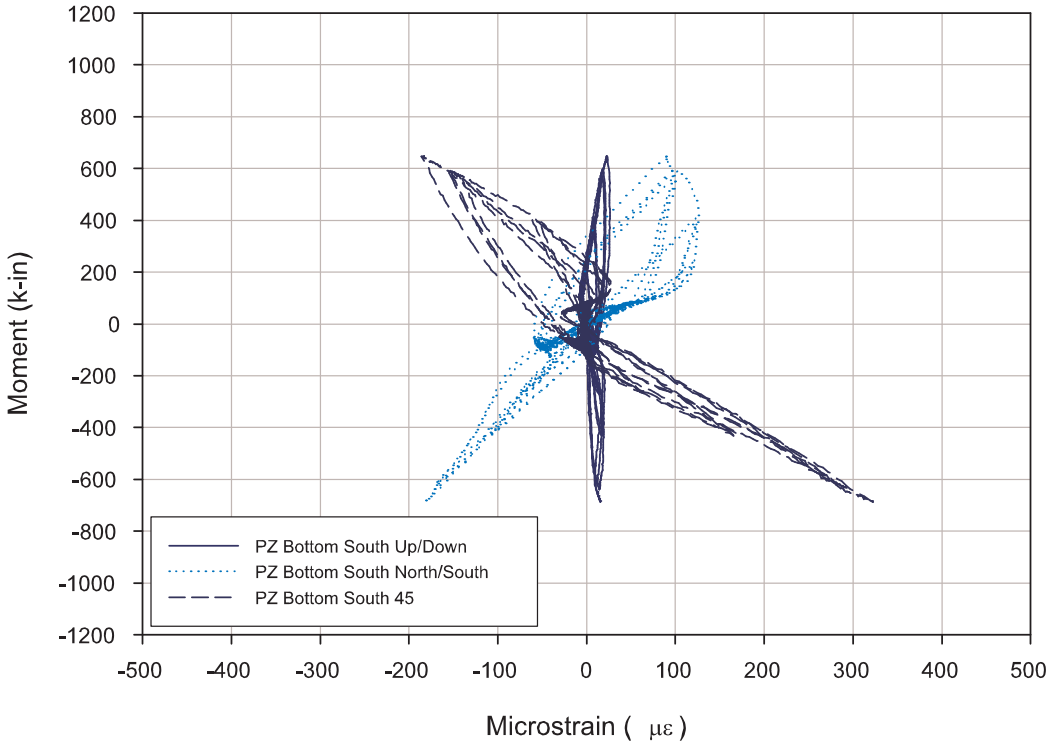

Figure B-55: Moment versus strain in bottom south panel zone rosette for steel tendon test II on 04/27/05.

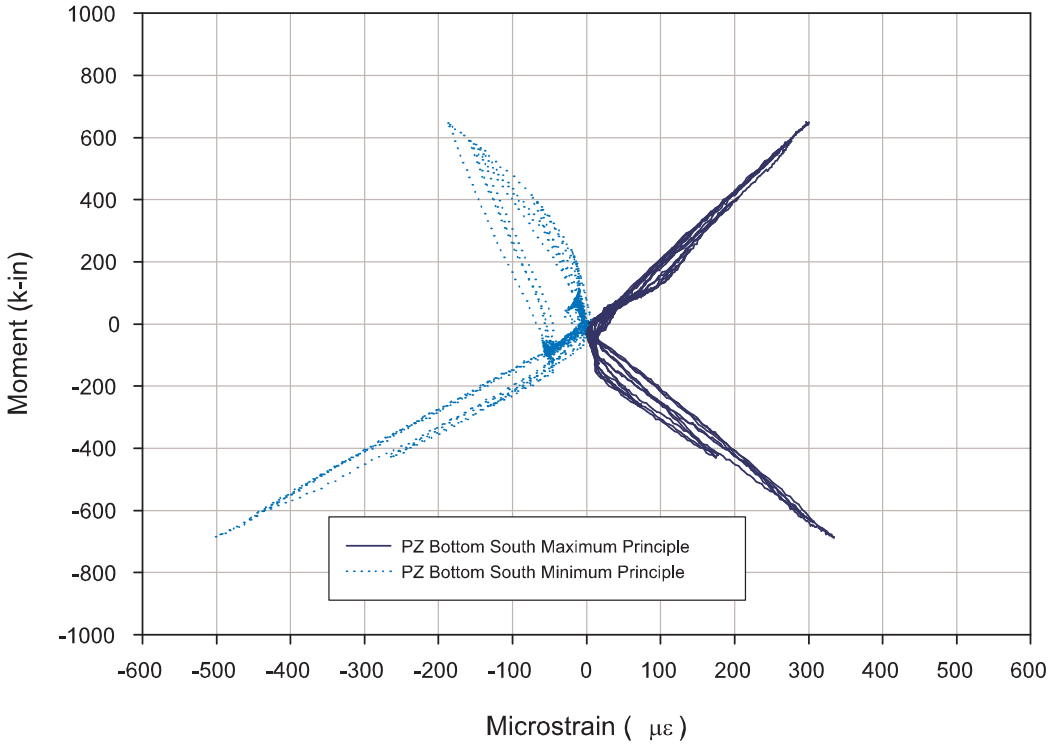

Figure B-56: Moment versus principle strains in bottom south panel zone rosette for steel tendon test II on 04/27/05.

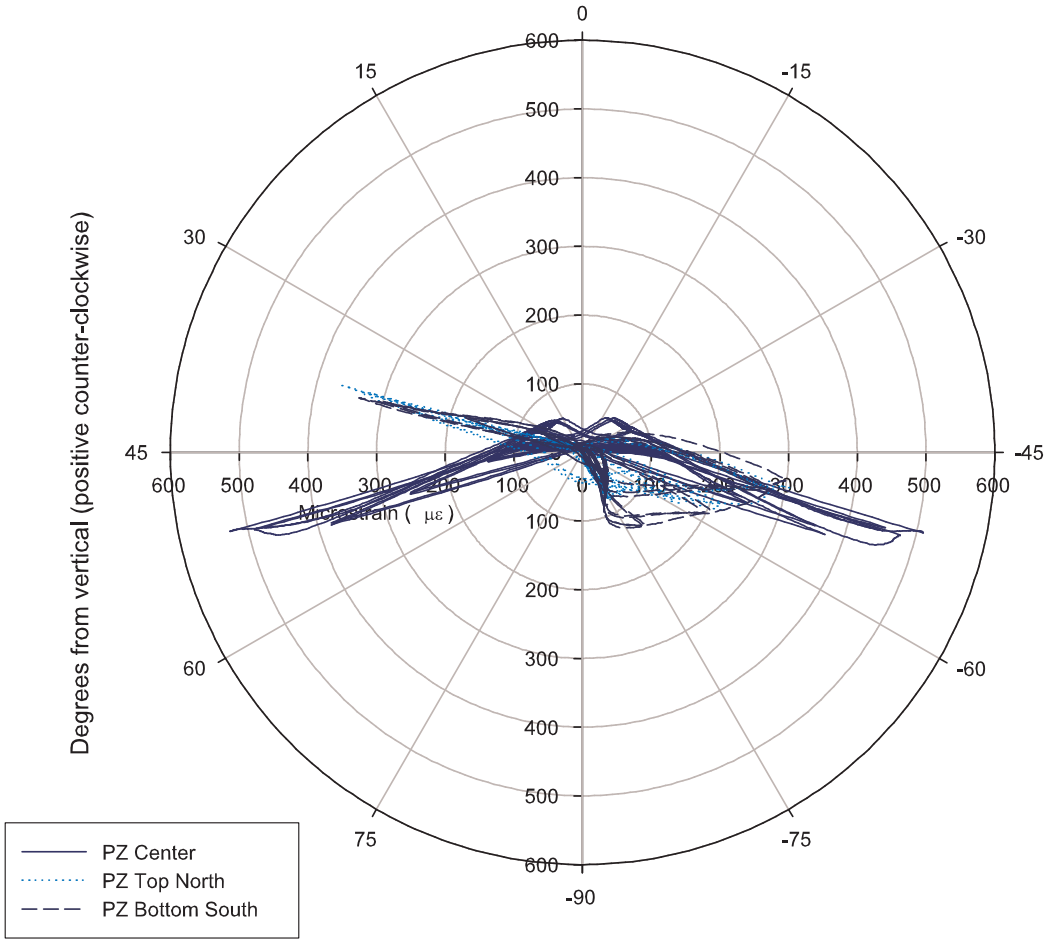

Figure B-57: Principle strain angles versus maximum principal strains in panel zone rosettes for steel tendon test II on 04/27/05.

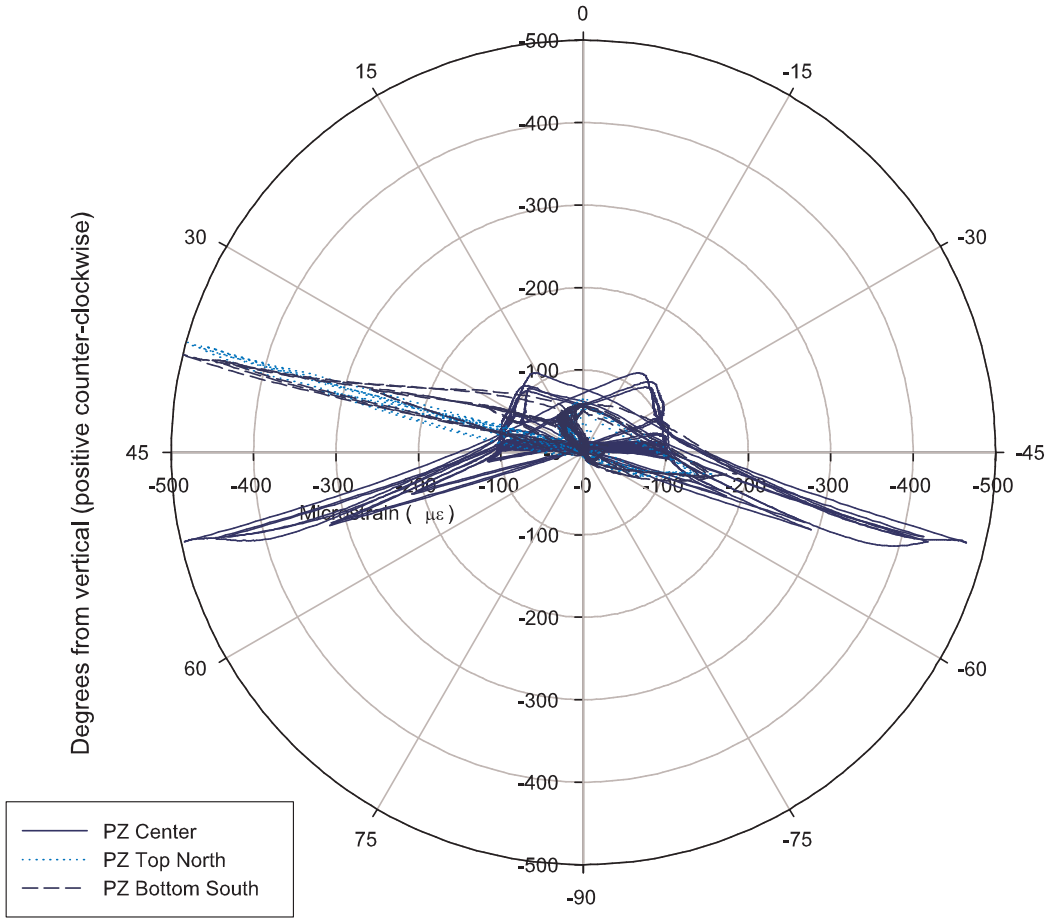

Figure B-58: Principle strain angles versus minimum principal strains in panel zone rosettes for steel tendon test II on 04/27/05.

B.3 Test III on 04/29/05

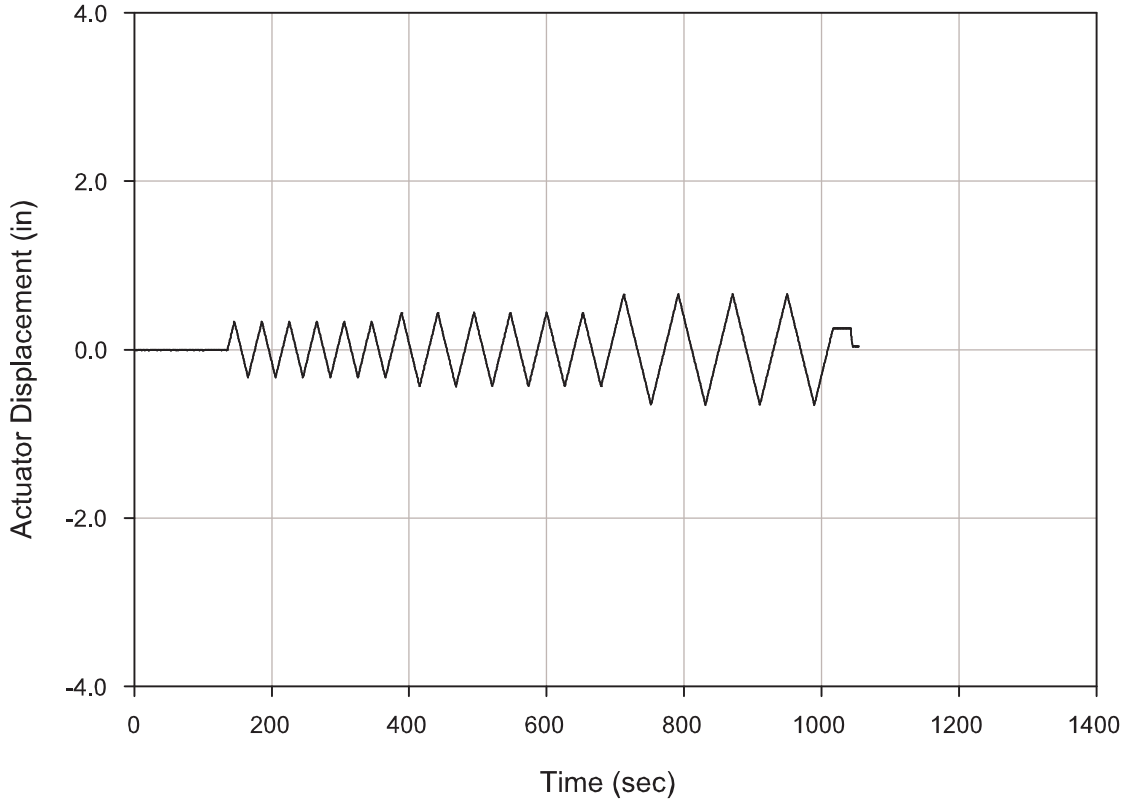

Figure B-59: Actuator displacement history for steel tendon test III on 04/29/05.

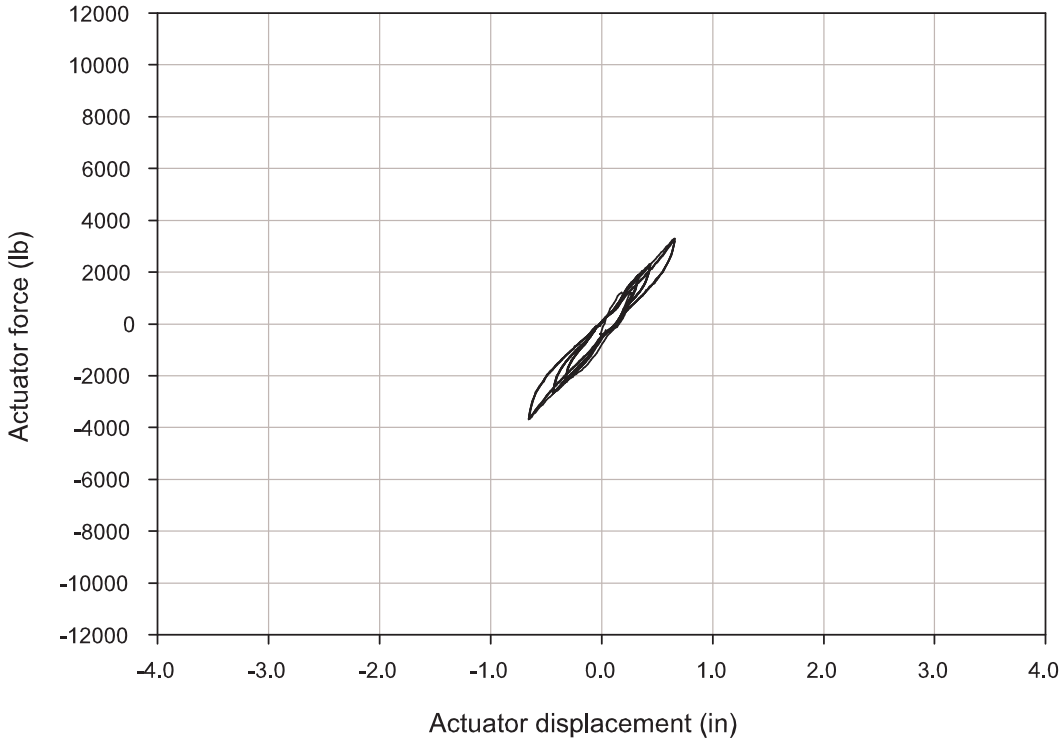

Figure B-60: Actuator force versus actuator displacement for steel tendon test III on 04/29/05.

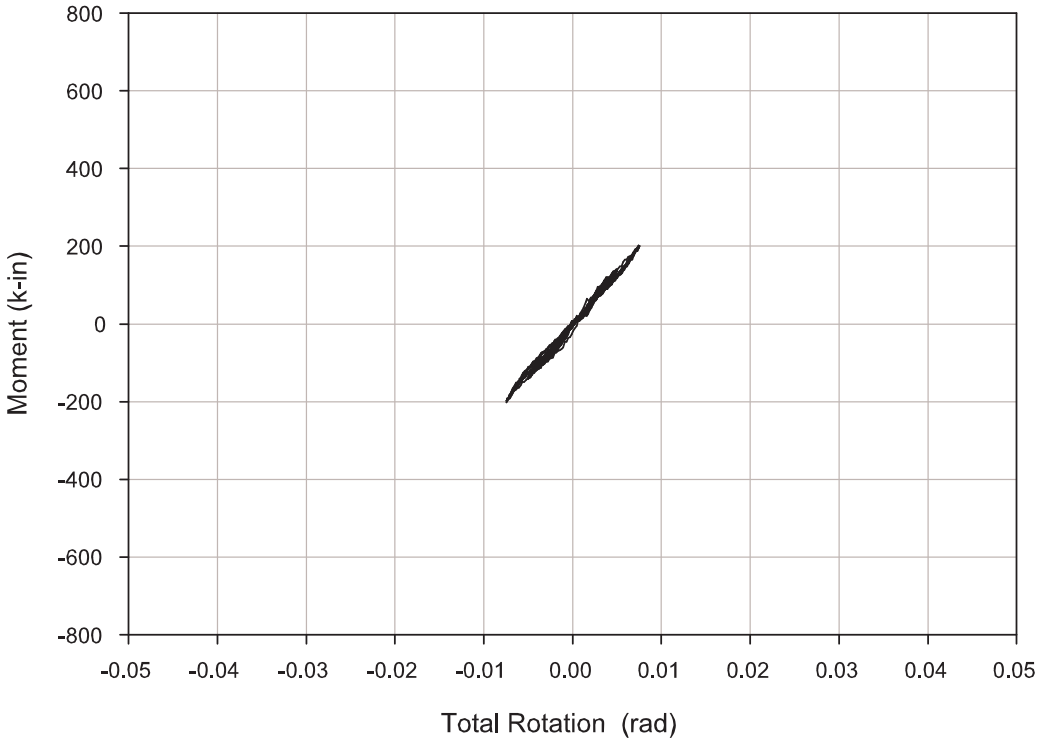

Figure B-61: Moment versus total rotation for steel tendon test III on 04/29/05.

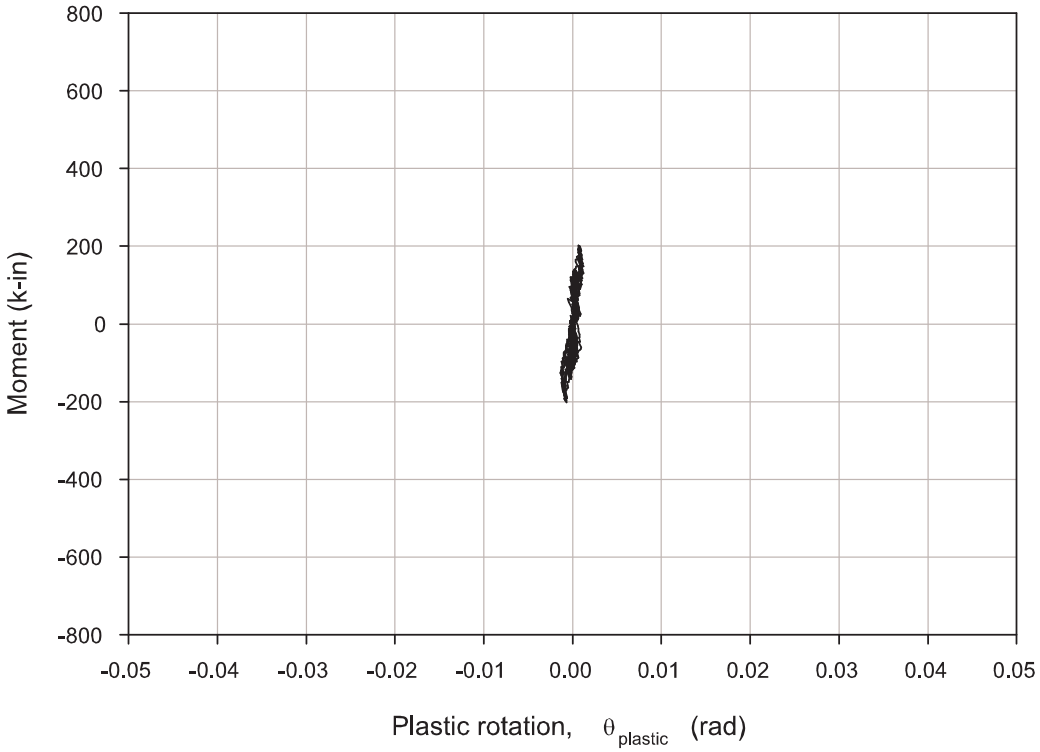

Figure B-62: Moment versus plastic rotation for steel tendon test III on 04/29/05.

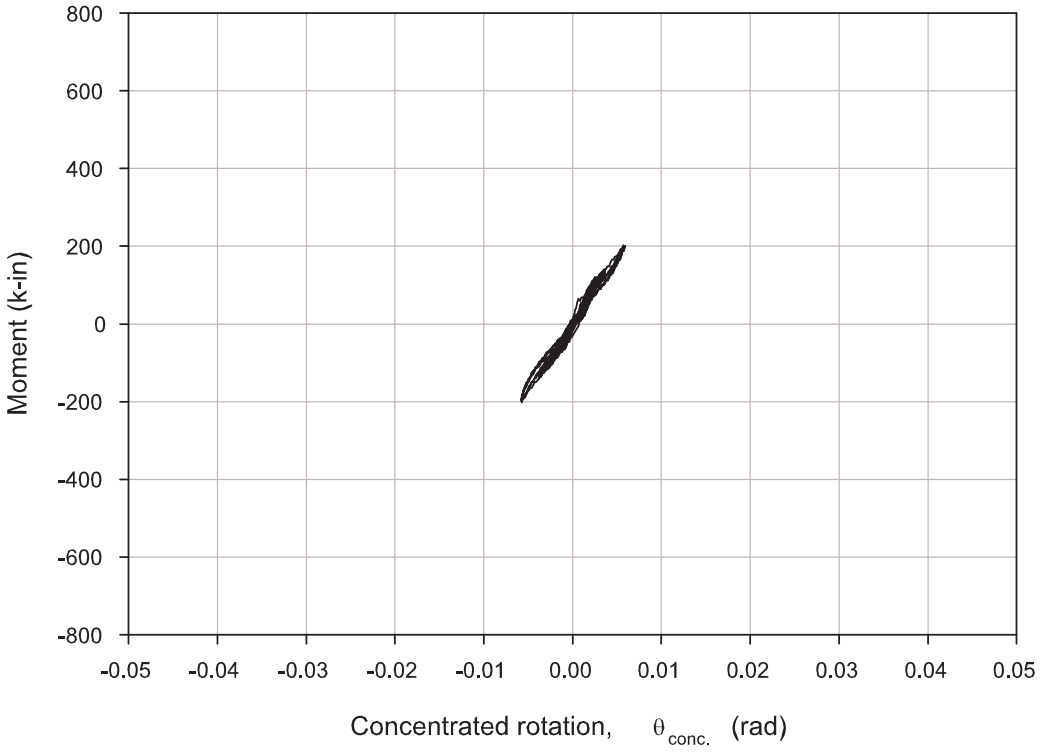

Figure B-63: Moment versus concentrated rotation for steel tendon test III on 04/29/05.

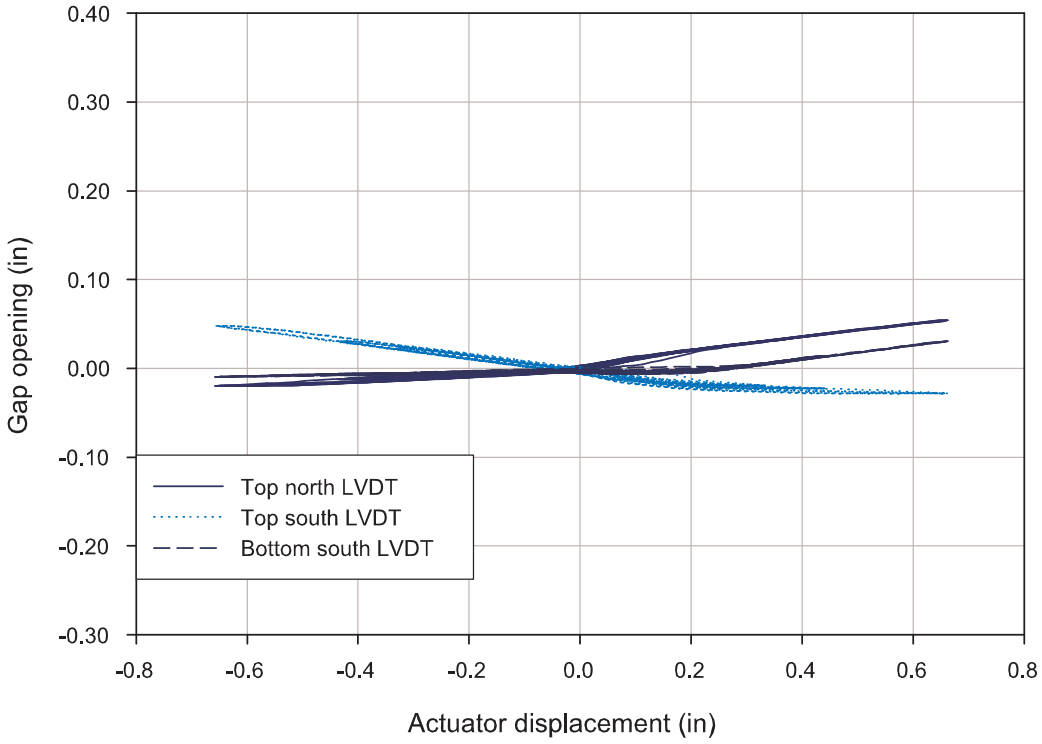

Figure B-64: Gap opening versus actuator displacement for steel tendon test III on 04/29/05.

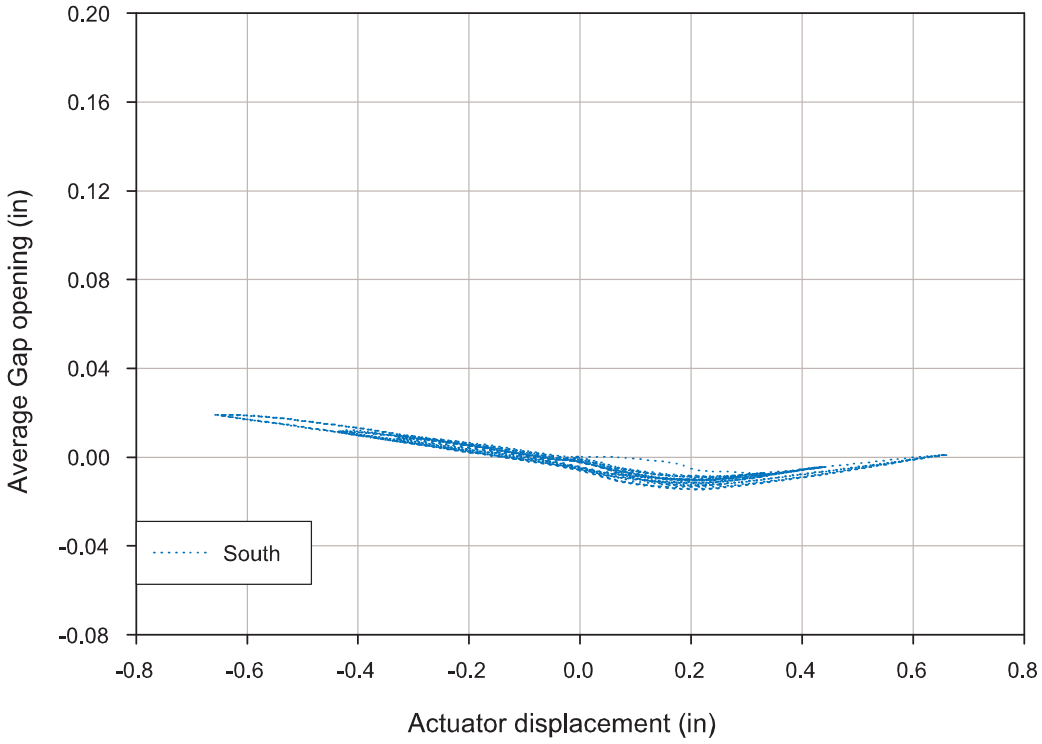

Figure B-65: Average gap opening versus actuator displacement for steel tendon test III on 04/29/05.

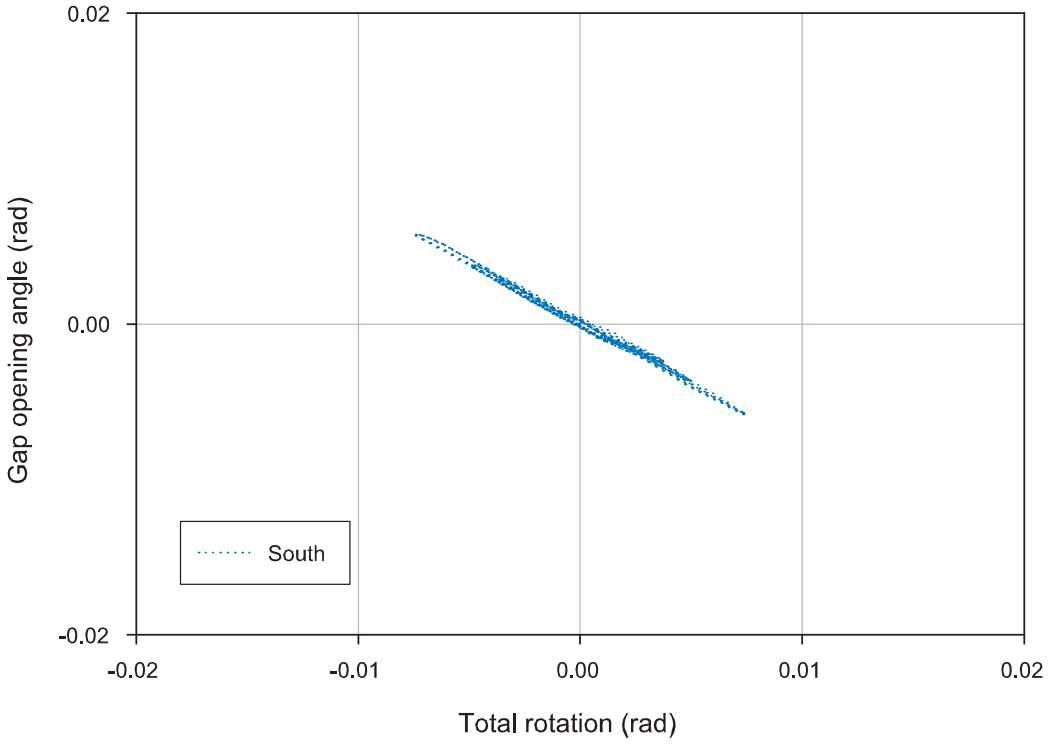

Figure B-66: Gap opening angle versus total rotation for steel tendon test III on 04/29/05.

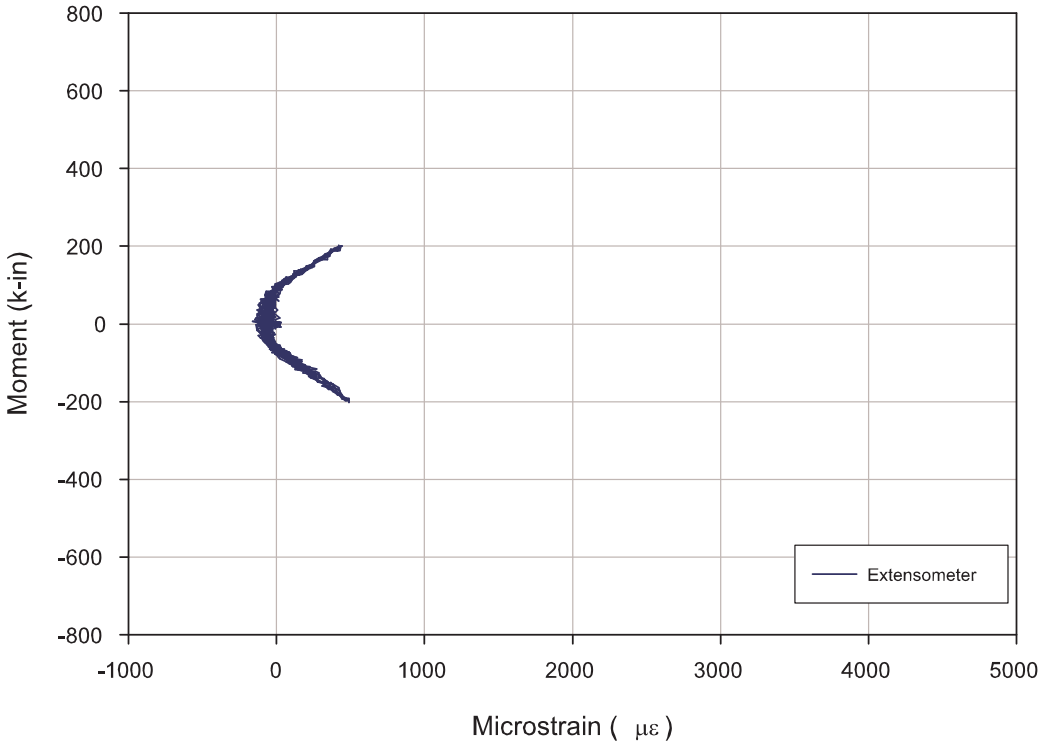

Figure B-67: Moment versus strain in Down West steel tendon for steel tendon test III on 04/29/05.

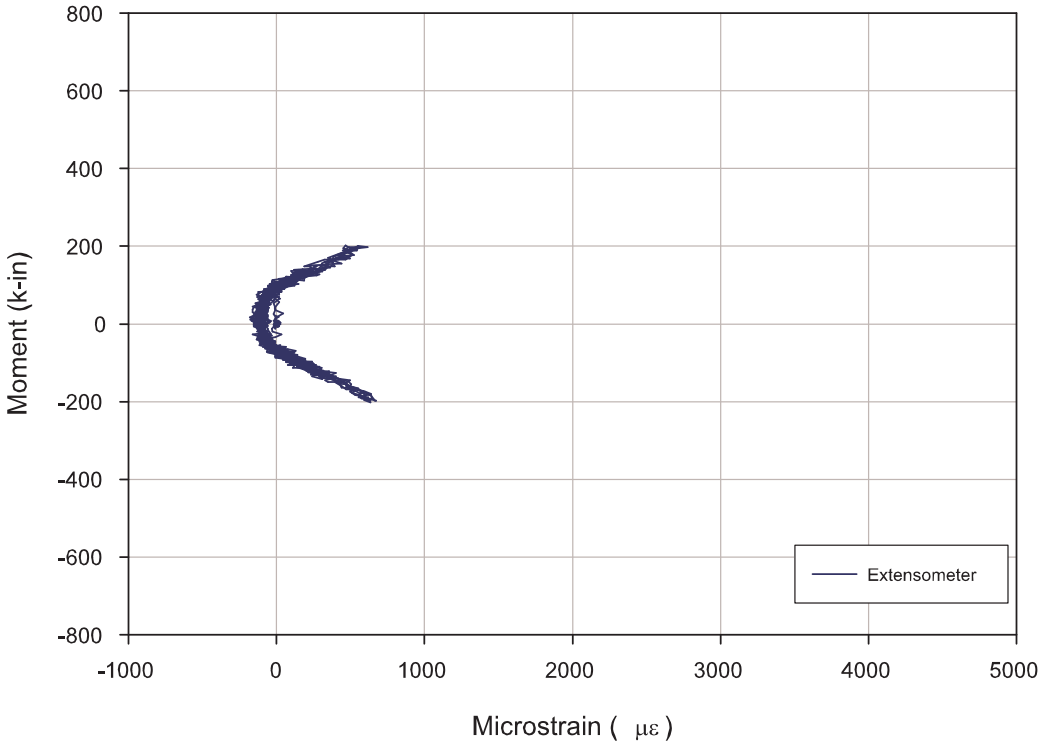

Figure B-68: Moment versus strain in Down East steel tendon for steel tendon test III on 04/29/05.

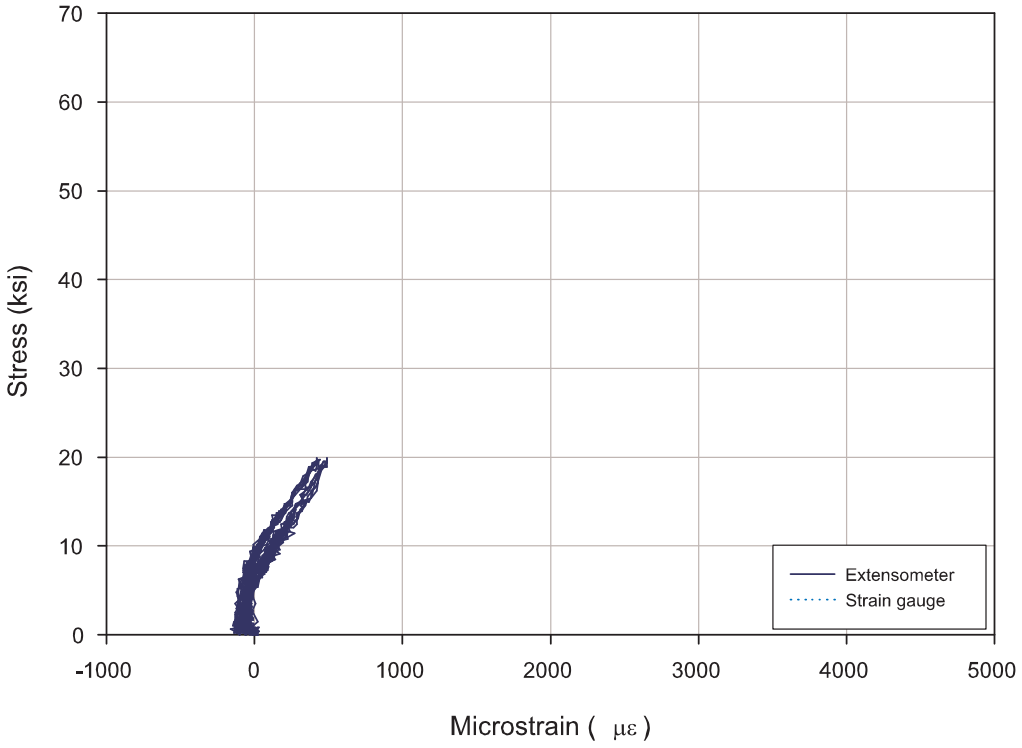

Figure B-69: Stress versus strain in Down West steel tendon for steel tendon test III on 04/29/05.

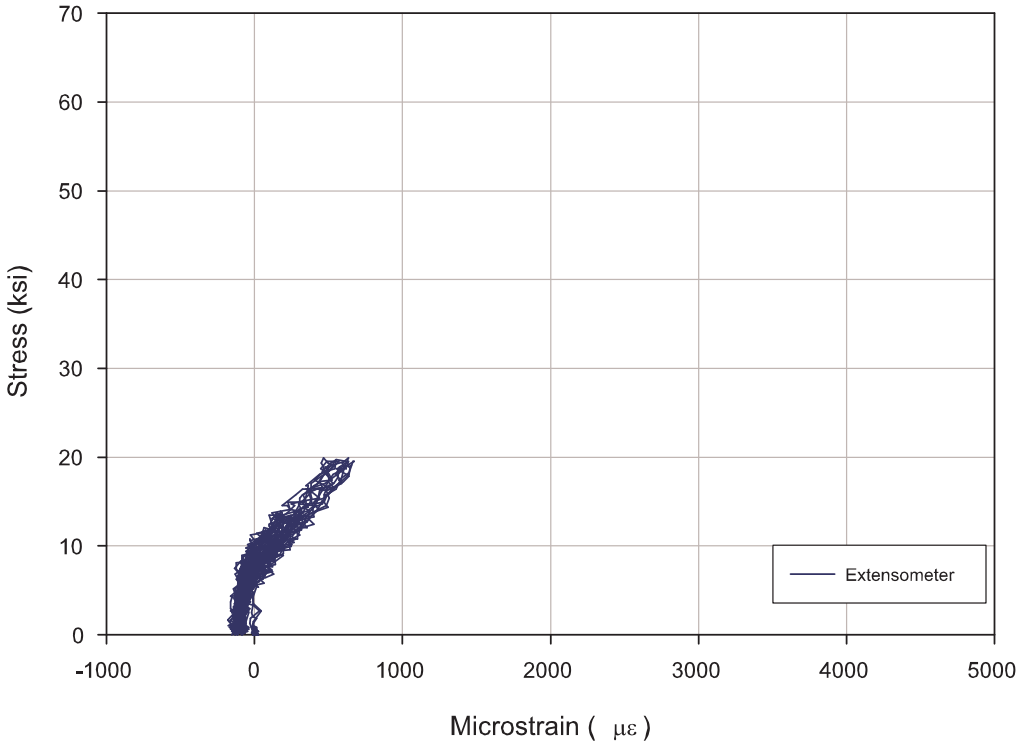

Figure B-70: Stress versus strain in Down East steel tendon for steel tendon test III on 04/29/05.

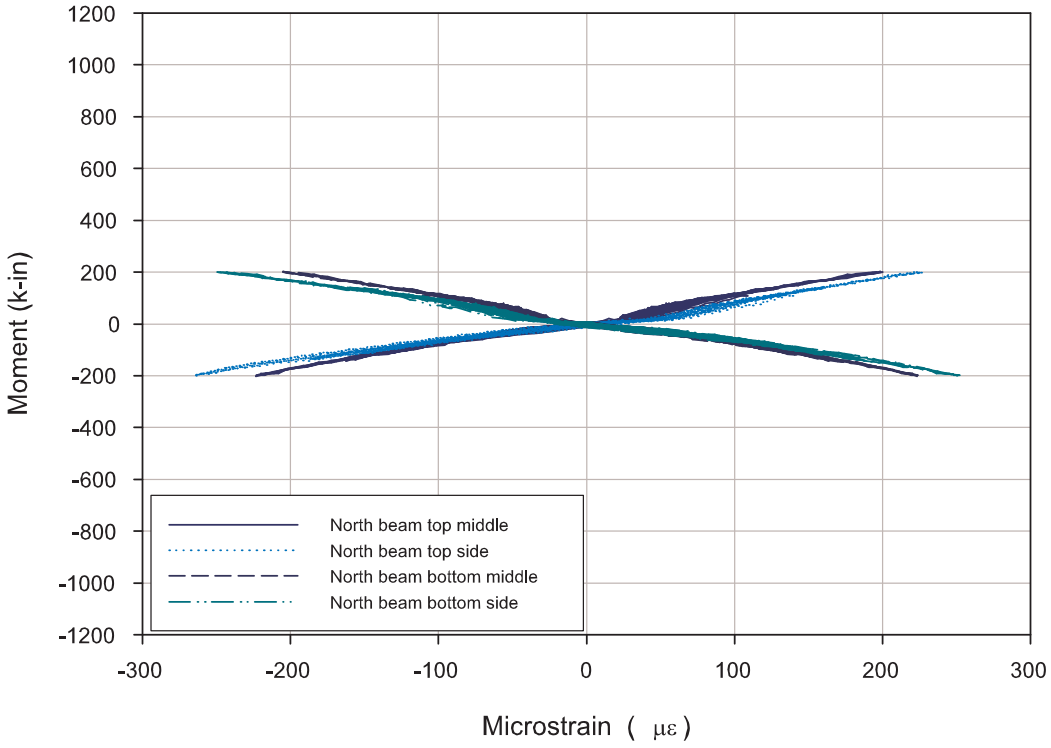

Figure B-71: Moment versus flange strain in north beam for steel tendon test III on 04/29/05.

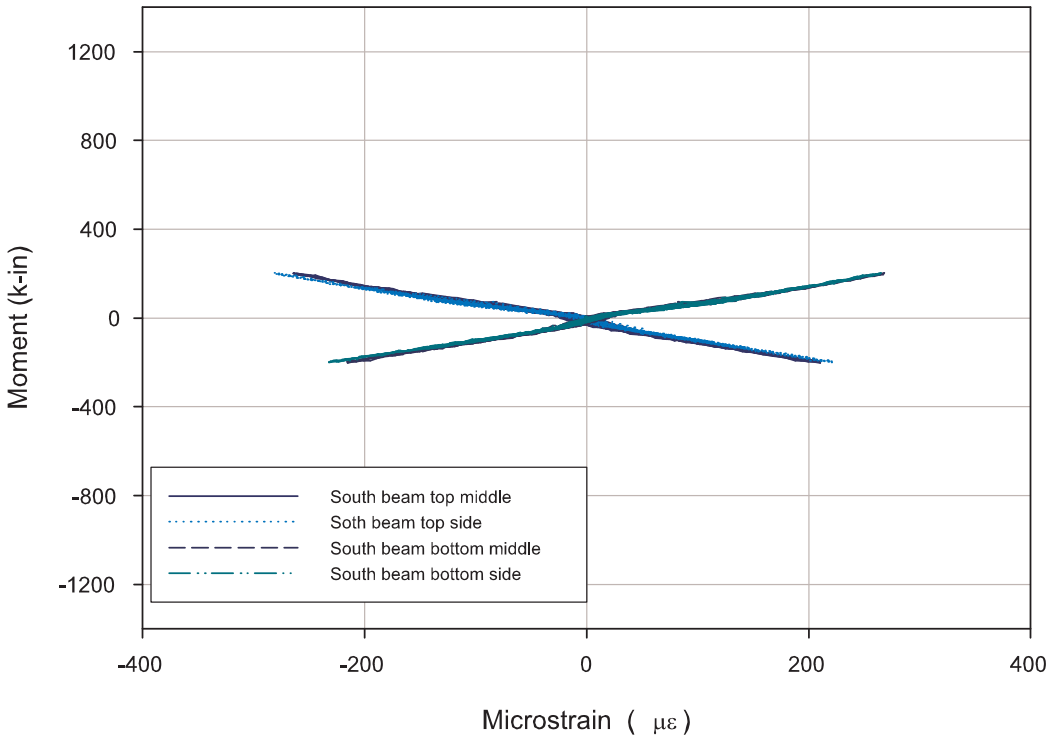

Figure B-72: Moment versus flange strain in south beam for steel tendon test III on 04/29/05.

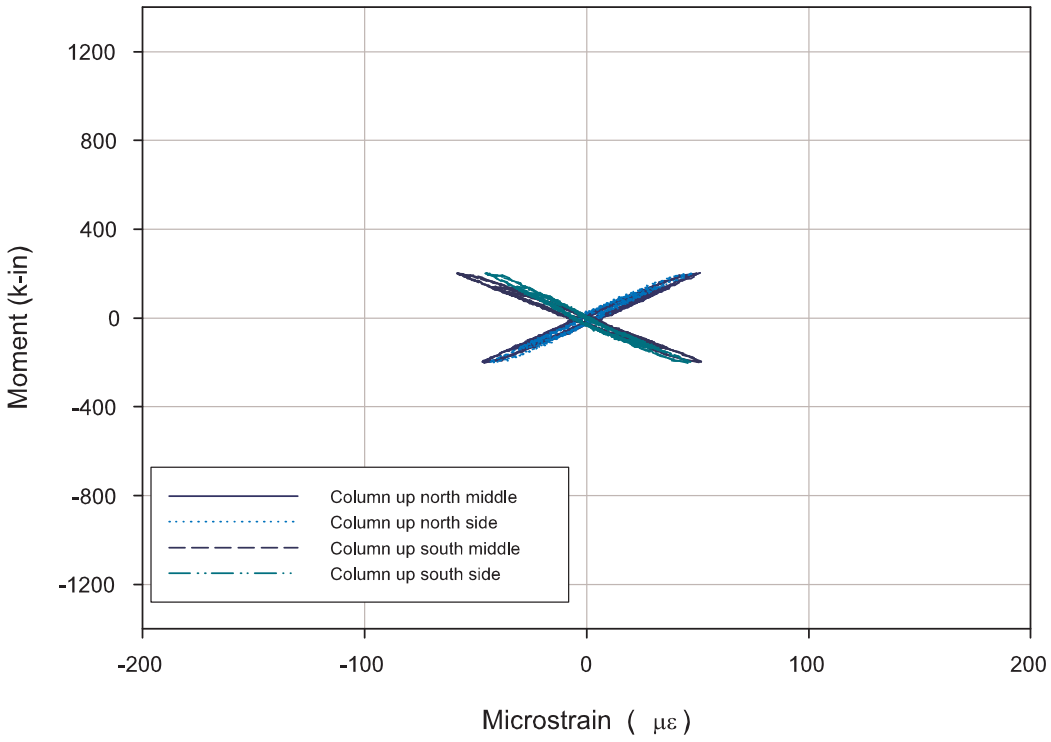

Figure B-73: Moment versus flange strain in upper portion of column for steel tendon test III on 04/29/05.

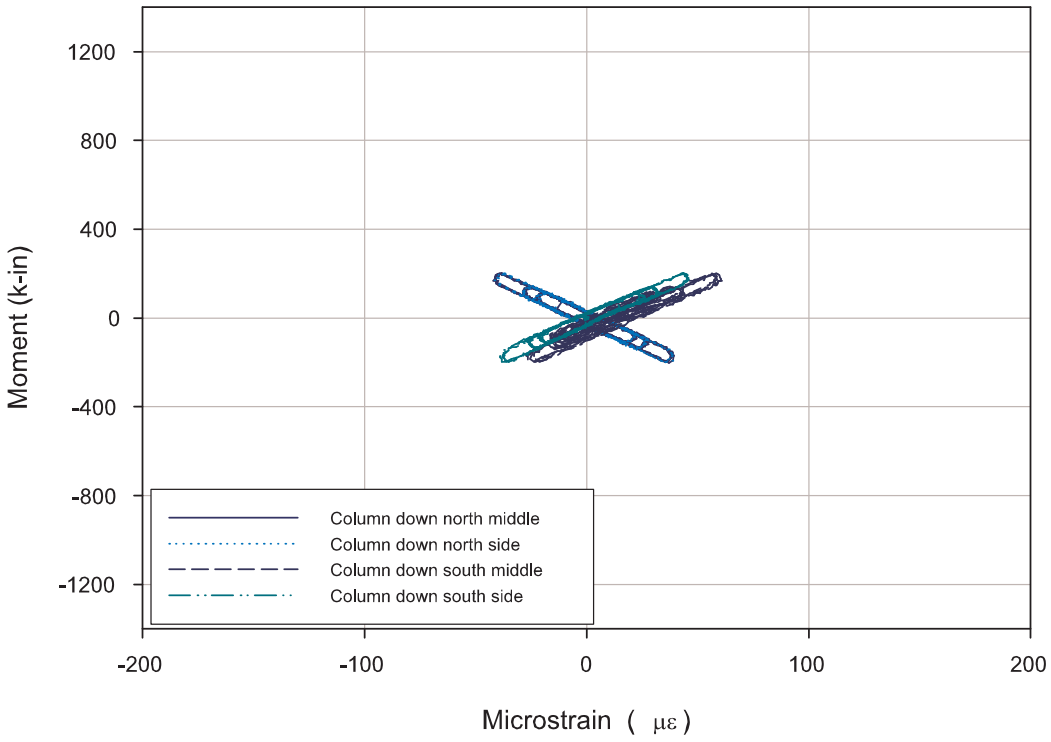

Figure B-74: Moment versus flange strain in lower portion of column for steel tendon test III on 04/29/05.

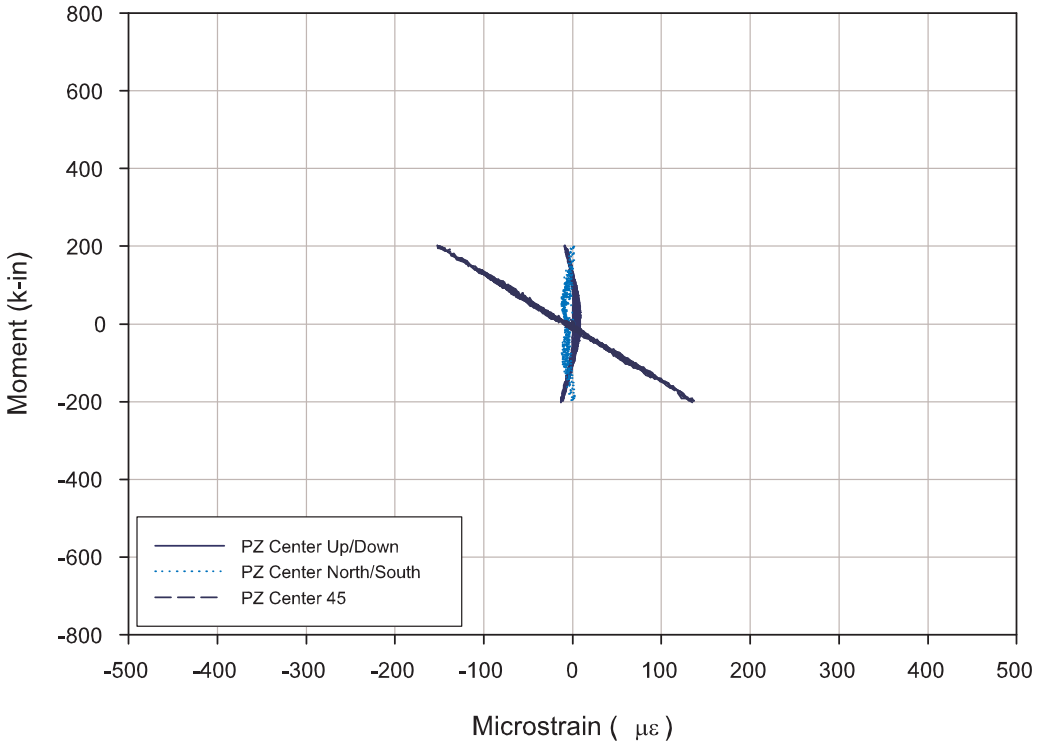

Figure B-75: Moment versus strain in center panel zone rosette for steel tendon test III on 04/29/05.

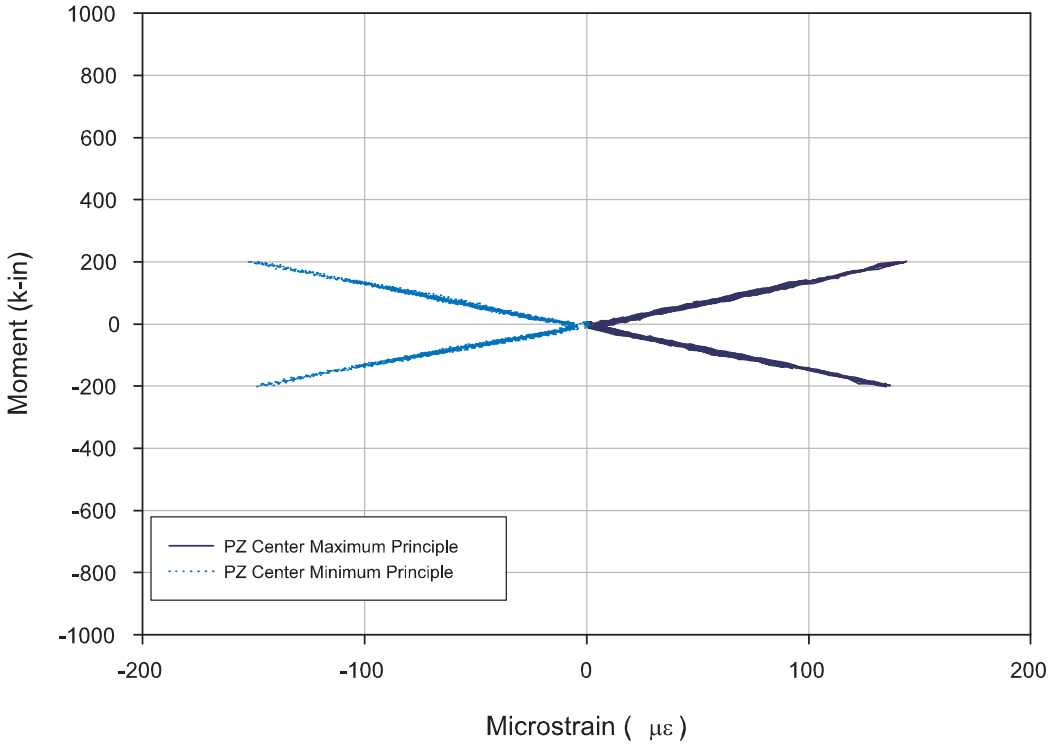

Figure B-76: Moment versus principle strains in center panel zone rosette for steel tendon test III on 04/29/05.

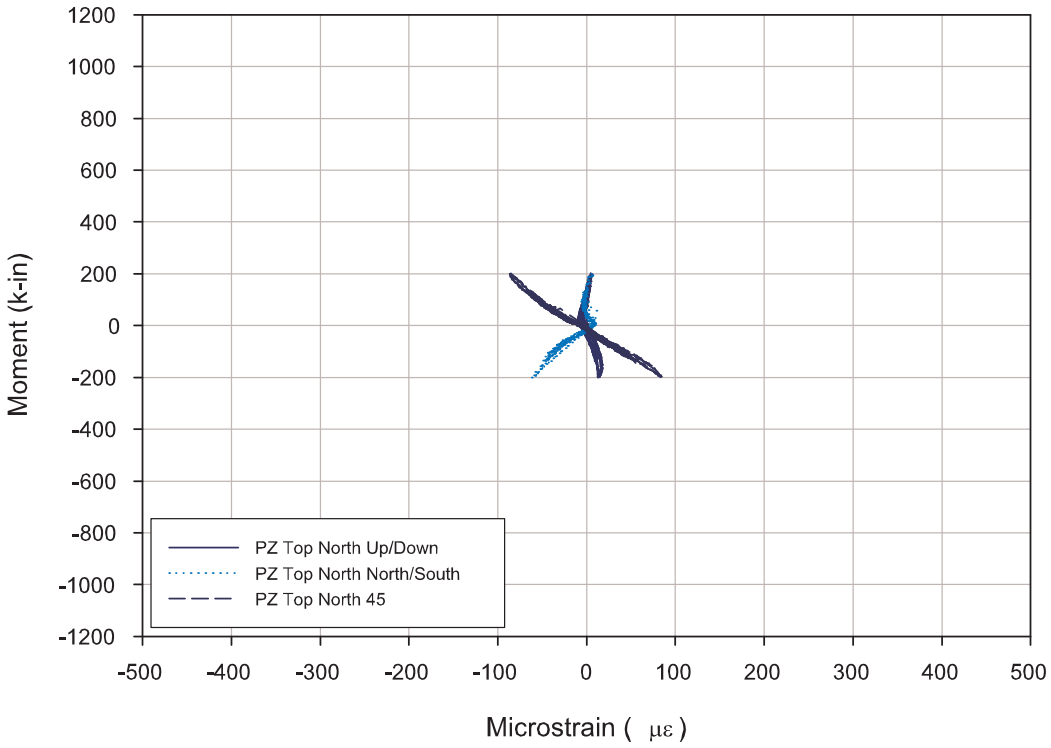

Figure B-77: Moment versus strain in top north panel zone rosette for steel tendon test III on 04/29/05.

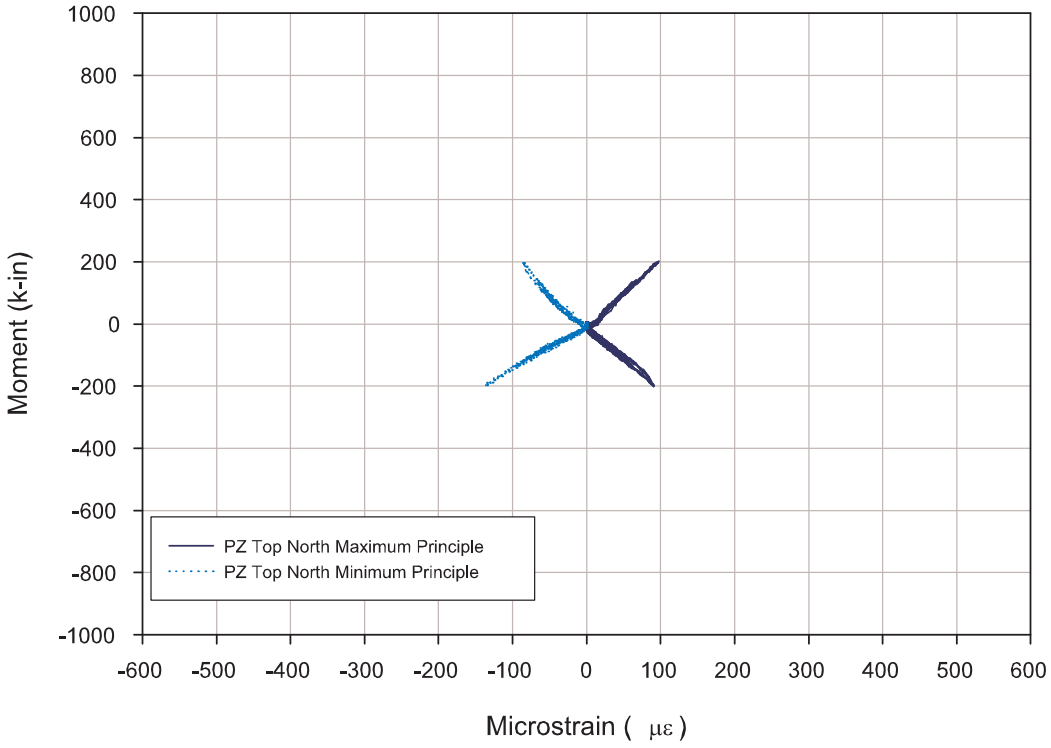

Figure B-78: Moment versus principle strains in top north panel zone rosette for steel tendon test III on 04/29/05.

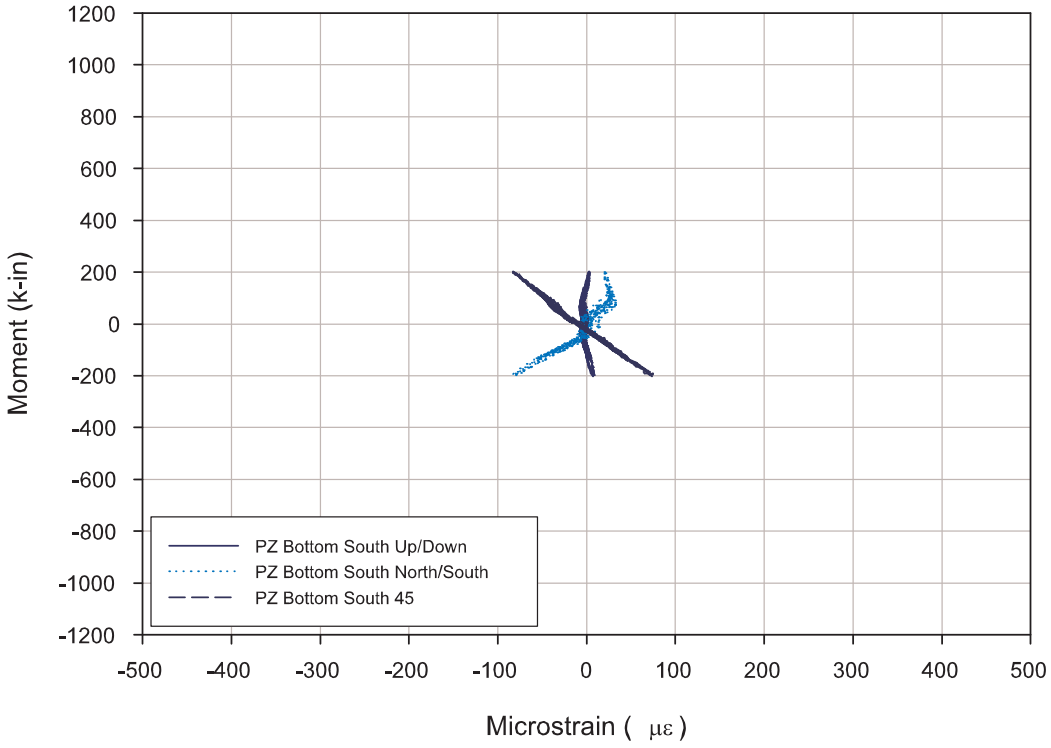

Figure B-79: Moment versus strain in bottom south panel zone rosette for steel tendon test III on 04/29/05.

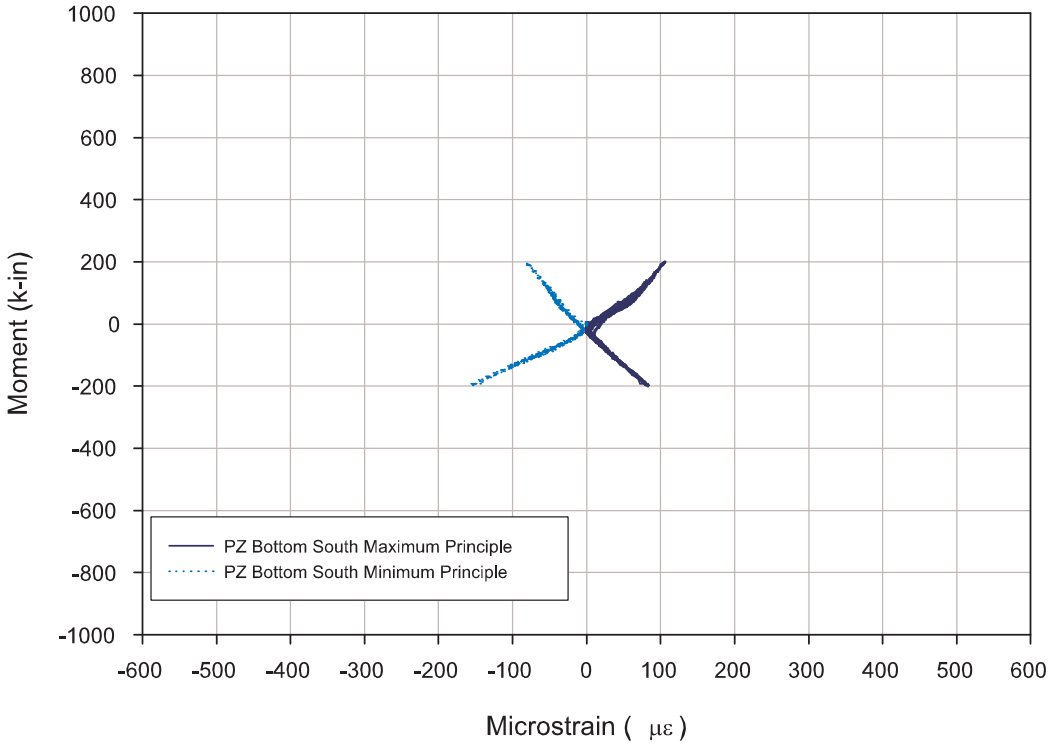

Figure B-80: Moment versus principle strains in bottom south panel zone rosette for steel tendon test III on 04/29/05.

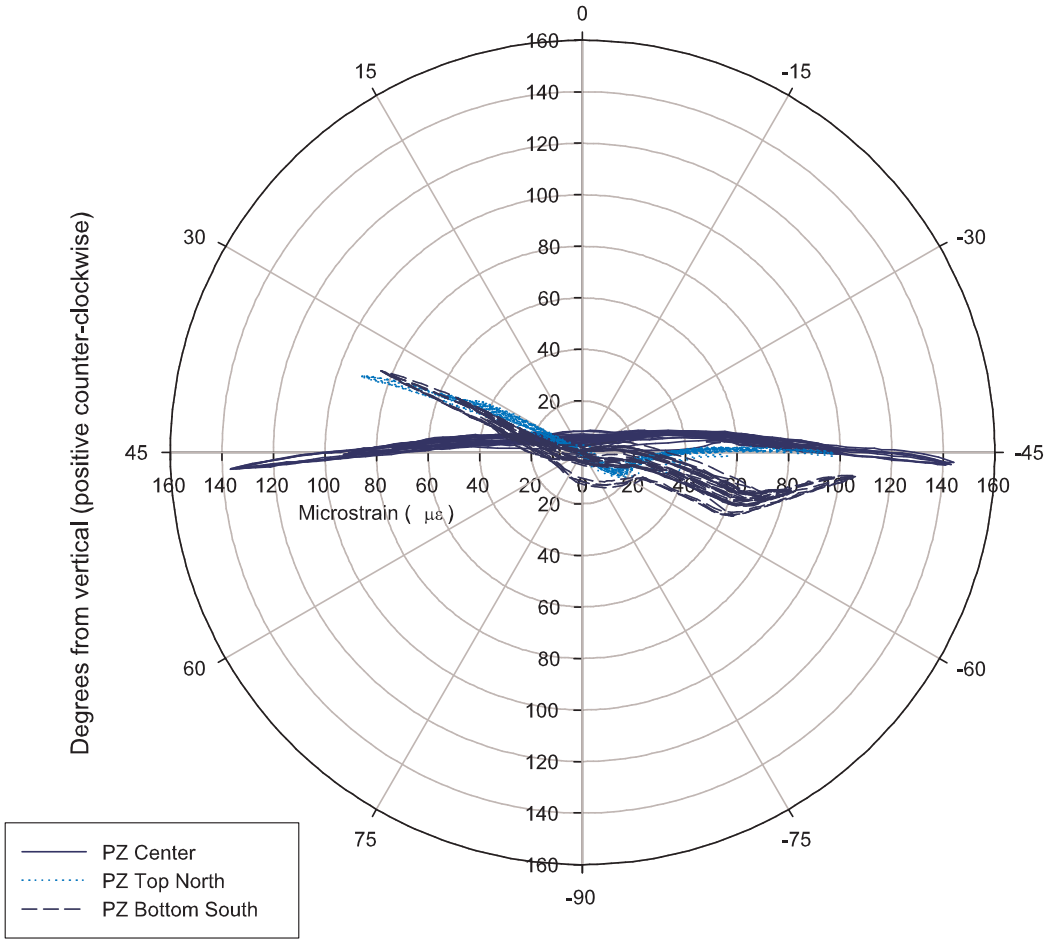

Figure B-81: Principle strain angles versus maximum principal strains in panel zone rosettes for steel tendon test III on 04/29/05.

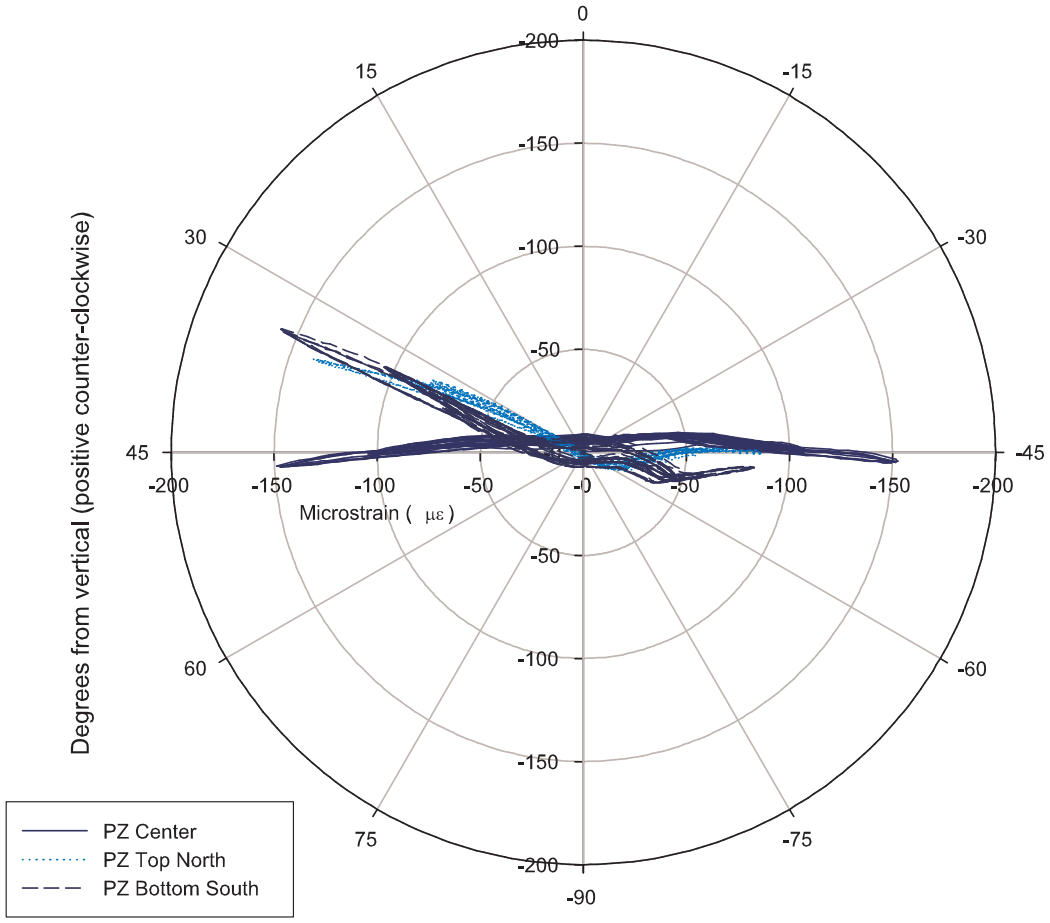

Figure B-82: Principle strain angles versus minimum principal strains in panel zone rosettes for steel tendon test III on 04/29/05.

APPENDIX C

NITINOL TENDON TEST DATA

C.1 Initial testing

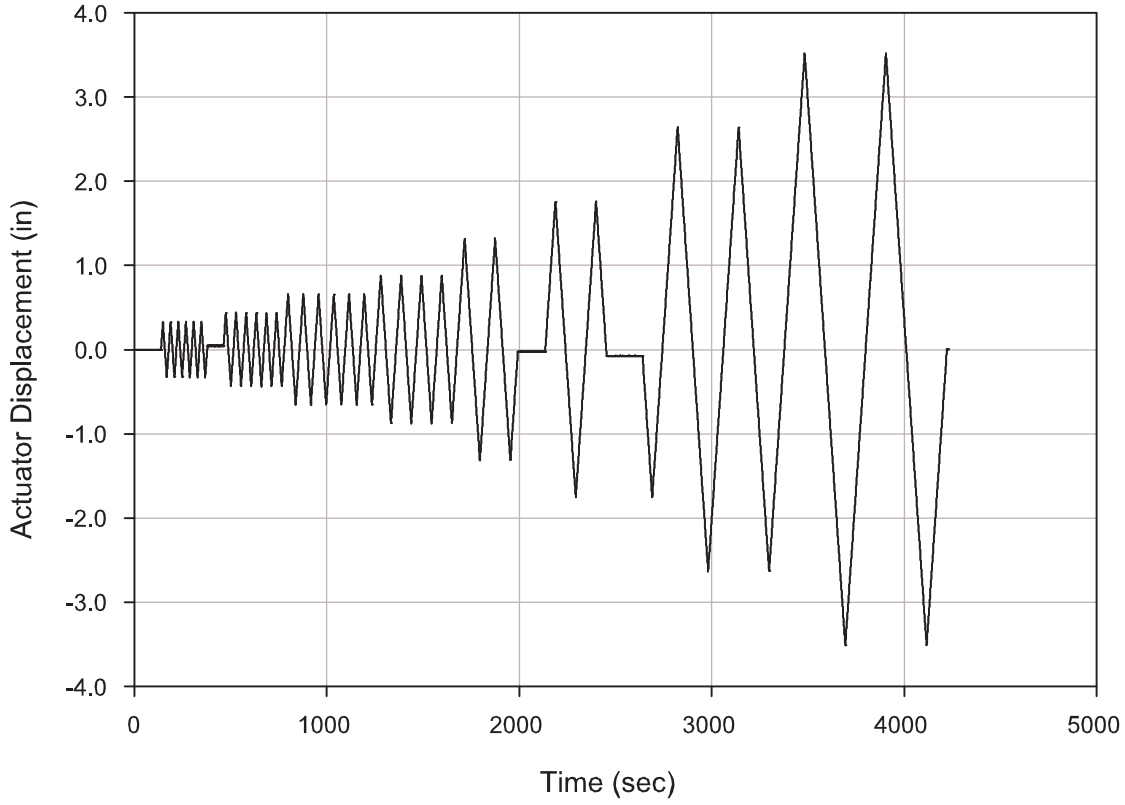

Figure C-1: Actuator displacement history for Nitinol tendon test.

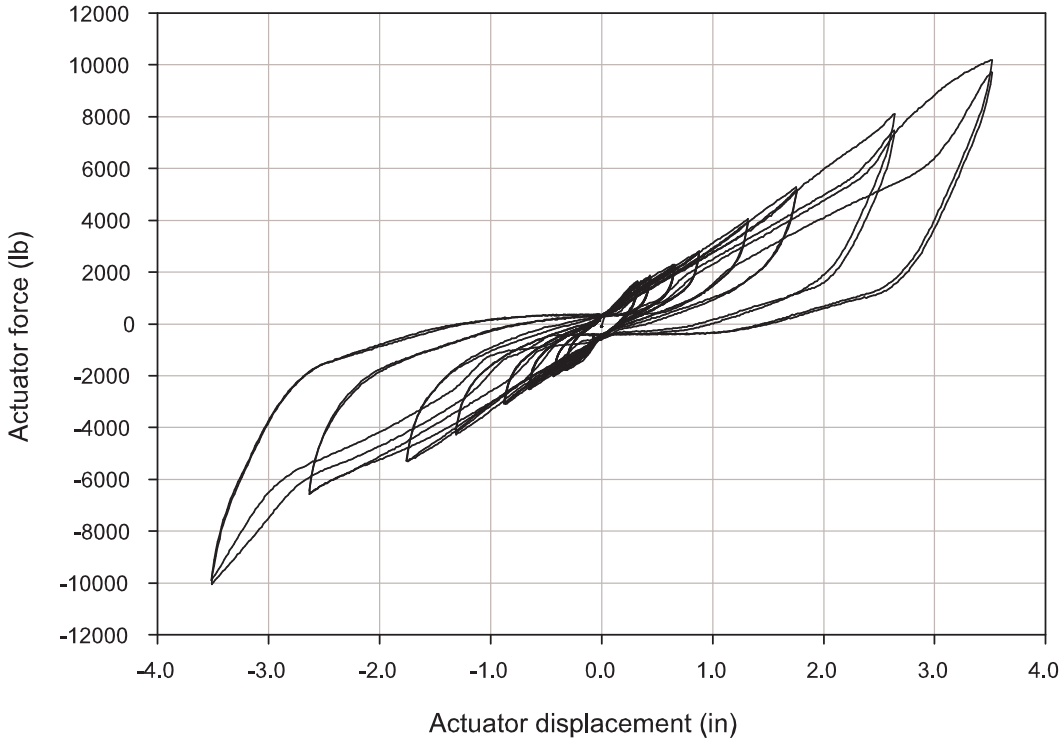

Figure C-2: Actuator force versus actuator displacement for Nitinol tendon test.

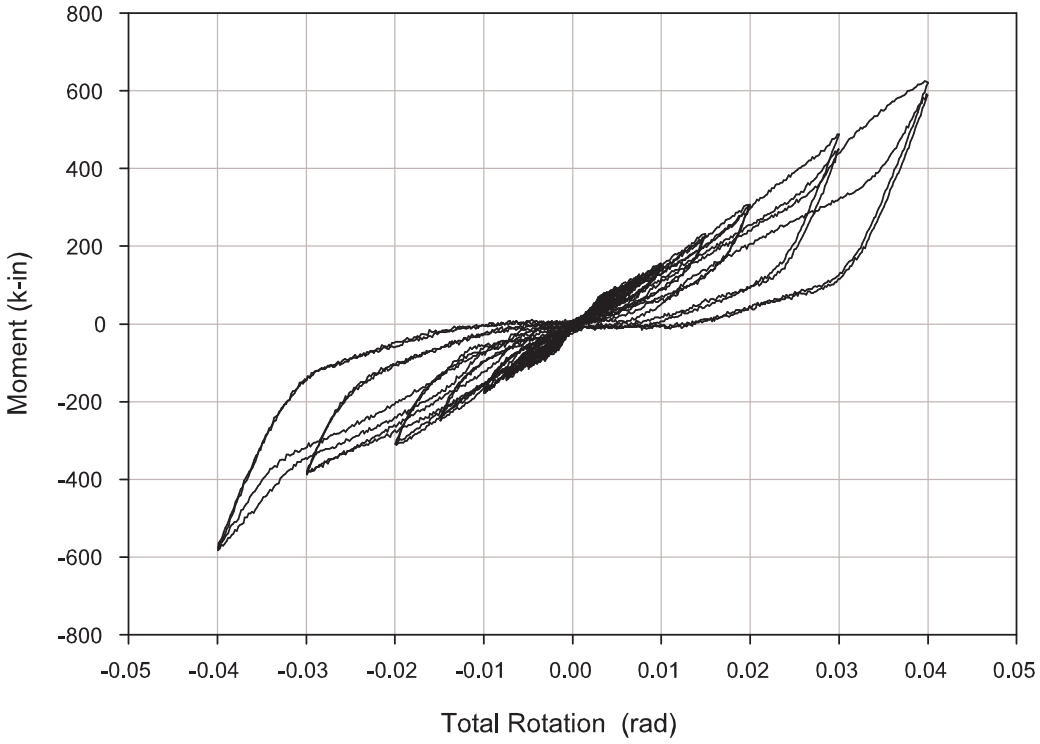

Figure C-3: Moment versus total rotation for Nitinol tendon test.

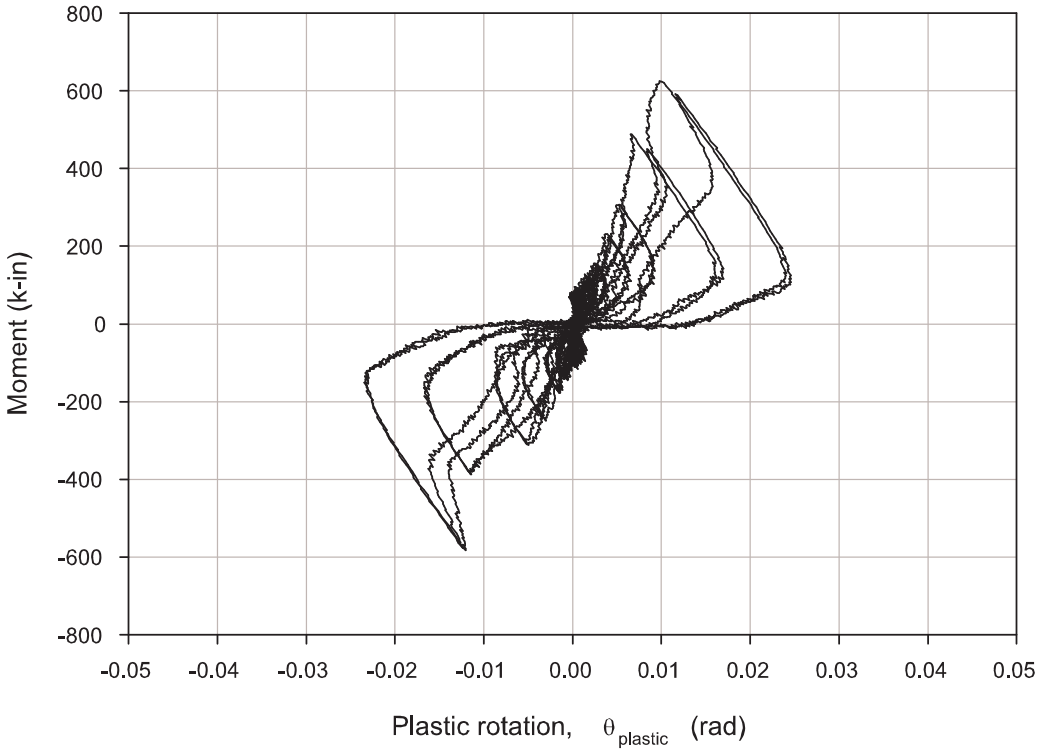

Figure C-4: Moment versus plastic rotation for Nitinol tendon test.

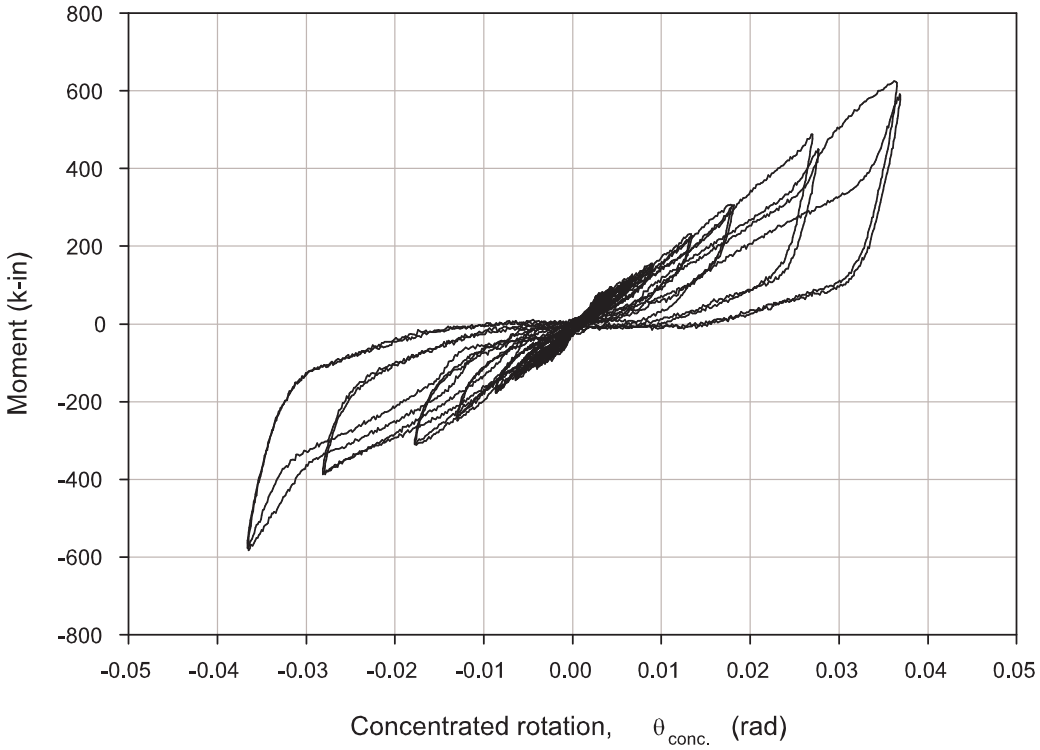

Figure C-5: Moment versus concentrated rotation for Nitinol tendon test.

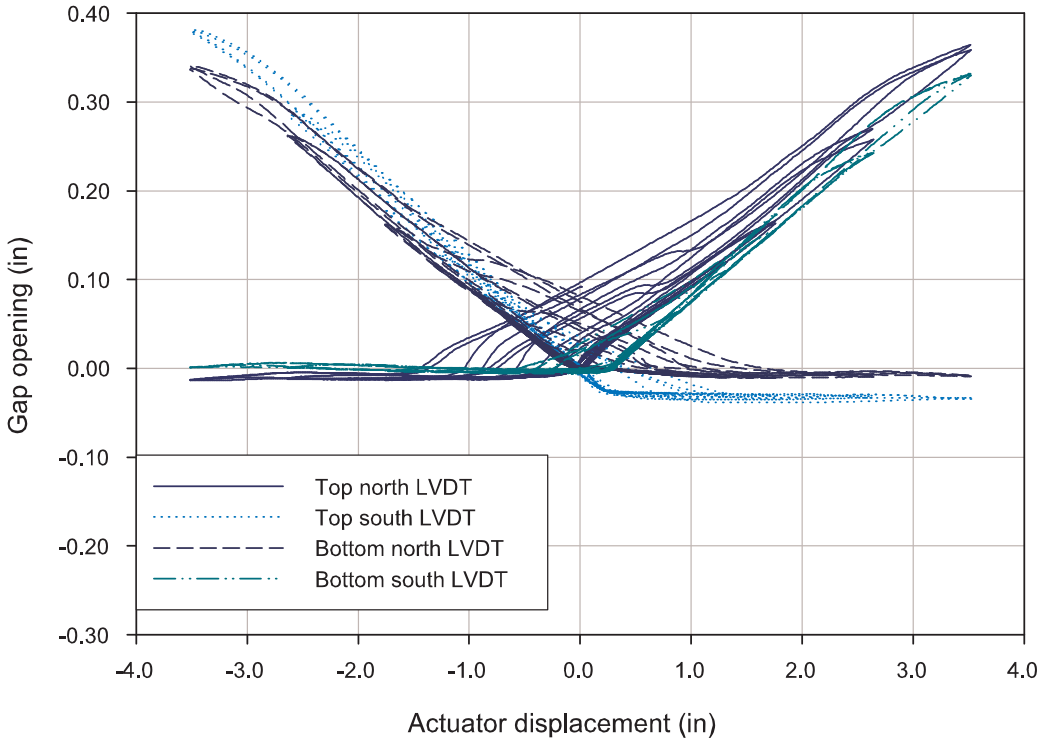

Figure C-6: Gap opening versus actuator displacement for Nitinol tendon test.

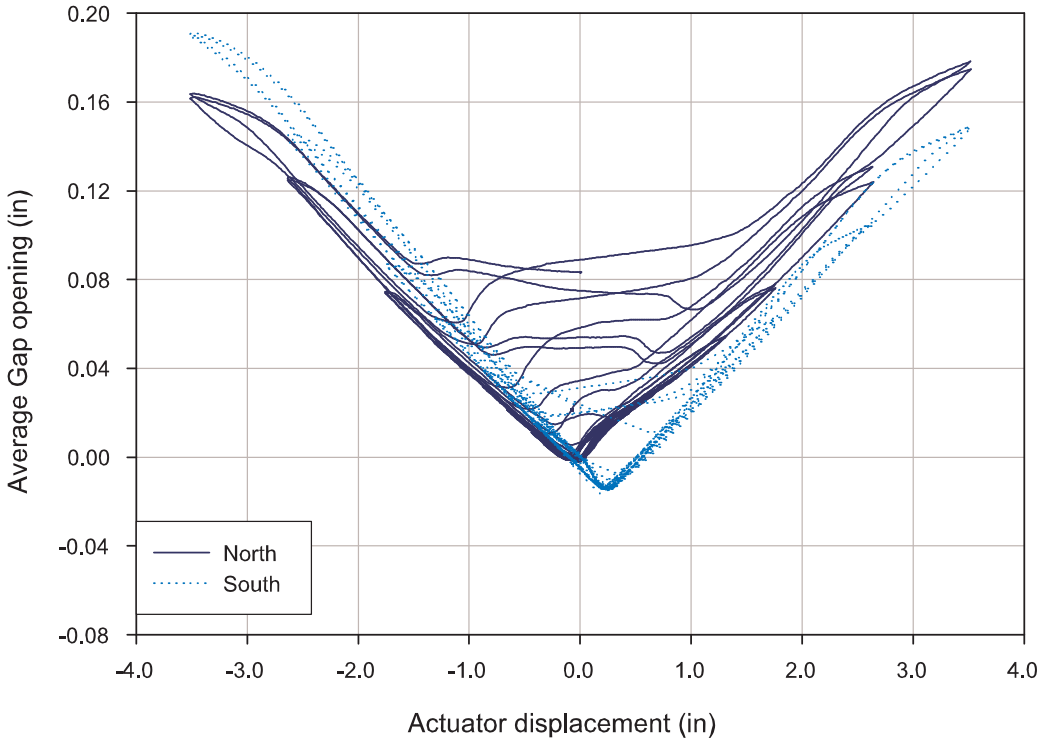

Figure C-7: Average gap opening versus actuator displacement for Nitinol tendon test.

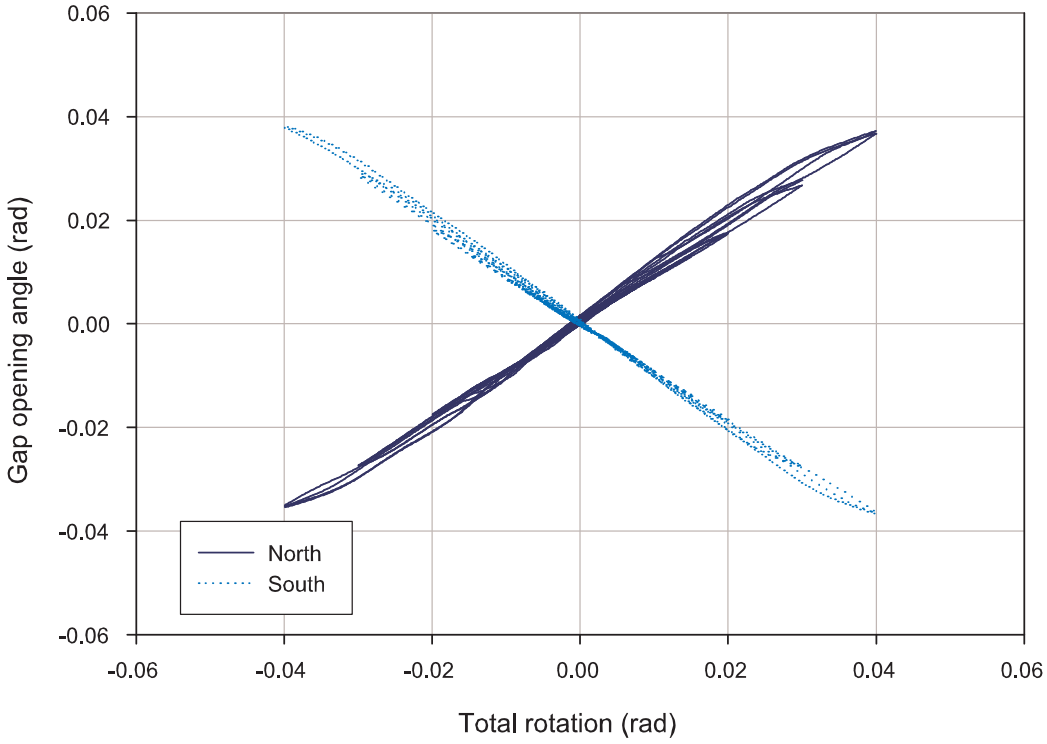

Figure C-8: Gap opening angle versus total rotation for Nitinol tendon test.

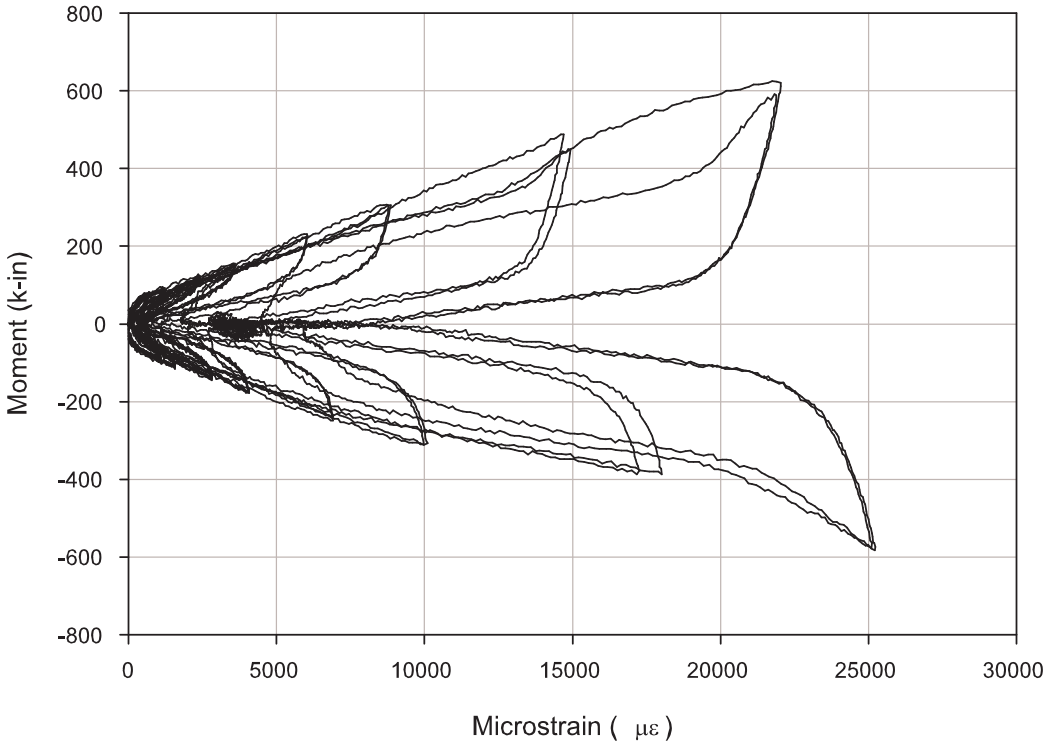

Figure C-9: Moment versus strain in Up West Nitinol tendon for Nitinol tendon test.

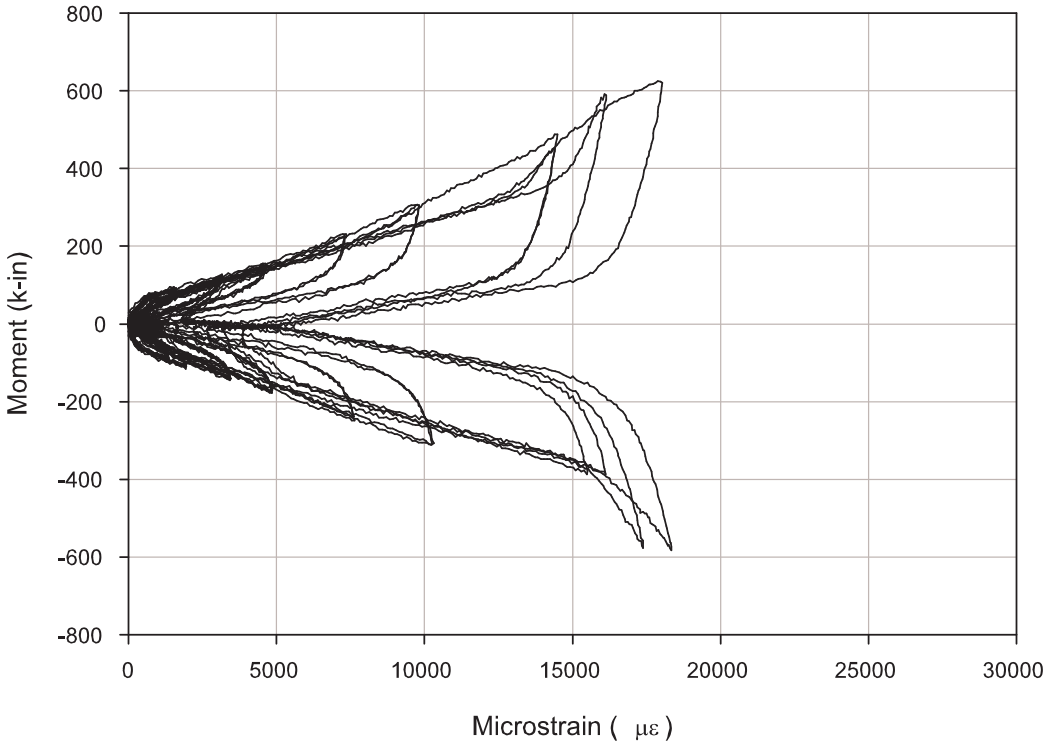

Figure C-10: Moment versus strain in Up East Nitinol tendon for Nitinol tendon test.

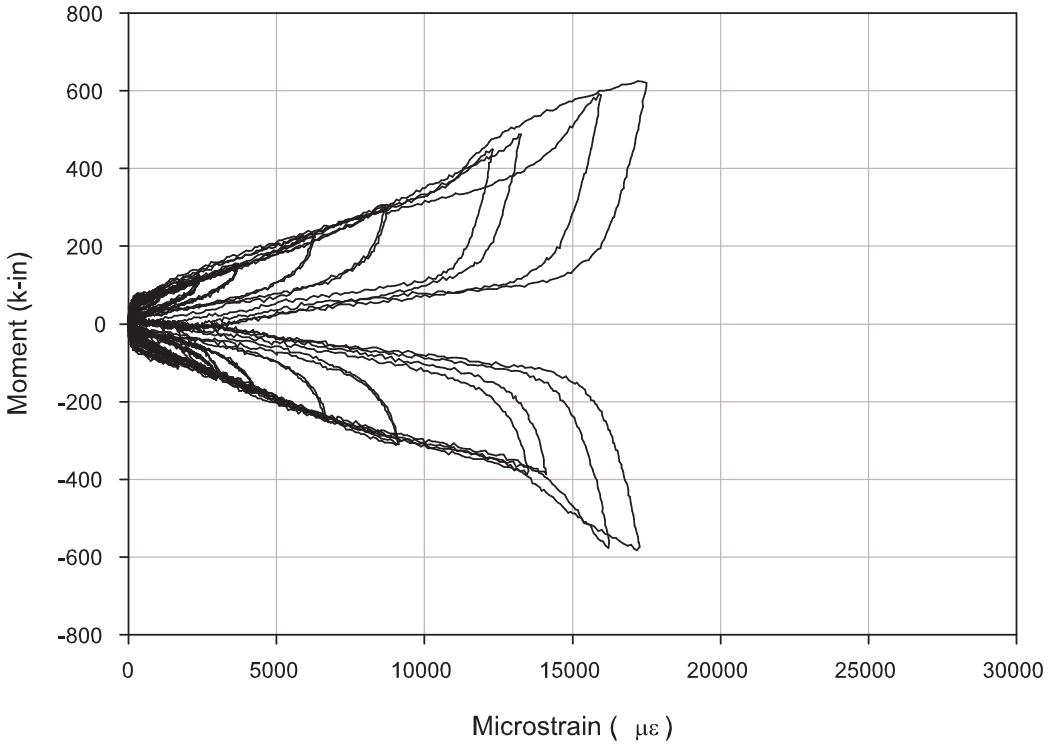

Figure C-11: Moment versus strain in Down West Nitinol tendon for Nitinol tendon test.

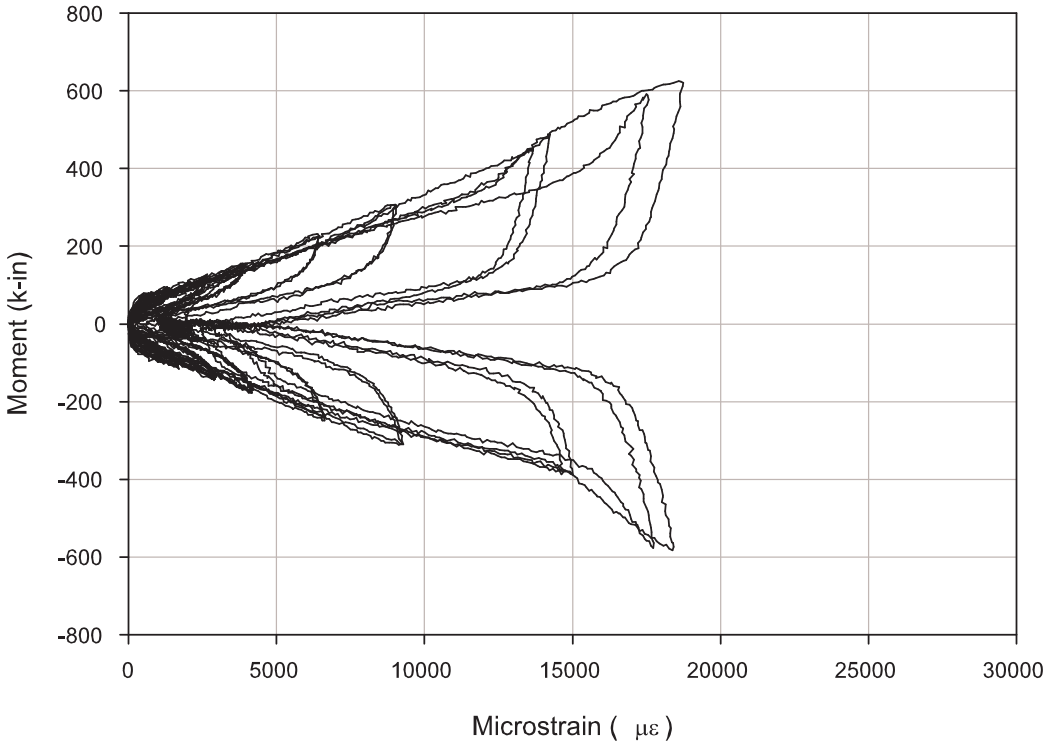

Figure C-12: Moment versus strain in Down East Nitinol tendon for Nitinol tendon test.

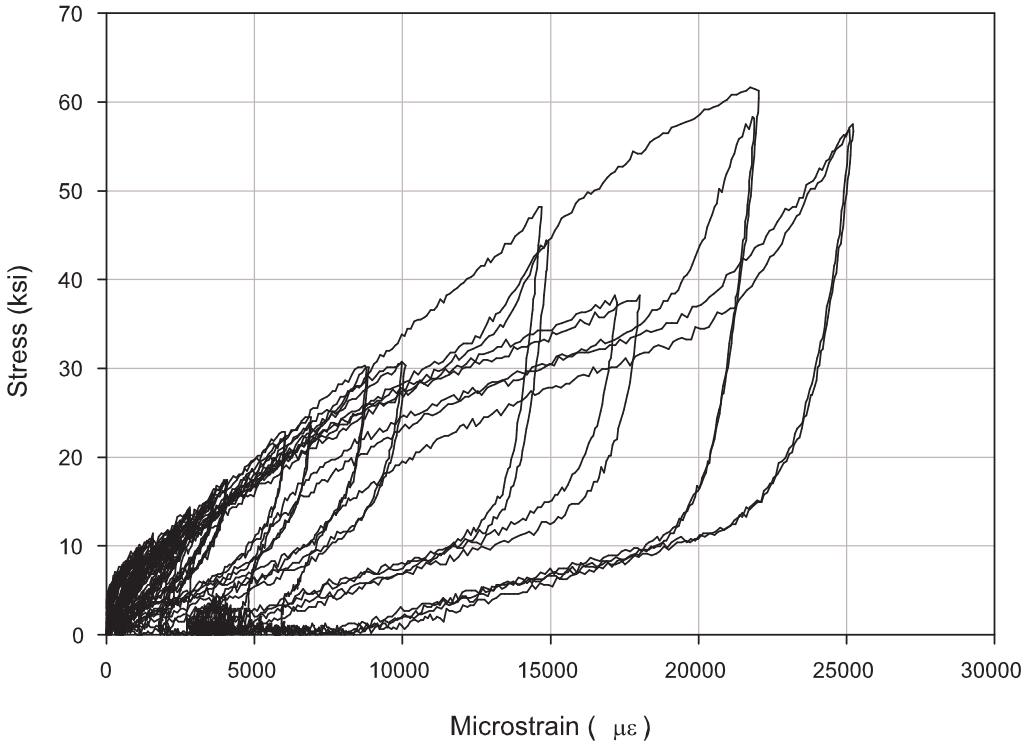

Figure C-13: Stress versus strain in Up West Nitinol tendon for Nitinol tendon test.

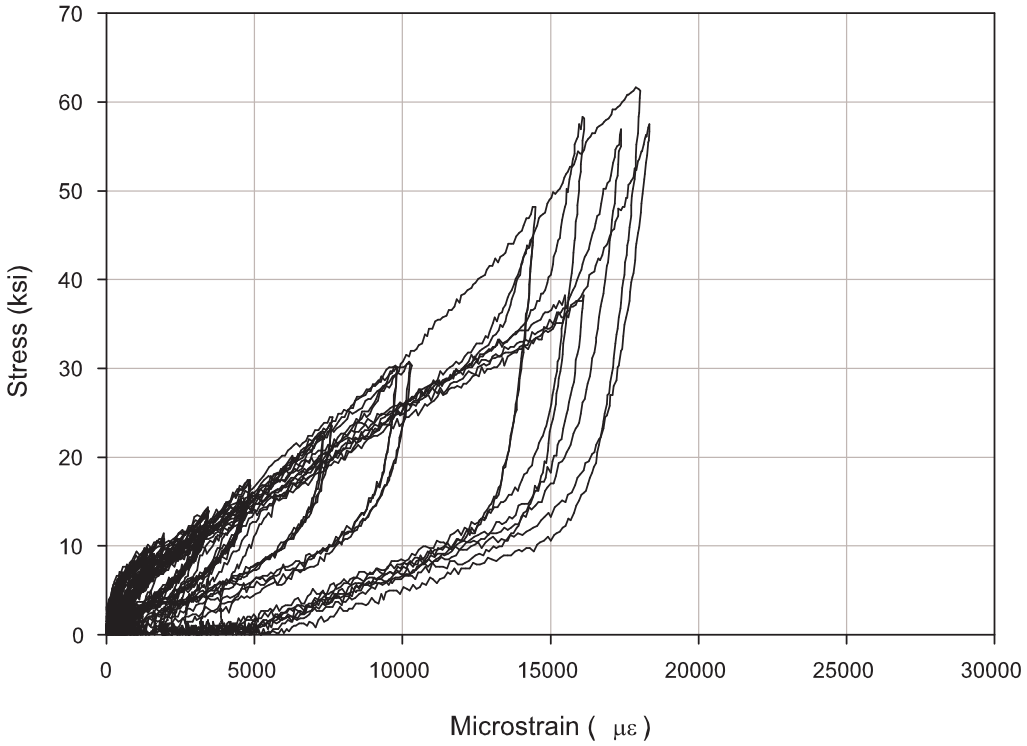

Figure C-14: Stress versus strain in Up East Nitinol tendon for Nitinol tendon test.

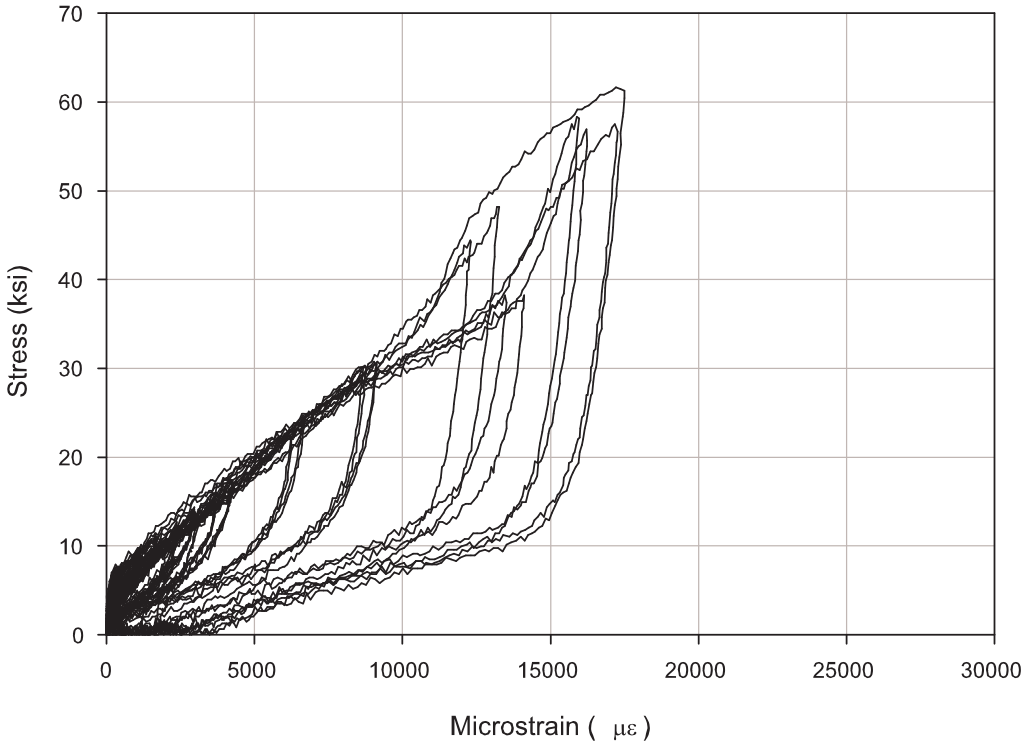

Figure C-15: Stress versus strain in Down West Nitinol tendon for Nitinol tendon test.

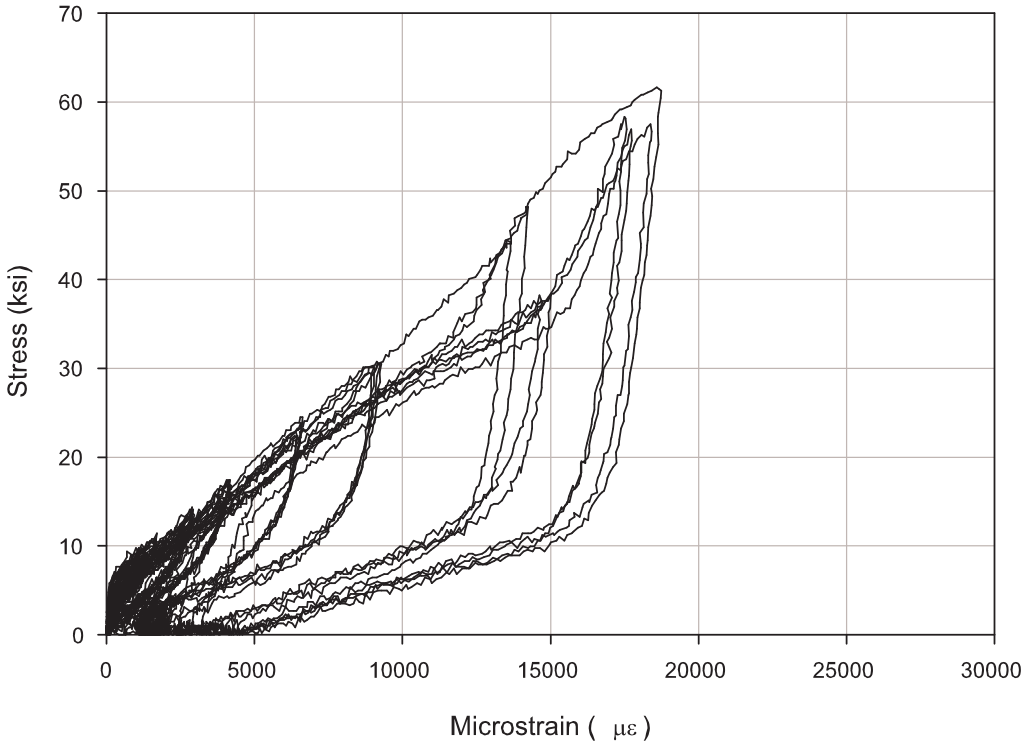

Figure C-16: Stress versus strain in Down East Nitinol tendon for Nitinol tendon test.

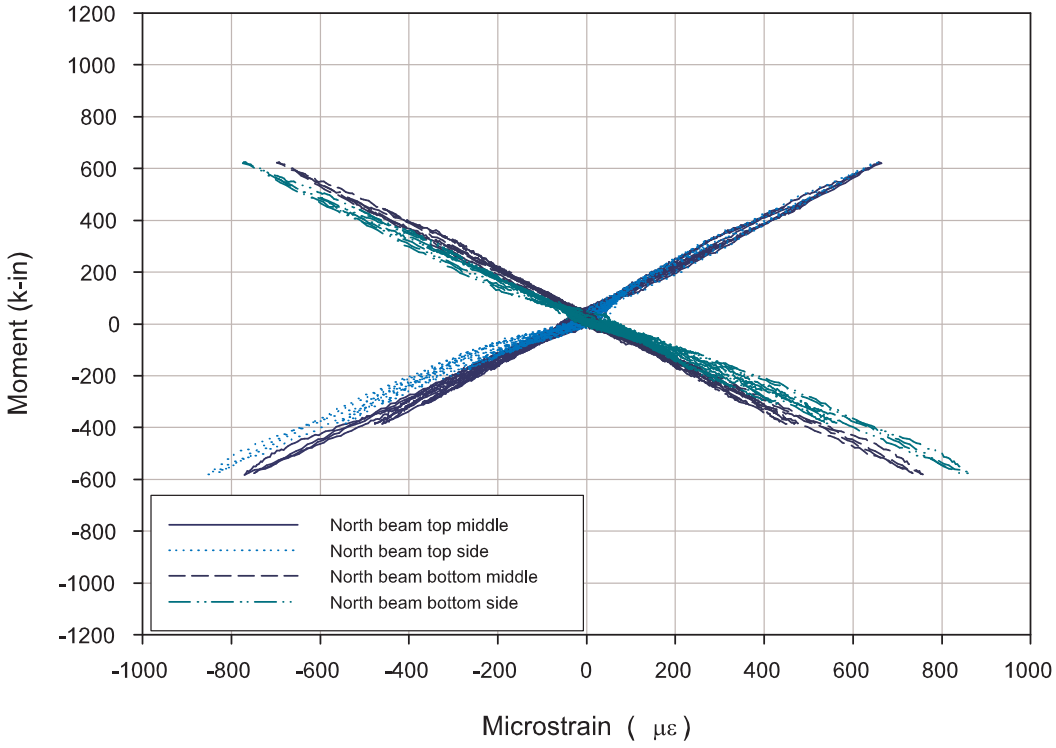

Figure C-17: Moment versus flange strain in north beam for Nitinol tendon test.

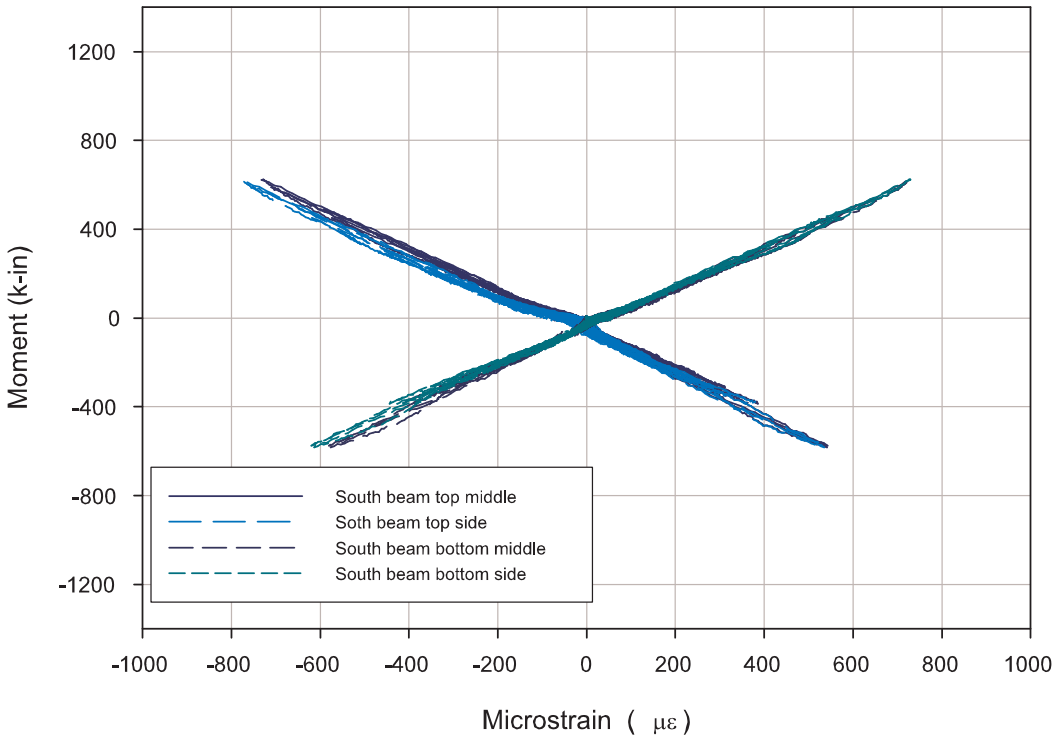

Figure C-18: Moment versus flange strain in south beam for Nitinol tendon test.

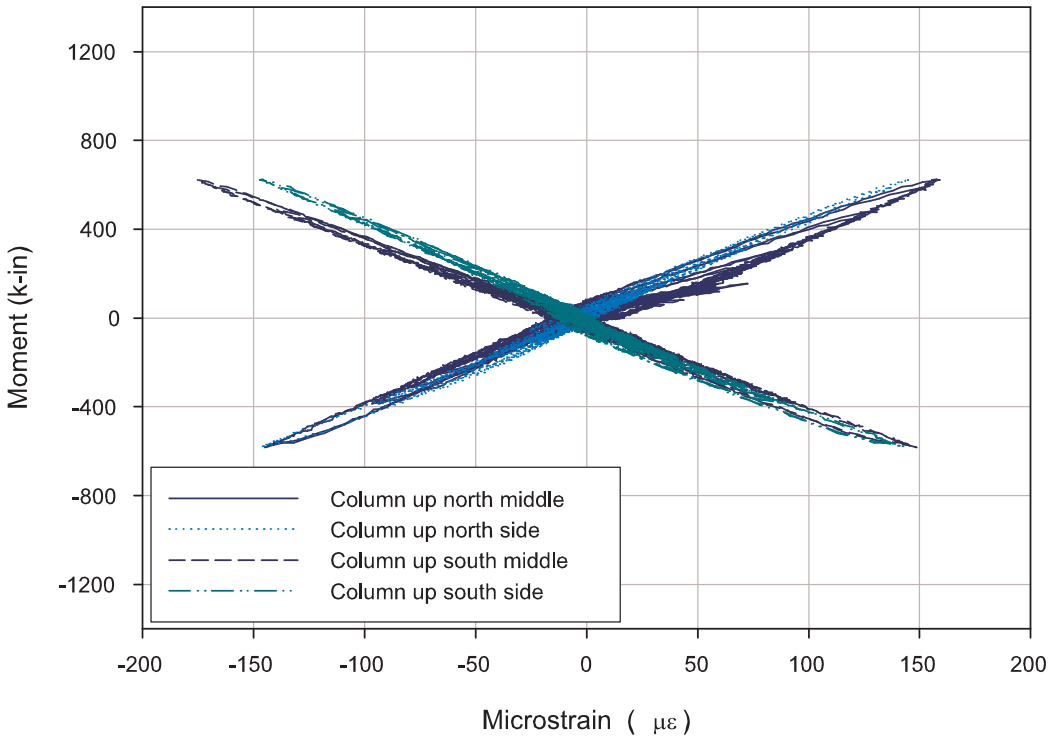

Figure C-19: Moment versus flange strain in upper portion of column for Nitinol tendon test.

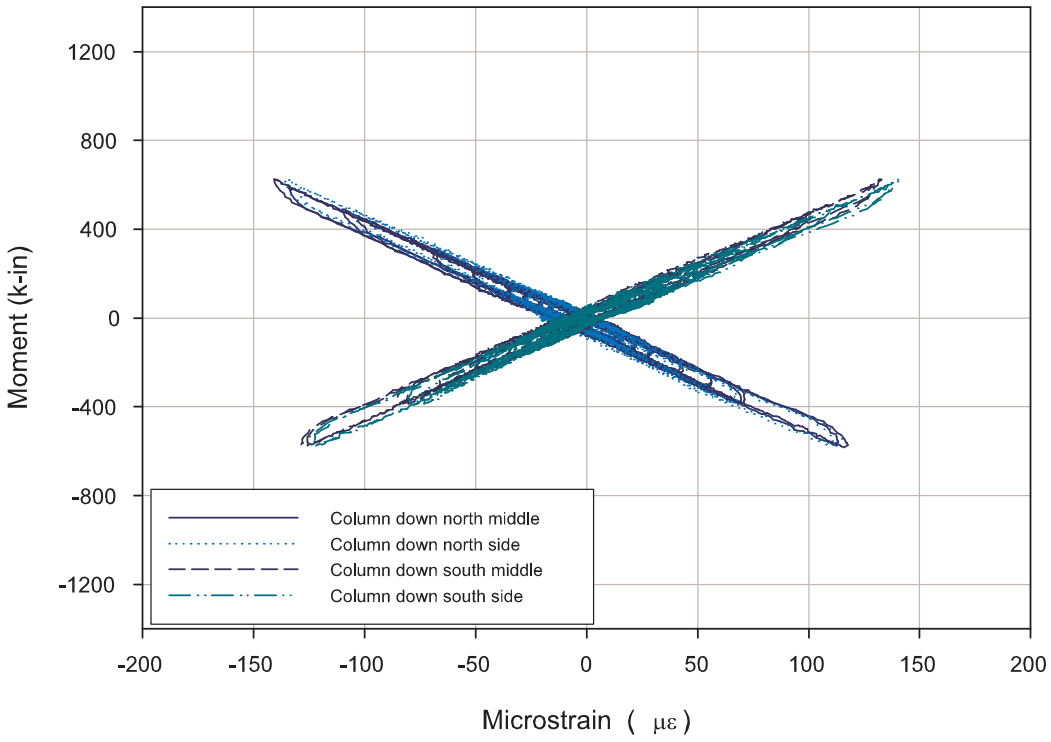

Figure C-20: Moment versus flange strain in lower portion of column for Nitinol tendon test.

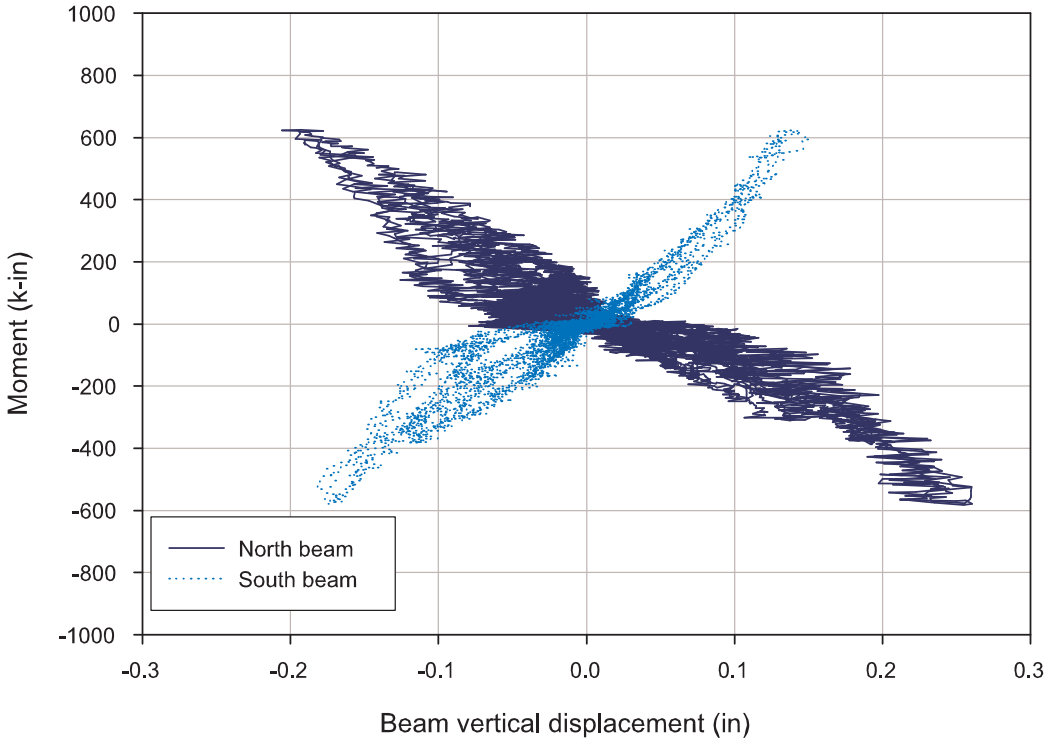

Figure C-21: Moment versus vertical displacement in beam for Nitinol tendon test.

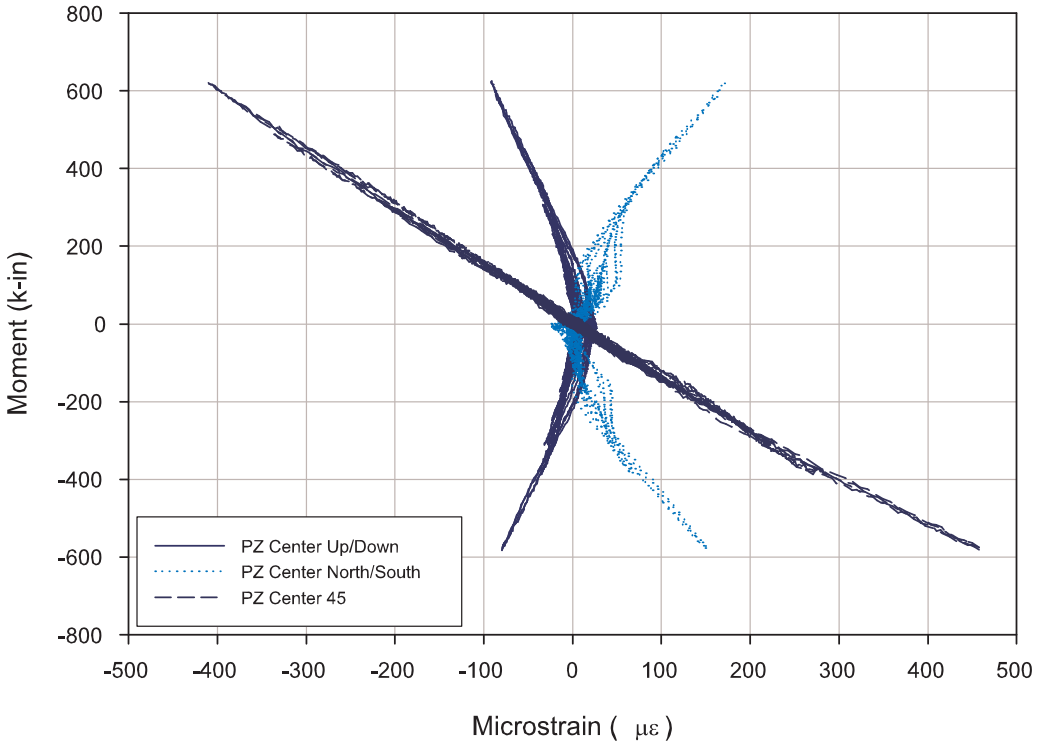

Figure C-22: Moment versus strain in center panel zone rosette for Nitinol tendon test.

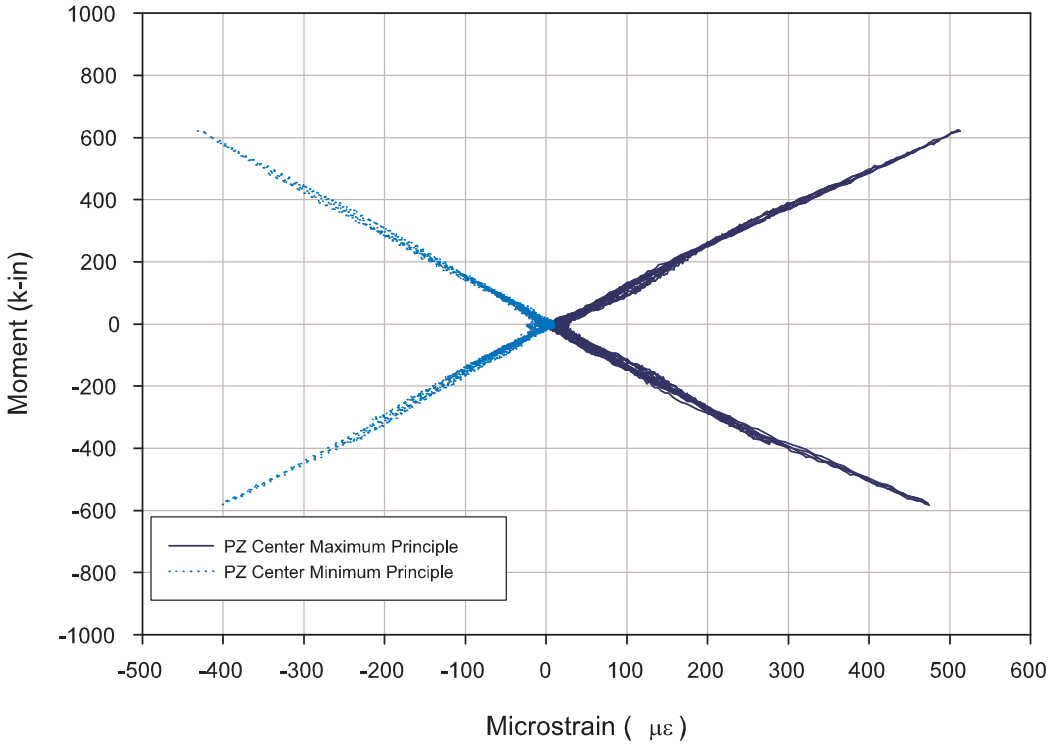

Figure C-23: Moment versus principle strains in center panel zone rosette for Nitinol tendon test.

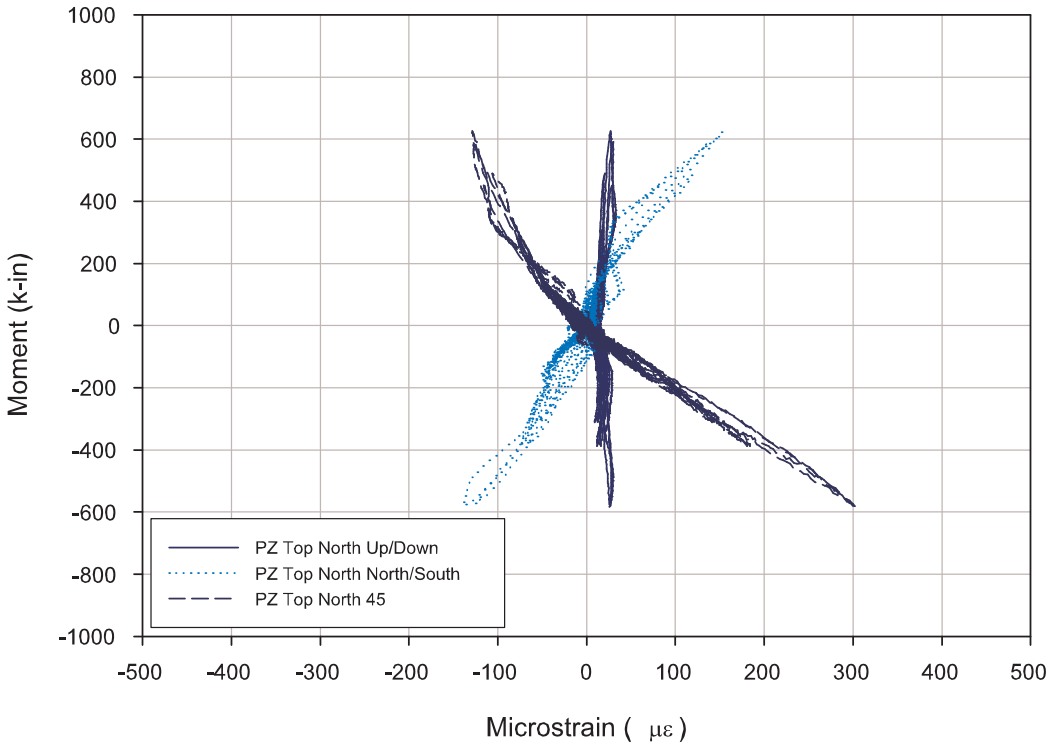

Figure C-24: Moment versus strain in top north panel zone rosette for Nitinol tendon test.

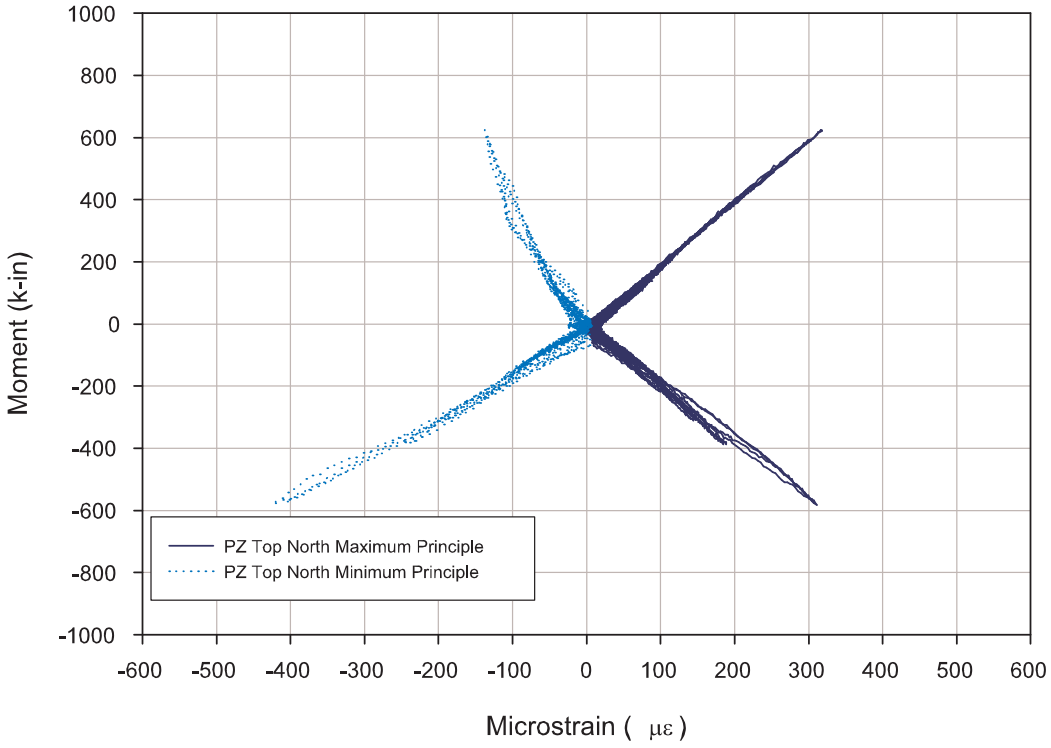

Figure C-25: Moment versus principle strains in top north panel zone rosette for Nitinol tendon test.

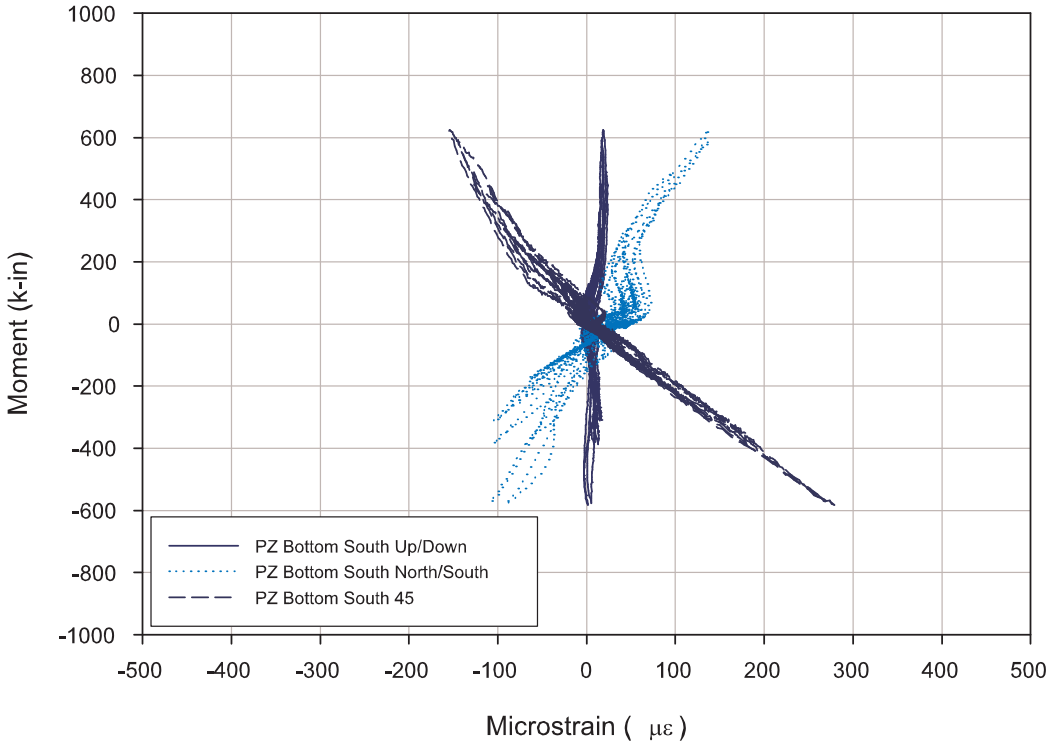

Figure C-26: Moment versus strain in bottom south panel zone rosette for Nitinol tendon test.

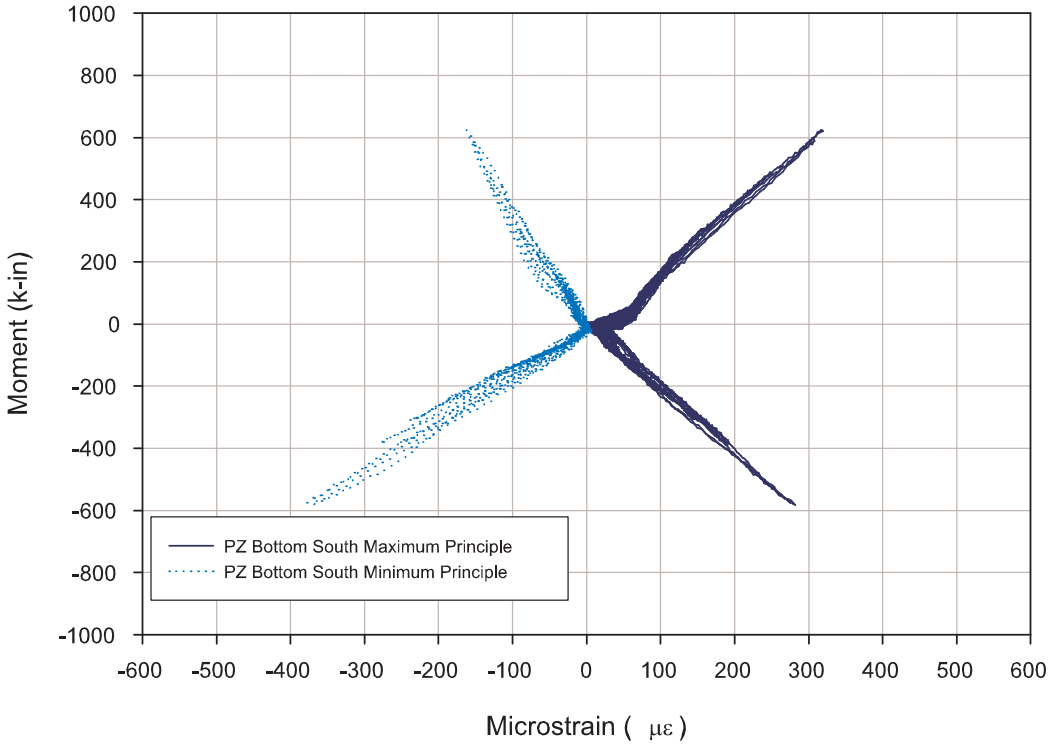

Figure C-27: Moment versus principle strains in bottom south panel zone rosette for Nitinol tendon test.

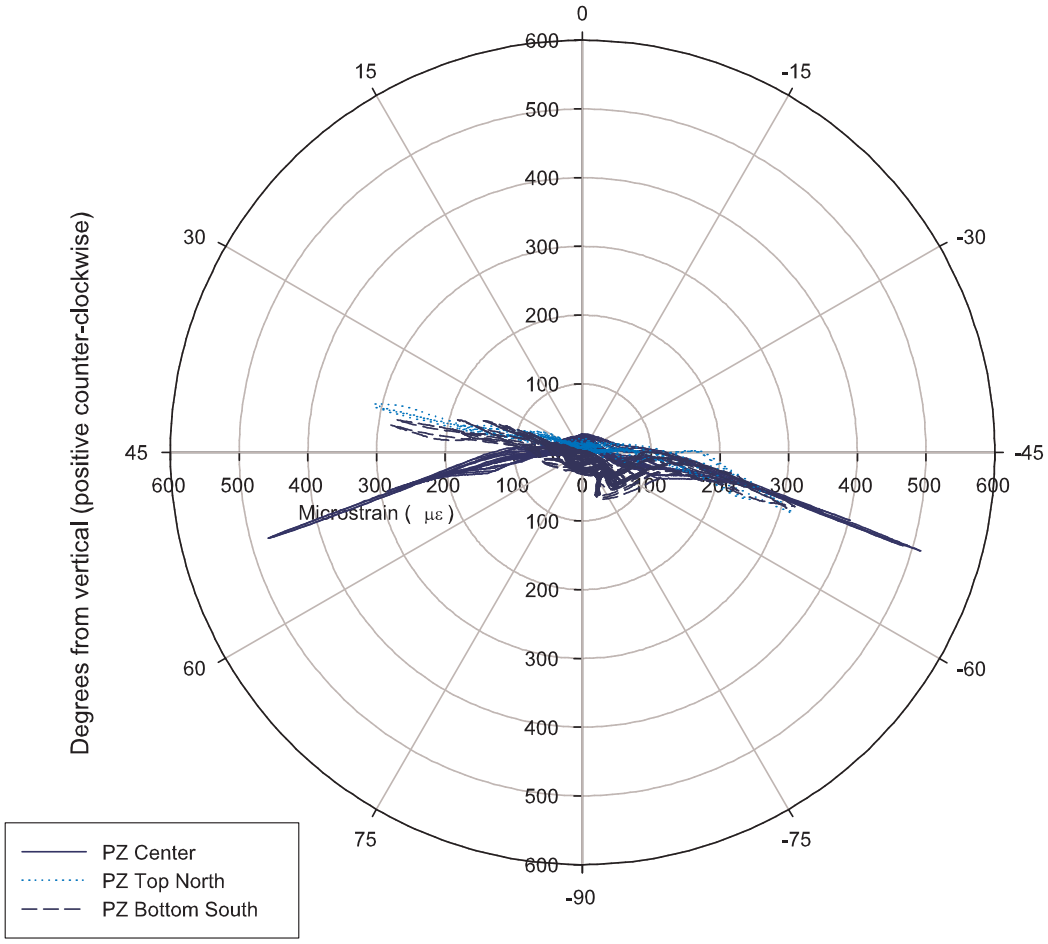

Figure C-28: Principle strain angles versus maximum principal strains in panel zone rosettes for Nitinol tendon test.

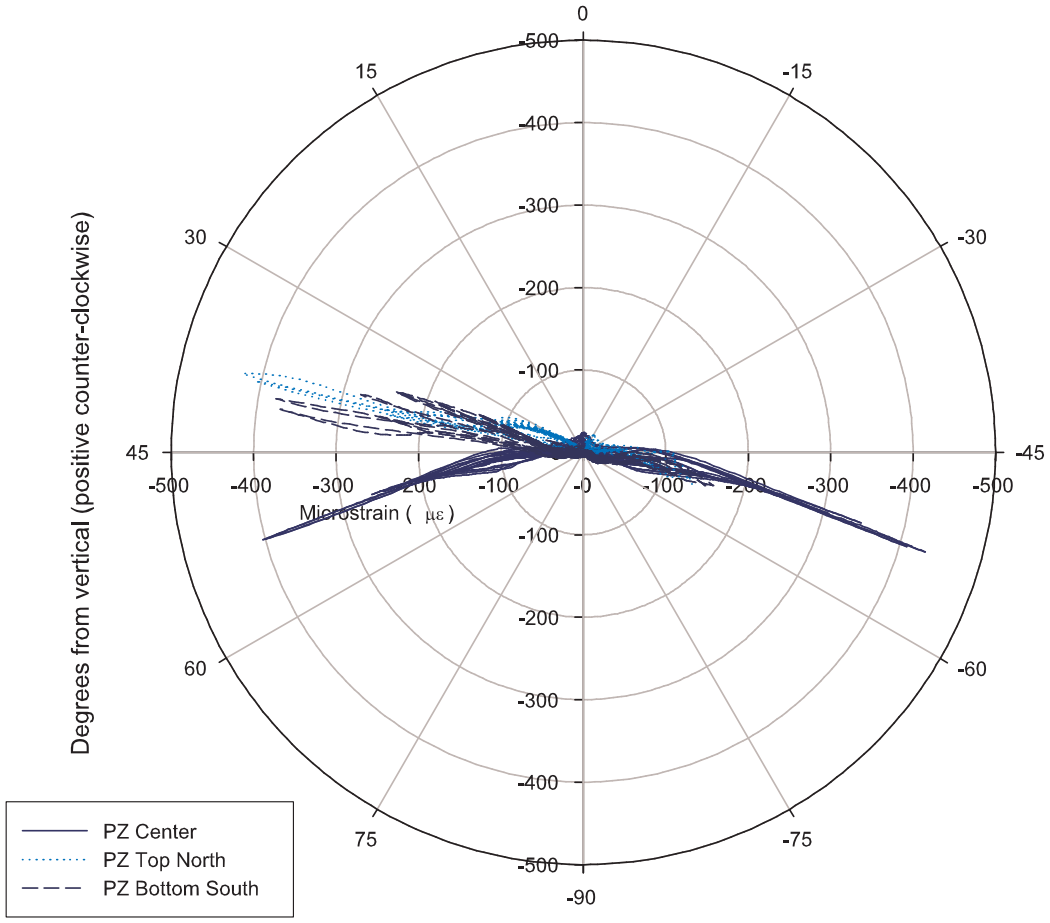

Figure C-29: Principle strain angles versus minimum principal strains in panel zone rosettes for Nitinol tendon test.

C.2 Higher drift cycle testing

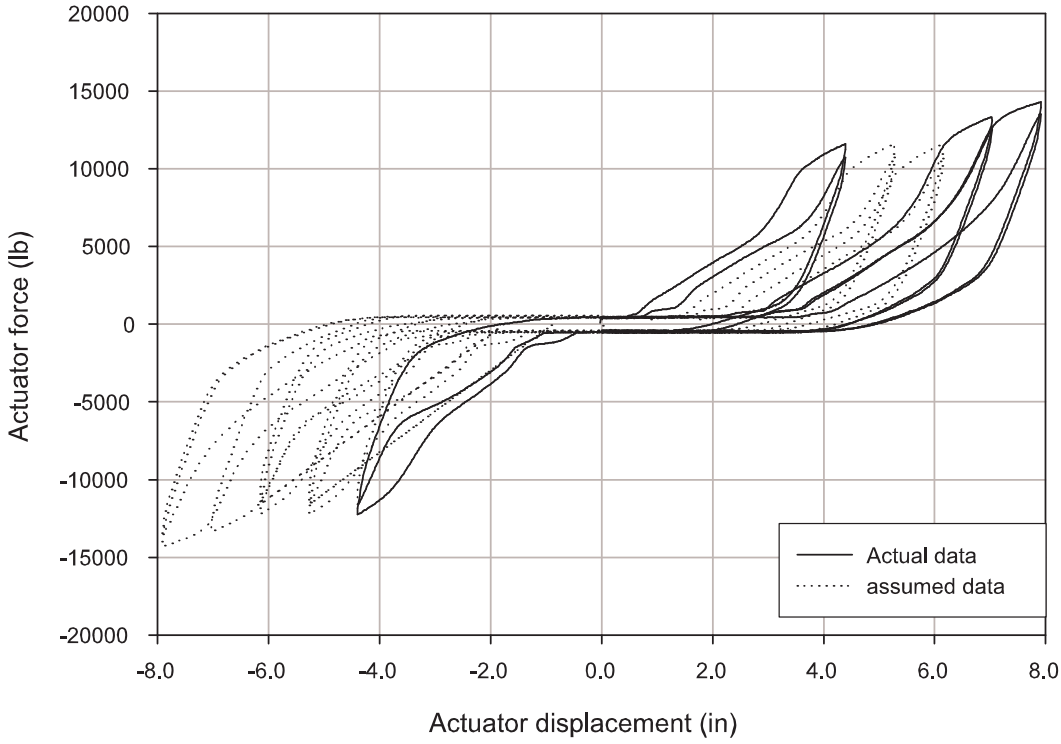

Figure C-30: Actuator force versus actuator displacement for the higher drift cycles of the Nitinol tendon test.

REFERENCES

[1] "Research on seismic resistant modular connectors at the university of arizona," *http://www.u.arizona.edu/ asumer/pt.html*, March 2005.

[2] Aiken, I. D., Nims, D. K., Whittaker, A. S., and Kelly, J. M., "Testing of passive energy dissipation systems," *Earthquake Spectra*, vol. 9, no. 3, p. 335, 1993.

[3] Aizawa, S., Kakizawa, T., and Higasino, M., "Case studies of smart materials for civil structures," *Smart Materials and Structures*, vol. 7, no. 5, pp. 617–626, 1998.

[4] Barbero Bernal, L. I., "Cyclic behavior of superelastic nickel-titanium and nickel-titanium-chromium shape memory alloys," Master's thesis, Georgia Institute Of Technology, 2004.

[5] Bruno, S. and Valente, C., "Comparative response analysis of conventional and innovative seismic protection strategies," *Earthquake Engineering and Structural Dynamics*, vol. 31, no. 5, pp. 1067–1092, 2002.

[6] Callister, W. D., *Materials science and engineering : an introduction*. Wiley, 6th ed., 2003.

[7] Castellano, M., Indirli, M., and Martelli, A., "Progress of application, research and development and design guidelines for shape memory alloy devices for cultural heritage structures in italy," in *Smart Systems for Bridges, Structures, and Highways-Smart Structures and Materials 2001-, Mar 5-7 2001*, vol. 4330 of *Proceedings of SPIE - The International Society for Optical Engineering*, (Newport Beach, CA), pp. 250–261, Society of Photo-Optical Instrumentation Engineers, 2001.

[8] Chen, S.-J., Yeh, C., and Chu, J., "Ductile steel beam-to-column connections for seismic resistance," *Journal of Structural Engineering*, vol. 122, no. 11, pp. 1292–1299, 1996.

[9] Cheok, G. S. and Stone, W. C., "Performance of 1/3-scale model precast concrete beam-column connections subjected to cyclic inelastic loads - report no. 4," Tech. Rep. NISTIR 5436, National Institute of Standards and Technology (NIST), June 1994 1994.

[10] Cheok, G. S., Stone, W. C., and Lew, H., "Performance of 1/3-scale model precast concrete beam-column connections subjected to cyclic inelastic loads - report no. 3," Tech. Rep. NISTIR 5246, National Institute of Standards and Technology (NIST), August 1993 1993.

[11] Chopra, A. K., *Dynamics of structures : theory and applications to earthquake engineering*. Prentice Hall, 2nd ed., 2001.

[12] Christopoulos, C. and Filiatrault, A., "Seismic response of post-tensioned energy dissipating moment resisting steel freames," in *12th European Conference on Earthquake Engineering*, (London, UK), 2002.

[13] Christopoulos, C., Filiatrault, A., and Uang, C.-M., "Behavior of steel moment resisting frames with post-tensioned energy dissipating connections," in *Seventh U.S. National Conference on Earthquake Engineering (NCEE)*, (Boston, MA), Earthquake Engineering Research Institute, 2002.

[14] Christopoulos, C., Filiatrault, A., and Folz, B., "Seismic response of self-centring hysteretic sdof systems," *Earthquake Engineering and Structural Dynamics*, vol. 31, no. 5, pp. 1131–1150, 2002.

[15] Christopoulos, C., Filiatrault, A., Uang, C.-M., and Folz, B., "Posttensioned energy dissipating connections for moment-resisting steel frames," *Journal of Structural Engineering*, vol. 128, no. 9, pp. 1111–1120, 2002.

[16] Clark, P. W., Aiken, I. D., Kelly, J. M., Higashino, M., and Krumme, R., "Experimental and analytical studies of shape-memory alloy dampers for structural control," in *Smart Structures and Materials 1995: Passive Damping, Mar 1-2 95*, vol. 2445 of *Proceedings of SPIE - The International Society for Optical Engineering*, (San Diego, CA, USA), pp. 241–251, Society of Photo-Optical Instrumentation Engineers, Bellingham, WA, USA, 1995.

[17] Clark, P. W., Frank, K., Krawinkler, H., and Shaw, R., "Protocol for fabrication, inspection, testing, and documentation of beam-column connection tests and other experimental specimens," Tech. Rep. SAC/BD-97/02, SAC Joint Venture, 1997.

[18] Constantinou, M. C., Soong, T. T., and Dargush, G. F., *Passive Energy Dissipation Systems for Structural Design and Retrofit*. Multidisciplinary Center for Earthquake Engineering Research, 1998.

[19] Delemont, M. A., "Seismic retrofit of bridges using shape memory alloys," Master's thesis, Georgia Institute Of Technology, 2001.

[20] DesRoches, R. and Smith, B. J., "Shape memory alloys in seismic resistant design and retrofit: a critical review of their potential and limitations," *Journal of Earthquake Engineering*, vol. 8, no. 3, pp. 415–429, 2004.

[21] DesRoches, R. and McCormick, J., "Properties of large diameter shape memory alloys under cyclical loading," in *Smart Structures and Materials 2003: Smart Systems and Nondestructive Evaluation for Civil Infrastructures, Mar 3-6 2003*, vol. 5057 of *Proceedings of SPIE - The International Society for Optical Engineering*, (San Diego, CA, United States), pp. 187–196, The International Society for Optical Engineering, 2003.

[22] DesRoches, R., McCormick, J., and Delemont, M., "Cyclic properties of superelastic shape memory alloy wires and bars," *Journal of Structural Engineering*, vol. 130, no. 1, pp. 38–46, 2004.

[23] Dolce, M. and Cardone, D., "Mechanical behaviour of shape memory alloys for seismic applications 2. austenite niti wires subjected to tension," *International Journal of Mechanical Sciences*, vol. 43, no. 11, pp. 2657–2677, 2001.

[24] Dolce, M., Cardone, D., Marnetto, R., Mucciarelli, M., Nigro, D., Ponzo, F. C., and Santarsiero, G., "Experimental static and dynamic response of a real r/c frame upgraded with sma re-centering and dissipating braces," in *13th World Conference on Earthquake Engineering*, (Vancouver, B.C., Canada), 2004.

[25] Dolce, M., Cardone, D., and Marnetto, R., "Implementation and testing of passive control devices based on shape memory alloys," *Earthquake Engineering and Structural Dynamics*, vol. 29, no. 7, pp. 945–968, 2000.

[26] El-Sheikh, M. T., Sause, R., Pessiki, S., and Lu, L.-W., "Seismic behavior and design of unbonded post-tensioned precast concrete frames," *PCI Journal*, vol. 44, no. 3, pp. 54–71, 1999.

[27] Engelhardt, M. D. and Sabol, T. A., "Reinforcing of steel moment connections with cover plates: benefits and limitations," *Engineering Structures*, vol. 20, no. 4-6, pp. 510–520, 1998.

[28] FEMA, *Recommended seismic design criteria for new steel moment-frame buildings*. FEMA 350, Washington D.C.: SAC Joint Venture ; Federal Emergency Management Agency, 2000.

[29] FEMA, *Recommended specifications and quality assurance guidelines for steel moment-frame construction for seismic applications*. FEMA 353, Washington D.C.: SAC Joint Venture ; Federal Emergency Management Agency, 2000.

[30] Fleischman, R. B. *Personal correspondance with B. Penar*, 2005.

[31] Friend, C. M. and Morgan, N., "Fatigue/cyclic stability of shape-memory alloys," in *First european conference on shape memory and superelastic technologies* (Van Mooleghem, W., Besselink, P., and Aslanidis, D., eds.), (Antwerp Zoo, Belgium), 1999.

[32] Gandhi, F. and Chapuis, G., "Passive damping augmentation of a vibrating beam using pseudoelastic shape memory alloy wires," *Journal of Sound and Vibration*, vol. 250, no. 3, pp. 519–539, 2002.

[33] Garlock, M. M., Ricles, J., and Sause, R., "Experimental studies on full-scale post-tensioned seismic-resistant steel moment connections," in *Seventh U.S. National Conference on Earthquake Engineering (NCEE)*, (Boston, MA), Earthquake Engineering Research Institute, 2002.

[34] Han, Y.-L., Li, A.-Q., Lin, P.-H., Li, Q., and Leung, A., "Structural vibration control by shape memory alloy damper," *Earthquake Engineering and Structural Dynamics*, vol. 32, no. 3, pp. 483–494, 2003.

[35] Hanson, R. D. and Soong, T. T., *Seismic design with supplemental energy dissipation devices*. Oakland, CA: Earthquake engineering research institute, 2001.

[36] Higashino, M., Aizawa, S., Clark, P. W., Whittaker, A. S., Aiken, I. D., and Kelly, J. M., "Experimental and analytical studies of structural control system using shape memory alloy," in *Second International Workshop on Structural Control*, (Hong Kong), 1996.

[37] Huang, X. and Liu, Y., "Effect of annealing on the transformation behavior and superelasticity of niti shape memory alloy," *Scripta Materialia*, vol. 45, no. 2, pp. 153–160, 2001.

[38] Inaudi, J. A. and Kelly, J. M., "Experiments on tuned mass dampers using viscoelastic frictional and shape-memory alloy materials," in *First World Conference on Structural Control*, (Los Angeles, California), 1994.

[39] Indirli, M., Castellano, M., Clemente, P., and Martelli, A., "Demo-application of shape memory alloy devices: The rehabilitation of the s. giorgio church bell-tower," in *Smart Systems for Bridges, Structures, and Highways-Smart Structures and Materials 2001-, Mar 5-7 2001*, vol. 4330 of *Proceedings of SPIE - The International Society for Optical Engineering*, (Newport Beach, CA), pp. 262–272, Society of Photo-Optical Instrumentation Engineers, 2001.

[40] Kaounides, L., "Advanced materials - corporate strategies for competitive advantages in the 1990s," tech. rep., 1995.

[41] Kasai, K., Hodgson, I., and Bleiman, D., "Rigid-bolted repair method for damaged moment connections," *Engineering Structures*, vol. 20, no. 4-6, pp. 521–532, 1998.

[42] Krumme, R., Hayes, J., and Sweeney, S., "Structural damping with shape memory alloys: one class of devices," in *Proceedings of SPIE - The International Society for Optical Engineering, Smart Structrures and Materials Conference*, (San Diego, CA), 1995.

[43] Lammering, R. and Schmidt, I., "Experimental investigations on the damping capacity of niti components," *Smart Materials and Structures*, vol. 10, no. 5, pp. 853–859, 2001.

[44] Leon, R., "Seismic performance of bolted and riveted connections," in *Background Reports: Metallurgy Mechanics, Welding, Moment connections and frame systems behavior*, vol. FEMA-288, Federal Emergency Management Agency, 1995.

[45] Liu, Y., Van Humbeeck, J., Stalmans, R., and Delaey, L., "Some aspects of the properties of niti shape memory alloy," *Journal of Alloys and Compounds*, vol. 247, no. 1-2, pp. 115–121, 1997.

[46] Mahin, S. A., "Lessons from damage to steel buildings during the northridge earthquake," *Engineering Structures*, vol. 20, no. 4-6, pp. 261–270, 1998.

[47] Malley, J. O., "Sac steel project: summary of phase 1 testing investigation results," *Engineering Structures*, vol. 20, no. 4-6, pp. 300–309, 1998.

[48] MANSIDE, "Third twelve monthly progress report (1/12/97 - 30/11/98)," tech. rep., 1998.

[49] McCormick, J. and DesRoches, R., "Damping properties of shape memory alloys for seismic applications," in *Proceedings of the 2004 Structures Congress - Building on the Past: Securing the Future, May 22-26 2004*, (Nashville, TN, United States), pp. 747–757, American Society of Civil Engineers, 2004.

[50] Melton, K., "Ni-ti based shape memory alloys," in *Engineering aspects of shape memory alloys* (Duerig, T. W., Melton, K., Stockel, D., and Wayman, C., eds.), Butterworth-Heinemann, 1990.

[51] Miyazaki, S., "Thermal and stress cycling effects and fatigue properties of ni-ti alloys," in *Engineering aspects of shape memory alloys* (Duerig, T. W., Melton, K., Stockel, D., and Wayman, C., eds.), Butterworth-Heinemann, 1990.

[52] Morgen, B. G. and Kurama, Y. C., "A friction damper for post-tensioned precast concrete moment frames," *PCI Journal*, vol. 49, no. 4, pp. 112–133, 2004.

[53] Ocel, J., DesRoches, R., Leon, R. T., Hess, W. G., Krumme, R., Hayes, J. R., and Sweeney, S., "Steel beam-column connections using shape memory alloys," *Journal of Structural Engineering*, vol. 130, no. 5, pp. 732–740, 2004.

[54] Ocel, J. M., "Cyclic behavior of steel beam-column connections with shape memory alloy connecting elements," Master's thesis, Georgia Institute Of Technology, 2002.

[55] Otsuka, K. and Ren, X., "Factors affecting the ms temperature and its control in shape-memory alloys," in *Proceedings of the International Conference on Shape Memory and Superelastic Technologies and Shape Memory Materials (SMST-SMM 2001), Sep 2-6 2001*, vol. 394-395 of *Materials Science Forum*, (Kumning, China), pp. 177–184, Trans Tech Publications Ltd, 2002.

[56] Porter, D. A. and Easterling, K. E., *Phase transformations in metals and alloys*. Van Nostrand Reinhold, 2nd ed., 1981.

[57] Prakash, V., Powell, G. H., and Campbell, S., *DRAIN-2DX Base Program Description and User Guide*. Berkeley, CA: NISEE/Computer Applications, Dept. of Civ. Engrg., University of California, Berkeley, 1993.

[58] Priestley, M. N. and MacRae, G. A., "Seismic tests of precast beam-to-column joint subassemblages with unbonded tendons," *PCI Journal*, vol. 41, no. 1, pp. 64–80, 1996.

[59] Ricles, J. M., Mao, C., Lu, L.-W., and Fisher, J. W., "Inelastic cyclic testing of welded unreinforced moment connections," *Journal of Structural Engineering*, vol. 128, no. 4, pp. 429–440, 2002.

[60] Ricles, J. M., Sause, R., Garlock, M. M., and Zhao, C., "Posttensioned seismic-resistant connections for steel frames," *Journal of Structural Engineering*, vol. 127, no. 2, pp. 113–121, 2001.

[61] Ricles, J., Sause, R., and Garlock, M. M., "Post-tensioned moment connections for seismic resistant steel frames," in *Fourth International Workshop on Connections in Steel Structures*, (Roanoke, VA), American Institute of Steel Construction (AISC), 2000.

[62] Ricles, J., Sause, R., Peng, S., and Lu, L., "Experimental evaluation of earthquake resistant posttensioned steel connections," *Journal of Structural Engineering*, vol. 128, no. 7, pp. 850–859, 2002.

[63] Rojas, P., Garlock, M. M., Ricles, J., and Sause, R., "Reducing seismic damage in steel frames using post-tensioning," in *Seventh U.S. National Conference on Earthquake Engineering (NCEE)*, (Boston, MA), Earthquake Engineering Research Institute, 2002.

[64] Scherngell, H. and Kneissl, A., "Influence of the microstructure on the stability of the intrinsic two-way shape memory effect," *Materials Science and Engineering A: Structural Materials: Properties, Microstructure and Processing Proceedings of the 1998 International Conference on Martensitic Transformations (ICOMAT 98), Dec 7-Dec 11 1998*, vol. A273-275, pp. 400–403, 1999.

[65] Scott, N. L., Hawkins, N. M., Kreger, M. E., Libby, J. R., Martin, L. D., Mast, R. F., Cheok, G. S., Nakaki, S., Sanders, J. C., Seagren, D. C., Stanton, J. F., Stephan, D. E., Stone, W. C., Ghosh, S., Lew, H., and Nigel Priestley, M., "Special hybrid moment frames composed of discretely jointed precast and post-tensioned concrete members (aci t1.2-xx) and commentary (t1.2r-xx)," *ACI Structural Journal*, vol. 98, no. 5, pp. 771–784, 2001.

[66] Sehitoglu, H., Anderson, R., Karaman, I., Gall, K., and Chumlyakov, Y., "Cyclic deformation behavior of single crystal niti," *Materials Science and Engineering*, vol. A 314, p. 6774, 2001.

[67] Soong, T. and Spencer, J., "Supplemental energy dissipation: State-of-the-art and state-of-the-practice," *Engineering Structures*, vol. 24, no. 3, pp. 243–259, 2002.

[68] Stone, W. C., Cheok, G. S., and Stanton, J. F., "Performance of hybrid moment-resisting precast beam-column concrete connections subjected to cyclic loading," *ACI Structural Journal (American Concrete Institute)*, vol. 92, no. 2, p. 229, 1995.

[69] Strnadel, B., Ohashi, S., Ohtsuka, H., Ishihara, T., and Miyazaki, S., "Cyclic stress-strain characteristics of ti-ni and ti-ni-cu shape memory alloys," *Materials Science & Engineering A: Structural Materials: Properties, Microstructure and Processing*, vol. A202, no. 1-2, pp. 148–156, 1995.

[70] Strnadel, B., Ohashi, S., Ohtsuka, H., Miyazaki, S., and Ishihara, T., "Effect of mechanical cycling on the pseudoelasticity characteristics of ti-ni and ti-ni-cu alloys," *Materials Science & Engineering A: Structural Materials: Properties, Microstructure and Processing*, vol. A203, no. 1-2, pp. 187–196, 1995.

[71] Sweeney, S. C. and Hayes, J. R., "Shape memory alloy dampers for seismic rehabilitation of existing buildings," in *Wind and Seismic effects, Proceedings of the 27th joint meeting*, (Tsukuba, Japan), 1995.

[72] Thomson, P., Balas, G., and Leo, P., "Use of shape memory alloys for passive structural damping," *Smart Materials and Structures*, vol. 4, no. 1, pp. 36–42, 1995.

[73] Tobushi, H., Shimeno, Y., Hachisuka, T., and Tanaka, K., "Influence of strain rate on superelastic properties of tini shape memory alloy," *Mechanics of Materials*, vol. 30, no. 2, pp. 141–150, 1998.

[74] Van Humbeeck, J., "Non-medical applications of shape memory alloys," *Materials Science and Engineering*, vol. A273275, p. 134148, 1999.

[75] Wayman, C. and Duerig, T. W., "An introduction to martensite and shape memory," in *Engineering aspects of shape memory alloys* (Duerig, T. W., Melton, K., Stockel, D., and Wayman, C., eds.), Butterworth-Heinemann, 1990.

[76] Wolons, D., Gandhi, F., and Malovrh, B., "Experimental investigation of the pseudoelastic hysteresis damping characteristics of shape memory alloy wires," *Journal of Intelligent Material Systems and Structures*, vol. 9, no. 2, pp. 116–126, 1998.